

Disease eradicators take  
aim at measles p. 958

Changing stereotypes while  
you sleep pp. 971 & 1013

Targeting neglected  
protozoan diseases p. 974

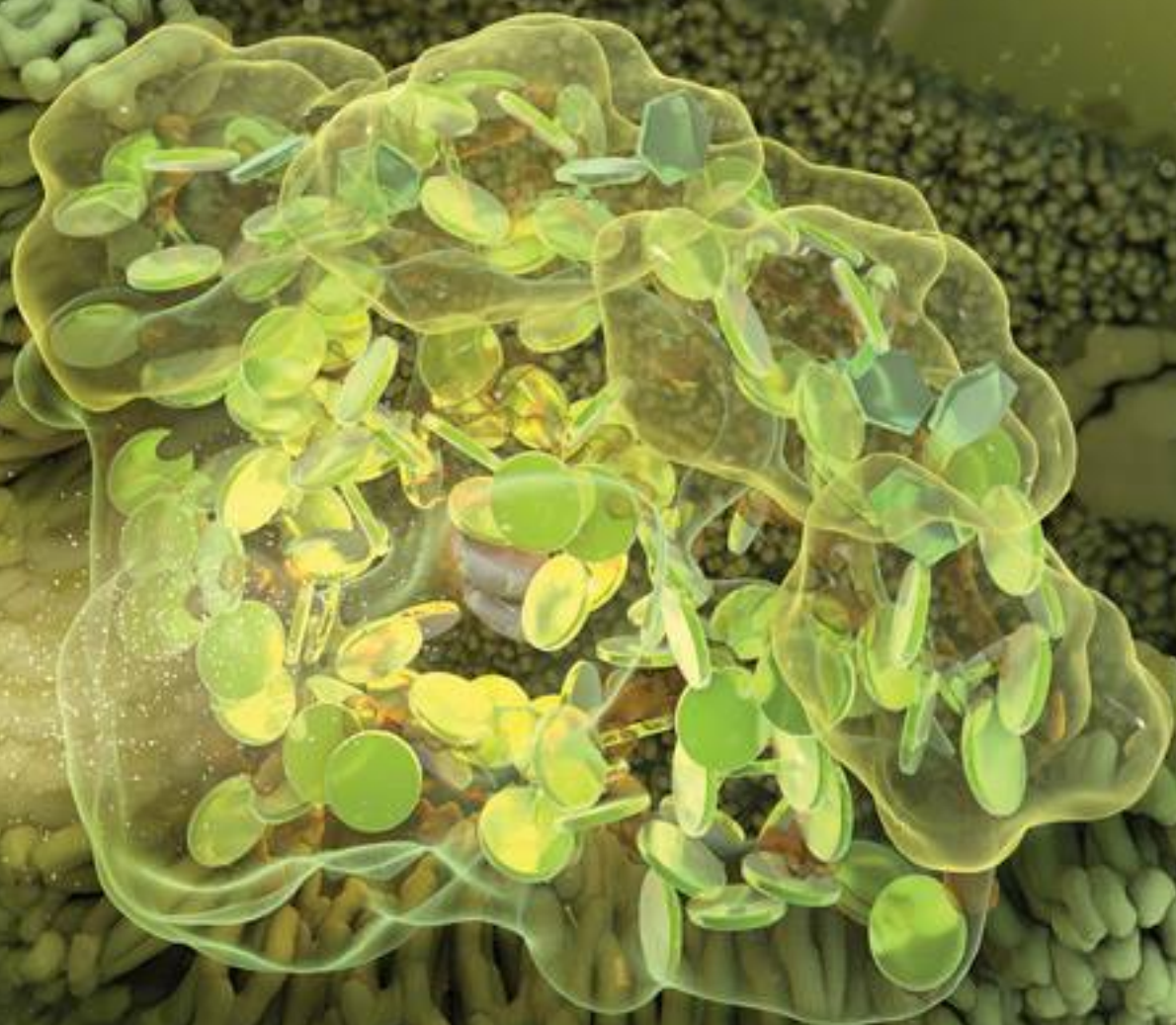
# Science

\$10  
29 MAY 2015  
sciencemag.org

AAAS

## *Light harvester*

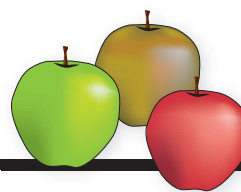
A close look at the machinery of photosynthesis pp. 970 & 989





# CONTENTS

29 MAY 2015 • VOLUME 348 • ISSUE 6238



973

The metamaterials  
fruits of labor



953

## NEWS

### IN BRIEF

**948** Roundup of the week's news

### IN DEPTH

#### **952 BRAZIL CUTS RED TAPE STIFLING BIODIVERSITY STUDIES**

New law eases draconian measures that brought bioprospecting to a standstill  
*By H. Escobar*

#### **953 READING THE TEA LEAVES FOR EFFECTS OF CLIMATE CHANGE**

Cloudy forecast for crops cherished for their complex flavors  
*By C. Larson*

#### **954 The endangered palates list** *By C. Larson*

► PODCAST

#### **954 REPORT FINDS MISCONDUCT BY SURGEON**

Papers omitted data on patient complications, investigator finds  
*By G. Vogel*

#### **956 DEBATE SHARPENS OVER PROPOSED CRITERIA FOR NSF GRANTS**

Supporters say new laws would bolster national priorities; critics see political interference  
*By J. Mervis*

### FEATURES

#### **958 IS MEASLES NEXT?**

Some disease fighters want to eradicate the most contagious virus of all. But does a world still fighting polio have the stomach to try?  
*By L. Roberts*

#### **962 In Vietnam, an anatomy of a measles outbreak** *By L. Roberts*

## INSIGHTS

### PERSPECTIVES

#### **964 CONGRESS'S ATTACKS ON SCIENCE-BASED RULES**

Proposed laws based on false premises could undermine science for the public interest  
*By A. A. Rosenberg et al.*

#### **967 BLOCKING STRESS RESPONSE FOR BETTER MEMORY?**

A drug that affects memory targets a constituent of a cellular stress response mechanism  
*By A. G. Hinnebusch*

► REPORT P. 1027

#### **968 TAMING THE TEMPERAMENTAL METAL TRANSFORMATION**

An alloy can undergo millions of cycles of shape changes in response to stress jumps  
*By R. D. James*

► REPORT P. 1004

#### **970 A CLOSE VIEW OF PHOTOSYSTEM I**

A high-resolution structure provides insight into solar energy conversion during photosynthesis  
*By R. Croce*

► RESEARCH ARTICLE P. 989

#### **971 EXPLOITING SLEEP TO MODIFY BAD ATTITUDES**

Targeted memory reactivation of training-induced social counterbias during sleep  
*By G. B. Feld and J. Born*

► REPORT P. 1013

#### **973 OBTAINING OPTICAL PROPERTIES ON DEMAND**

Reconfigurable metamaterials provide a flexible platform for nanophotonic technology  
*By N. I. Zheludev*

#### **974 OVERCOMING NEGLECT OF KINETOPLASTID DISEASES**

Drug development offers hope for controlling diseases that affect millions of people worldwide  
*By G. Bilbe*

#### **976 EXPANDING THE ROLE OF METABOLISM IN T CELLS**

A protein links mitochondrial energetics to T cell proliferation  
*By D. O'Sullivan and E. L. Pearce*

► RESEARCH ARTICLE P. 995

#### **977 FLEXIBLE GENE POOLS**

Rapid genetic exchange leads to mosaic genomes in cyanobacterial populations  
*By M. M. Desai and A. M. Walczak*

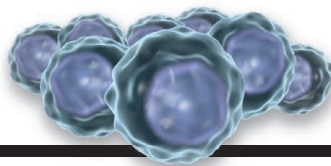
► REPORT P. 1019

Science Staff .....	946
AAAS News & Notes .....	983
New Products .....	1044
Science Careers .....	1046



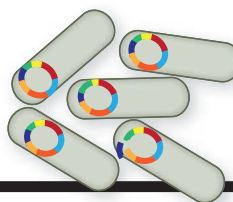
949





# 976 & 995

T cell metabolic  
reprogramming



# 977 & 1019

Maintaining  
microbial diversity

## BOOKS ET AL.

### 979 BIOCODE

By D. Field and N. Davies,  
reviewed by M. A. Goldman

### 980 MARKS OF GENIUS

By S. Hebron, curator,  
reviewed by A. Robinson

### 980 SPURIOUS CORRELATIONS

By T. Vigen

## LETTERS

### 981 TIME FOR A DATA REVOLUTION IN CHINA

By R. Chen et al.

### 981 QUALIFYING POLLINATOR DECLINE EVIDENCE

By J. Ghazoul

### 982 RESPONSE

By D. Goulson et al.

### 982 TECHNICAL COMMENT ABSTRACTS



# RESEARCH

## IN BRIEF

985 From *Science* and other journals

## REVIEW

### 988 POROUS MATERIALS

Function-led design of new  
porous materials

A. G. Slater and A. I. Cooper

REVIEW SUMMARY; FOR FULL TEXT

dx.doi.org/10.1126/science.aaa8075

## RESEARCH ARTICLES

### 989 PHOTOSYNTHESIS

Structural basis for energy transfer  
pathways in the plant PSI-LHCI  
supercomplex X. Qin et al.

► PERSPECTIVE P. 970

### 995 T CELL METABOLISM

The protein LEM promotes  
CD8<sup>+</sup> T cell immunity through  
effects on mitochondrial respiration  
I. Okoye et al.

► PERSPECTIVE P. 976

## REPORTS

### 1001 INORGANIC CHEMISTRY

Synthesis and characterization of  
P<sub>2</sub>N<sub>3</sub><sup>-</sup>: An aromatic ion composed of  
phosphorus and nitrogen  
A. Velian and C. C. Cummins

### 1004 SHAPE MEMORY ALLOYS

Ultralow-fatigue shape memory alloy  
films C. Chluba et al.

► PERSPECTIVE P. 968

### 1007 MEMORY

Engram cells retain memory under  
retrograde amnesia T. J. Ryan et al.

### 1013 COGNITIVE NEUROSCIENCE

Unlearning implicit social biases  
during sleep X. Hu et al.

► PERSPECTIVE P. 971

### 1016 PALEOCLIMATE

Enhanced tropical methane production  
in response to iceberg discharge in the  
North Atlantic R. H. Rhodes et al.

### 1019 MICROBIAL DIVERSITY

Fine-scale diversity and extensive  
recombination in a quasisexual  
bacterial population occupying a  
broad niche M. J. Rosen et al.

► PERSPECTIVE P. 977

### 1024 CELL ADHESION

Mechanical strain induces E-cadherin-  
dependent Yap1 and  $\beta$ -catenin  
activation to drive cell cycle entry  
B. W. Benham-Pyle et al.

## 1027 STRESS RESPONSES

Mutations in a translation initiation  
factor identify the target of a memory-  
enhancing compound Y. Sekine et al.

► PERSPECTIVE P. 967

## 1031 IMMUNE TOLERANCE

Group 3 innate lymphoid cells mediate  
intestinal selection of commensal  
bacteria-specific CD4<sup>+</sup> T cells  
M. R. Hepworth et al.

## 1036 CANCER

The transcription factor GABP  
selectively binds and activates the  
mutant TERT promoter in cancer  
R. J. A. Bell et al.

## 1040 EMBRYO DEVELOPMENT

A cysteine-clamp gene drives embryo  
polarity in the midge *Chironomus*  
J. Klomp et al.

## DEPARTMENTS

### 947 EDITORIAL

Watchdogs of the European system  
By James Wilsdon

### 1050 WORKING LIFE

All in the family  
By Rachel Bernstein

## ON THE COVER



Proteins inside the  
chloroplast of a  
plant cell, including  
the supercomplex  
of photosystem I  
and light-harvesting  
complex I, work  
together to turn light  
into chemical energy.

A high-resolution crystal structure by Qin  
et al. reveals the positions of chlorophylls a  
and b (shown in the foreground as circular  
and hexagonal disks, respectively) and  
carotenoids (shown in orange). See pages  
970 and 989. *Illustration: Valerie Altounian/*  
*Science; structure based on experimental*  
*atomic coordinates (PDB ID 4XK8)*

SCIENCE (ISSN 0036-8075) is published weekly on Friday, except the last week in December, by the American Association for the Advancement of Science, 1200 New York Avenue, NW, Washington, DC 20005. Periodicals mail postage (publication No. 484460) paid at Washington, DC, and additional mailing offices. Copyright © 2015 by the American Association for the Advancement of Science. The title SCIENCE is a registered trademark of the AAAS. Domestic individual membership and subscription (51 issues): \$153 (\$74 allocated to subscription). Domestic institutional subscription (51 issues): \$1282. Foreign postage extra: Mexico, Caribbean (surface mail) \$55; other countries (air assist delivery) \$85. First class, airmail, student, and emeritus rates on request. Canadian rates with GST available upon request. GST #R1254 88122. Publications Mail Agreement Number 1069624. Printed in the U.S.A. Change of address: Allow 4 weeks, giving old and new addresses and 8-digit account number. Postmaster: Send change of address to AAAS, P.O. Box 96178, Washington, DC 20090-6178. Single-copy sales: \$10.00 current issue, \$15.00 back issue prepaid includes surface postage; bulk rates on request. Authorization to photocopy material for internal or personal use under circumstances not falling within the fair use provisions of the Copyright Act is granted by AAAS to libraries and other users registered with the Copyright Clearance Center (CCC) Transactional Reporting Service, provided that \$30.00 per article is paid directly to CCC, 222 Rosewood Drive, Danvers, MA 01923. The identification code for Science is 0036-8075. Science is indexed in the Reader's Guide to Periodical Literature and in several specialized indexes.



# Watchdogs of the European system

**H**enry Kissinger, as U.S. Secretary of State, is famously said to have asked: “If I want to call Europe, who do I call?” Until recently, the scientific community thought it had an answer to this question: the chief scientific adviser (CSA) to the president of the European Commission (EC). Two weeks ago, that changed.

For 3 years, Anne Glover, a Scottish microbiologist, served as the CSA, a high-profile ambassador for European science and a champion of scientific evidence in the machinery of Brussels policymaking. She worked tirelessly to build a network of science advisers or equivalents across the 28 member states of the European Union (EU). All of this came to an abrupt halt in November 2014, when the handover to a new EC under President Jean-Claude Juncker saw the CSA role vanish overnight. This provoked dismay from scientific organizations, who condemned it as a backward move, out of step with the onward march of evidence-informed policy making.

Viewed from the Berlaymont, the EC’s headquarters, the decision was more finely balanced. Although the model of a presidential or prime ministerial science advisor is firmly established in countries such as the United States, United Kingdom, Ireland, and New Zealand, it sits more awkwardly with the political cultures of Germany, France, and other EU countries, which tend to rely on committees and other distributed sources of expertise. Brussels also has a distinct political culture, and, as Anne Glover admits, an individual with few resources was ill equipped to intervene effectively in the delicate balance of its decision-making.

President Juncker insisted that he was still committed to scientific advice and asked Carlos Moedas, the Commissioner for Research, Science and Innovation, to lead a review of how it could be better organized. Two weeks ago, the findings were unveiled. As expected, the CSA remains dead and buried and will be replaced by a seven-strong “high-level group” of experts, who will be appointed be-

fore the end of the year. These experts, described by a senior official as “watchdogs of the system,”\* will be fully independent but supported by a team of around 25 staff from the EC’s research directorate. Further resources of “up to €6 million” will be offered to Europe’s national academies to enable them to play a greater role in the provision of advice.† Good working links will also be developed to the EC’s in-house science service, the Joint Research Centre.

On paper, this is an elegant solution to a tricky design brief. Involving the academies is a particularly smart move, as it will allow the high-level group to draw on a far deeper pool of expertise. The group will also reach out to universities across Europe and to global networks of expertise, such as the recently formed International Network for Government Science Advice.

However, parts of the new mechanism still need to be fine-tuned. Anne Glover drew fire from some quarters for speaking out in support of genetically modified crops. Will the new group be similarly independent and free to engage in controver-

sial debates, or will it only be able to answer questions posed to it by the EC? Another unknown is how the group will be selected. The EC says that scientific excellence is the main criterion, but as with all EU bodies, it will have to nod to the diversity of member states. The group is also meant to combine insights from several disciplines, which suggests at least one social scientist and one engineer joining natural scientists in the mix. And of course, connecting science to policy is a serious craft in itself, so a Nobel Prize may be less of a trump card than a few years of experience in a policy role.

A search committee for the seven advisers will start work any day now. After a turbulent few months, the EC has an opportunity to put in place a genuinely world-class, interdisciplinary, and independent advisory system. Europe’s scientists, its policy-makers—and above all, its 500 million citizens—deserve nothing less.

– James Wilsdon



*James Wilsdon (@jameswilsdon) is a professor of science and democracy at the Science Policy Research Unit, University of Sussex, Brighton, UK. E-mail: J.Wilsdon@sussex.ac.uk*



***“...the EC has an opportunity to put in place a genuinely world-class, interdisciplinary, and independent advisory system.”***

\*<http://sciencebusiness.net/news/77034/%E2%80%98Watchdogs-of-the-system%E2%80%98-the-EU%E2%80%99s-new-scientific-advisory-panel-explained>. †<http://news.sciencemag.org/europe/2015/05/breaking-european-commission-create-new-high-level-science-advice-panel>.



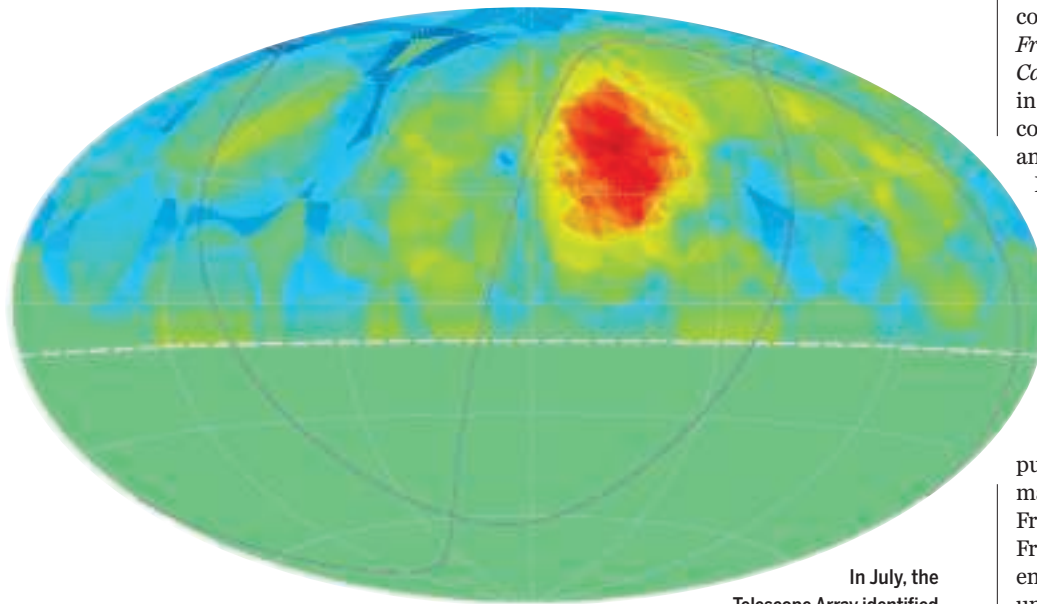
# NEWS

“Climate change constitutes a serious threat to global security, an immediate risk to our national security, and ... it will impact how our military defends our country.”

**President Barack Obama** on 20 May, to the graduating Coast Guard Academy class. The same day, the White House released a new report on the security implications of climate change.

## IN BRIEF

### Massive cosmic ray detector grows



In July, the Telescope Array identified a potential cosmic ray hotspot (in red).

**J**apan will spend \$3.7 million to expand a huge array of particle detectors that studies the highest energy cosmic rays. The current Telescope Array (TA) consists of 507 detectors spread over 700 square kilometers of Utah desert to detect the avalanches of particles triggered when the rays strike the atmosphere. The international collaboration of 130 physicists will add 400 detectors, nearly quadrupling its area. TA also has three batteries of telescopes that detect the light from particle avalanches, and researchers hope the U.S. National Science Foundation will fund two more. Japan paid two-thirds of TA's original \$25 million cost. The rays' origins remain unknown. Physicists with the even larger Pierre Auger Observatory in Argentina reported in 2007 that the rays seem to emerge from the fiery hearts of certain galaxies. Although that result hasn't held up, last July TA researchers reported hints of a hotspot in the northern sky. The expanded TA will test whether the hotspot is real, says Hiroyuki Sagawa of the University of Tokyo, TA's spokesperson, and "with two observatories we can see the whole sky."

## AROUND THE WORLD

### Editors sacked in OA clash

**LAUSANNE, SWITZERLAND** | A fast-growing open-access (OA) publishing company has dismissed virtually the entire leadership of two medical journals amid a heated conflict over editorial independence.

*Frontiers in Medicine* and *Frontiers in Cardiovascular Medicine* were launched in 2014 as part of Frontiers, an OA company founded and run by husband-and-wife couple Henry and Kamila

Markram, both neuroscientists at the Swiss Federal Institute of Technology.

(Henry Markram also created the controversial €1 billion Human Brain Project.) On 7 May, the two journals removed 31 editors after the editors complained that company staff were interfering with editorial decisions and violating core principles of medical publishing. The editors say Frontiers' publication practices are designed to maximize profits, not the quality of papers. Frederick Fenter, executive editor at Frontiers, says the company had to fire the entire group because they were holding up the publication of papers until their demands were met, which he likens to "extortion." <http://scim.ag/OAconflict>

### House committee OKs cures act

**WASHINGTON, D.C.** | A committee in the U.S. House of Representatives last week unanimously approved the 21st Century Cures Act, a major effort to spur medical innovation. The bill creates an Innovation Fund within the National Institutes of Health (NIH) with \$10 billion in mandatory funds for 5 years, which will support young scientists; high-risk, high-reward research; and a program to allocate \$500 million a year in matching funds to NIH's institutes for specific research areas. The bill also sets up another fund to dole out an annual \$110 million for the next 5 years to support several efforts at the Food and Drug Administration, including the evaluation of new drug development tools and the use of patient feedback in the review of new therapies. The bill next goes to the House floor for a vote.





These jaws and teeth may belong to Lucy's cousin.

## 'Lucy' was not alone

**T**he famous human relative known as "Lucy" may have shared her territory with a related species. Since the 3.2-million-year-old skeleton was discovered in Ethiopia in 1974, many other fossils of her species, *Australopithecus afarensis*, have been found nearby. But claims for other australopithecine species living at the same time have been controversial (*Science*, 28 March 2003, p. 1994). Now, in this week's issue of *Nature*, scientists working in Ethiopia report uncovering a new species they call *A. deyiremeda* in sediments dated 3.3 million to 3.5 million years old. (In the local Afar language, *deyi* means "close" and *remeda* means "relative.") The new fossils, including parts of two upper jaws and two lower jaws plus some associated teeth, have smaller teeth and more forward-facing cheekbones than *A. afarensis*. If these differences represent a new species, at least two early human relatives may have lived in close proximity and carved out separate ecological niches during a critical period in human evolution.

It will then need to be reconciled with a Senate version still in discussion. <http://scim.ag/21centcureOK>

## World Heritage Site under attack

**PALMYRA, SYRIA** | Archaeologists are concerned that Islamic State militants, who took control of the ancient city of Palmyra last week, killing hundreds of people, will also destroy its monuments and artifacts. Palmyra, one of six World Heritage Sites in Syria, was at a crossroads of Greek, Roman, and Persian cultural influences and contains Roman barracks and temples, a medieval citadel, and the Temple of Bel, which dates

to the 1st century C.E. The group destroyed another World Heritage Site, Hatra, in northern Iraq, and also sells antiquities as a source of funding, according to Katharyn Hanson, a specialist in protecting cultural heritage at the University of Pennsylvania. Legislation has been introduced in the U.S. House of Representatives to ban the sale of antiquities imported from Syria, but it has not come up for a vote.

## Scientists seek volunteer readers

**SAN DIEGO, CALIFORNIA** | Biomedical research is often slow and incremental, but the discovery of a hidden connection can provide a leap forward. Last week, researchers at the Scripps Research Institute launched an initiative, dubbed Mark2Cure, that will ask volunteers to help find these often needle-in-a-haystack links by scanning papers for key terms to help create a powerful searchable database. The National Institutes of Health already spends millions of dollars hiring professional curators to do this sort of work. Now, the Scripps team aims to engage laypeople to do

the same job—in small chunks at a time using their own computers—for free. The campaign is first reaching out to a highly motivated crowd—the small community of people affected by NGLY1 deficiency, a newly discovered genetic disorder that can cause liver problems, poor reflexes, an inability to produce tears, and sometimes seizures. <http://scim.ag/Mark2Cure>

## U.S. push-pull on ITER

**WASHINGTON, D.C.** | For the second year in a row, Senate budgetmakers have moved to pull the United States out of ITER, the huge and hugely over budget international fusion experiment under construction in Cadarache, France. The cut comes in the Senate version of the so-called energy and water spending bill, which would fund the Department of Energy and other agencies for fiscal year 2016. But nixing ITER is hardly a done deal: On 1 May, legislators in the House of Representatives passed their own version of the energy and water bill, which includes \$150 million for the U.S. contribution to ITER—the amount the White House has requested. The Senate subcommittee had also moved to cut funding to ITER last year, when the Democrats controlled the Senate. But the final budget bill for fiscal year 2015, signed by President



Roman funerary temple in Palmyra, dating to the 3rd century C.E.

PHOTOS: (TOP TO BOTTOM) LAURA DEMPSEY; © ROBERT PRESTON/PHOTOGRAPHY/ALAMY





## Robin mom fooled by fake egg

**C**owbirds are the ultimate deadbeat parents: They sneak their eggs into the nests of other birds. Such behavior has prompted the evolution of eggs of many shapes, sizes, colors, and patterns and a recognition system to help duped parents identify their own eggs. To study this arms race, animal behaviorist Mark Hauber of Hunter College in New York City is using 3D printers, working out the right materials to use to make fake eggs convincing. This week in *PeerJ*, Hauber and colleagues highlight the importance of color: They report that robins accepted 3D eggs painted blue, like real robins' eggs—but rejected beige 3D “cowbird” eggs. And egg patterns may be even more important than color, which is limited in variability because nature has only two eggshell pigments to work with, Hauber and colleagues reported last week in *Biology Letters*. To test patterns' importance, the team is using a device called EggBot, which paints precision patterns for Easter eggs and other decorations, to “make incredibly faithful replicas and fine-tune variations on the theme,” Hauber says.

3D printed robin's egg (at left) fits right in.

Barack Obama on 16 December 2014, contained \$150 million for the project. <http://scim.ag/ITERpushpull>

## Big cuts to non-‘core’ sciences

**WASHINGTON, D.C.** | You won't actually find the numbers anywhere in the bill, but a congressional spending panel has endorsed a 16% cut in funding next year for the social and geosciences at the National Science Foundation (NSF). The cuts result from a new formula created by the chair of NSF's spending panel, Representative John Culberson (R-TX), which requires NSF to spend 70% of its research dollars on four directorates. Although NSF's overall research spending in 2016 would grow by only 0.7% in the bill, Culberson provides an 8% boost to the favored disciplines and holds other research activities at 2015 levels. That leaves the social and geosciences directorates with \$255 million less than they have this year.

## Gay marriage study retracted

**LOS ANGELES, CALIFORNIA** | An author of a study concluding that even relatively short conversations with a gay canvasser could make voters more supportive of gay marriage and equality has asked that it be withdrawn. Last week, political scientist Donald Green of Columbia University sent a retraction request to *Science* after he became

convinced that his co-author Michael J. LaCour, a political science Ph.D. candidate at the University of California, Los Angeles, had made up data for the December 2014 paper. The study drew on apparent in-person and Internet surveys of some 9500 registered voters in California. However, researchers attempting a follow-on study found that the survey company cited by the paper claimed no knowledge of the project. A tweet on LaCour's Twitter account last week said he is preparing to offer a defense “at my earliest opportunity.” *Science* has added an Editorial Expression of Concern to the paper. <http://scim.ag/gaymarret>

## New RIKEN head's tenure plan

**WAKO, JAPAN** | New RIKEN President Hiroshi Matsumoto wants to introduce a tenure system at Japan's network of national laboratories. As elsewhere, beginning scientists in Japan are on a treadmill of short-term appointments. This has skewed research toward quick results needed to burnish resumes for recurring job hunts and “creates a very difficult situation for young researchers,” Matsumoto said at a press conference last week. A tenure scheme would offer the hope of a stable career path and help retain the best young talent. Matsumoto also intends to push RIKEN scientists and administrators to routinely use English to smooth international cooperation. He wants to give researchers

more flexibility in spending appropriated funds and to hire more technicians, too. “My mission is to support the capabilities and the ideas of researchers,” he said.

## NEWSMAKERS

### Famed mathematician dies


**John Forbes Nash Jr.**, who shared the 1994 Nobel memorial prize in economics, died on 23 May at the age of 86. Nash did



trailblazing work in algebraic geometry, the theory of partial differential equations, and the theory of noncooperative games. His 1950 doctoral dissertation from Princeton University explored the Nash

equilibrium, a strategic deadlock that can arise in several-player games. Researchers have applied the concept to topics including arms control, macroeconomics, and political science. Nash suffered from a decades-long mental illness, described in the biography *A Beautiful Mind* and a film by the same name. His honors included the John von Neumann Theory Prize; the 1994 Nobel; and the 2015 Abel Prize, presented by the king of Norway. Nash and his wife, Alicia de Lardé Nash, were returning from the Oslo award ceremony when their taxi lost control and crashed, killing both.





Shipping this kind of velvet worm out of Brazil was labeled biopiracy.

## NATURAL RESOURCES

# Brazil cuts red tape stifling biodiversity studies

New law eases draconian measures that brought bioprospecting to a standstill

By **Herton Escobar**, in São Paulo, Brazil

**W**hen Carlos Jared tried to ship a jar of dead velvet worms collected in Brazil's Atlantic Forest to a colleague in Germany in 2006, he had no plans to derive a drug or other product from the creatures. He just wanted to probe the reproductive system of a rare invertebrate that gives birth to live young. But Brazilian authorities denounced him as a "biopirate."

The evolutionary biologist at the Instituto Butantan in São Paulo had run afoul of a law aiming to clamp down on what Brazil perceived as rampant pillaging of its biological resources. Jared hadn't filled out all the paperwork required under law MP 2186, so the worms were confiscated. Worse was yet to come. "They dragged my name through the mud. It was a psychological massacre," he says. It took him 6 years to get another permit for fieldwork, and he is still fighting in court thousands of dollars in fines.

Jared is not the only scientist to run afoul of the draconian regulations, sometimes because of nothing more than a clerical oversight. "Biodiversity was deemed so valuable that nobody was allowed to research it anymore," says Eduardo Pagani, drug develop-

ment manager at the Brazilian Biosciences National Laboratory in Campinas. "They locked it in a safe and criminalized anyone who tried to work with it."

But after years of wrangling over how to fix the statute, in which officials sought to balance the interests of scientists, the agricultural industry, and biotech firms with those of indigenous populations demanding compensation for traditional knowledge, Brazil President Dilma Rousseff last week signed a law that is raising hopes among

ter Aldo Rebelo while unveiling the law.

The scientific community has greeted the new law with a sigh of relief. "It's an enormous improvement from what we have now," says Helena Nader, president of the Brazilian Society for the Advancement of Science in São Paulo. "We hope this will get scientists and industry excited about working with biodiversity again. There is a lot of untapped potential there," adds Eliana Fontes, a biosafety expert at the Brazilian Agricultural Research Corp. in Brasília and a former president of the Genetic Heritage Management Council (CGEN), the legal body that was created to regulate and enforce MP 2186, now superseded by the biodiversity law.

When MP 2186 came on the books in 2001, its intentions were good. It was passed in response to a contract between the nonprofit company Bio-Amazonia and Novartis that gave the European drug giant exclusive rights to research, patent, and sell products derived from microbes collected in the Brazilian Amazon. (The agreement drew a public outcry and was annulled.) While MP 2186's goal was to combat biopiracy, its wording cast suspicion on even standard research practices involving life forms. "It was so difficult to get permits that I seriously considered not doing research in Brazil anymore," says

---

***"It's an enormous improvement from what we have now."***

**Helena Nader**, Brazilian Society for the Advancement of Science

scientists. Like its predecessor, the new "biodiversity law" regulates research on "genetic resources": an all-encompassing term covering everything from genes and proteins to oils and fragrances. It sets rules for sharing benefits with indigenous peoples when R&D leads to a product, such as a drug, shampoo, energy drink, or industrial enzyme, while eliminating bureaucratic hassles and encouraging biodiversity research. Scientists will no longer be "molested" or "bullied" by unreasonable regulation, said science minis-

Emilio Bruna, an ecologist at the University of Florida in Gainesville who studies habitat fragmentation in the Amazon and the Cerro. Two of his students moved their projects to Costa Rica and Ecuador.

Amendments to MP 2186 gradually eased restrictions on basic research. But prospecting for natural compounds remained a daunting challenge. Before starting research, scientists and companies had to get permission from CGEN and sign a benefit-sharing contract with the indigenous group identified with a particular resource. "How can you sign a contract for a product when you don't know if it's going to work, or even if it's going to exist?" asks Paulo Sérgio Beirão, a biochemist at the Federal University of Minas Gerais in Belo Horizonte.

Under the new law, Brazilian scientists need not ask CGEN for permission to do research. All they must do is register their project in a database and document permission from the appropriate indigenous group. Contracts and other legal matters will come into play only if research leads to a product. "A clear distinction is made now between scientific research and technological development for commercial purposes," says Francine Leal, an environmental lawyer in Curitiba who has consulted on the law. Foreign scientists are prohibited from prospecting for genetic resources in Brazil, unless they are part of a company or institution that strikes a partnership with a Brazilian counterpart.

The law is getting a cool reception from indigenous and other local groups, who believe the rules of access to traditional knowledge and benefit sharing are skewed in favor of companies. "The law moves in the right direction for science and technology," says Carlos Joly, a plant ecologist at the University of Campinas and a key figure in the regulation of biodiversity research in Brazil, "but there are still major problems with it." For instance, he says, the law is blurry about the rights of indigenous and local communities to withhold access to traditional knowledge, if they felt an agreement would not benefit them.

Jared, at least, would have fared better under the new law, which abolishes the case-by-case permits for shipments abroad: It only requires noting them in a registry. "The spirit of the law," Fontes says, "is to trust researchers." But for Jared, the moment may have passed. He can retrieve his velvet worms from the University of São Paulo's zoology museum, where they were deposited for safekeeping, but the German colleague he hoped to collaborate with has long since retired. ■

*Herton Escobar writes for O Estado de São Paulo.*

## AGRICULTURAL RESEARCH

# Reading the tea leaves for effects of climate change

Cloudy forecast for crops cherished for their complex flavors

By **Christina Larson**,  
in Xishuangbanna, China

"Taste it," Selena Ahmed says, offering a delicate green bud plucked from a tea plant on a terraced hillside here. It's like a tiny cup of espresso: bitter at first, then a caffeine buzz. When

Ahmed returns to Montana State University, Bozeman, the ethnobotanist will analyze chemical constituents of the leaves along with other data, looking for clues to how climate change will affect the taste of the tea for which southwestern China's Yunnan province is famed.

"We drink tea for the quality, not because it's providing energy [from] calories," says Sean Cash, an applied economist at Tufts University in Massachusetts, who works

What they find could have implications for scores of other crops, from coffee to chocolate to cherries, whose taste and value also depend on local climates (see p. 954). "Our agricultural system has adapted to a set of conditions that are now in flux," says Samuel Myers, an epidemiologist at Harvard Medical School in Boston who studies how rising carbon dioxide concentrations in the atmosphere alter crop nutrients. "Understanding the implications on both quantity and quality is very important."

"Rainfall is central for tea," says Colin Orians, a chemical ecologist at Tufts, who is collaborating with Ahmed and Cash. In Xishuangbanna, "the monsoon rains come, and within 5 days, the quality of tea really drops. You can see big shifts in the chemistry." During the summer monsoon, which brings 80% of the annual rainfall, tea leaves grow



A Hua farmer in Yunnan province picks tea leaves that will later be fermented into the prized pu'er variety.

with Ahmed. The complex mix of phytochemicals responsible for its taste may be far more sensitive to climate than are the yields of commodity crops. And an ideal place to study the relationship is tropical Yunnan, known for an oxidized and fermented black tea called pu'er, one of China's most prized and already being touched by climate change. Earlier this year Cash, Ahmed, and others embarked on a 4-year project backed by the U.S. National Science Foundation that examines the linkages among climate, tea quality, and farmer livelihoods.

roughly twice as quickly as in the dry season. That's not as happy a prospect for farmers as it sounds, says Wenyan Han of the Tea Research Institute in Hangzhou. "Quality and yield often exist in inverse balance," he says. "If one goes up, the other goes down." Here in the Bulang Mountains, pu'er harvested in the spring, before the monsoon, tastes richer and fetches a premium: \$680 per kilogram, compared with \$405 for summer pu'er, harvested during the rainy season.

Orians and colleagues have traced the chemical shifts responsible. During the



## The endangered palates list

Climate change threatens crops beloved for rich flavors rather than caloric content. Here are a few of the most vulnerable:

**COFFEE** Growers face a grim outlook for the Arabica bean, source of 70% of the global coffee supply. According to a 14 April report in *PLOS ONE*, a temperature rise of 2°C to 2.5°C by midcentury will wreak havoc on Arabica harvests globally. Brazil will “suffer great losses,” losing up to 25% of its territory suitable for the highland-loving plants, says Peter Läderach of the International Center for Tropical Agriculture in Cali, Colombia.

**COCOA** Warmer weather and more frequent droughts in West Africa, especially Ghana and Ivory Coast, will raise evapotranspiration rates in cocoa plants, which means less water for pods and lower yields of chocolate’s main ingredient.

**MAPLE SYRUP** Late winter, when the mercury begins to edge above freezing, is the time to tap sugar maples. Sap flows “when temperatures fluctuate around freezing, between day and night,” says Joshua Rapp, a biologist at the University of California, Davis. Warming in eastern North America is shortening the sap season and curtailing maple syrup production.

**CHERRIES** Wild temperature swings are bad news for fruits. Cherry trees are especially sensitive. In 2012, a frigid winter followed by a warm spring destroyed 90% of Michigan’s tart cherry crop, decimating supplies for pies, jams, and confections.

**TOBACCO** Call it global warming’s health dividend. The leaves and roots of tobacco grown in elevated CO<sub>2</sub> environments have less nicotine, the secondary metabolite that makes cigarettes addictive, according to the Institute of Plant Genetics and Crop Plant Research in Germany. ■

monsoon, when growth speeds up, leaf concentrations of two key groups of secondary metabolites—catechins and methylxanthines—fall to half their dry-season levels, they reported last October in *PLOS ONE*. Secondary metabolites protect plants from threats such as excess UV exposure or pests, and some of these compounds have potent effects in humans as well. Catechins, also found in blackberries and grapes, are antioxidants linked to improved cardiovascular health, reduced prostate cancer risk, and lower blood cholesterol. Caffeine and other methylxanthines are central nervous stimulants.

Dilution is unlikely to be the only explanation for the fall in secondary metabolites during the monsoon, Ahmed says. Higher temperatures, cloudier days, and different insect pests could all have an effect. “If a plant doesn’t have a cue to produce high concentrations or specific secondary metabolites, it won’t,” she says. Her team has identified 59 seasonally unique compounds in tea, the majority of them in the higher quality spring tea, they reported last November in the *Journal of Chromatography A*.

The mix is likely to change. Average temperatures in Kunming, Yunnan’s capital, have climbed 1.5°C over the past 50 years. And the monsoon is arriving later: In 2011, it began some 22 days later than in 1980, Cash and colleagues report in a paper under review at *Climatic Change*.

Because land warms faster than ocean, the land-sea temperature gradient that drives Asian monsoon systems will increase. “In very broad brushstrokes for the 21st century,” summer precipitation “may be more intense,” says Caroline Ummenhofer, a geographer at the Woods Hole Oceanographic Institution in Massachusetts, although she notes that the projections are uncertain.

“Climate change is not necessarily all doom and gloom for farmers,” Ahmed notes. If the dry season grows drier and the wet season grows wetter, as most climate models predict, the dry-season harvest could become even more valuable as the stressed plants boost their production of secondary metabolites and improve pu’er tea’s flavor.

But prolonged dryness has diminishing returns. “If the weather is too dry, that can reduce the number of buds” or kill plants, Ahmed says. That’s already a concern in India’s Assam region, famed for its black tea. Summer days in Assam more frequently top 35°C—the “upper limit for growing tea,” says Ellie Biggs, a geographer at the University of Southampton in the United Kingdom.

Tea lovers can only hope that the prognosis for tea in a changing climate doesn’t pan out like the finest pu’er: bitter and black. ■



### REGENERATIVE MEDICINE

## Report finds misconduct by surgeon

Papers omitted data on patient complications, investigator finds

By Gretchen Vogel

**A**n investigation has concluded that surgeon Paolo Macchiarini, famous for transplanting tissue-engineered tracheae into more than a dozen people, committed scientific misconduct in publications describing the results of the operations. The Karolinska Institute in Stockholm, where Macchiarini is a visiting professor, commissioned the external inquiry after allegations arose in August 2014.

The investigator, Bengt Gerdin, professor emeritus of surgery at Uppsala University, examined six papers about the patients and one on animal tests of the procedure and found “a systemic misrepresentation of the truth that leads the reader to have a false impression of the success of the technique,”



Paolo Macchiarini made headlines for giving patients new tracheae.

he told *Science*. That constitutes misconduct, he says. He faults the papers for inaccurate or misleading descriptions of the condition of patients at the time of publication and for stating that ethical permission had been obtained for the work although there is none on record. The report, submitted to the Karolinska vice chancellor on 13 May, concludes that Macchiarini “is primarily responsible for incorrect or incomplete data published in numerous articles and thus guilty of scientific misconduct.”

Macchiarini has disputed the allegations, but he told *Science* that he could not comment further on Gerdin’s report, which is in Swedish, until he had received an official version in English. He and his colleagues attracted widespread attention by developing a technique intended to help patients whose tracheae were badly damaged by cancer, injury, or birth defects. They designed a polymer scaffold, which is seeded with the patient’s stem cells to construct a replacement trachea (*Science*, 19 April 2013, p. 266). The stem cells are supposed to grow over the scaffold and eventually develop into a living organ.

The allegations of misconduct came from four researchers at the Karolinska Institute and the affiliated Karolinska University Hospital, where several of the operations took place. The four critics—who co-authored several of the controversial papers—became concerned in the fall of 2013 when they learned of serious com-

plications in the first patient to receive an artificial trachea at Karolinska. (They say they were not involved in the care of that patient after the initial surgery in 2011. He was treated at a hospital at Karolinska’s Huddinge campus, 25 kilometers from the critics’ primary location in Solna.) When they looked into the case records of the three patients operated on at Karolinska, they concluded that the papers failed to mention the serious complications the patients had suffered, and ultimately asked Karolinska to investigate.

In particular dispute is a paper published in December 2011 in *The Lancet*. It claims that, 5 months after surgery, the recipient, a 36-year-old graduate student, had no complications and the graft was showing early signs of tissue growth. However, there are no clinical records of the patient’s status 5 months after surgery, Gerdin points out; the available clinical data in the records were from August, 11 weeks after surgery. In November, several weeks after the paper was accepted but before it was published, the patient was readmitted to Karolinska with complications that ultimately required a stent to keep his airway open. The engineered trachea had significant problems, the critics say in their complaint, but Macchiarini did not notify *The Lancet*. Nor did he mention the complications in a *Lancet* review paper published 3 months later. That paper says that the graft was in good condition 8 months after surgery.

In his initial written response to the accusations, Macchiarini denied any misrepresentation. Philipp Jungebluth, an assistant professor at Karolinska who was recruited with Macchiarini as a postdoctoral researcher, also maintains that all the papers in question are accurate. Both he and Macchiarini say that the complications that arose after the paper was accepted were not relevant, because the article was intended to provide a clinical snapshot. Jungebluth says that despite the complications, the patient did well for at least a year after his initial surgery. He finished his master’s degree and had a second child after the transplant, Jungebluth notes. All the patients who received artificial tracheae were complex medical cases who had no other options, he says, and post-transplant complications were to be expected.

The four physicians who reported concerns about Macchiarini also alleged that he did not get proper authorization from an ethics review board for the surgeries and failed to get informed consent from the patients. Such issues fall under Swedish health care law rather than scientific misconduct regulations, Gerdin says, so he did not pass judgment on what kind of approval was needed. The Swedish Medical Products Agency referred the case to a prosecutor earlier this month.

A separate investigation by Karolinska’s ethics council into allegations of misconduct brought by Pierre Delaere, a surgeon at UZ Leuven in Belgium, was completed in April. Delaere, who has developed a different method for replacing a damaged trachea, has long criticized Macchiarini’s work, saying that his papers do not reflect the true condition of the trachea recipients. That report concluded that Delaere’s complaints were either due to a difference of opinion or were too vague to be substantiated. Gerdin says he does not disagree with that report. The allegations brought by the Karolinska researchers were more concrete, Gerdin says, and addressed specific discrepancies between patient records and published papers.

Gerdin’s report says Macchiarini bears the primary responsibility for the misconduct. However, he also faults the Karolinska Institute for failing to anticipate that Macchiarini’s surgeries would need clear ethical oversight and the co-authors for signing off on papers that were inaccurate.

Macchiarini and the researchers who brought the complaints have 2 weeks to comment on Gerdin’s findings. Karolinska’s vice chancellor will then decide what action to take, a Karolinska representative says. A decision is expected in June. ■



## SCIENCE POLICY

# Debate sharpens over proposed criteria for NSF grants

Supporters say new laws would bolster national priorities; critics see political interference

By Jeffrey Mervis

**“**In the national interest.” The phrase sounds innocuous, but it lies at the heart of a heated, 2-year debate between lawmakers and science advocates about how Congress should oversee research funding at the National Science Foundation (NSF).

That debate was at full boil last week, when the U.S. House of Representatives passed the America COMPETES Act, which sets policy for NSF and two other federal research agencies, and the House Appropriations Committee adopted a 2016 spending bill that includes NSF. Both actions aim to ensure that everything NSF funds will be “in the national interest,” according to the influential Texas legislators behind the two bills, Republican representatives Lamar Smith and John Culberson.

But many scientists believe that the bills, if enacted without any changes, would have disastrous consequences. The scientists and their allies say congressional Republicans are using the phrase to cut spending they don’t like and to give lawmakers undue influence over NSF’s grantmaking system.

Over the past 2 years, Smith, who chairs the House science committee, and other conservatives have complained that NSF has wasted tax dollars by funding dozens of grants in the social and behavioral sciences or that relate to climate change. The COMPETES Act, which passed the House on 20 May without the support of a single Democrat, is meant to end that alleged waste. The bill sets nonbinding spending targets for each of NSF’s six research directorates, reducing support for the social and behavioral sciences and for the geosciences while boosting it for biology, engineering, computing, and math and physical sciences. “What

our bill does is reduce funds for low priorities like a survey of Norwegian tourism and teaching TV meteorologists about climate change,” Smith noted.

It also orders NSF to certify that every grant satisfies one or more of a checklist of societal goals. “It requires that all grants serve the national interest,” Smith said during the 3-hour floor debate on the bill. The “national interest” goals listed in Section 106 of the bill are beyond reproach, ranging from economic growth to improved scientific literacy. But critics of COMPETES say that the



Would NSF’s past support of Google founders Larry Page, left, and Sergey Brin pass muster today?

language threatens NSF’s use of peer review to choose the most worthy research ideas—and, they add, it’s almost impossible to predict if a piece of basic research will one day serve the national interest.

“Section 106 exemplifies the majority’s efforts to impose their own personal beliefs and ideologies on the process of scientific discovery,” warned Representative Bill Foster (D-IL), a former physicist, during debate on his amendment to remove the language. “Accountability should be measured according to the transparency and integrity of the grant review process, not according to what types of science some of us believe in.” Only four Republicans sided with Foster, and his amendment was defeated.

Smith says that NSF is on his side, cit-

ing comments from NSF Director France Córdova during a hearing earlier this year. Córdova was discussing a new NSF initiative to improve the readability and quality of grant abstracts, frequent fodder for Smith and other critics, when she remarked that Section 106 was “very compatible” with the NSF initiative as well as its mission to “further the national interest.”

But that doesn’t mean Córdova agrees with that section of the bill, which the White House has already threatened to veto for a variety of reasons. Córdova declined further comment on the legislation. NSF’s governing body, the National Science Board, applauds NSF’s new approach to abstracts in a resolution passed this month that does not mention the COMPETES Act. Asked for clarification on whether the board supports Smith’s position, a spokesperson said that “all board members strongly believe that promoting the progress of science is intrinsically in the national interest.”

Smith’s use of the phrase is okay with Representative Daniel Lipinski (D-IL), the top Democrat on the science committee’s research subcommittee. Though he opposed the overall COMPETES bill, Lipinski voted against the Foster amendment and thinks that his colleagues’ fears are unwarranted. “It does not do anything to undermine the grantsmaking process,” Lipinski said about Section 106. “This will help NSF defend worthwhile grants that are attacked by critics who sometimes misrepresent projects.”

A few hours before Foster’s amendment was rejected, Culberson got the House Appropriations Committee to endorse Smith’s views in a separate bill setting funding for NSF in 2016. “NSF is directed to comply with section 106 and provide periodic updates to the Committee on its transparency activities,” declares a report accompanying a \$51 billion spending bill for NSF and several other federal agencies, which was written by the subpanel Culberson chairs.

Will Smith and Culberson prevail? Both bills are a long way from the finish line. The Senate has yet to draft its version of a COMPETES bill. And although Congress must eventually approve a 2016 budget for all agencies, it’s anybody’s guess what the final version will look like. But right now the Texans—and their definition of national interest—are riding high. ■



## FEATURES



Kenya's first mass measles campaign reached 13 million children in 2002.

Downloaded from [www.sciencemag.org](http://www.sciencemag.org) on May 29, 2015





# IS MEASLES NEXT?

Some disease fighters want to eradicate the most contagious virus of all. But does a world still fighting polio have the stomach to try?

By **Leslie Roberts**

**S**teve Cochi is not your stereotypical disease warrior. You won't see him parachuting into hot zones on the hunt for the next exotic virus. He's not a regular on radio shows or in front of the camera. Cautious, unassuming, with thick white hair, wire rim glasses, and an almost cherubic face, the 63-year-old physician and epidemiologist is most comfortable behind the scenes.

But for the past 25 years, Cochi has been pushing one of the boldest—and some might venture foolhardy—ideas in public health. He wants the world to undertake a huge new effort to eradicate measles. Not just tame the virus or control the outbreaks resurging across globe, but obliterate it, wipe it off the face of the earth, as has only been done once for a human pathogen, smallpox, in 1977, and as the world fervently hopes will happen soon with polio.

It's inexcusable not to, says Cochi, who is a senior adviser on global immunization at the U.S. Centers for Disease Control and Prevention (CDC) in Atlanta. Measles killed an estimated 145,000 people in 2013, mostly children in Africa, and left many more deaf, blind, or otherwise disabled. We have the means to eradicate it, says Cochi, whose mentor at Duke University School of Medicine was Sam Katz, a co-developer of the measles vaccine. "For measles you just need two doses of vaccine," says longtime collaborator Andrea Gay of the United Nations Foundation in Washington, D.C. "There are

few things you can say that about. ... Why wouldn't you do it?"

That's why Cochi, Gay, and a small cadre of like-minded colleagues have spent years quietly lobbying the World Health Assembly (WHA) to put measles eradication at the top of the global agenda, right up there with polio, and declare a target date for eradication.

But they've got a problem, or two or three. First is the perception issue. Although measles is one of the leading childhood killers, people in wealthy countries tend to think of it as a minor annoyance, a rash and a fever but no big deal—certainly not big enough to justify another multi-billion, multiyear initiative.

It would be fiendishly difficult. Measles is the most contagious virus on Earth, infecting virtually everyone who is not vaccinated.

But mostly there is polio, which hasn't disappeared as it was supposed to in 2000, despite more than \$11 billion and counting and nearly 30 years of effort. Until it does, the world will not have the money or the energy for another huge eradication campaign, no matter how laudatory the goal. "I am not against measles eradication," says David Heymann, a veteran of the smallpox wars who oversaw the Global Polio Eradication Initiative while at the World Health Organization (WHO). "But we've all been burned by polio."

Reluctantly, Cochi cedes the point. "We are waiting in the wings." But not idly, others say: A stealth eradication campaign is already well under way, with Cochi at its helm.

PHOTO: © KAREN KASMAUSKI/SCIENCE FACTION/CORBIS

**MEASLES BEGINS** innocuously enough, with a cough, runny nose, inflamed eyes, a sore throat, and a slight fever. Three to 5 days later, the distinctive rash erupts, starting on the face and working its way down the arms and trunk and finally to the legs and feet. Fever spikes, as high as 104°F or 105°F (about 40°C). Ear infections are a common complication. Some kids in the United States are hospitalized, but for the majority, the rash fades and infection resolves in about a week.

But more than half of the estimated 10 million infected with measles each year in the developing world fare far worse. The virus suppresses the body’s defense system, especially in those already immune-compromised or with malnutrition or vitamin A deficiency, leaving them vulnerable to secondary bacterial infections. The problems are compounded by a lack of health care. Pneumonia is the most common cause of death; diarrhea and dehydration is a close second. Measles

is one of the top five preventable causes of blindness. Deafness is common. Inflammation of the brain can cause seizures and sometimes permanent brain damage. In poor countries, the fatality rate is 2% to 15%, soaring to 25% in the worst outbreaks.

Everyone who has witnessed a measles outbreak wants to reduce the toll, says Walter Orenstein, who has devoted his career to fighting the disease and is now associate director at the Emory Vaccine Center in Atlanta. But “going the final mile, going to zero,” is a completely different game, he says. Zero is in Cochi’s genes.

He is descended from a line of dedicated disease eradicators who came up through CDC in the 1960s and 1970s: William Foege, Ciro de Quadros, Donald R. Hopkins, and Donald A. Henderson, to name just a few. Most served in the Epidemic Intelligence Service, CDC’s famed boot camp for disease detectives, and many cut their eyeteeth

fighting smallpox in Africa. When they triumphed over smallpox in 1977, they and thousands of others had pulled off what many thought impossible: the first eradication of an infectious disease. Their feat is still heralded as the crowning achievement of public health, the ultimate triumph of man (and they were men) over microbe, and a permanent gift to humanity, which need never suffer the horrible disease again. They were itching for another conquest.

Henderson, the gruff physician and epidemiologist who led WHO’s global smallpox campaign, recalls a meeting in 1980, just 1 month after WHO had officially certified that smallpox was gone. Public health luminaries gathered in Washington, D.C., to decide what to eradicate next. “I told them that was the wrong question,” says Henderson, who is now a professor emeritus at the John Hopkins Bloomberg School of Public Health in Baltimore, Maryland. “Smallpox was done by the skin of its teeth,” he said. Better to invest in immunizing children against all preventable diseases, including measles, and forgo what he has called “the blinding beacon” of eradication. “I was overruled,” he says.

Don Hopkins made an impassioned plea for measles in the 19 June 1982 issue of *The Lancet*. Hopkins was fresh back from battling smallpox in West Africa, where CDC also ran a measles control program. There he had seen firsthand the devastation measles wrought—at the time it was killing an estimated 2.6 million children a year—and how people clamored for the vaccine. “They would take smallpox only on one condition—that we give them measles vaccine,” he says.

What’s more, measles was one of the very few viruses that met the strict scientific criteria of “eradicable.” Not only was there an excellent vaccine and a good diagnostic, but like the smallpox and polio viruses—and unlike Ebola—the measles virus also has no animal host in which to hide. In Africa, Hopkins saw how the virus crumbled in the face of aggressive vaccination, disappearing in Gambia for more than a year.

Hopkins, who soon became deputy director of CDC, had powerful allies, most important Foege, then agency director, who seconded Hopkins’s call in an article a few months later. “We were all similarly minded,” says Alan Hinman, one of Hopkins’s co-authors now at the Task Force for Global Health in Decatur, Georgia. “We all thought measles should go next.”

But measles was eclipsed by polio, a far less serious disease. “Polio cripples; measles kills,” Cochi says. In the prevaccine era, polio paralyzed roughly 650,000 a year, whereas measles killed as many as 5 million or 6 million. But polio had terrified a generation of parents when it swept through the United

### The hit list

Measles lacks features that have made polio so hard to eradicate, including silent cases and vaccine-derived transmission. But it is far more contagious—hence harder to stamp out—than smallpox, the one virus successfully eradicated. Some of the challenges are highlighted.

	SMALLPOX (ERADICATED)	POLIO	MEASLES
Clinical presentation	Fever and rash	Acute, flaccid, paralysis	Fever and rash
Asymptomatic infections or carriers	No	Yes	No
Primary mode of transmission	Respiratory droplets	Fecal-oral Oral-oral	Respiratory droplets
Reproduction number (Number of cases a single infection will generate)	5–7	4–13	12–18
Community immunity to stop transmission	80%–85%	75%–92%	92%–94%
Serotypes	1	3	1
Vaccine delivery	Intradermal injection	Oral drops	Subcutaneous injection
Number of vaccine doses needed to stop transmission	1	≥3	1–2
Vaccine efficacy	1 dose = 95%	3 doses* Type 1 = 73% Type 2 = 90% Type 3 = 70%	2 doses = 99%
Waning of protective immunity	Yes	Humoral: No Intestinal: Yes	No
Vaccine-derived virus infection and transmission	No	Yes	No
Period of contagiousness	25 days	4–6 weeks	9 days

\* >95% in industrialized countries



States in the 1940s and 1950s. Measles, on the other hand, was a shrug. “Parents didn’t seem to mind that their kids had measles,” says Orenstein, who led the national immunization program that eliminated measles from the United States.

And polio had a most persuasive advocate and “salesman par excellence,” as Henderson describes him: Albert Sabin, a national hero for inventing the oral polio vaccine (OPV). Sabin’s grand vision was to deliver his easy-to-use polio drops in mass campaigns to reach every child, and voilà, polio would disappear. “Just a few drops on the tongue. How easy it would be,” Henderson recalls.

Rotary International kick-started the polio eradication effort with \$120 million. (It has since contributed \$1.3 billion.) At the Pan American Health Organization, de Quadros began an aggressive campaign to drive polio out of the Americas. The die was cast in 1988, when WHO committed to eradicating polio by 2000—never imagining that the program would still be dragging on 15 years later.

**MANY OF THE MEASLES** advocates enlisted in the polio wars, among them Cochi, who joined CDC in the 1980s, after 2 years as a pediatrician on a Navajo reservation in New Mexico. At CDC, he quickly found his niche working on vaccine-preventable diseases, logging long hours chasing polio in Nigeria, Pakistan, Bangladesh, and India, to name just a few countries. Soon Cochi was the “go-to” guy for unvarnished advice on polio eradication, says Bruce Aylward, the longtime leader of the polio eradication effort. “Steve has been hugely influential.”

While the polio campaign unfolded during the 1990s, Cochi and others then at CDC, including Peter Strebel and Mark Grabowsky, began laying the groundwork for what they hoped would be the next eradication push—sitting on various acronym-studded expert panels, writing tens of papers, and participating in countless international meetings, including one in 1996 that concluded measles eradication was technically feasible, with a target date within the next 10 or 15 years.

In 2000, the time seemed ripe to go public. Polio seemed to be winding down. Measles had been eliminated in the United States—all cases since then have been “imported” from other countries—and it was on the way out in the entire region of the Americas. The last case in the Americas occurred in 2002, showing the world for the first time the virus could be beaten in poor countries.

At an immunization meeting in Pretoria in December 2000, Cochi pulled aside a small but well-placed group to talk about measles. African governments were desperate for help fighting the outbreaks still exploding there. Could they provide it, he asked? The experts went home and enlisted support from their respective organizations.

Thus was born the Measles Initiative, a loose-knit partnership of five organizations—the American Red Cross, CDC, the United Nations Children’s Fund, the United Nations Foundation, and WHO—with Cochi as its unofficial ringleader. Renamed the Measles & Rubella Initiative in 2012 when it expanded its scope, the initiative did not have an explicit eradication goal, but its intentions were pretty clear when it called for “a world without measles.”

**IN SOME WAYS**, measles would be easier than polio (see table, p. 960). The measles

mistakenly grabbed the wrong bottle out of the refrigerator and mixed the powder with a powerful muscle relaxant. Within minutes, 15 children under age 2 died, mostly of suffocation. Once reconstituted, the vaccine’s shelf life is only 6 hours, so clinic workers are sometimes reluctant to prepare a batch for just a few kids. They ask mothers to bring them back later, but that often doesn’t happen. Researchers are working on easier-to-use vaccines, but they are still years away.

“In most mass campaigns you are lucky to get 90% coverage, probably 85%,” Henderson says. “That is not going to interrupt measles transmission.”

Toda Kohei, one of the original polio warriors, is now with WHO in Vietnam and has spent much of the past year battling a huge measles outbreak there (see sidebar, p. 962). Kohei desperately wants to see measles disappear. But, he says, “we have to see the virus for what it is. Measles is too

much the virus to fight with. We need to be a little bit humble and modest.”

Still, the first several years of the initiative were a huge success. The partners helped 70 resource-strapped countries launch mass measles vaccination campaigns. The world met the first global target—a 50% reduction in measles deaths from 1999 levels by 2005—

with time to spare. By 2008, mortality had dropped 78% globally and a stunning 92% in Africa. But despite persistent lobbying by the initiative, WHA held off declaring an official eradication goal.

Then, beginning in 2009, “the bottom dropped out,” Cochi says. Hammered by the global recession, the initiative lost close to 75% of its international funding. Mass vaccination campaigns were canceled or scaled back in high-risk countries, routine measles vaccination suffered, and global progress stalled. The following year, measles exploded in southern African countries. By 2011, deaths had climbed back to 200,000, up from 170,000 in 2008.

In some wealthy countries, measles ran headfirst into a strong and increasingly vocal antivaccination movement, mostly among the well-educated, fueled by a long-discredited link between autism and the measles, mumps, and rubella vaccine and by nonchalance about what is seen as a mild disease. The drop in immunization has reversed progress in Europe, which had 37,000 measles cases last year, and left the United States battling repeated importations, like the ongoing one that started in Disneyland in late 2014 and has now spread to 19 states and the District of Columbia.



*“If we have to wait to solve the problem of routine immunization [to start measles eradication], we will be waiting for decades.”*

Steve Cochi, CDC

vaccine is far better than OPV, providing 99% protection with just two doses. And almost every case of measles is visible, so you know where the enemy is. Not so for polio, which paralyzes just one in about 200 people it infects and so can circulate undetected, sometimes for years, before it strikes again.

But measles poses different challenges, key among them its exquisite contagiousness. Transmitted by respiratory droplets or aerosols, the virus can linger in the air for up to 2 hours after an infected person leaves the room, and kids are often infected in hospitals or doctors’ waiting rooms. The virus’s reproduction number—the number of infections a single case will generate in an unvaccinated population—is a staggering 12 to 18, compared with 5 to 7 for smallpox and 1.5 to 2.5 for Ebola. To stop measles transmission, more than 95% of the population has to be vaccinated, as opposed to about 80% in most places for smallpox and polio.

And the measles vaccine is far harder to deliver than polio drops. It must be injected, so mass campaigns require armies of trained health care workers, not the volunteers who dispense polio drops. It has to be reconstituted in the field, a step that has on rare occasions led to accidents. Last year in northern Syria, for instance, a health worker

It had also become abundantly clear that the poliovirus was not going away anytime soon. Cases were down 99% from 1988 levels, but the last 1% would not budge, entrenched in India, Afghanistan, Pakistan, and Nigeria, some of the world's poorest countries and toughest places to work.

It turned out the vaccine virus in OPV could revert and actually spark outbreaks of its own. Another problem was that OPV, very effective in high-income countries, did not work as well in the hot, crowded slums in poor countries where polio often holes up. In some places, armed conflict made mass polio campaigns impossible. In others, rumors about vaccine dangers and an anti-Muslim plot derailed them. Over the past few years, opposition has taken a horrifying turn, with polio workers being singled out and murdered in Pakistan.

Some experts began asking publicly whether polio eradication was feasible—and if it was, whether it was worth all the money, when bigger public health problems were going wanting. As the campaign dragged on and costs ballooned, donors were in a bind, tapped out but too far in to pull the plug.

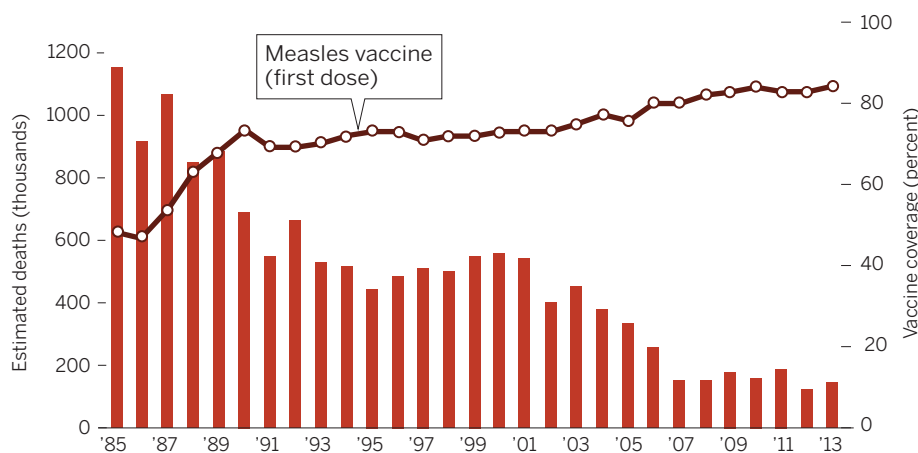
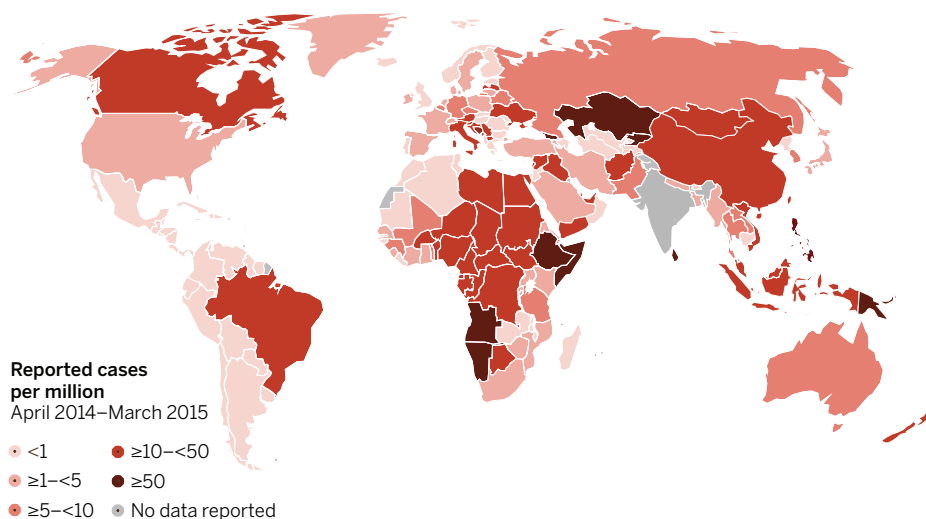
“Eradication is a monolith,” Henderson says. “It tramples everything in its way.”

**FOR NOW, THE MEASLES INITIATIVE** is simply trying to regain lost ground, Cochi says. Routine immunization rates remain stuck at 84%, about where they were in 2008 and well below the 2015 target of 90%. The regions that vowed to eliminate measles by 2015 or earlier are badly off track. Global deaths have dropped back to 145,000, but outbreaks are sweeping Asia and Africa. Measles is on the upswing throughout the Middle East, and health experts are scrambling to avert a huge epidemic in the West African countries where Ebola has left fragile health care systems reeling. Seventy percent of measles cases now occur in just six countries, not coincidentally many of the same places polio and smallpox proved so hard to dislodge. In 2011, WHO said that although measles can and should be eradicated, no official program should be launched until there is progress toward both polio eradication and the 2015 measles goals.

The partners now steer clear of the word “eradicate,” emphasizing instead that they are helping the remaining five WHO regions reach their stated goal to “eliminate” the virus by 2020. It's more than semantics: Eradication means no more measles cases, anywhere, period, whereas elimination means stopping indigenous transmission within a defined geographic area. But the partners concede that if all regions met their elimination goals, then, ipso facto, measles

## The global toll of measles

As immunization rates climbed, measles deaths plummeted, but progress stalled in 2007. Cases and deaths are concentrated in Africa and Asia.



would be eradicated. “In a sense we have an eradication goal; we just don’t recognize it as such,” Orenstein says. “It is a stealth campaign” until polio is gone, Gay concurs.

Even then, the world may have soured on eradication. Matt Hanson at the Bill & Melinda Gates Foundation in Seattle calls the dramatic drop in measles mortality “one of the great public health successes,” and the foundation contributes about \$40 million a year to the fight. But that’s a trifle compared with the more than \$2 billion it has invested in polio eradication. “Bill made a conscious decision,” Cochi says. “The foundation could ... not afford to operate on two fronts.”

The same goes for Gavi, the global vaccine alliance in Geneva, Switzerland. Reducing measles deaths is high on the alliance’s agenda, but at the moment, “eradication is not Gavi’s goal,” says CEO Seth Berkley. The international health community has other

priorities, he and others say, and the big one is boosting routine immunization and otherwise shoring up weak health systems in poor countries.

Cochi insists the world must do both: Eradicate measles while simultaneously boosting routine immunization. “If we have to wait to solve the problem of routine immunization, we will be waiting for decades,” he says. In the meantime, he adds, hundreds of thousands of children will die of a disease that could be prevented today, with two shots of an inexpensive vaccine.

There are some encouraging signs, Cochi and his CDC colleagues say. Funding is up slightly, and just in the past few months, hopes have risen that wild poliovirus may at last be gone from Africa, leaving just two endemic countries, Afghanistan and Pakistan. With polio finally on the way out, the measles advocates predict, discussion will inevitably turn to what to eradicate next. ■



# INSIGHTS



## PERSPECTIVES

### SCIENCE AND REGULATION

# Congress's attacks on science-based rules

Proposed laws based on false premises could undermine science for the public interest

By A. A. Rosenberg,<sup>1\*†</sup> L. M. Branscomb,<sup>2\*</sup> V. Eady,<sup>3\*</sup> P. C. Frumhoff,<sup>4\*</sup> G. T. Goldman,<sup>1</sup> M. Halpern,<sup>1</sup> K. Kimmell,<sup>4</sup> Y. Kothari,<sup>1</sup> L. D. Kramer,<sup>5\*</sup> N. F. Lane,<sup>6\*</sup> J. J. McCarthy,<sup>7\*</sup> P. Phartiyal,<sup>1</sup> K. Rest,<sup>4</sup> R. Sims,<sup>\*</sup> C. Wexler<sup>1</sup>

**T**here is a growing and troubling assault on using credible scientific knowledge in U.S. government regulation that will put science and democracy at risk if unchecked. We present five examples, and the false premises on which they are based, of current attempts in the U.S. Congress in the supposed pursuit of transparency and accountability but at the expense of the role of science in policy-making.

Over the past century, the federal government has striven to protect public health, safety, and the environment. Many statutory mandates require administrative agencies to craft regulations informed by credible, legitimate, and salient scientific assessments (1, 2) that prescribe actions and obligations of government entities, private sector enterprises, and individuals to protect the public interest. The federal laws that create these science-based mandates—such as the Clean Air Act, the Occupational Safety and Health Act, and the Consumer Product Safety Act—are perceived as inconvenient and expensive by some corporate actors. Consequently, congressional leaders are pressured to render these long-standing and well-regarded

laws ineffective by undermining their scientific foundations (3).

This should raise alarm among all scientists. Each year, thousands of experts from academia, industry, and government serve on agency advisory panels and boards, peer-review panels, and National Academies' study committees. Many more conduct research relevant to important public policy decisions. The regulations that result from these scientific inputs have led to profound improvements in air and water quality, protections for workers and the public, and environmental safeguards (3).

Regrettably, five major bills have recently advanced in the U.S. Congress that would transform the scientific advisory process. Four passed the House of Representatives

#### POLICY





Five major bills have recently advanced in the U.S. Congress that would severely limit the scientific advisory process.

last year but failed to advance in the Senate. Four of the five bills were reintroduced and three passed the House this year; with the fourth likely to pass soon. All have Senate sponsors. Although effective advocacy by scientists has helped stymie their progress thus far, any of these bills could be attached to must-pass legislation, and some presidential candidates are already embracing them as necessary reforms.

The bills employ insidious, albeit creative, approaches to weaken the ability of science to inform federal rule-making. One approach is to shift regulatory decisions from career employees in federal agencies working with experts to politicians in Congress vulnerable to special-interest influence. The Regulations from the Executive in Need of Scrutiny (REINS) Act, which backers say will

make regulatory agencies more accountable and reduce undue burdens on businesses, requires joint congressional approval within 70 legislative days for any new or updated major rule with an annual economic impact of \$100 million or more. If either chamber fails to act, the agency cannot move forward with the rule until the next Congress convenes and jointly approves the rule. The act suggests no criteria for Congress in evaluating a rule. Agencies, on the other hand, must adhere to specific statutory requirements—including basing decisions on science in many cases—and must defend their decisions in court. Given the current gridlock on Capitol Hill, few regulatory protections would survive both houses of Congress. Rather than increasing accountability—which of course is a worthwhile goal—the proposed mechanism for approval would, in effect, prevent science-based rules from ever being implemented.

A second approach is to tie up federal agencies in additional and redundant bureaucracy, even as their budgets decrease. This will make efficient rule-making even more difficult if not impossible. The Regulatory Accountability Act, with a stated goal of reducing costs to business, passed the House

in February, and imposes more than 70 new requirements on development, analysis, and public engagement processes that agencies must follow in updating or creating new rules (4). This includes additional formal administrative hearings that would give regulated industry and others the opportunity to directly challenge and cross-examine the agency on the science underlying its cost-benefit analysis. The act makes the least costly approach the default option for new public health and safety regulations even if it is less protective, a change from current laws which typically prioritize public health protection over cost. The act also gives the White House Office of Management and Budget the power to override independent scientific advice on the costs, benefits, and risks of proposed regulations, enabling implementation of regulations that might not reflect the best available science as required by statute.

Or take the Sound Science Act. Introduced in the House last year and likely to resurface in the current Congress, the legislation is ostensibly designed to improve the scientific basis for regulations. The bill requires agencies to hold additional public comment periods specifically on all scientific findings throughout the process and each time a new finding is considered. Furthermore, agencies must give “greatest weight to information that is based on experimental, empirical, quantifiable, and reproducible data.” But, as scientists know well, and as AAAS (American Association for the Advancement of Science, which publishes *Science*) has noted (5), some good science cannot be easily subjected to reproducible experiments. Should modeling studies be excluded? Is qualitative information not to be considered? The decision about how to weigh different types of information should be a scientific decision, not a political mandate. Although, in many cases, such weighting may be appropriate, this decision should be left to technical experts who understand how to interpret the data. Otherwise, decisions might not be based on the best understanding of the scientific evidence.

A third approach is to limit the information that regulators can use. The Secret Science Reform Act, passed by the House in February 2015, mandates that the Environmental Protection Agency (EPA) may only put forward a regulation if all of the data, models, methods, and other information in the science studies used in its development are publicly available, accessible, and reproducible. Supposedly, the data are required so that the “public” can analyze the data for themselves, although, in practice, it is likely that special interest groups will hire scientists to reanalyze the data to cast doubt on results that are not to their liking in order to delay the regulatory process. Although

<sup>1</sup>Center for Science and Democracy, Union of Concerned Scientists, Cambridge, MA 02138, USA. <sup>2</sup>University of California, San Diego, La Jolla, CA 92093, USA. <sup>3</sup>Conservation Law Foundation, Boston, MA 02110, USA. <sup>4</sup>Union of Concerned Scientists, Cambridge, MA 02138, USA. <sup>5</sup>William and Flora Hewlett Foundation, Menlo Park, CA 94025, USA. <sup>6</sup>Baker Institute of Public Policy, Rice University, Houston, TX 77005, USA. <sup>7</sup>Harvard University, Cambridge, MA 02138, USA. \*Steering Committee member, Center for Science and Democracy, Union of Concerned Scientists. †Corresponding author. E-mail: arosenberg@ucsusa.org



scrutiny of the science used in rule-making is important, this act would drain time and resources from rule-making processes that already include expert peer review, the release of summarized data, and ample opportunities for public and stakeholder input.

Although greater access to data can be a laudable goal, confidential health records, confidential business information, or protected intellectual property should not be disclosed. And although the bill carefully states that it does not require the release of confidential information, the EPA is prohibited from moving forward with a regulation unless all data are public. So although EPA is charged with protecting public health, say with regard to ozone or mercury emissions from power plants, it may not utilize any studies that analyze confidential public health data as a basis for action. This restriction applies to any actions the agency might take from rule-making to guidance, standard-setting, or scientific assessment of toxic substances. In other words, the EPA may not act on the basis of data it is legally restricted from releasing; therefore, it may not act.

A fourth approach is to change the composition and operation of the science advisory process itself. The EPA Science Advisory Board Reform Act, passed by the House this year, would set a quota for state, local, and tribal government officials and clarify that industry experts with ties to a regulated industry are not barred from advisory board membership, while barring independent scientists from serving if they have received an EPA grant within the last 3 years (and preventing their acceptance of an EPA grant for 3 years after they serve). Concurrently, the legislation makes it difficult for board members to discuss their scientific views that are not already published. Procedurally, the board is required to solicit and respond in writing to public comments on the state of the science and may not place time limits on that process. In reporting back to the EPA, the board must ensure that the views of the public are reflected and encourage dissenting members to report their views. Taken together, these changes give political and legal operatives greater influence over the advisory board while marginalizing independent scientists, as well as greater opportunity for frivolous and resource-consuming challenges to the board's findings.

Procedurally and monetarily, any of these proposals, if enacted, will delay and complicate an already complex regulatory process. The Congressional Budget Office estimated that the Secret Science Reform Act alone could cost EPA \$250 million annually at a time when its mandate has increased and its budget has been cut (6).

The bills described above are based on three false premises. The first premise is that regulations put forward by federal agencies reflect agency and executive branch "overreach." In reality, the rule-making process provides many opportunities to check such overreach, including by the judiciary.

The second premise is that corporations need more opportunity to influence the scientific information used in rule-making. But many industries already support technically proficient scientists and skilled advocates in every step of the process to argue their perspectives (7). By comparison, community groups and many civil society organizations can never match corporate resources for influencing government.

The third premise is that regulations only impose costs on industry, and public benefits are negligible. Yet just 10 rules proposed in the last 5 years are estimated to result in saving more than 10,000 lives and preventing 300,000 cases of disease, illness, or injury annually (8). Nine of the 10 rules—including actions on protecting workers from silica exposure, controlling mercury

### ***"The bills use insidious... approaches to weaken the ability of science to inform federal rule-making."***

pollution, and preventing salmonella contamination in eggs—are estimated to have monetized social benefits that substantially exceeded monetized compliance costs even though many benefits cannot be monetized (9). Further, it is important to recognize that risk-mitigation costs not borne by industry will not evaporate but will become a public burden.

Attacks on the science advisory process as the foundation of regulatory action have a profound, chilling effect on the willingness of scientists to contribute to the process of advancing critical health, safety, and environmental protections. Restrictions on expert participation, requirements for multiple rounds of public comments, and procedural hurdles will subject the advisory process to greater industry and political influence and discourage independent scientists from participating in advisory activities. Many scientists are honored to serve the public as independent experts to inform the policy process, and most do so without compensation. As barriers for participation rise, their willingness to engage will plummet. The end result may be that mostly experts paid by special interests will serve.

The scientific community needs to push back. Elected officials respond to constituents, and there are scientists in every congressional district. With leadership from professional societies and scientific organizations, scientists across the country should tell their members of Congress how much they value the opportunity to engage in informing policy and how important it is that these attacks on the process are defeated.

The present system is far from perfect, but there are better solutions to ensure that science advice remains reflective of the evidence and resistant to special interest manipulation. To that end, with leadership from professional societies, science-based organizations, and academic institutions, better pathways must be created for independent scientists to share their expertise. This includes providing greater training for early career scientists on the advisory process and creating career-based incentives and time for them to participate. It also includes institutionalizing professional recognition for work and activity that informs policy-making. Public service should be a central component of what it means to be a scientist.

Further, public trust in science increases when we all have access to the same base of evidence. To that end, we must improve and fully implement conflict of interest and disclosure standards and strengthen peer review while increasing the public accessibility of scientific information. The stakes are high, as our collective well-being and the strength of our democracy depend on our success. ■

#### REFERENCES

1. W. C. Clark, G. Majone, *Sci. Technol. Human Values* **10**, 6 (1985).
2. National Research Council, *Analysis of Global Change Assessments: Lessons Learned* (NRC, Washington, DC, 2007).
3. Center for Public Integrity, "Consider the source: Chamber spends early, often on GOP congressional candidates" (CPI, Washington, DC, 2012); [www.publicintegrity.org/2012/03/09/8356/chamber-spends-early-often-gop-congressional-candidates](http://www.publicintegrity.org/2012/03/09/8356/chamber-spends-early-often-gop-congressional-candidates).
4. R. V. Percival, C. H. Schroeder, A. S. Miller, J. P. Leape, *Environmental Regulation: Law, Science and Policy* (Aspen Press, New York, 2013).
5. E. Kesler, Modernization? The Regulatory Accountability Act of 2015 Adds 74 New Steps to the Rule-Making Process (CPRBlog, Center for Progressive Reform, Washington, DC, 2015); [www.progressivereform.org/CPRBlog.cfm?idBlog=CFEFB5B4-9B44-75BE-CF2636189D408F57](http://www.progressivereform.org/CPRBlog.cfm?idBlog=CFEFB5B4-9B44-75BE-CF2636189D408F57).
6. AAAS, Statement on Farm Bill section 12307 (AAAS, Washington, DC, 2014); [www.aaas.org/page/aaas-statement-farm-bill-section-12307](http://www.aaas.org/page/aaas-statement-farm-bill-section-12307).
7. Congressional Budget Office, "Cost Estimate: H.R. 1030 Secret Science Reform Act of 2015" (CBO, Washington, DC, 2015); <https://www.cbo.gov/publication/50025>.
8. T. O. McGarrity, W. E. Wagner, *Bending Science: How Special Interests Corrupt Public Health Research* (Harvard Univ. Press, Cambridge, MA, 2008).
9. Center for Effective Government, *The Benefits of Public Protections: Ten Rules That Save Lives and Protect the Environment* (Center for Effective Government, Washington, DC, 2014); [www.foreffectivegov.org/node/13160](http://www.foreffectivegov.org/node/13160).

10.1126/science.aab2939

# Blocking stress response for better memory?

A drug that affects memory targets a constituent of a cellular stress response mechanism

By Alan G. Hinnebusch

Two years ago, a small molecule was discovered that enhanced the memory of rodents (1). Pinpointing the target of this compound, called integrated stress response inhibitor (ISRIB), could guide the development of cognitive disorder treatments. Two groups have now identified a target. On page 1027 of this issue, Sekine *et al.* (2) report, as do Sidrauski *et al.* (3), that ISRIB increases the activity of eukaryotic translation initiation factor 2B (eIF2B), a factor that regulates protein synthesis in a pathway underlying the cellular response to stress.

A highly conserved cellular response to diverse forms of stress entails suppression of bulk protein synthesis, but also, paradoxically, the increased expression of certain transcription factors that mount an adaptive response. This two-pronged response is triggered by phosphorylation of the  $\alpha$  subunit of eIF2. This modification decreases eIF2 activity, attenuating virtually all translation except for those messenger RNAs harboring particular regulatory elements—upstream open reading frames—that enable their translation to be induced instead (4). In mammals, this mechanism governs activating transcription factor 4 and 5 (ATF4 and ATF5), and because the responses to multiple stresses are integrated by four distinct kinases that phosphorylate eIF2 $\alpha$ , it has been called the integrative stress response (5). Protein kinase RNA-like endoplasmic reticulum kinase (PERK) mediates this response when unfolded proteins accumulate in the endoplasmic reticulum (ER) and represents an important leg of the unfolded protein response (6). ISRIB was identified in a screen for compounds that inhibit PERK, and was found to act downstream of phosphorylated eIF2 [eIF2( $\alpha$ P)], overcoming the effects of the modified factor on translation. Sekine *et al.* and Sidrauski *et al.* now report that ISRIB stimulates eIF2B, a

guanine nucleotide exchange factor (GEF) for eIF2 and a regulatory target of eIF2( $\alpha$ P) (see the figure).

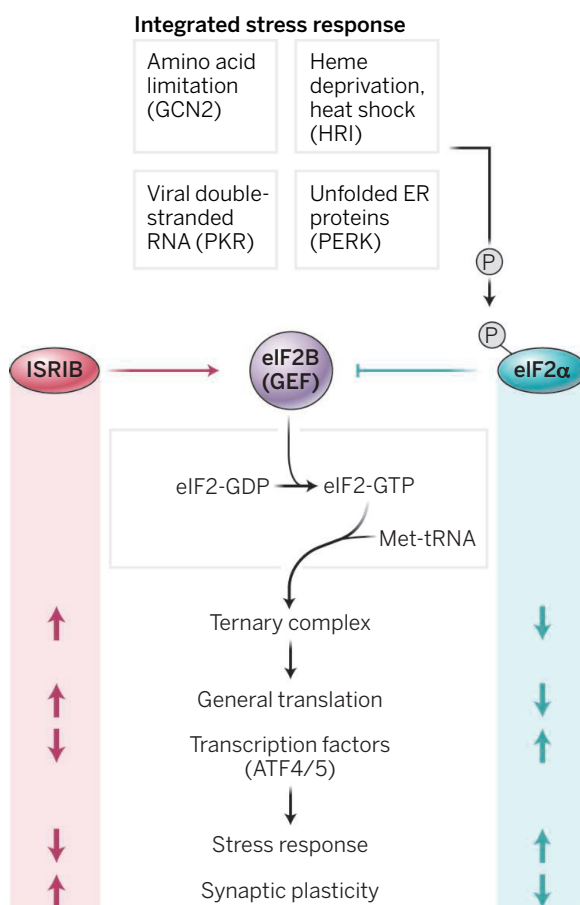
eIF2B is a complex of five subunits ( $\alpha$  to  $\epsilon$ ), three of which ( $\alpha$ ,  $\beta$ , and  $\delta$ ) comprise a regulatory subcomplex that binds tightly to eIF2( $\alpha$ P) in a manner that prevents the catalytic moiety within eIF2B $\epsilon$  from provoking release of guanosine 5'-diphosphate (GDP) from eIF2 and attendant formation of eIF2-GTP (guanosine 5'-triphosphate) (4). eIF2-GTP delivers initiator methionyl transfer RNA to the small ribosomal subunit via a ternary complex of eIF2-GTP-Met-tRNA<sub>i</sub> (7). Mutations in the yeast eIF2B regulatory module weaken its binding to eIF2( $\alpha$ P), render eIF2B insensitive to eIF2( $\alpha$ P) inhibition, and impair the stress response mechanism

(8). One possibility was that ISRIB also works by overcoming the ability of eIF2( $\alpha$ P) to inhibit eIF2B and thereby blocks the integrated stress response.

Sidrauski *et al.* implicate eIF2B as a possible target of ISRIB by identifying eIF2B $\delta$  and  $\epsilon$  in a screen for genes whose inhibition by short hairpin RNA (shRNA) reversed the drug's ability to attenuate expression of ATF4 (stress response) (3). Biochemical assays of purified proteins demonstrated that ISRIB stimulates nucleotide exchange on eIF2 by eIF2B. This effect was limited to unphosphorylated eIF2, however, as the drug did not allow eIF2( $\alpha$ P)-GDP to be accepted as a substrate for eIF2B. Although these results suggest that ISRIB boosts the intrinsic activity of eIF2B, Sidrauski *et al.* did not

rule out that ISRIB could weaken binding of phosphorylated eIF2 $\alpha$  to the regulatory subcomplex of eIF2B to overcome competitive inhibition by a small fraction of eIF2( $\alpha$ P) that might contaminate the eIF2 preparation (3). However, this can be dismissed by complementary findings from Sekine *et al.*, who also showed that ISRIB can stimulate eIF2B GEF activity, either in cell extracts or using purified components. This was observed even when eIF2 contained a nonphosphorylatable variant of the  $\alpha$  subunit. Thus, ISRIB most likely boosts eIF2B activity to compensate for, rather than eliminate, the inhibitory effect of eIF2( $\alpha$ P) on the exchange reaction.

Interestingly, Sekine *et al.* found that in cellular mutants in which both prongs of the integrated stress response were restored in the presence of ISRIB, eIF2B activity was no longer stimulated by ISRIB. The mutations affected closely spaced residues in eIF2B $\delta$ . Sekine *et al.* used clustered regularly interspaced short palindromic repeats (CRISPR) genome editing of cells to show that two such mutations are sufficient to reverse all effects of ISRIB in suppressing the integrated stress response and stimulating eIF2B GEF activity. Hence, the  $\delta$  subunit of eIF2B could be the direct target of ISRIB. This possibility is consistent with results from Sidrauski *et al.* suggesting that



**On target.** The drug ISRIB dampens the integrated stress response by stimulating eIF2B to counteract the effects of eIF2 $\alpha$  phosphorylation (P) on general and gene-specific translation. GCN2, general control nonderepressible 2; HRI, heme-regulated eIF2 $\alpha$  kinase; PKR, protein kinase R; PERK, protein kinase RNA-like endoplasmic reticulum kinase.

Laboratory of Gene Regulation and Development,  
National Institutes of Health, Bethesda, MD, USA.  
E-mail: ahinnebusch@nih.gov



the drug specifically stabilizes eIF2B $\delta$  from thermal denaturation (3).

How ISRIB enhances eIF2B activity remains unknown. The drug exhibits twofold rotational symmetry, and both the spacing and orientation of its distal aromatic rings are crucial for potency. The results of structure-activity relationship studies by Sidrauski *et al.* suggest that the two halves of the drug make similar interactions with their target, as the same modifications of the two aromatic rings had additive effects on activity (3). As eIF2B forms a dimer of heteropentamers (9, 10), the stereochemical properties of ISRIB could be explained if it engages chemically similar moieties symmetrically arranged across the dimer interface. Indeed, Sidrauski *et al.* found that ISRIB promotes formation of eIF2B dimers in vitro (3). Although this could account for the stimulatory effect of ISRIB on GEF activity, there is no direct evidence that dimerization is crucial for activity. The drug also increased association of eIF2B $\alpha$  with the other eIF2B subunits, which might enhance GEF activity (11) independent of eIF2B $\alpha$ 's role in dimerization (10).

There is strong evidence that eIF2 $\alpha$  phosphorylation and the integrated stress response are important regulators of hippocampal synaptic plasticity, with dual effects of inducing long-term depression while suppressing long-term potentiation and the different types of learning associated with each phenomenon. By dampening the integrated stress response, ISRIB impedes long-term depression that is induced by metabotropic glutamate receptors and a specific type of learning in the mouse (12). By contrast, ISRIB or genetic ablation of constituents of the integrated stress response enhances memory in a learning paradigm in the mouse that requires long-term potentiation (1, 13). By establishing that ISRIB acts directly on a key component of the integrated stress response, the new findings should encourage investigation of whether ISRIB, or related compounds with this mode of action, are useful for treating cognitive disorders in humans. ■

## REFERENCES

1. C. Sidrauski *et al.*, *eLife* **2**, e00498 (2013).
2. Y. Sekine *et al.*, *Science* **348**, 1027 (2015).
3. C. Sidrauski *et al.*, *eLife* **4**, 10.7554/eLife.07314 (2015).
4. A. G. Hinnebusch, *Annu. Rev. Microbiol.* **59**, 407 (2005).
5. H. P. Harding *et al.*, *Mol. Cell* **11**, 619 (2003).
6. P. Walter, D. Ron, *Science* **334**, 1081 (2011).
7. A. G. Hinnebusch, in *Translational Control of Gene Expression*, N. Sonenberg, J. W. B. Hershey, M. B. Mathews, Eds. (Cold Spring Harbor Laboratory Press, Cold Spring Harbor, New York, 2000), pp. 185–243.
8. T. Krishnamoorthy *et al.*, *Mol. Cell Biol.* **21**, 5018 (2001).
9. Y. Gordiyenko *et al.*, *Nat. Commun.* **5**, 3902 (2014).
10. N. C. Wortham *et al.*, *FASEB J.* **28**, 2225 (2014).
11. D. D. Williams *et al.*, *J. Biol. Chem.* **276**, 24697 (2001).
12. G. V. Di Prisco *et al.*, *Nat. Neurosci.* **17**, 1073 (2014).
13. M. Costa-Mattioli *et al.*, *Cell* **129**, 195 (2007).

10.1126/science.aac4832

## SHAPE-MEMORY ALLOYS

# Taming the temperamental metal transformation

An alloy can undergo millions of cycles of shape changes in response to stress jumps

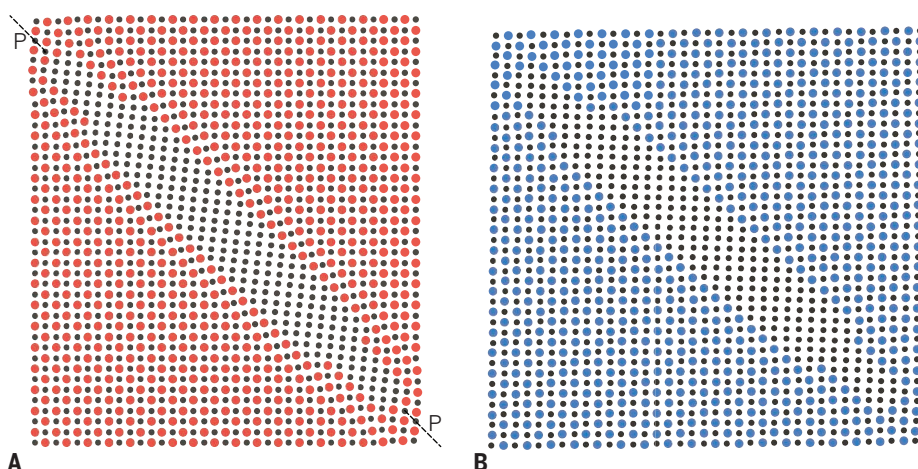
By Richard D. James

One of the most delightful scientific demonstrations is the shape-memory effect in binary nickel-titanium (NiTi): Stretch out a spring of this alloy so it is apparently permanently deformed, drop it into a cup of hot coffee, and it literally jumps back to its original shape (1). However, looks can be deceiving. Repeat performances are limited—especially if the spring had to lift a weight while recovering—because failure by fracture would occur after a few thousand cycles. Also, the temperature at which the spring recovers can change by 10°C after the first few cycles. These effects are believed to be the result of progressive damage in the material as it goes through a large solid-to-solid first-order phase transformation (one requiring heating or cooling) that underlies the shape-memory effect. Thus, it comes as a breathtaking development that, on page 1004 of this issue, Chluba *et al.* (2) demonstrate 10 million cycles with nearly exact repeatability of a comparable phase transformation under

the exceedingly demanding conditions of full stress-induced transformation.

Applied scientists have largely avoided using shape-memory alloys because of these reliability issues, but slightly Ni-rich NiTi has been a technological success in medical devices such as stents (in excess of \$5 billion worldwide) by taking advantage of the related stress-induced transformation. Note that for the shape-memory effect, the alloy returns to its original shape after heating, whereas during stress-induced transformation, it recovers the original shape when the loading force is removed.

These applications are successful because only a one-time full transformation cycle is needed (or at most a few cycles), and NiTi is generally reliable under the very small strains needed. In the case of stents, this one-time cycle consists of severely deforming the cylindrical stent to a tiny radius, inserting it into a small plastic tube at the end of a guide wire, and then deploying it out of the tube with a cleverly designed mechanism once inside the human body. The transformation temperature  $T_c$  in NiTi (which is easily modified



**Staying aligned.** A possible realization of the idea of Chluba *et al.* for decreasing fatigue in shape-memory alloys. Under the cofactor conditions satisfied by their alloy  $\text{Ti}_{54.7}\text{Ni}_{30.7}\text{Cu}_{12.3}\text{Co}_{2.3}$ , there are planes that undergo no distortion by the shape-memory transformation. One of these planes, designated P-P, is shown schematically in (A). Despite the large deformation caused by the transformation to martensite (B), the flattened precipitate that forms undergoes pure rotation and remains epitaxial (the matching uncolored regions in both panels remain aligned), which eases the transformation. These precipitates nevertheless are available to pin lattice dislocations, which leads to substantial strengthening.

## Potential uses of multimillion-cycle phase transformation materials

TECHNOLOGY	PROPERTIES SWITCHED	APPLICATIONS
Actuation	Shape-memory effect	Medical and automotive actuators Remote field-induced cycling of in vivo devices
Sensing	Magnetoelectric properties Dielectric tensor Susceptibility	Variety of mechanical, electrical, and magnetic sensors Optical sensors and smart windows Power electronics
Information storage	Magnetoelectric properties	Magnetic element switching by focused electric fields
Switching	Multiferroic properties	Variety of electromagnetic and optical switches
Solid-state refrigeration	Magnetization Polarization	Magnetocaloric effect Electrocaloric effect
Direct energy conversion	Magnetization Polarization	Solar or thermal heat-to-electricity conversion Waste heat conversion in digital devices; powering spacecraft

by minor compositional changes) governs which effect can be used. Shape memory occurs when  $T_c$  is above room temperature, whereas stress-induced transformation occurs when  $T_c$  is below room temperature and involves no heating.

For decades, putting the shape-memory effect “to work” has been a tantalizing prospect for researchers. In one full shape-memory cycle, the work output per volume of a NiTi wire is enormous (3). When lifting a weight during the “return” phase of the shape-memory effect, the wire can sustain a huge stress of 500 MPa while undergoing a contraction of 5%. Typically, such demanding conditions will lead to failure after only about 10 cycles. By comparison, the strain of the alloy  $\text{Ti}_{54.7}\text{Ni}_{30.7}\text{Cu}_{12.3}\text{Co}_{2.3}$  found by Chluba *et al.* is smaller, 1.5 to 2.0%, and the maximum stress in each cycle is 400 MPa. However, this strain is appreciable, and 400 MPa is a very large stress—twice the yield stress of a typical structural steel used in building construction—and such high values should transfer to actuation via the shape-memory effect.

What is most interesting about this alloy is that the emerging scientific strategy that underlies its discovery may be transferable to other alloy systems. This alloy closely satisfies the cofactor conditions, mathematical relations among the lattice parameters of the two phases that were derived on the basis of purely theoretical considerations (4) [it is the second alloy satisfying these conditions, the first being  $\text{Zn}_{45}\text{Au}_{30}\text{Cu}_{25}$  (5)]. If the cofactor conditions are satisfied, there is a remarkable degree of fitting between phases. Apparently, the plethora of low-energy microstructures, possible under the

cofactor conditions, plays an important role in the repeatability of the transformation.

However, satisfaction of the cofactor conditions is not the whole story. The highly nonstoichiometric composition  $\text{Ti}_{54.7}\text{Ni}_{30.7}\text{Cu}_{12.3}\text{Co}_{2.3}$  leads to the formation of near-stoichiometric TiCu precipitates. Despite the large strains, these precipitates have an approximate epitaxial relation to both phases (see the figure). This relation evokes the original strategy of the 1960s that led to the slightly Ni-rich  $\text{Ni}_{50.6}\text{Ti}_{49.4}$  often used today. This alloy supports  $\text{Ni}_4\text{Ti}_3$  near-epitaxial precipitates that strengthen the ordinarily soft high-temperature phase, leading to an improved (but far from perfect) shape-memory effect in  $\text{Ni}_{50.6}\text{Ti}_{49.4}$ .

***“For decades, putting the shape-memory effect ‘to work’ has been a tantalizing prospect for researchers.”***

One consequence of the cofactor conditions is the presence of planes in the crystal lattice of one phase that are transformed without distortion to the other phase. Could it be that a family of flattened precipitates aligned with these planes can lead to strengthening and still not impede the transformation? Although the general picture is now clearer, we still have much to learn about the relation between conditions of compatibility and subtle processing steps that yield alloy-strengthening precipitates.

What is on the horizon is quite unrelated to the NiTi system but involves a variety of alloys that not only have a large first-order phase transformation but also exhibit “ferroic” properties—ferromagnetism or ferro-

electricity (6, 7)—as well as ferroelasticity. Phase transformations can lead to a strong multiferroic response because ferroelectricity and ferromagnetism are highly sensitive to lattice parameters, which undergo large changes at a phase transformation. Thus, a material can transform from strongly magnetic to nonmagnetic just by heating and cooling a few degrees, and phase transformations could also switch transport and optical properties. Furthermore, the presence of latent heat may allow for direct conversion of heat into electricity.

The coupling of elasticity, electricity, magnetism, and temperature creates many possibilities for sensors, actuators, micro-electronic and optical devices, information storage media, magneto-electro-caloric technology, and energy conversion devices (see the table). Materials are likely to emerge from this strategy of multiferroism by phase transformation (8, 9) that could satisfy strong conditions of compatibility between phases, together with appropriate strengthening mechanisms via controlled precipitation. ■

### REFERENCES AND NOTES

1. K. Bhattacharya, *Microstructure of Martensite: Why It Forms and How It Gives Rise to the Shape Memory Effect* (Oxford Univ. Press, Oxford, 2003).
2. C. Chluba *et al.*, *Science* **348**, 1004 (2015).
3. P. Krulvitch *et al.*, *J. Microelectromech. Syst.* **5**, 270 (1996).
4. X. Chen *et al.*, *J. Mech. Phys. Solids* **61**, 2566 (2013).
5. Y. Song, X. Chen, V. Dabade, T. W. Shield, R. D. James, *Nature* **502**, 85 (2013).
6. H. E. Karaca *et al.*, *Adv. Funct. Mater.* **19**, 983 (2009).
7. N. A. Spaldin, M. Fiebig, *Science* **309**, 391 (2005).
8. R. Kainuma *et al.*, *Nature* **439**, 957 (2006).
9. J. Liu, T. Gottschall, K. P. Skokov, J. D. Moore, O. Gutfleisch, *Nat. Mater.* **11**, 620 (2012).

### ACKNOWLEDGMENTS

Supported by MURI project grant FA9550-12-1-0458 and NSF Partnerships for International Research and Education grant OISE-0967140.



## STRUCTURAL BIOLOGY

# A close view of photosystem I

A high-resolution structure provides insight into solar energy conversion during photosynthesis

By **Roberta Croce**

**P**hotosystem I (PSI) is an extremely efficient solar energy converter, producing one electron for nearly every photon absorbed (1). This large multipigment-multiprotein complex is an essential constituent of the photosynthetic membrane of plants, algae, and cyanobacteria. The energy of the photons absorbed by the PSI pigments is transferred to chlorophylls in the reaction center, where charge separation occurs. The high chlorophyll concentration in PSI maximizes light harvesting while minimizing the cost of protein synthesis; furthermore, its absorption spectrum is broad and extends to the far-red wavelengths (2). PSI is very stable and only becomes photodamaged in the absence of electron acceptors (3). The structure of the *Pisum sativum* (pea) PSI at 2.8 Å resolution reported by Qin *et al.* on page 989 of this issue (4) helps to explain how the pigment-protein complex achieves its remarkable performance.

The structure shows the details of 16 proteins, mostly integral membrane proteins, which provide the scaffold for more than 200 cofactors, including 155 chlorophylls and 35 carotenoids. The core part of the complex, which contains 98 chlorophylls, has been conserved during evolution. As shown by Ben-Shem *et al.*, who solved the first structure of the PSI-LHCI (light-harvesting complex I) supercomplex (5), the core is very similar to that of cyanobacterial PSI (6), with which it shares 10 of the 12 subunits. In plants, the absorption cross section of the core is increased by four LHCI subunits (Lhca1 to Lhca4), which form a belt on one side of the core (5) and bind 57 chlorophylls and 13 carotenoids (4). The high resolution of this part of PSI is the real breakthrough of the Qin *et al.* study.

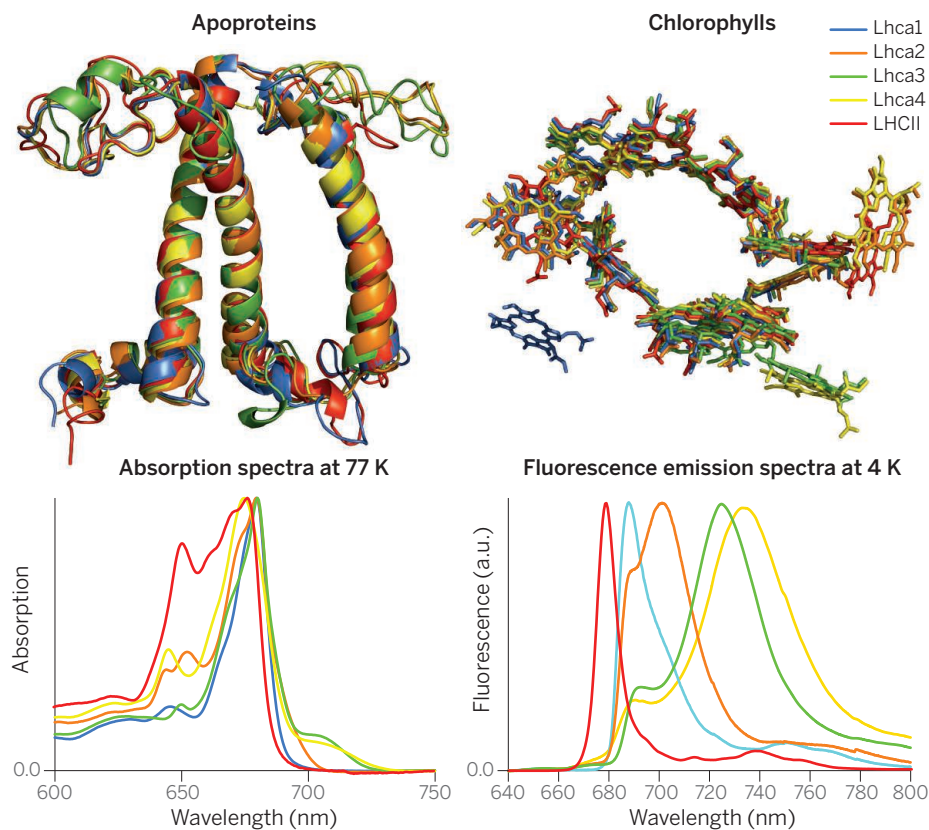
The PSI light-harvesting complexes are members of a large family functioning as outer antenna in plants and green algae. They are the most abundant membrane proteins on Earth. In these complexes, up to 18 pigments (chlorophyll a, chlorophyll b,

and several carotenoid species) are coordinated by a small apoprotein (7). Despite a highly conserved structure and pigment organization, each light-harvesting complex has specific biochemical and spectroscopic characteristics (see the figure), implying that small structural differences can lead to large differences in functionality. In each complex, the protein acts as a smart matrix that modulates the affinity of the binding sites for different pigments and tunes their spectroscopic properties (8).

High-resolution structures are necessary to understand the molecular basis of light

harvesting in these complexes. Previously, the structures of only two members of this family, LHCI and CP29, were available (7, 9). Qin *et al.* now provide high-resolution structures of four additional light-harvesting complexes that reveal the chemical nature and the geometrical arrangement of each pigment in each binding site.

A particularly interesting aspect is the fact that the light-harvesting complexes of PSI contain several chlorophylls with red-shifted spectra, called red forms, which expand the light-harvesting capacity of PSI to the far-red region (2); many photons are available in this region of the spectrum, particularly at the bottom of the plant canopy (10). The introduction of far-red absorbing pigments in other light-harvesting complexes could enhance the use of far-red-photons. This is one of the proposed strategies to improve the efficiency of the photosynthetic process in algae and crops (8, 11). Qin *et al.*'s structure is an excellent



**Similar structure, different properties.** The figure compares the structures (4, 9) and spectroscopic properties [(2) and references therein] of Lhca1 to Lhca4 and LHCI, which are all members of the light-harvesting complex family. The apoproteins (side view) are composed of three transmembrane helices, which are almost perfectly superimposed. This part of the structure contains the ligands that coordinate most of the chlorophylls. The location and orientation of the chlorophylls (top view) is also very similar for the five complexes. However, the absorption spectra differ considerably, indicating that small differences in the environment of the pigments can have a large influence on the selectivity of the binding sites for chlorophylls a and b and on their absorption properties. The fluorescence spectra of the five complexes are dominated by the emission of the red-most (lowest-energy) pigments, which in all four Lhcas originate from the same chlorophylls. These spectra highlight the effect of the environment on tuning the spectroscopic properties of the pigments.

Department of Physics and Astronomy, Faculty of Sciences,  
VU University Amsterdam, NL-1081 HV Amsterdam, Netherlands.  
E-mail: r.croce@vu.nl

source of information for understanding the design rules of light harvesting and the origin of the red forms.

The structure also reveals particulars of the connections between light-harvesting complexes and the core and between each other. These data are crucial for detailed modeling and understanding of excitation energy transfer and trapping in PSI. It is the extremely fast excitation energy transfer that makes PSI the record holder for quantum efficiency, because it allows the protein complex to outcompete the intrinsic de-excitation mechanisms of the chlorophylls, which occur on a nanosecond time scale. On average, it takes less than 50 ps after absorption of a photon by one of the 155 chlorophylls of PSI to create charge separation in the reaction center (2), leading to 99% quantum efficiency.

Fast excitation energy transfer is often associated with an energetic funnel, meaning that the excitation is transferred from high-energy to low-energy pigments, with a close distance between all pigments (8). Qin *et al.*'s structure indicates that this does not apply to the entire PSI. A surprising result is the absence of most of the "gap chlorophylls" that in the previous structure were observed between the Lhca belt and the core (12). Their absence leaves a large spatial gap between the light-harvesting subunits Lhca2 and Lhca4 and the core. To reach the reaction center, excitations from the Lhca belt should then mainly flow via Lhca1 and Lhca3. Yet at first sight these pathways seem to be slow, because they contain a series of uphill energy transfer steps that involve both the red forms and chlorophyll b pigments, which are higher in energy than chlorophyll a pigments. Qin *et al.*'s data need to be integrated with theoretical and experimental results to understand the high efficiency of PSI even in the presence of these putative slow transfer steps. ■

#### REFERENCES

1. N. Nelson, *J. Nanosci. Nanotechnol.* **9**, 1709 (2009).
2. R. Croce, H. van Amerongen, *Photosynth. Res.* **116**, 153 (2013).
3. K. Sonoike, *Physiol. Plant.* **142**, 56 (2011).
4. X. Qin, M. Suga, T. Kuang, J.-R. Shen, *Science* **348**, 989 (2015).
5. A. Ben-Shem, F. Frolow, N. Nelson, *Nature* **426**, 630 (2003).
6. P. Jordan *et al.*, *Nature* **411**, 909 (2001).
7. X. Pan, Z. Liu, M. Li, W. Chang, *Curr. Opin. Struct. Biol.* **23**, 515 (2013).
8. R. Croce, H. van Amerongen, *Nat. Chem. Biol.* **10**, 492 (2014).
9. Z. Liu *et al.*, *Nature* **428**, 287 (2004).
10. D. R. Ort, X. Zhu, A. Melis, *Plant Physiol.* **155**, 79 (2011).
11. R. E. Blankenship, M. Chen, *Curr. Opin. Chem. Biol.* **17**, 457 (2013).
12. A. Amunts, H. Toporik, A. Borovikova, N. Nelson, *J. Biol. Chem.* **285**, 3478 (2010).

10.1126/science.aab3387

#### NEUROSCIENCE

## Exploiting sleep to modify bad attitudes

Targeted memory reactivation of training-induced social counterbias during sleep

By Gordon B. Feld and Jan Born

Since the age of enlightenment in the 18th century, liberty and equality have spread across the Western world, leading to a decline in explicit racism and sexism. Nevertheless, the tendency to hold implicit prejudices of race or gender continues to drive discrimination (1, 2). Indeed, recent news has been filled with reports on the rise of nationalistic groups, excessive police violence against minority group members, persisting unequal pay for women, and sexual harassment all across the developed world. On page 1013 in this issue, Hu *et al.* (3) show how such unwanted attitudes may be persistently changed by a social counterbias training when the fresh memories of this training are systematically reactivated during sleep after training.

Sleep, and specifically deep or slow-wave sleep [non-rapid eye movement (REM) sleep], benefits memory formation by reactivating neuronal traces that were formed during the preceding period of wakefulness. This reactivation of specific memories leads to their strengthening and transformation (4). Such reactivation can be experimentally induced during slow-wave sleep by presenting cues that were present during the prior period of memory acquisition. Initial studies showed that an odor present during learning of object locations enhances these memories when the participant is reexposed to the odor during slow-wave sleep after learning (5). These findings have been confirmed in numerous studies investigating different memory systems and also when auditory instead of olfactory cues are used (6–8). This basic research has firmly established the possibility of influencing sleep to enhance specific newly learned memories by targeted memory reactivation.

The findings by Hu *et al.* now suggest that this method can also be used to influence implicit attitudes that are known to typically manifest themselves early during childhood and remain very stable into adulthood (9). Before a 90-min nap, participants underwent training aimed at countering typical implicit gender and racial biases by learning to associate genders and

faces with opposing attributes; that is, to associate female faces with science-related words and black faces with "good" words (see the figure). Critically, presentation of the to-be-learned counterassociations was combined with a sound, which served as a cue to promote the reactivation of the newly learned associations during a subsequent nap while the participant was deep in slow-wave sleep. Only when this sound was re-presented during slow-wave sleep

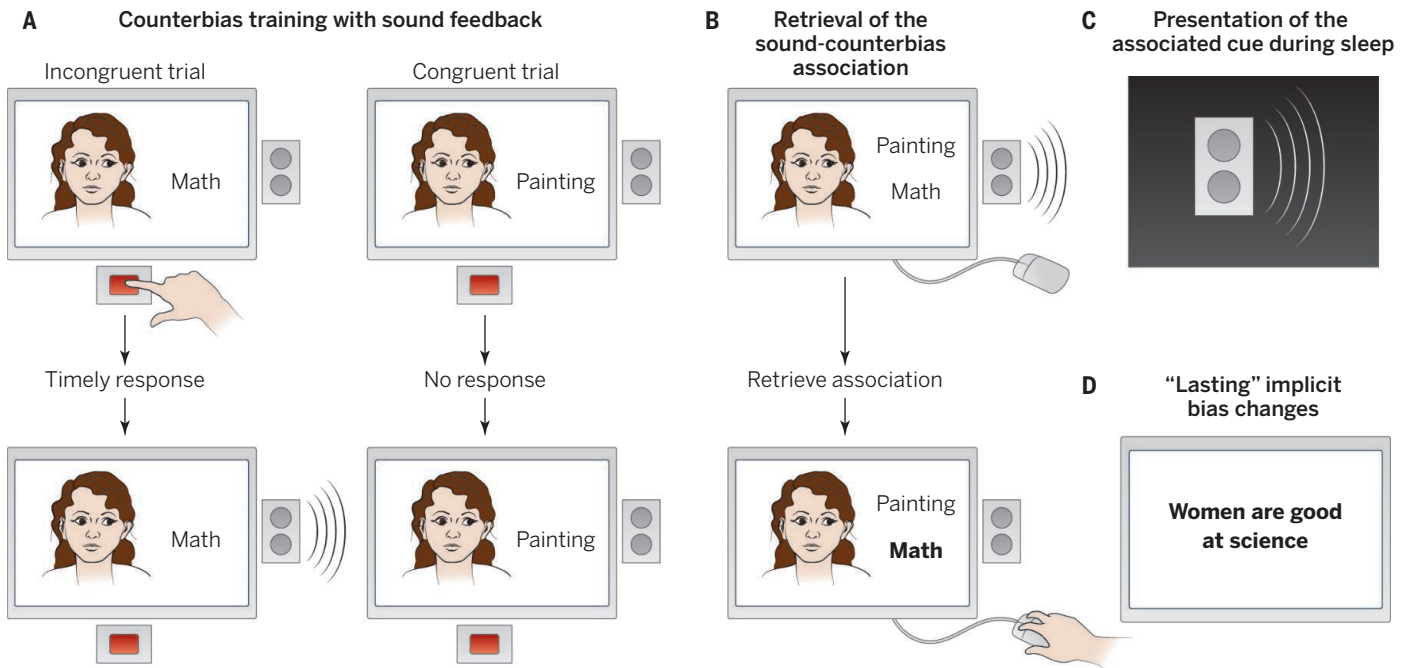
**"...this method can be used to break long-lived, highly pervasive response habits deeply rooted in memory..."**

did the posttraining reduction in implicit social bias survive and was even evident 1 week later. These findings are all the more convincing as the authors conducted the reactivation step during a 90-min daytime nap. During normal sleep at night, the effects are expected to be even stronger, owing to the generally deeper and longer periods of slow-wave sleep and REM sleep. Additionally, the accompanying neuroendocrine milieu makes nocturnal sleep even more efficient for memory reinforcement.

Previous studies have shown that such targeted reactivation of memory during sleep can effectively extinguish unwanted behavior such as experimentally induced fear in humans (10, 11). The present study is the first to demonstrate that this method can be used to break long-lived, highly pervasive response habits deeply rooted in memory and thereby influence behavior at an entirely unconscious level. A hallmark of such automatically implemented habit memories is that their retrieval escapes cognitive control exerted over consciously recalled explicit memory by the prefrontal cortical-hippocampal system. In this regard, Hu *et al.*'s data

University of Tuebingen, Institute of Medical Psychology and Behavioral Neurobiology, Otfried-Müller-Straße 25, 72076 Tuebingen, Germany. E-mail: jan.born@uni-tuebingen.de; gordon.feld@uni-tuebingen.de





**Sleeping your way out of a bad attitude.** Implicit social bias scores could be improved by applying a counterbias intervention comprising two tasks: counterbias training with sound feedback and retrieval of the sound-counterbias association. This training-induced improvement was then stabilized by re-presenting the sound cue during sleep. **(A)** On the counterbias training, participants were shown separate pictures of men and women of different racial groups together with words from the opposing categories “science/art” and “good/bad”. When seeing an “incongruous” pair (e.g., face of a woman and the word “math”), participants had to respond by pressing a button. “Correct” and timely responses received a feedback sound. Congruent trials afforded no response. **(B)** On the sound-counterbias retrieval task, participants were instructed to drag and drop a face (e.g., a female face) onto the incongruous word (e.g., “math”) whenever they heard the sound that was associated with this specific counterbias during the preceding counterbias training. **(C)** The sound was then used to cue, and thereby reactivate, the memory of the newly learned counterbias association when the participant entered slow-wave sleep during a subsequent 90-min nap. **(D)** A stable reduction of implicit social bias, persisting 1 week later, was only achieved if the counterbias intervention was cued during the nap.

suggest that sleep is a brain state stabilizing even strong habit-like implicit memories. This putatively makes them susceptible to modification through treatments targeting, in the first place, the explicit hippocampus-dependent memory system.

Hu *et al.* certainly demonstrate the striking potential of targeted memory reactivation during sleep to modify deeply rooted attitudes. Together with the ongoing debate on the longevity and effectiveness of social bias interventions (12), these findings raise a number of questions regarding the underlying neurophysiological and psychological mechanisms. One is why such enduring modifications cannot be achieved by targeted reactivations during wakefulness. Perhaps countering the preexisting racial or gender bias by memory reactivation during sleep leads to an immediate weakening of the original bias memory trace, indicating that during sleep even very old traces can reenter a labile state. Alternatively, the procedure might induce an extinction-like suppression of the original bias by a newly learned counterbias. Such new learning of response suppression implicates the activation of the machinery of synaptic plasticity during sleep. Here, another detail of Hu *et al.*'s findings is of interest, suggesting that the long-term improvement in social

bias was additionally linked to posttraining REM sleep, which represents a state of increased synaptic plasticity. This indeed fits a “sequential” view on sleep's role in memory formation (4): Each bout of slow-wave sleep and accompanying reactivation transforms the new counterbias traces and primes the participating synapses for lasting synaptic changes that are induced during the subsequent phase of REM sleep (e.g., by activation of immediate early genes and protein synthesis).

However, new learning of an extinction-like suppression also suggests that effects might depend strongly on the learning context. If so, the risk of spontaneous recovery of the original social bias is increased when the person leaves the behavior modification setting, as well as with increasing time after the treatment. Unless the underlying mechanisms are understood, there is a risk that seemingly marginal changes in the procedures of targeted memory reactivation during sleep might produce precisely opposite results of the desired effects. Indeed, just such reversals have been seen in studies applying this method to counter fear responses (13). The possibility of such an outcome is further suggested by interventions that paradoxically increase social bias instead of reducing it (14).

There is little doubt that the study of Hu *et al.*—with its clear implications for society—will motivate research to resolve these remaining issues. However, Aldous Huxley's description of a dystopian “brave new world” where young children are conditioned to certain values during sleep reminds us that this research also needs to be guided by ethical considerations. Sleep is a state in which the individual is without willful consciousness and therefore vulnerable to suggestion. Beyond that, Hu *et al.*'s findings highlight the breadth of possible applications to permanently modify any unwanted behavior by targeted memory reactivation during sleep. ■

#### REFERENCES

1. N. Ellefson, M. Barreto, *Curr. Opin. Behav. Sci.* **3**, 142 (2015).
2. A. G. Greenwald, M. R. Banaji, *Psychol. Rev.* **102**, 4 (1995).
3. X. Hu *et al.*, *Science* **348**, 1013 (2015).
4. S. Diekmann, J. Born, *Nat. Rev. Neurosci.* **11**, 218 (2010).
5. B. Rasch *et al.*, *Science* **315**, 1426 (2007).
6. T. Schreiner, B. Rasch, *Cereb. Cortex* **10**, 1093/cercor/bhu139 (2014).
7. M. Schönauer *et al.*, *J. Cogn. Neurosci.* **26**, 143 (2014).
8. J. D. Rudoy, J. L. Voss, C. E. Westerberg, K. A. Paller, *Science* **326**, 1079 (2009).
9. Y. Dunham *et al.*, *Trends Cogn. Sci.* **12**, 248 (2008).
10. K. K. Hauner *et al.*, *Nat. Neurosci.* **16**, 1553 (2013).
11. J. He *et al.*, *Sleep* **38**, 423 (2015).
12. E. L. Paluck, D. P. Green, *Annu. Rev. Psychol.* **60**, 339 (2009).
13. S. Diekmann, J. Born, *Sleep* **38**, 337 (2015).
14. L. Legault *et al.*, *Psychol. Sci.* **22**, 1472 (2011).

10.1126/science.aab4048

# Obtaining optical properties on demand

Reconfigurable metamaterials provide a flexible platform for nanophotonic technology

By Nikolay I. Zheludev<sup>1,2</sup>

With the developments in nanotechnology that enable atoms, singly or in clumps, to be moved and arranged at will, we now have the capability of creating metamaterials that can display properties not found in naturally occurring media. Today lenses are being developed that image more sharply than glass lenses, and materials can be designed that make objects invisible or bend light beams into any chosen trajectory. We look here at the impact that metamaterials are having on photonics (see the figure).

Despite the achievements so far, photonic metamaterials cannot yet be used for many practical applications because of limitations associated with energy dissipation in the metals used to construct them. Alternatives are being sought in oxides and nitrides (1), topological insulators, and two-dimensional materials, which could offer improved plasmonic response, and in high-index dielectrics delivering resonant metamaterial properties with negligible losses (2). Planar phase and intensity holograms exploiting metamaterials with spatially variable characteristics may have potential for novel applications (3, 4). Metamaterials with zero dielectric permittivity (5) and topologically protected surface modes (6) promise new waveguide technologies; metamaterials with tailored hyperbolic dispersion (7) can enhance luminescence and improve optical gain. An emerging direction is to use metamaterials for optical computation (8) and thermal and radiation management.

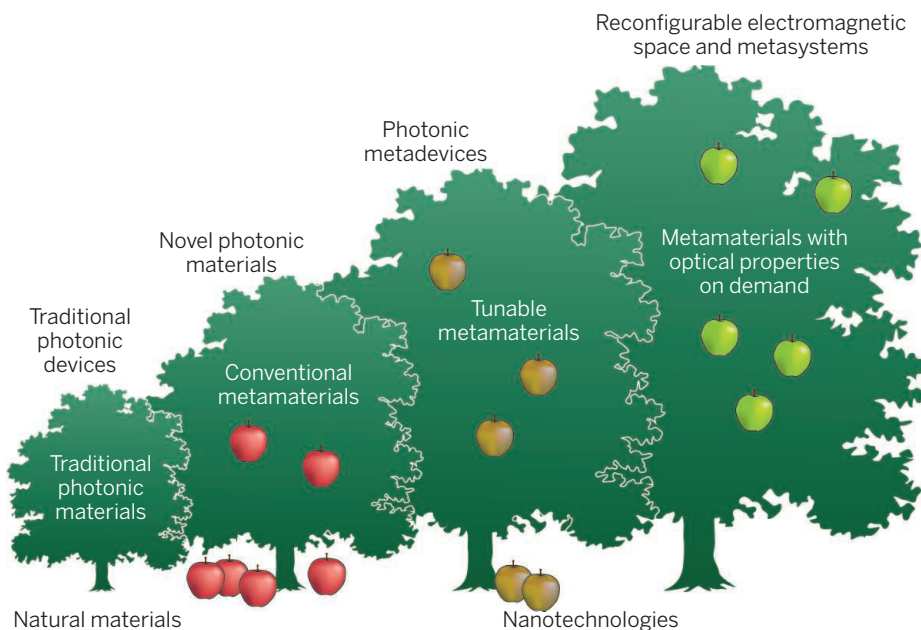
The most remarkable recent development in this materials science is that we can now tune and switch metamaterial optical properties (9). However, today's challenge is not only to achieve homogeneous change of optical response across the entire volume of the metamaterial, but to develop the "on-demand" control of individual metamolecules in the material. By analogy with electronic random access memory, such structures are called "randomly accessible metamaterials." These

metamaterials will not only allow for modulation of light's intensity or phase, but will offer full active control of the wavefront of electromagnetic radiation, tailoring of the near field, and ultimately multichannel data processing. Developing randomly accessible photonic metamaterials is a challenge: The metamolecules would have to be subwavelength optical switches with a physical volume of about  $10^{-19}$  m<sup>3</sup>. To have an impact on telecommunications technologies, such switches must also be fast and energy-efficient.

Do we have in sight physical processes that can sufficiently alter the optical properties of individual metamolecules such that they can change the phase and intensity of the transmitted and reflected light? Liquid crystal and digital micromirror spatial light modulators are well known, but they have pixels at least a few micrometers in size, too big for metamaterial applications, and their bandwidth is only a few tens of kilohertz at best, whereas electro-optical crystal modulators are fast but bulky. However, there are emerging technologies that can deliver not

only metamolecular-level switching controlled by electric or magnetic signals, but also switching with light. These are nano-optomechanical, phase-change, and coherent control technologies.

Some exceptional opportunities are provided by nano-optomechanics that takes advantage of the changing balance of forces at the nanoscale. At the submicrometer dimensions of the metamolecules, electromagnetic forces compete with elastic forces and can thus be used to reconfigure the shape of individual metamolecules or their mutual arrangement. Structured semiconductor nanomembranes are the ideal platform for such nano-optomechanical reconfigurable metamaterials (10). These structures can be driven thermoelastically, electrically, and magnetically. They can also be reconfigured by light-induced forces between elements of illuminated metamolecules. Their nonlinear, switching, electro-optical and magneto-optical characteristics can surpass those of natural media by orders of magnitude. Moreover, the nanoscale metamaterial building



**Mighty metamaterials forest.** Metamaterials were first developed as artificial media structured on a size scale smaller than the wavelength of external stimuli. They showed novel, now well-understood electromagnetic properties, such as negative index of refraction or optical magnetism, allowing devices such as optical cloaks and superresolution lenses. Tunable, nonlinear, switchable, gain-assisted, sensor, and quantum metamaterials appeared and increased the potential for device integration of metamaterial technology. The coming challenge is to develop metamaterials with on-demand optical properties that may be independently controlled for every individual metamolecule of the nanostructure.

<sup>1</sup>Centre for Photonic Metamaterials, Optoelectronics Research Center, University of Southampton, Southampton SO17 1BJ, UK.

<sup>2</sup>Centre for Disruptive Photonic Technologies, The Photonics Institute, Nanyang Technological University, Singapore 637371. E-mail: niz@orc.soton.ac.uk



blocks can be moved very fast, potentially offering gigahertz bandwidth switching. The first generation of randomly accessible reconfigurable metamaterials or nanomembranes, providing control in a single spatial dimension, have been realized and can function as refocusable lenses or dynamic diffraction gratings.

Phase change is another technology that can work for metamolecular-level switching. Initially developed for rewritable optical discs, it offers a mechanism for nonvolatile switching of optical properties within a nanoscale volume (11). This provides a new platform for creating optical components that are written, erased, and rewritten as two-dimensional binary or grayscale patterns into a film of chalcogenide glass using tailored trains of femtosecond pulses. Reconfigurable bichromatic and multifocus Fresnel zone plates, superoscillatory lenses with subwavelength focus, grayscale holograms, and a dielectric metamaterial with on-demand resonances have been demonstrated.

Another emerging technology for controlling and switching the manifestation of optical properties in metamaterials is coherent control. A highly absorbing plasmonic metamaterial film of subwavelength thickness that is placed in the node of a standing wave formed by counterpropagating control and signal waves will see zero electric field and so will not absorb the light. Any change in the phase or intensity of the control wave will distort the standing wave pattern and destroy the regime of zero absorption. This effect can underpin various forms of optical switching (12) operating down to the level of a few photons and with a modulation bandwidth up to 100 THz, presenting powerful opportunities for laser spectroscopies, image processing, and data handling in the locally coherent networks that are increasingly part of the mainstream telecommunications agenda. ■

## REFERENCES

1. G. V. Naik, V. M. Shalae, A. Boltasseva, *Adv. Mater.* **25**, 3264 (2013).
2. Y. Yang, I. I. Kravchenko, D. P. Briggs, J. Valentine, *Nat. Commun.* **5**, 5753 (2014).
3. N. Yu, F. Capasso, *Nat. Mater.* **13**, 139 (2014).
4. S. Larouche, Y. J. Tsai, T. Tyler, N. M. Jokerst, D. R. Smith, *Nat. Mater.* **11**, 450 (2012).
5. R. Maas, J. Parsons, N. Engheta, A. Polman, *Nat. Photonics* **7**, 907 (2013).
6. A. B. Khanikaev et al., *Nat. Mater.* **12**, 233 (2013).
7. A. Poddubny, I. Iorsh, P. Belov, Y. Kivshar, *Nat. Photonics* **7**, 948 (2013).
8. A. Silva et al., *Science* **343**, 160 (2014).
9. N. I. Zheludev, Y. S. Kivshar, *Nat. Mater.* **11**, 917 (2012).
10. J. Valente, J. Y. Ou, E. Plum, I. J. Youngs, N. I. Zheludev, *Nat. Commun.* **6**, 7021 (2015).
11. Q. Wang et al., *Appl. Phys. Lett.* **104**, 121105 (2014).
12. X. Fang, K. F. MacDonald, N. I. Zheludev, *Light Sci. Appl.* **4**, e292 (2015).

10.1126/science.aac4360

## INFECTIOUS DISEASES

# Overcoming neglect of kinetoplastid diseases

Drug development offers hope for controlling diseases that affect millions of people worldwide

By Graeme Bilbe

Of the 17 neglected tropical diseases listed by the World Health Organization (WHO) (1), three are caused by parasitic kinetoplastid protozoa: human African trypanosomiasis (HAT; also known as sleeping sickness), leishmaniasis, and Chagas disease. The three diseases are responsible for high mortality and morbidity among the world's poorest populations. Although these and other neglected diseases have received increased attention over the past decade, new drugs are still scarce: From 2000 to 2011, only 4% of new drugs and vaccines were registered for neglected diseases (2). However, the drug development pipeline, with sustained resources and research efforts, should see the delivery of new drugs for these diseases over the next decade.

**KINETOPLASTID DISEASES.** Transmitted by insects, these poverty-related infectious diseases are genetically highly diverse. They cause a spectrum of often chronic visceral and disfiguring skin diseases that can be fatal and that exact a high socioeconomic burden on patients and their families. Most cases occur in impoverished countries with poor health resources, but the diseases are also re-emerging in Europe and the United States.

HAT is caused by *Trypanosoma brucei* (see the first figure). It is transmitted by the bite of an infected tsetse fly and is fatal without treatment. Active case detection and treatment have led to a fall in the number of cases, currently estimated at 20,000, and sustained efforts are vital to ensure that the WHO's target to eliminate

HAT as a public health problem by 2020 is achieved and maintained. The initial hemolympathic phase of the disease generally goes undiagnosed without active surveillance.

Leishmaniasis is caused by *Leishmania* parasites that are transmitted by phlebotomine sandflies. Visceral leishmaniasis (fatal without treatment) and cutaneous leish-

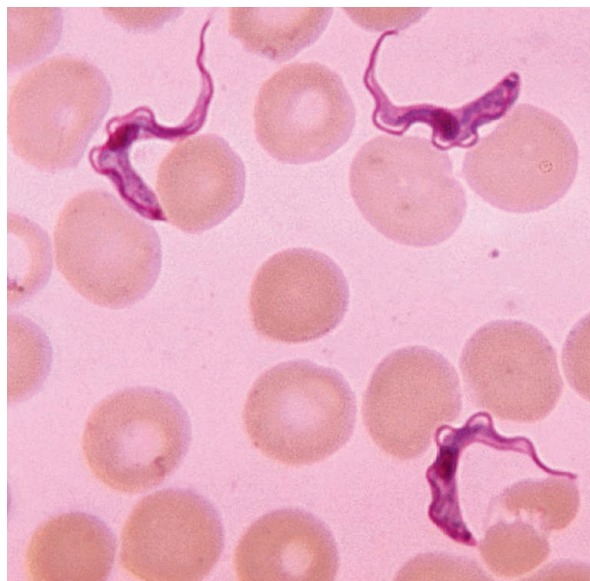
maniasis are the two most common forms of the disease, which is prevalent in 98 countries with 350 million people at risk. Leishmaniasis was long considered not to be a public health threat to high-income countries, but population increases, migration, and climate change may be spreading it, as highlighted by a recent seri-

ous outbreak in Madrid, Spain (3). Of even greater concern is the change in epidemiology of the more serious visceral form due to the spread of HIV (4).

Chagas disease is caused by *T. cruzi* parasites. An estimated 6 million to 7 million people worldwide are infected with the parasite. The disease is endemic in 21 countries of Latin America, where it causes more deaths than malaria, but can remain asymp-



INFECTIOUS DISEASE SERIES



*Trypanosoma* sp. parasites in blood smear from a patient with African trypanosomiasis. The parasites are about 16 to 42  $\mu$ m long.

ILLUSTRATION: C. SMITH/SCIENCE; IMAGE: CDC/MYRON G. SCHULTZ

tomatic for many years. Chronic symptomatic disease, which most often affects the heart and digestive tract, develops in up to 30% of cases.

**DRUG DISCOVERY CHALLENGES.** There is a need for affordable treatments that are adapted for use in resource-poor settings and can withstand the environmental conditions of endemic countries. Challenges to drug discovery and development include a lack of understanding of drug targets and obstacles to developing high-throughput screening technologies. In addition, there is a paucity of animal models predicting efficacy in patients, with further challenges in performing clinical studies that meet international standards in resource-poor settings.

Given the relatedness of the kinetoplastids, it is hoped that future oral therapies developed for one species may have utility against another. However, this goal remains unmet, because the biology of the parasites during disease and the essential biological pathways necessary for parasite survival in the host are not well understood, and selection of lethal drug targets unique to the parasite has not been possible to date. For leishmaniasis, varying levels of drug efficacy are documented for South Asian, East African, and Latin American patient populations (5, 6), illustrating the lack of understanding of parasite diversity and parasite-host interaction in the action of therapeutic agents.

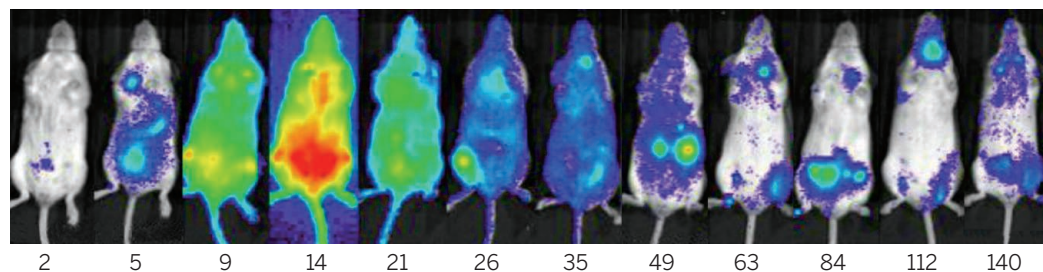
Translation into the clinic is a further challenge for kinetoplastid disease therapies. Kinetoplastid parasites are accomplished evaders of host immune response, complicating animal testing of drugs and the interpretation of animal test data. Lack of knowledge about parasite evasion mechanisms and the complexities of drug action in animal models can lead to an overestimation of “cure” in humans. Lewis *et al.* have used noninvasive bioluminescence imaging to show how *T. cruzi* parasite load varies by tissue type over time (see the second figure) (7). The results highlight the need for serial sampling of accessible tissue compartments to demonstrate the absence of parasites in patients during and after treatment, as well as for improved biomarkers and diagnostics for Chagas disease.

Not all drug candidates will advance unhindered through development, and resis-

tance to new drugs may render new tools quickly ineffective in therapeutic settings. Alternatives will thus be needed. However, the rise of resistance can be countered by developing combinations of drugs with different mechanisms of action, as has been shown with older drug combinations such as NECT (nifurtimox-eflornithine combination therapy) for HAT or sodium stibogluconate and paromomycin for visceral leishmaniasis. Only new drugs will overcome the remaining serious issues of drug administration and toxicity.

Further challenges are faced as candidate drugs progress into clinical studies. A human experimentally induced infection model for malaria (8) allows rapid testing of promising candidates in healthy volunteers inoculated with low numbers of parasites and treated with a test drug. Should

There is also a continued need for rapid, sensitive, and specific diagnostic tests for patient screening and to confirm parasitological cure following treatment. In the case of HAT, although a first generation of rapid diagnostic tests (RDTs) with high sensitivity and specificity has been developed, they still need to be deployed, particularly in order to extend passive screening in fixed health facilities. A second generation of RDTs based on recombinant antigens is in development, but the need to find a confirmatory surrogate marker of parasitological cure following treatment remains. The need for rapid tests goes beyond clinical trials; for instance, by mobile teams in Africa who travel to villages far from treatment centers to screen, diagnose, and determine the state of HAT progression. Disease staging requires examination of cerebrospinal



**Hide and seek.** Bioluminescence imaging of mice infected with *T. cruzi* parasites shows that infection is highly dynamic in space and time (7). The figure shows snapshots of infection in the same mouse over the course of 140 days. The colors indicate the bioluminescence intensity from low (blue) to high (red).

the test substance show lack of efficacy against the parasite, a proven treatment is administered to prevent the development of full-blown disease in healthy volunteers. Combining safety and efficacy tests in this way can expedite progress to large-scale field trials in patients. Unfortunately, drugs for kinetoplastid diseases cannot currently be tested in this way, and new treatments require lengthy follow-up to demonstrate sustained recovery by the patient.

It is also crucial that evidence-based clinical research in endemic countries is conducted to the same standards as those demanded in the developed world. Careful consideration is needed to ensure that patient consent is properly obtained. Local ethical requirements need to be met and cultural needs respected. It is often necessary to improve site infrastructure by equipping sites with solar energy or generators to run laboratory equipment and to guarantee the cold chain required for samples, together with Internet access for the transmission of clinical data. Local personnel need to be trained in the conduct of clinical trials to conform to international standards, and accessing sites can be difficult, especially during the rainy season.

fluid obtained by lumbar punctures, and needs to be carried out at diagnosis and after treatment. Ultimately, rapid tests will become part of the tool kit needed to carry out a “test and treat” strategy at the village level for disease elimination.

**THE DRUG PIPELINE.** Until 2009, therapies for the advanced, neurologic phase of HAT were toxic or difficult to administer. The main treatment, the arsenic compound melarsoprol, required 10 painful daily injections, with ~5% treatment-related mortality. The current combination of oral nifurtimox and infusions of eflornithine (NECT) is a vast improvement, but requires patient hospitalization. Two compounds undergoing clinical evaluation may become the first oral-only treatments: fexinidazole and SCYX-7158 are in phase IIb/III and phase I trials, respectively (9), and are potentially useful for both stages of the disease.

Pentavalent antimonials have long been used to treat visceral leishmaniasis despite requiring slow, painful injections or infusions; side effects include cardiotoxicity and pancreatitis. Parasite resistance to such therapies is on the increase. New formulations and alternative treatments (including



liposomal amphotericin B, miltefosine, and low-cost paromomycin) have become available over the past decade, but each has disadvantages, such as difficult administration, toxicity, or cost. There are also regional differences in response to therapy. Exploratory studies are evaluating the efficacy of fexinidazole in visceral leishmaniasis patients, and several potential oral drug candidates are undergoing preclinical evaluation.

Benznidazole and nifurtimox are the only available treatments with potential to cure Chagas disease, but have many side effects. Recent trials with two azole class compounds—posaconazole and the ravuconazole pro-drug E1224—showed neither to be sufficiently effective alone (10, 11), although benznidazole monotherapy did show sustained effect for 12 months and longer. More clinical studies are under way to determine the efficacy and tolerability of benznidazole at lower doses and/or with altered treatment duration, and in combination with E1224.

**OUTLOOK.** Neglected diseases still lack sufficient investment. Attempts to mitigate the lack of resources through collaborations, open sharing of information to avoid duplication of research effort, and harnessing new technologies to enhance discovery programs are ongoing. However, sustainable funding is needed to ensure the development of a new generation of orally active therapies. Progress toward effective oral therapies for Chagas disease and visceral leishmaniasis is slow and will require continued efforts in discovery and development for at least another decade. However, notable advances have been made in the development of HAT treatments, with orally active therapies close to finishing pivotal clinical trials. These drugs should become part of the arsenal in ongoing efforts to eliminate this deadly disease. ■

#### REFERENCES

1. WHO/Department of control of neglected tropical diseases. *Investing to overcome the global impact of neglected tropical diseases. Third WHO report on neglected tropical diseases* (WHO, Geneva, Switzerland, 2015); see [http://apps.who.int/iris/bitstream/10665/152781/1/9789241564861\\_eng.pdf](http://apps.who.int/iris/bitstream/10665/152781/1/9789241564861_eng.pdf).
2. B. Pedrique et al. *Lancet Glob. Health* **1**, e371 (2013).
3. A. Arce et al., *Euro Surveill.* **18**, 20546 (2013).
4. B. Monge-Maillou, F. F. Norman, I. Cruz, J. Alvar, R. López-Vélez, *PLOS Negl. Trop. Dis.* **8**, e3021 (2014).
5. A. Hailu et al., *PLOS Negl. Trop. Dis.* **4**, e709 (2010).
6. E. A. Khalil et al., *PLOS Negl. Trop. Dis.* **8**, e2613 (2014).
7. M. D. Lewis et al., *Cell. Microbiol.* **16**, 1285 (2014).
8. J. S. McCarthy et al., *PLOS ONE* **6**, 6 (2011).
9. G. Eperon et al., *Expert Rev. Anti Infect. Ther.* **12**, 1407 (2014).
10. I. Molina et al., *N. Engl. J. Med.* **370**, 1899 (2014).
11. DNDi, *Drug Trial for Leading Parasitic Killer of the Americas Shows Mixed Results But Provides New Evidence for Improved Therapy* (DNDi, Geneva, Switzerland, 2013); see [www.dndi.org/media-centre/press-releases/1700-e1224.html](http://www.dndi.org/media-centre/press-releases/1700-e1224.html).

10.1126/science.aaa3683

#### IMMUNOLOGY

## Expanding the role of metabolism in T cells

A protein links mitochondrial energetics to T cell proliferation

By David O'Sullivan and Erika L. Pearce

Understanding the mechanistic processes that govern T cell responses is crucial to enhancing immunotherapies against human disease. Naïve CD8 T cells extensively proliferate in response to antigen, creating a large pool of effector T cells that clear tumors or infected cells. During this process, T cells metabolically reprogram to meet energy demands and supply biosynthetic precursors necessary for proliferation (1). On page 995 of this issue, Okoye *et al.* (2) identify lymphocyte expansion molecule (LEM), a protein that targets T cell metabolism and enhances proliferation. LEM improved CD8 T cell-mediated viral and tumor clearance and boosted memory T cell numbers. These findings suggest that modulating T cell metabolism by targeting LEM could alter the course of cancer, autoimmunity, or infection.

Okoye *et al.* identified LEM by analyzing antiviral CD8 T cell responses in mice that had chemically induced germline mutations. Increased numbers of virus-specific CD8 T cells were found in one mouse (called Retro). The enhanced expression of LEM in this mouse was consistent with a mutation in the *BC055111* gene. Through a series of experiments, the authors predicted that this mutation led to stabilization of LEM messenger RNA (mRNA) through the loss of an alternative splicing factor/splice factor 2 (ASF/SF2) binding site, and a subsequent reduction in nonsense-mediated decay, a targeted process that can degrade mRNA.

Okoye *et al.* infected Retro mice with lymphocytic choriomeningitis (LCMV) clone 13, which establishes a chronic infection, and found reduced viral titers that correlated with increased numbers of virus-specific CD8 T cells and lysis of infected cells. On a per cell basis, killing by Retro CD8 T cells was identical to that of wild-type cells, indi-

cating that the greater antiviral immunity in Retro mice was not due to enhanced function as a consequence of LEM, but rather due to increased numbers of CD8 T cells.

Although Retro mice exhibited enhanced T cell responses and reduced viral titers, they died 2 weeks after infection, whereas all wild-type mice survived. Elevated effector T cell-mediated cytotoxicity in Retro mice suggested a pathology resulting in a fatal loss of vascular integrity (3). There is a trade-off between killing infected cells and limiting damage to healthy tissue. Reaching the right balance is crucial for an effective immune response and is context dependent. Consistent with this idea, in contrast to infection with LCMV clone 13, Retro mice infected with LCMV Armstrong, which causes an acute infection, exhibited no mortality, despite still having appreciably more effector CD8 T cells. Of note, Retro CD8 T cells exhibited reduced programmed cell death-1 (PD-1) expression after LCMV clone 13 infection. PD-1 negatively regulates T cell activation, and lower expression can cause sustained

---

**“...metabolism can determine biological outcomes in the immune system.”**

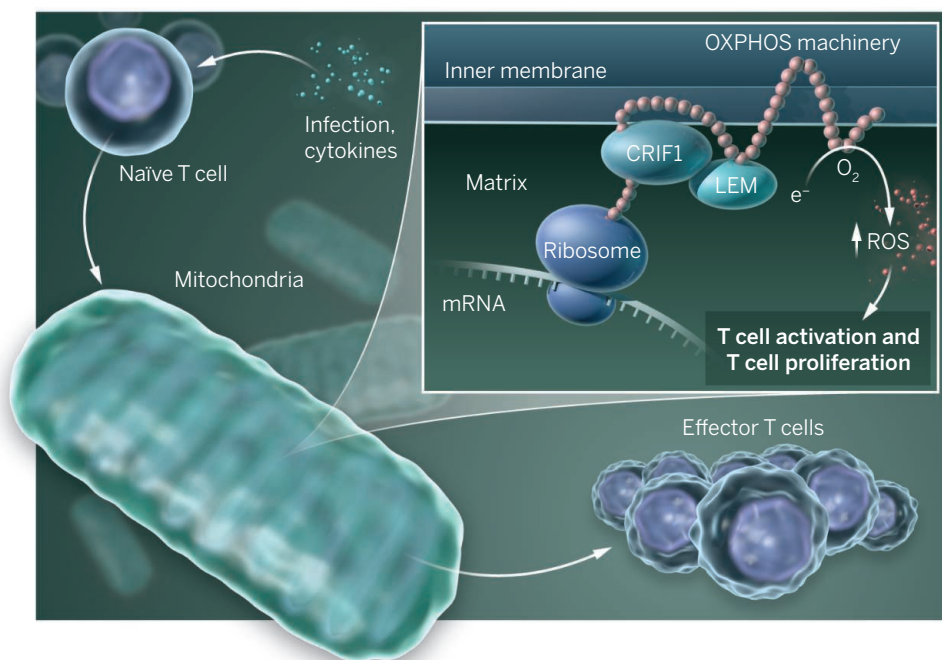
---

effector T cell responses (4). Reduced PD-1 expression with increased proliferation (and thus a larger CD8 T cell response) in Retro mice may be a deadly combination in chronic infection. In infections like LCMV clone 13, where antigen expression is sustained, PD-1 mediated signaling and T cell exhaustion may be a protective mechanism to limit pathologic T cell responses (3, 5).

Although reduced PD-1 expression and enhanced CD8 T cell proliferation could be detrimental during chronic infection, they are likely to be favorable in cancer or acute infection. In a B16 melanoma mouse model, CD8 T cells from Retro mice reduced tumor burden. Also, memory T cells increased after infection with LCMV Armstrong. This may be due not to a direct function of LEM in memory T cells, but to the larger primary immune response, from which memory T cells emerge. This is supported by the decrease in LEM in both wild-type and Retro CD8 T cells 8 days after infection, when effector T cells begin to die and memory T cells persist; it is also consistent with the lower frequency of memory T cell precursors in Retro mice, despite their greater numbers.

---

Department of Pathology and Immunology, Washington University School of Medicine, St. Louis, MO, 63110, USA.  
E-mail: [erikapearce@path.wustl.edu](mailto:erikapearce@path.wustl.edu)



To identify how LEM promotes CD8 T cell proliferation, Okoye *et al.* used yeast two-hybrid screens and immunoprecipitation to pinpoint LEM binding partners. They found that LEM associates with CR6 interacting factor 1 (CRIF1), a protein required for the synthesis and insertion of polypeptides into the inner mitochondrial membrane, which is needed for effective oxidative phosphorylation (OXPHOS) (6) (see the figure). Loss of CRIF1 or LEM inhibited T cell proliferation. LEM-CRIF1 interaction increased both the expression of proteins necessary for OXPHOS and the activity of protein complexes of the electron transport chain. Despite the increased OXPHOS in Retro CD8 T cells, no decrease in the extracellular acidification rate, an indicator of aerobic glycolysis, was observed, suggesting a substantial net increase in adenosine 5'-triphosphate (ATP) production. Localization of CRIF1 to the nucleus has previously been linked to negative regulation of the cell division cycle (7). Perhaps CRIF1 recruitment to the mitochondria removes a cell cycle block, while concomitantly enhancing OXPHOS.

The production of reactive oxygen species (ROS) derived from OXPHOS is crucial for T cell activation and proliferation (8). Okoye *et al.* hypothesized that enhanced ROS production augments proliferation of Retro T cells. On day 8 after LCMV infection, Retro CD8 T cells had increased amounts of ROS, which was reduced by the superoxide dismutase mimetic, MnTBAP. Administration of MnTBAP in Retro mice after LCMV infection also reduced T cell proliferation and elevated LCMV titers. The authors concluded that mitochondrial-derived ROS drives CD8 T cell expansion in Retro mice.

**Metabolic reprogramming.** Upon activation, naïve T cells undergo a change in metabolism to support proliferation and development into effector T cells. Activation drives LEM expression, and its interaction with CRIF1 enhances OXPHOS and ROS production.

Although this is a plausible hypothesis, further studies are needed to identify a direct link between LEM, mitochondrial ROS, and T cell proliferation. Deletion of CRIF impairs activity of all electron transport chain complexes except complex II, and promotes ROS production (3). It is conceivable that LEM-CRIF interactions, in addition to enhancing OXPHOS, may alter the balance in expression and activity of electron transport chain complexes, affecting ROS or redox balance in a way that promotes proliferation. How increased ROS is sustained at day 8 after infection when LEM expression is reduced, and whether the effects of MnTBAP are specific to mitochondrial ROS in CD8 T cells remain to be determined. Also, what role enhanced OXPHOS, and thus a likely increase in ATP production and carbon flux through the mitochondria, has in the observed phenotype is still unclear. Nonetheless, the finding that LEM controls T cell proliferation by metabolic reprogramming further establishes that metabolism can determine biological outcomes in the immune system. ■

#### REFERENCES

1. E. L. Pearce *et al.*, *Science* **342**, 1242454 (2013).
2. I. Okoye *et al.*, *Science* **348**, 995 (2015).
3. H. Frebel *et al.*, *J. Exp. Med.* **209**, 2485 (2012).
4. M. E. Keir *et al.*, *Annu. Rev. Immunol.* **26**, 677 (2008).
5. D. E. Speiser *et al.*, *Nat. Rev. Immunol.* **14**, 768 (2014).
6. S. J. Kim *et al.*, *Cell Metab.* **16**, 274 (2012).
7. H. K. Chung *et al.*, *J. Biol. Chem.* **278**, 28079 (2003).
8. L. A. Sena *et al.*, *Immunity* **38**, 225 (2013).

10.1126/science.aac4997

## MICROBIOLOGY

# Flexible gene pools

Rapid genetic exchange leads to mosaic genomes in cyanobacterial populations

By Michael M. Desai<sup>1</sup>  
and Aleksandra M. Walczak<sup>2</sup>

Evolution acts to shape genetic variation within populations. However, in microbial communities, it is often surprisingly difficult to characterize what the “population” actually represents. This makes it hard to interpret the diversity often observed in microbial communities. To what extent is diversity within a microbial species (or operational taxonomic unit, typically defined to span ~3% 16S rRNA sequence divergence) representative of one population occupying a single ecological niche? Do multiple sequence clusters in a given population represent distinct functionally diverse strains? And by how much does genetic exchange blur the boundaries of strains and species? On page 1019 of this issue, Rosen *et al.* (1) show that rapid genetic exchange maintains extensive diversity of mosaic genomes in a cyanobacterial biofilm community, despite the action of selection on many individual loci.

Naturally occurring microbial diversity has traditionally been studied with approaches based on short but conserved genomic regions such as 16S ribosomal RNA, or on sequencing a few distinct loci (multilocus sequence typing, MLST). These methods provide a relatively coarse view of the population structure. The results suggest that microbial populations often consist of multiple distinct sequence clusters, each of which contains closely related genotypes. These sequence clusters can be interpreted as functionally distinct “ecotypes” that occupy specific ecological niches (2).

Advances in sequencing technology now make it possible to probe microbial diversity at much finer resolution. However, it is difficult to understand the overall structure of genomes based on short-read sequences from natural microbial populations. In particular, it remains unclear whether extensive diversity across a microbial genome in whole-population sequencing data arises from a small number of distinct but coherent strains (see the figure, panel A) or



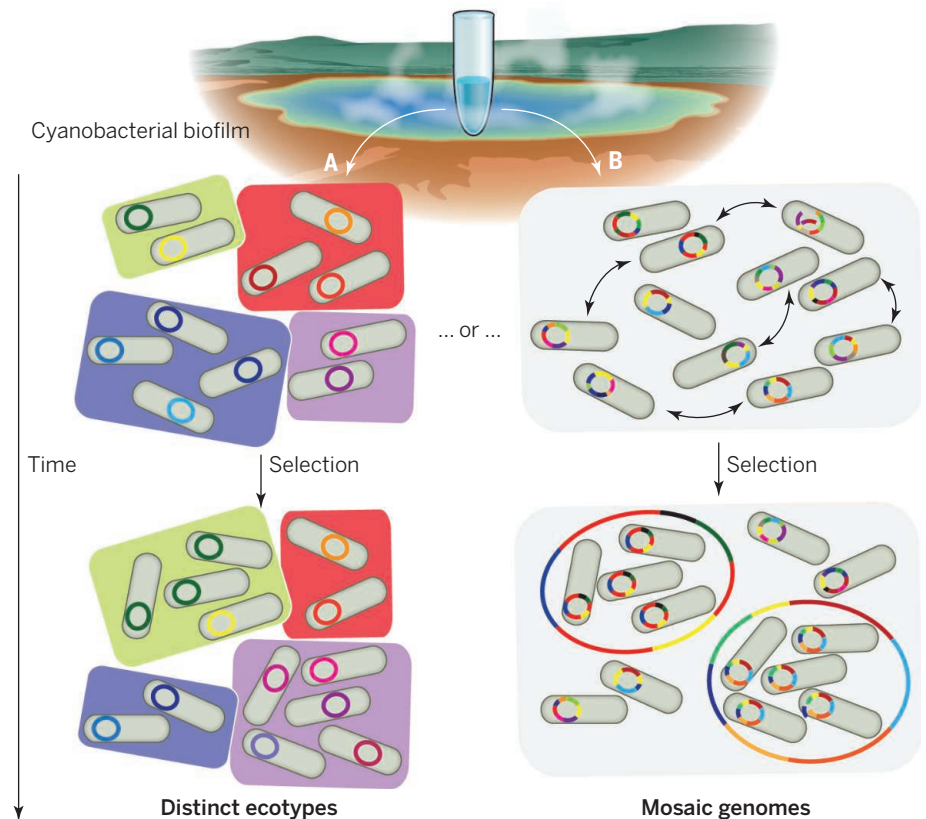
whether there is a more flexible gene pool, with individuals freely exchanging parts of their genome (3) (see the figure, panel B).

To address these questions, microbial ecologists have recently used isolate and single-cell sequencing methods, which circumvent the limitations of short-read sequencing of mixed communities. Studies of isolate genomes from *Vibrio* bacteria (4) and thermophilic archaea (5) show that recombination maintains genome-wide diversity despite selective sweeps that purge genetic variation at individual advantageous loci. A recent study of ~1000 individual *Prochlorococcus* genomes showed that these communities consist of a set of coherent strains. Each strain is characterized by specific alleles of a set of core genes (a conserved “genomic backbone”), along with a smaller group of strain-specific flexible genes (6). These strains fluctuate in frequency with time but coexist stably over long time scales, supporting the idea that they represent distinct ecotypes (see the figure, panel A).

Rosen *et al.* now introduce an alternative framework to analyze the structure of *Synechococcus* cyanobacterial biofilms. They begin by sequencing whole-population samples at multiple specific loci, an extension of traditional MLST. By sequencing each locus relatively deeply (sampling many individual cells), the authors can characterize within-locus genetic variation. This deep-sequencing approach is related to methods used in other systems (such as laboratory evolution experiments), but is relatively uncommon in microbial ecology. To analyze the data, the authors first use a traditional measure of correlations between sites, known as linkage disequilibrium, to estimate recombination rates. They then study the joint distribution of allele frequencies at two sites (a less commonly used measure of how a mutation at one site correlates with a mutation at another site) as a function of the distance between these sites.

This combination of data and analysis sheds light on both the structure of the variation in the population and the evolutionary forces that lead to this structure. If the community consists of coherent strains evolving in well-separated niches, allele frequencies among members of the same strain should be correlated even at long genomic distances. Instead, Rosen *et al.* find that these correlations decay rapidly with distance, arguing for a freely recombining gene pool without coherent strains corresponding to stable ecotypes (see the figure, panel B).

<sup>1</sup>Departments of Organismic and Evolutionary Biology and of Physics, Harvard University, Cambridge, MA 02138, USA.  
<sup>2</sup>CNRS, Laboratoire de Physique Théorique, Ecole Normale Supérieure, 75 231 Paris Cedex 05, France.  
 E-mail: awalczak@lpt.ens.fr



**Structures of genomic diversity in a cyanobacterial biofilm.** Diversity can be organized into coherent strains, each adapted to a specific ecological niche (A). Alternatively, extensive genetic exchange can lead to mosaic genomes despite the action of selection on many individual loci (B). Rosen *et al.* show that patterns of diversity in a cyanobacterial biofilm community support the latter view.

To probe the effects of natural selection in these populations, Rosen *et al.* exploit methods for correcting PCR and sequencing errors (7) to focus particularly on rare alleles. The idea is that selection acts to rapidly increase or decrease the frequency of mutations, so that alleles are either new and rare or old and common. Frequency correlations between sites will be strong for rare alleles, which are new and have not had time to recombine. Without selection and recombination, we expect the opposite effect: Only high-frequency alleles should be correlated. By comparing site frequency correlations at different distances as a function of allele frequency with neutral expectations, Rosen *et al.* can narrow down the possible evolutionary scenarios.

The results from this analysis show that variable selection pressures act on many individual loci. These selection pressures likely include frequency-dependent or local selection pressures that change the frequencies of individual alleles (8, 9). But instead of creating coherent strains, these selection pressures only structure diversity on local genomic scales, with recombination dominating on longer scales. This leads to a highly diverse “quasisexual” population without distinct genome-wide ecotypes (see the figure, panel B).

This evolutionary scenario is much more complex than is typically envisioned by evolutionary models. Nevertheless, these cyanobacterial communities are ultimately subject to the same laws of population genetics as other systems. Rosen *et al.* show that with appropriate theoretical and experimental methods, it is possible to characterize the evolutionary forces acting in these cyanobacteria. The authors do so with much less raw sequencing data than would be required in the case of single-cell genomics. Their approach shows how carefully designed empirical methods, guided by theoretical expectations, make it possible to tease apart the ecological and evolutionary forces that shape complex patterns of diversity in microbial communities. ■

#### REFERENCES

1. M.J. Rosen *et al.*, *Science* **348**, 1019 (2015).
2. F.M. Cohan, *Annu. Rev. Microbiol.* **56**, 457 (2002).
3. E.E. Allen *et al.*, *Proc. Natl. Acad. Sci. U.S.A.* **104**, 1883 (2007).
4. B.J. Shapiro *et al.*, *Science* **336**, 48 (2012).
5. H. Cadillo-Quiroz *et al.*, *PLOS Biol.* **10**, e1001265 (2012).
6. N. Kashtan *et al.*, *Science* **344**, 416 (2014).
7. M.J. Rosen *et al.*, *BMC Bioinformatics* **13**, 283 (2012).
8. M.F. Polz *et al.*, *Trends Genet.* **29**, 170 (2013).
9. O.X. Cordero, M.F. Polz, *Nat. Rev. Microbiol.* **12**, 263 (2014).

10.1126/science.aab3957

## GENOMICS

# Digitizing the biosphere

## Will sequencing every organism on Earth safeguard against the next mass extinction?

By Michael A. Goldman

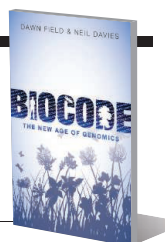
Species are becoming extinct more rapidly than we can catalog, let alone understand them, and some have argued that we are hurtling toward a sixth mass extinction (1). In their brief book, *Biocode: The New Age of Genomics*, Dawn Field and Neil Davies propose that to safeguard Earth's biodiversity, we should produce an exhaustive DNA sequence catalog of every organism on our planet. They argue persuasively that an "Earth Biocode" is both conceivable, because of advances in technology, and urgent, because of the impending loss of species and destabilization of our biota.

*Biocode* begins with a review of the history of genetics, although it reads more like a story than a textbook, describing, for instance, a letter Francis Crick wrote to his son about his breakthrough in characterizing the structure of DNA rather than recapitulating the classic paper. Many of the key characters are there, but Rosalind Franklin and Erwin Chargaff are among those forgotten.

The book quickly becomes a rapid-fire catalog of recent research triumphs, touching upon much that is exciting in genomics right now. Both authors are professionally involved in biodiversity and in biocode projects—Field has collaborated on a metagenomic study of microbes in the "L4 site" in the Western Channel Observatory, and Davies is the lead principal investigator of the Moorea Biocode Project, an initiative that

**Biocode**

**The New Age of Genomics**  
Dawn Field and Neil Davies  
Oxford University Press, 2015.  
208 pp.



seeks to sequence all nonmicrobial species on the Pacific island of Moorea.

I wish I could say that I came away from reading *Biocode* with a clear, crisp definition of the term, but I think I understand it less right now than I did before. The authors initially compare the biocode to a barcode and define it as a standardized snippet of DNA that is unique to each species. However, later on it's also defined as "two or more interacting genomes." Each of my own cells could be considered to contain two "interacting genomes" in the form of two homologous sets of chromosomes, but I could also be considered an ensemble of my own genome and that of billions of associated microbes. Which sequences would define my biocode?

As the authors' definition expands to include sequences for every organism on Earth, biocode becomes Biocode, and within a few pages, it is "at the heart of the genomic synthesis that is defining the coming decade—and this century of biology." Whether or not you agree with this assessment, the authors are right when they point out that we have only begun to understand a small slice of the grand diversity that is life on Earth and that it is fast slipping through our fingers as a result of human-induced climate change, habitat destruction, and exploitation.

It's not just the endangered species that concern Field and Davies. They argue that

Researchers are working to create a comprehensive inventory of all nonmicrobial life on the French Polynesian island of Moorea.

we must also prioritize sequencing of "foundation" species whose presence or absence in an ecosystem can cause a cascade of changes and whose loss will have profound consequences for the many organisms with which they interact.

But what can DNA really tell us? Recently, researchers have had modest success modeling cellular phenotypes from genetic information (2) and building synthetic life (3–5), but we are far from being able to model complex life forms. We also know, for example, that identical twins can have a radically different influence on the world, even though they happen to be indistinguishable genetically. The authors acknowledge that many phenomena happen at higher levels of organization, but they maintain that while "answers to questions in the life sciences do not end with DNA—they start there."

In its final chapters, *Biocode* becomes downright inspiring, encouraging lay readers to collect and contribute samples to genomic research projects through citizen science initiatives. By the end, we are left with the impression that no field of science, no matter how holistic or reductionist, is exempt from a crucial role in understanding and planning for our planet's future.

**REFERENCES**

1. A. D. Matzke *et al.*, *Nature* **471**, 51 (2011).
2. J. Karr *et al.*, *Cell* **150**, 389 (2012).
3. H. O. Smith, C. A. Hutchison, C. Pfannkoch, J. C. Venter, *Proc. Natl. Acad. Sci. U.S.A.* **100**, 15440 (2003).
4. D. G. Gibson *et al.*, *Science* **319**, 1215 (2008).
5. D. G. Gibson *et al.*, *Science* **329**, 52 (2010).

The reviewer is at the Department of Biology, San Francisco State University, San Francisco, CA 94132-1722, USA.  
E-mail: goldman@sfsu.edu

10.1126/science.aaa9481



## EXHIBITION

# A display of brilliance

The Weston Library's inaugural exhibition showcases original works from the world's best and brightest

By Andrew Robinson

When the Protestant zeal of the Reformation overtook Oxford University in the 1540s, it lost its library. In a purge of all traces of Roman Catholicism, its books were burnt or sold to local tradesmen for repurposing. Its principal library today, the Bodleian, was founded in 1602 by Sir Thomas Bodley. A graduate of Oxford who later served as an ambassador of Queen Elizabeth I, Bodley returned to Oxford in 1598 and offered to collect the university a new library at his own expense. Shortly thereafter, the philosopher Sir Francis Bacon presented Bodley with a copy of his newly published *The Advancement of Learning* (1605). Bacon's accompanying letter praised Bodley for having built "an Ark to save learning from deluge."

By the early 18th century, the Bodleian was legally entitled to receive one copy of any new book published in the United Kingdom. Today, its collections consist of more than 11 million printed items, in addition to 70,000 e-journals and vast quantities of materials in other formats. By far the largest library in the United Kingdom, the Bodleian is also one of the world's great libraries. With the opening of the Weston Library in March 2015, the Bodleian collections are now available to researchers through facilities designed for the digital age and to the public through both permanent and changing exhibitions.

*Marks of Genius*, the Weston Library's inaugural exhibition, consists mainly of world-changing books, maps, and manuscripts from the Bodleian collections, along with some paintings and sculptures. Each work can also be viewed in an accompanying catalog (1), stimulatingly contextualized by the exhibition's curator, Stephen Hebron, with occasional help from outside experts. The overall aim of the exhibition is to illuminate the indefinable—but indispensable—concept of genius across the humanities and sciences. "If the various forms the character of genius has taken over the centuries have anything in common," observes Hebron, "it is that they celebrate the variety and creativity of human beings."

The scientific works on display include a beautifully illustrated translation of one of

the first books to appear in print: Pliny the Elder's *Historia Naturale* (Natural History), published in Venice in 1476. The exhibition features first editions of Johannes Kepler's *Astronomia Nova* (New Astronomy), published in Prague in 1609, which describes the elliptical orbits of the planets around the sun, and Isaac Newton's *Philosophiæ Naturalis Principia Mathematica* (Mathematical Principles of Natural Philosophy), published in London in 1687, which introduces the inverse square law of gravity and the three universal laws of motion. Featured manuscripts include Euclid's *Stoicheia* (Elements), the oldest manuscript of a classical Greek author to bear a date (888), and a draft of Mary Shelley's *Frankenstein*, complete with corrections, revisions, and additions by her poet husband, Percy. An exquisite map of the insulin molecule with the atomic positions rendered in black and red, attributed to Dorothy Hodgkin and dated 1968, and a fine portrait of Galileo presented to the university in 1661 by his last pupil, Vincenzo Viviani, are also on display.

In 1931, Albert Einstein wrote a few lines

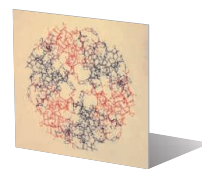
## Marks of Genius Masterpieces from the Collections of the Bodleian Libraries

Stephen Hebron, curator

Weston Library, Oxford, UK.

21 March to 20 September 2015.

<http://genius.bodleian.ox.ac.uk>



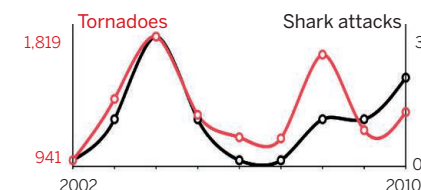
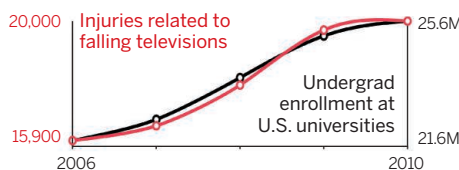
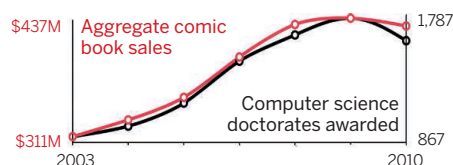
in German on a modest, unheaded sheet of paper, accepting Oxford's offer of an honorary doctorate. The note appears in the accompanying catalog alongside a blackboard chalked by Einstein while delivering three Oxford lectures about relativity in 1931. The blackboard is now a very popular exhibit at the nearby Museum of the History of Science. Less well known is a second, blank Einstein blackboard, kept in the museum's store. Its chalk "marks of genius" were erased by a cleaner: a fate that might have amused Einstein, given the dismissive reception of relativity by many physicists, universities, and the Nobel Prize committee.

10.1126/science.aab1331

## REFERENCES

1. S. Hebron, *Marks of Genius: Masterpieces from the Collections of the Bodleian Libraries* (Bodleian Library, University of Oxford, Oxford, 2014).

The reviewer is the author of *Sudden Genius?* and *Genius: A Very Short Introduction*, both published by Oxford University Press. E-mail: [andrew.robinson33@virgin.net](mailto:andrew.robinson33@virgin.net)



Correlations are critical in scientific analysis, but given enough data, it is possible to find things that correlate, even when they shouldn't. More examples of how not to use statistics can be found on the author's website, [tylervigen.com](http://tylervigen.com).

## STATISTICS

### Spurious Correlations

Tyler Vigen

Hachette Books, 2015, 207 pp.



The number of civil engineering doctorates awarded in the United States between 2000 and 2009 was strongly correlated (95.9%) with mozzarella cheese consumption during the same period. Does that mean aspiring engineers should start stockpiling this delicious dairy staple? Of course not—the similarity in variance is purely a coincidence, identified by a technique known as "data dredging," in which one data set is blindly compared to hundreds of others until a correlation is identified. Presented as a series of graphs prepared from real data sets, *Spurious Correlations* serves as a hilarious reminder that correlation most certainly does not equal causation.

10.1126/science.aac5518

Edited by Jennifer Sills

## Time for a data revolution in China

IN MARCH 2015, China's Premier Keqiang Li proposed that government data should be open to the public (1). This offers some hope for data sharing in China. How to put the advocacy of openness into practice, however, remains challenging.

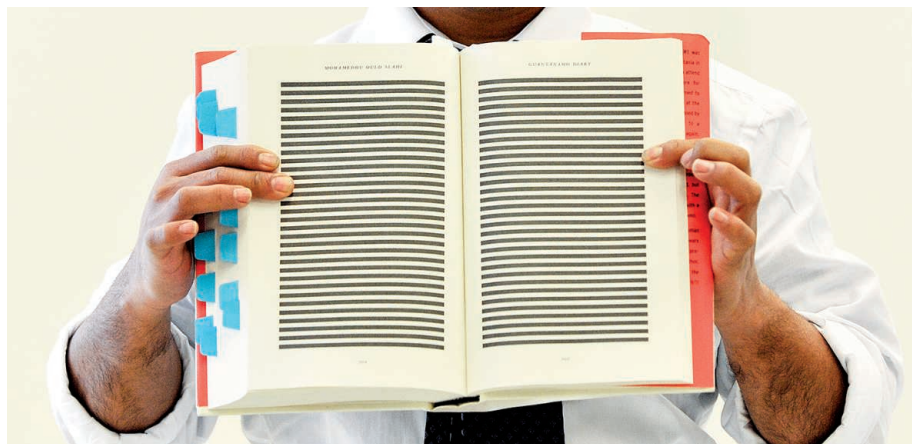
According to the UN Secretary General's Independent Expert Advisory Group on a Data Revolution for Sustainable

to declare even relatively innocuous data as state secrets. This is partly because the rule set for classified information is not clear in the "Open Government Information Regulations," which went into effect in May 2008 (4). Reasons for low data openness include, among others, fear that government data tampering will be uncovered; recognition that data gathering methods are often faulty; fear of retribution for release of data from higher officials; the power accrued from access to information; and the desire on the part of data holders to gain some benefit in return for access.

To make government data more easily and widely available, several things need to happen. First, bureaucrats need to understand that open data can benefit the

Group on a Data Revolution for Sustainable Development, "A World that counts: Mobilising the data revolution for sustainable development" (2014); [www.undatarevolution.org/report/](http://www.undatarevolution.org/report/).

3. A. Hsu, A. de Sherbinin, H. Shi, *Environ. Dev.* **3**, 39 (2012).
4. State Council of P.R. China, "Regulations of the People's Republic of China on Open Government Information" (2007); [www.most.gov.cn/yw/200704/t20070424\\_43317.htm](http://www.most.gov.cn/yw/200704/t20070424_43317.htm) [in Chinese].
5. Examples include Xue Feng, a Chinese-American geologist who was sentenced to 8 years in prison because he had obtained data on the locations of Chinese oil wells (6); Zheng Sun, an officer from the National Bureau of Statistics of China who was sentenced to 6 years in prison because he released gross domestic product and consumer price index data (7); Zhiwen Wu, a Ph.D. in economics who was sentenced to 5 years and 6 months in prison because he shared data with others (8); and possibly Gao Yu, who was sentenced to 7 years in prison because she shared government information (9).
6. M. Hvistendahl, *Science* **339**, 384 (2013).
7. D. Guoyuan, "National Bureau of Statistics official who leaked important economic data is sentenced" (2011); <http://news.qq.com/a/2011024/001187.htm> [in Chinese].
8. "Ph.D. in economics who leaked the country's economic data 144 times sentenced to 5 and a half years" (2012); <http://news.sohu.com/20120331/n339468955.shtml>.
9. H. Pin, "Gao Yu's real crime," *New York Times* (15 April 2015); <http://cn.nytimes.com/opinion/20150415/c15ho/en-us/>.



Government data sharing in China remains limited.

Development, the data revolution is composed of, among other things, two major developments: big data and open data (2). Government census and survey data can be major engines for transparency and innovation. They cover continuous time periods, large areas, and diverse groups. Open government data benefits scientific research, economic development, environmental management, social justice, and political decision-making. However, government data sharing is very limited in China (3). Much data, ranging from social statistics to the results of environment and resource surveys, are kept from the public. The potential of these data is largely untapped because they are released only in highly aggregated forms, meaning that spatial and temporal patterns cannot be examined. In addition, insufficient information is provided on the data gathering methods.

Poor government data accessibility also affects data sharing between individuals, industry sectors, and organizations, and even between different government sectors in China. This results in redundant data collection efforts. Chinese officials are quick

economy, the environment, public participation, and decision-making. Second, there needs to be a clearer legal definition for what information needs to be classified, so that this decision is not left up to the discretion of data holders. Third, if data are released in compliance with the policy, individuals should not be penalized for sharing information (5). Finally, China should comply with international standards of data collection, documentation, maintenance, and disclosure.

Ruishan Chen,<sup>1\*</sup> Alex De Sherbinin,<sup>2</sup>  
Chao Ye<sup>3</sup>

<sup>1</sup>School of Public Administration, Hohai University, Nanjing, 210098, China. <sup>2</sup>Center for International Earth Science Information Network (CIESIN), Columbia University, Palisades, NY 10964 USA.

<sup>3</sup>College of Geographic Sciences, Nanjing Normal University, Nanjing 210023, China.

\*Corresponding author. E-mail: chenrsh04@gmail.com

### REFERENCES AND NOTES

1. "Li Keqiang's Declaration on Government Data: Open!," *The Beijing News* (7 March 2015); [www.gov.cn/guowuyuan/2015-03/07/content\\_2829215.htm](http://www.gov.cn/guowuyuan/2015-03/07/content_2829215.htm) [in Chinese].
2. The Secretary-General's Independent Expert Advisory

## Qualifying pollinator decline evidence

THE POLLINATION CRISIS has garnered perhaps more public interest than any other environmental problem short of climate change. It is therefore remarkable that it is based on such limited science. D. Goulson *et al.* ("Bee declines driven by combined stress from parasites, pesticides, and lack of flowers," *Review*, 27 March, p. 1435; published online 26 February) acknowledge that evidence for pollinator declines is almost entirely confined to honey bees and bumblebees in Europe and North America. Yet they conclude that "it is probably reasonable to assume that declines are also occurring elsewhere across the globe." This is a possibility, but not one that can be well justified by current evidence. Their statement extrapolates data from north temperate bumblebees (a single and rather unrepresentative clade), which include less than 0.6% of the 20,000 worldwide bee species. The data are also derived from among the most intensively farmed landscapes in the world. Concern about future food insecurity due to pollinator losses rests on this shaky foundation, despite, as yet, any sign of declining crop production (1, 2).

Goulson *et al.* also bemoan minimal uptake of pollinator-promoting incentives on farmland. They attribute this to insufficient understanding among farmers of the economic benefits of pollinators. I expect, however, that farmers are more familiar with the economics of farming than ecologists. Although pollinators might elevate crop production, this has to be set



in the context of other farm management interventions (3). It is difficult to envisage a more pollinator-dependent crop than Californian almonds, which Goulson *et al.* suggest are threatened by continuing honey bee decline. Yet, the 60-year decline of honey bees has been paralleled by increasing almond production and associated profits (4). The most productive years have been the past five (2010 to 2014) when honey bee colonies have been at their lowest since records began in 1947 (5).

We should make every effort to harness the public interest in pollinators to emphasize the value of, and need for, conservation. In doing so, we should not, however, blind ourselves to the limitations of our own data.

**Jaboury Ghazoul**

Department of Environmental Systems Science, ETH Zurich, Zurich, Switzerland. E-mail: jaboury.ghazoul@env.ethz.ch

#### REFERENCES

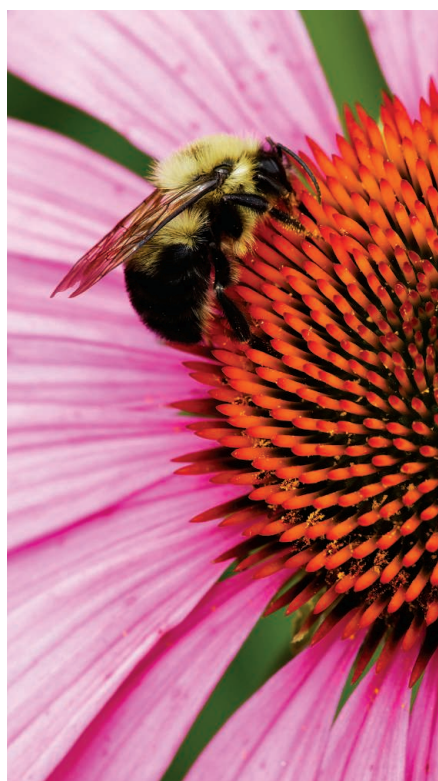
1. J. Ghazoul, L. P. Koh, *Front. Ecol. Environ.* **8**, 9 (2010).
2. M. A. Aizen, L. A. Garibaldi, S. A. Cunningham, A. M. Klein, *Curr. Biol.* **18**, 1572 (2008).
3. V. Boreux, C. G. Kushalappa, P. Vaast, J. Ghazoul, *Proc. Natl. Acad. Sci. U.S.A.* **110**, 8387 (2013).
4. J. Ghazoul, *Conserv. Biol.* **22**, 1651 (2007).
5. U.S. Department of Agriculture National Agricultural Statistics Service, "2014 California almond objective measurement report" (USDA, Sacramento, CA, 2014).

#### Response

GHAZOUL IS ACCURATE in pointing out that we have no population data on the majority of pollinators, that the data we do have are biased toward a small number of taxa (bumblebees, honey bees, and butterflies), and that data are far better for Europe and North America than for elsewhere. These points are made very clearly in our original manuscript. Of course, one could make this same statement about insects in general, or indeed about all biodiversity, yet few doubt that there really is a biodiversity crisis. If we were to wait until we had good population data for all pollinators [note that there are an estimated 1600 pollinators in the United Kingdom alone (1)] before taking action to conserve them, then we would be waiting a long time indeed.

Of course, data do exist for other regions. For example, bumblebee declines are occurring in Asia and South America (2, 3), as described in our manuscript. Data also exist for other species. The recent IUCN red data list for European bees (4) examines all 1965 European bee species, and concludes that about 287 of these are "threatened" or "near threatened," while noting that insufficient data were available to make any judgment for 1101 species. They also note that 37% of the 407 species for which there is information on population change are in decline.

Ghazoul argues that the data for declines in pollinators are largely based on social



bees, which may be unrepresentative of the majority of bees. This is true, but we should bear in mind that in the temperate Northern Hemisphere (which makes up a large proportion of the global land-mass), bumble-bees and honey bees are the predominant pollinators for a great many crops and wildflowers, being generally far more numerous than other bee species [e.g., (5, 6)]. Of course, this is not to deny the important role played by many other insects in pollination.

Finally, Ghazoul criticizes our mention of the California almond industry, in which we say "should honey bee stocks in North America fall much further, the viability of almond production in California would be threatened." He argues that there is no reason to suppose that the pattern of increased yield (gained by planting larger areas), despite falling honey bee numbers, will not continue. By inference, he is suggesting that this broadly applies to the future for insect-pollinated crops. This would be a remarkably optimistic interpretation of the situation.

What we probably can agree on is that there is an urgent need for long-term monitoring of pollinators at an international scale so that we have hard data on the pattern and extent of declines, a challenge that the global community of researchers has so far failed to tackle.

**Dave Goulson, \*Elizabeth Nicholls, Ellen Rotheray, Cristina Botias**

School of Life Sciences, University of Sussex, Falmer, Brighton, BN1 9QG, UK.

\*Corresponding author. E-mail: d.goulson@sussex.ac.uk

#### REFERENCES

1. Department for Environment, Food, and Rural Affairs, "The national pollinator strategy: For bees and other pollinators in England" (2014); [www.gov.uk/government/uploads/system/uploads/attachment\\_data/file/409431/pb14221-national-pollinators-strategy.pdf](http://www.gov.uk/government/uploads/system/uploads/attachment_data/file/409431/pb14221-national-pollinators-strategy.pdf).
2. P. H. Williams, J. L. Osborne, *Apidologie* **40**, 367 (2009).
3. R. Schmid-Hempel *et al.*, *J. Anim. Ecol.* **83**, 823 (2014).
4. A. Nieto *et al.*, "European red list of bees" (IUCN, European Commission, Luxembourg, 2014).
5. K. C. R. Baldock *et al.*, *Proc. R. Soc. London Ser. B* **282**, 20142849 (2015).
6. V. Riedinger *et al.*, *Landscape Ecol.* **29**, 425 (2014).

#### TECHNICAL COMMENT ABSTRACTS

##### Comment on "Evidence for mesothermy in dinosaurs"

*M. D. D'Emic*

Grady *et al.* (Reports, 13 June 2014, p. 1268) suggested that nonavian dinosaur metabolism was neither endothermic nor ectothermic but an intermediate physiology termed "mesothermic." However, rates were improperly scaled and phylogenetic, physiological, and temporal categories of animals were conflated during analyses. Accounting for these issues suggests that nonavian dinosaurs were on average as endothermic as extant placental mammals.

Full text at <http://dx.doi.org/10.1126/science.1260061>

##### Comment on "Evidence for mesothermy in dinosaurs"

*Nathan P. Myhrvold*

Grady *et al.* (Reports, 13 June 2014, p. 1268) studied dinosaur metabolism by comparison of maximum somatic growth rate allometry with groups of known metabolism. They concluded that dinosaurs exhibited mesothermy, a metabolic rate intermediate between endothermy and ectothermy. Multiple statistical and methodological issues call into question the evidence for dinosaur mesothermy.

Full text at <http://dx.doi.org/10.1126/science.1260410>

##### Response to Comments on "Evidence for mesothermy in dinosaurs"

*John M. Grady, Brian J. Enquist, Eva Dettweiler-Robinson, Natalie A. Wright, Felisa A. Smith*

D'Emic and Myhrvold raise a number of statistical and methodological issues with our recent analysis of dinosaur growth and energetics. However, their critiques and suggested improvements lack biological and statistical justification.

Full text at <http://dx.doi.org/10.1126/science.1260299>





Westernization of Chinese diets may be related to a rise in inflammatory bowel disease there.

## Surge in gastrointestinal disease spurs U.S.-China collaboration

Researchers from countries with complex political relations are collaborating to fight pressing health threats

By Kathy Wren

In the 1950s, physicians in the United States and Europe began reporting a rise in cases of inflammatory bowel disease (IBD), which increased roughly threefold by the 1990s. A similar trend began in Japan in the 1970s. Now, reports of the once-rare condition are doubling rapidly in China.

For decades, researchers understood little about IBD, which includes Crohn's disease and ulcerative colitis. But the new swell in Chinese cases offers researchers "an opportunity that is unparalleled" to understand what causes the disease and how it might ultimately be treated or prevented, said John Allen, clinical chief of digestive diseases at Yale University and president of the American Gastroenterological Association (AGA).

"We have built our entire theory of both etiology and treatment around assumptions that are now in question," Allen said, such as that IBD is a disease found only

Western, industrialized nations, primarily affecting Caucasians from Europe. A new collaboration between the AGA and the Chinese Society for Gastroenterology aims to correct that course.

Allen described the agreement at the 29 April conference, "Science Diplomacy 2015: Scientific Drivers for Diplomacy," in a session about how medical challenges can lead to international science cooperation. The day-long conference was organized by the AAAS Center for Science Diplomacy and drew more than 200 people, including representatives from the U.S. State Department and other federal agencies, as well as UNESCO, The World Academy of Sciences in Trieste, Italy, and the Academy of Sciences of Cuba. Sessions at the conference covered the roles of institutions and networks in science diplomacy, cooperation during political strain, working with shared resources, and other topics.

International research collaborations such as the one described by Allen, while important in their own right, also advance

the goals of diplomacy, said Rush Holt, AAAS CEO and executive publisher of the *Science* family of journals. "The principles of science—transparency, open communication, and evidence-based thinking—go a long way to diffusing difficult situations, breaking through barriers, and developing relationships that can yield benefits that go beyond the scientific research that might be discussed," Holt said in a plenary address.

A general picture of IBD has emerged in recent years, in which genetic predisposition, inflammatory processes, and environmental factors such as diet and hygiene affect the makeup of the gut's microbes and contribute to the condition. The memorandum of cooperation signed last September by the U.S. and Chinese gastroenterology associations lays the groundwork for an effort to sequence the gut microbiota of both rural and urban Chinese individuals. By comparing these genetic sequences, the researchers hope to uncover clues to how IBD develops and why it is more likely to arise in urban areas where lifestyles are more like those in the United States and Europe.

The time is ripe for this research because the sequencing and analysis tools are now available and because professional medical societies are on the rise in China. After the introduction of a market-based society in the 1980s, Chinese hospitals generally operated independently of each other, with very little focus on clinical research, according



to Allen. But the newly established Chinese Society for Gastroenterology has about 20,000 members and provides a much-needed organizational system for planning the research effort. Now, “when we throw the rope over there, someone is actually catching it,” said Allen.

Other countries with limited cooperation in the policy sphere are joining forces to solve another major public health problem: multidrug-resistant tuberculosis (MDR-TB). Tuberculosis kills 2 million people every year, and strains resistant to multiple drugs are now spreading rapidly, particularly in Russia, India, China, and South Africa.

In the 1990s, treating MDR-TB was considered a low priority by the World Health Organization. That changed somewhat after Paul Farmer and Jim Yong Kim, who went on to found Partners In Health, showed that MDR-TB could be treated successfully. Today, however, less than 1% of newly diagnosed cases of MDR-TB are treated each year, said panelist Gail Cassell, citing figures from a series of meetings hosted by the Institute of Medicine. Cassell is executive vice president of TB drug development at the Infectious Disease Research Institute and a senior lecturer at Harvard Medical School.

Understanding the genetic changes that lead to TB resistance is ground zero for fighting this disease, said Cassell: “Until you have the full spectrum of antimicrobial resistance, you cannot prescribe the right drug for the right patient at the right time.”

Cassell, along with Valery Danilenko, head of the department of Post-Genomic Biotechnology at the Russian Academy of Sciences’ Vavilov Institute of General Genetics in Moscow, and Dmitry Maslov, a research associate in that department, described an international effort launched in 2011 to sequence MDR-TB strains and support the development of new diagnostic tests, vaccines, and drugs.

The consortium includes researchers from many countries, including South Africa, Iran, Sweden, and others, who are using facilities in the United States, China, and Russia to sequence and analyze strains of drug-resistant *Mycobacterium tuberculosis*. ■

#### Screeners needed for journalism awards

Scientists from the U.S. and abroad who will be in the Washington, DC, area between late August and late September are needed to review the scientific accuracy of entries in the prestigious AAAS Kavli Science Journalism Awards competition. If you can volunteer, please contact Earl Lane (elane@aaas.org) for screening dates and categories.



John Holdren (left) and Rush Holt

## Forum on S&T policy spotlights basic research, public trust

By Kathy Wren and Earl Lane

**T**he importance of basic research for the nation’s scientific and economic future was a recurring theme as more than 400 elected officials, government and business leaders, researchers, educators, and others gathered for the 40th annual AAAS Forum on Science and Technology Policy.

Participants at the conference, held on 30 April and 1 May in Washington, DC, explored strategies for nurturing research and innovation, at the federal level and beyond, during times of continuing fiscal austerity.

Several science-funding bills were in play on Capitol Hill as the conference convened, but legislators had not proposed a replacement for the expired congressional deal that had offset some of the worst effects of the across-the-board budget cuts known as sequestration. In sessions throughout the conference, participants delved into the factors driving the tight budget environment.

Many speakers echoed a call to better support basic research, including Rep. Jim Cooper (D-TN), Flavia Schlegel, assistant director-general for natural sciences at UNESCO, and France Córdova, director of the National Science Foundation. “Our nation’s future, including our preparedness for that future, depends on innovation,” Córdova said. “Innovation in turn depends, in large part, on discovery, and discovery is fueled by basic research. This pursuit is not discretionary.”

“A lot of folks think of basic research as a sort of frivolous approach where we’re indulging the whims of scientists who just want to follow their curiosity,” said John Holdren, White House science and technology adviser, when AAAS CEO and *Science* Executive Publisher Rush Holt asked Holdren what he most wished the general public understood about science. Without investing in basic research and “the effort simply to understand more fully the universe, our world, ourselves, we are undermining our future,” Holdren said.

Researchers whose work is targeted as an example of wasteful government spending need to do a better job explaining the value of their work, panelists agreed in a session on defending grants against unjustified attacks. The importance of engaging with the public, through storytelling, data-sharing projects that seek public feedback, and other strategies, also took center stage in a session on public opinion and policy.

William Press, a computer scientist and computational biologist at the University of Texas at Austin (and a former AAAS president), urged scientists to separate facts and value judgments, in order to gain the trust of a public that is skeptical about science. Speaking in the William D. Carey lecture, Press outlined two quite different story lines for science—one tied to research, discovery, and innovation and what “can” be done, the other related to educating the public and advocating for what “should” be done. “Both are valuable,” he said, but scientists should take care to distinguish between them. ■

# RESEARCH

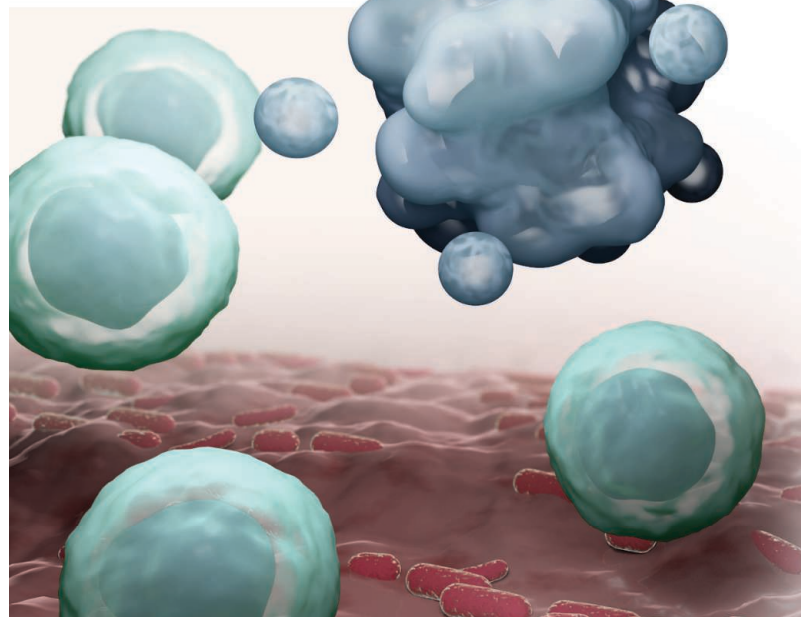
## Greenland icebergs fueled tropical methane production

Chluba et al., p. 968



## IN SCIENCE JOURNALS

Edited by Stella Hurtley



### IMMUNE TOLERANCE

## Innate lymphoid cells keep gut T cells in check

**T** trillions of bacteria inhabit our guts. So do many types of immune cells, including T cells, which might be expected to attack these bacteria. How, then, do our bodies manage to keep the peace? Working in mice, Hepworth *et al.* report one such mechanism. A population of immune cells, called innate lymphoid cells, directly killed CD4<sup>+</sup> T cells that react to commensal gut microbes. Some of the specifics of this process parallel how the immune system keeps developing self-reactive T cells in check in the thymus. Furthermore, this peacekeeping process may be disrupted in children with inflammatory bowel disease. — KLM

Science, this issue p. 1031

Keeping the peace in the gut

### PHOTOSYNTHESIS

## Photosystem I enters into the spotlight

Plants rely on large complexes of proteins, chlorophyll, and other cofactors to turn light into chemical energy. Qin *et al.* present the crystal structures of photosystem I (PSI) and the light-harvesting complex I (LHCI) supercomplex from pea plants (see the Perspective by Croce). The well-resolved structure of the outer antenna complexes and their interaction with the PSI core provide a structural basis for calculating excitation energy transfer efficiency. Moreover, the organization and orientation of chlorophyll and carotenoid cofactors within and between PSI and LHCI hint at energy transfer and photoprotection mechanisms. — NW

Science, this issue p. 989;  
see also p. 970

### INORGANIC CHEMISTRY

## An aromatic phosphorus and nitrogen ring

In chemistry, the term “aromatic” denotes the energy stabilization associated with electrons being shared among atoms in a ring. Benzene is the best-known aromatic compound, although numerous related hydrocarbons also manifest the property. Velian and Cummins now report a rare instance of an inorganic aromatic compound: a negatively charged pentagonal ring composed of three nitrogen and two phosphorus atoms. — JSY

Science, this issue p. 1001

### EMBRYO DEVELOPMENT

## How to generate head-to-tail polarity in a midge

Animal genomes do not remain static but gain and lose essential

genes over time. One such case is the *bicoid* gene of flies. *Bicoid* plays an important role in early *Drosophila* development during the generation of head-to-tail polarity, but most flies lack *bicoid*. Which genes then serve the same function in other

insects? Now, Klomp *et al.* report a structurally unrelated gene that serves essentially the same function as *bicoid* in a mosquito-related midge but does so through a different genetic mechanism. — BAP

Science, this issue p. 1040



The mosquito-related midge *Chironomus riparius*



## TYPE 1 DIABETES

**A gene therapy approach for diabetes**

Gene therapy is being used with increasing success to treat a growing group of diseases. What about diabetes? Akbarpour *et al.* used a lentiviral vector to express insulin in liver cells of a mouse model of type 1 diabetes. The therapy induced regulatory T cells specific for insulin and halted immune cell infiltration into the pancreatic islets. Moreover, when gene therapy was combined with a single dose of monoclonal antibody to CD3, it stopped disease progression in diabetic mice. Thus, expressing an autoantigen in liver cells can induce antigen-specific tolerance in autoimmune disease. — ACC

*Sci. Transl. Med.* **7**, 289ra81 (2015).

## SHAPE MEMORY ALLOYS

**Memory alloys that avoid exhaustion**

Shape memory alloys can pop back into shape after being deformed. However, often these alloys cannot cope with a large number of deformation cycles. Chluba *et al.* find an alloy that avoids this pitfall, deforming 10 million times with very little fatigue (see the Perspective by James). Such low-fatigue materials could be useful in a plethora of future applications ranging from refrigerators to artificial heart valves. — BG

*Science*, this issue p. 1004; see also p. 968

## COGNITIVE NEUROSCIENCE

**Sleep on it: Consolidating implicit learning**

A good night's sleep is one of the best ways to fix recently learned information into long-lasting memory. Recent evidence suggests that recent memories are reactivated during sleep and woven into existing representations of stored information. Hu *et al.* now demonstrate that triggering

memory consolidation during sleep can help set into place recently learned anti-bias training (see the Perspective by Feld and Born). Changes in people's stereotypical attitudes toward race and gender were maintained for up to 1 week after training. — GJC

*Science*, this issue p. 1013; see also p. 971

## CANCER

**A mutant promoter's partner in crime**

Telomerase is an enzyme that maintains the ends of chromosomes. *TERT*, the gene coding for the enzyme's catalytic subunit, is not expressed in healthy somatic cells, but its expression is reactivated in the majority of human cancers. The resultant high levels of telomerase help cancer cells survive and multiply. Recurrent mutations in the promoter region of *TERT* are associated with high telomerase levels in multiple cancer types. Bell *et al.* show that a specific transcription factor called GABP is selectively recruited to the mutant form of the *TERT* promoter, which activates *TERT* gene expression — PAK

*Science*, this issue p. 1036

## BIOSYNTHESIS

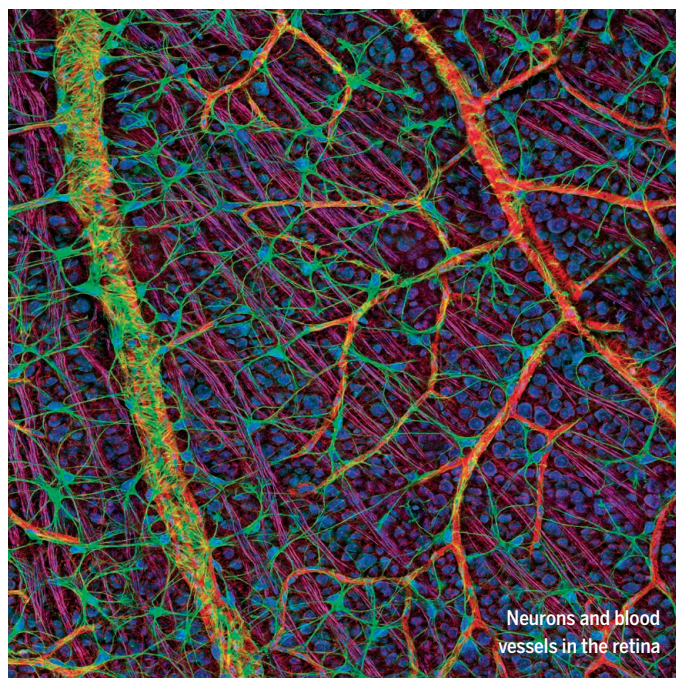
**Harnessing the power of heterologous biosynthesis**

Environmentally derived bioactive compounds obtained from filamentous fungi, plants, and bacteria have provided drugs for treating a whole variety of human diseases. However, it is often difficult to produce these compounds industrially or in the laboratory. Zhang *et al.* introduced different biosynthetic pathways into a surrogate *Escherichia coli* host to generate diverse chiral pairs of compounds. Several of the generated analogs were active against an erythromycin-resistant *Bacillus subtilis* strain. — ASH

*Sci. Adv.* **10**, 1126. sciadv.1500077 (2015).

## IN OTHER JOURNALS

Edited by **Sacha Vignieri**  
and **Jesse Smith**



Neurons and blood vessels in the retina

## NEURODEVELOPMENT

**Coordinating neurons with blood vessels**

**T**he retina develops as interleaved layers of neurons and blood vessels. Usui *et al.* show that in mice, the development of blood vessel layers depends on signals from amacrine cells, a type of interneuron in the retina. Too much or too little signal resulted in too many or too few blood vessels, particularly affecting the intermediate vascular plexus (a network of blood vessels) embedded within the retina. This cellular crosstalk coordinates neuronal demand for oxygen with the blood's ability to supply it. With the intermediate vascular plexus poorly formed, photoreceptors (a type of neuron) degenerate, leading to deficits in vision. — PJH

*J. Clin. Invest.* **10**, 1172/JCI80297 (2015).

## PHYSICS

**Cooling a semiconductor with polaritons**

Shining light onto a solid to cool it may seem counterintuitive, because the light will temporarily increase the solid's energy. To go back to its low-energy state, the solid may then emit photons more energetic than the ones it absorbed initially, effectively lowering its temperature. Such cooling methods are well established, but place stringent requirements on the material

being cooled. Klemmt *et al.* show that exciton-polaritons, exotic part-photon, part-exciton quasiparticles, can be used to cool a semiconductor microcavity. The cooling mechanism depends on the ability of the polaritons to absorb the energy of lattice vibrations and shortly thereafter to leave the solid as light. At low enough laser power, this process overpowers a competing heating process in which two photons are absorbed simultaneously. — JS

*Phys. Rev. Lett.* **114**, 186403 (2015).

## MICROBIOLOGY

### A new role for nitrogen fixers

North American coniferous forests harbor large amounts of the bacteria called bradyrhizobia. This genus made its name as obligatory symbionts of legumes, able to snatch atmospheric nitrogen via the *nif* gene product and supply it as nitrate to the plant and to fertilize soils. In return, the bacterium's *nod* genes allow it to live within the safety of the plants' roots. But legumes are rare in coniferous forests. Nevertheless, VanInsberghe *et al.* discovered that diverse bradyrhizobia, all lacking *nif* and *nod* genes, occur abundantly in these forests' soils. They are not symbionts, but they have other metabolic talents, depending on their environment. The symbionts are instead the minority in the genus. — CA  
*ISME J.* 10.1038/ismej.2015.54 (2015).

## DRUG TRIAL ECONOMICS

### Surrogates stimulate cancer investments

Allowing the use of surrogate (nonmortality) endpoints in clinical trials could lead drug companies to invest more in treatments for early-stage cancers and prevention. Long lags occur from when a drug patent is filed until it can be commercialized, a result of lengthy clinical trials that often have to demonstrate impacts on survival. Long lags leave less time for companies to recoup investments before patent expiration, skewing investment toward late-stage cancers for which shorter survival times lead to faster trials. Budish *et al.* compiled drug and trial data back to 1973 and show that the use of surrogate endpoints increased private drug research investments for cancers that otherwise would have long commercialization lags and diminished investment. — BW

*Am. Econ. Rev.* 10.1257/aer.20131176 (2015); final accepted version at <http://economics.mit.edu/files/10363>.

## GENOME EDITING

### Toward better control of genome editing

Thanks to the CRISPR-Cas system, scientists can now modify nearly any location in the genome. A stumbling block to therapeutic use, however, is that Cas9 (an endonuclease) cleaves DNA at areas of interest but often also at off-target sites. Scientists hope to overcome this by engineering versions of Cas9 with higher specificity for the target DNA. Zetsche *et al.* and Davis *et al.* explored regulating the activity of Cas9 through two different approaches, both of which relied on pharmacological activation of the enzyme. By restricting the amount of active Cas9, both strategies achieved increases in specificity. These and other specificity-enhancing approaches may give scientists

the ability to better control genome modification. — VV

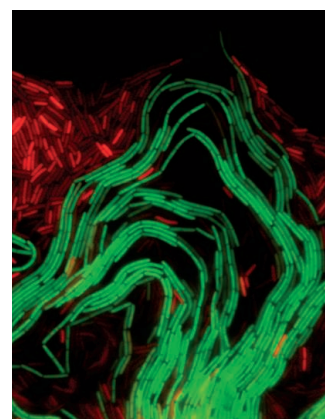
*Nat. Biotechnol.* **33**, 139 (2015);

*Nat. Chem. Biol.* **11**, 316 (2015).

## MICROBIOLOGY

### Cooperation causes van Gogh to appear

Cell-cell interactions underlie many fundamental aspects of biology, even when those cells are normally considered autonomous, such as bacteria. Van Gestel *et al.* studied how *Bacillus subtilis* cooperate to allow a colony to move en bloc across a surface. The cells bundled themselves into so-called van Gogh bundles consisting of regimented rows of cells that generate looping strands at the outer edge of the colony. These loops then push themselves away, allowing the bacteria to move to pastures



*B. subtilis* divides the labor between two cell types (in red and green) to move across a solid surface

new. Two distinct types of cell are needed to form the bundles, one to form a sort of intercellular glue and the other to form a slippery track. — SMH

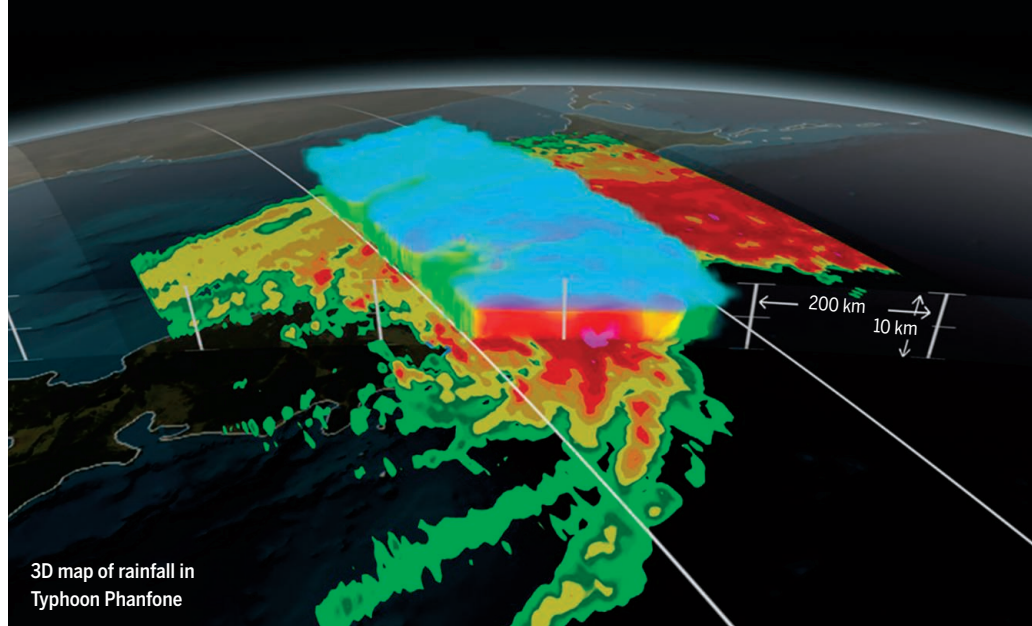
*PLOS Biol.* 10.1371/journal.pbio.1002141 (2015).

## GLOBAL PRECIPITATION

### Where the hard rain is and will be falling

Extreme precipitation events are rare, but they are very important in the global hydrological cycle. Accordingly, it is important to be able to characterize their distribution, frequencies, and magnitudes. Liu and Zipser report observations recovered over a full year by instruments on the Global Precipitation Mission Core Observatory satellite, which provide diurnal three-dimensional coverage of the entire subpolar world and categorize precipitation events by their area, depth, and convective intensity. These types of events are important to include in global climate models, in order for them to accurately describe the global water cycle. — HJS

*Geophys. Res. Lett.* 10.1002/2015GL063776 (2015).





## ALSO IN SCIENCE JOURNALS

Edited by Stella Hurtley

## POROUS MATERIALS

**It's all about the holes**

From kitchen sieves and strainers to coffee filters, porous materials have a wide range of uses. On an industrial scale, they are used as sorbents, filters, membranes, and catalysts. Slater and Cooper review how each application will limit the materials that can be used, and also the size and connectivity of the pores required. They go on to compare and contrast a growing range of porous materials that are finding increasing use in academic and industrial applications. — MSL

*Science*, this issue p. 988

## T CELL METABOLISM

**LEM gets T cells the energy they need**

During an infection, T cells proliferate extensively to build a sufficient army to defeat the invading pathogen. Carefully regulated changes in metabolism let T cells do this, but the specific nature of these changes is not fully understood. Using forward genetics in mice to screen for genes that regulate T cell immunity, Okoye *et al.* identified a mutation in the gene that encodes a protein they named lymphocyte expansion molecule (LEM) (see the Perspective by O'Sullivan and Pearce). LEM enhanced T cell immunity, including both proliferation and memory cell generation, in response to chronic viral infection. LEM facilitated these changes through effects on mitochondrial respiration. — KLM

*Science*, this issue p. 995;  
see also p. 976

## MEMORY

**Experimental recovery from retrograde amnesia**

When memory researchers induce amnesia, they normally assume that the manipulations prevent the memory engram from effective encoding at consolidation. In accordance with this, Ryan *et al.* found that after the injection of

protein synthesis inhibitors, animals could not retrieve a memory. However, to their surprise, the memory could nevertheless be reactivated by light-induced activation of the neurons tagged during conditioning. Increased synaptic strength that is the result of cellular consolidation is thus not a critical requisite for storing a memory. — PRS

*Science*, this issue p. 1007

## PALEOCLIMATE

**The tropical impact of iceberg armadas**

The massive discharges of icebergs from the Greenland ice sheet during the Last Glacial Period are called Heinrich events. But did Heinrich events cause abrupt climate change, or were they a product of it? Methane levels represent a proxy for climate, because methane production increases mostly due to wetter conditions in the tropics. Rhodes *et al.* report a highly resolved record of atmospheric methane concentrations, derived from an ice core from Antarctica. Methane levels varied—i.e., the tropical climate changed—in response to cooling in the Northern Hemisphere caused by Heinrich events. — HJS

*Science*, this issue p. 1016

## MICROBIAL DIVERSITY

**Quasi-sexual microbe populations**

Astonishing levels of fine-scale microbial diversity have been uncovered by DNA sequencing of natural populations. How this diversity is shaped and maintained and what its environmental or clinical implications might be is unclear. Using custom-made advanced statistical methods, Rosen *et al.* analyzed the evolutionary structure of a photosynthetic bacterium that grows in the hot springs of Yellowstone Park (see the Perspective by Desai and Walczak). The populations behaved neither as clones nor “ecotypes” but more like sexual organisms. These

cyanobacteria have high recombination rates that maintain diversity and prevent selective sweeps that would otherwise reduce diversity. — CA

*Science*, this issue p. 1019;  
see also p. 977

## STRESS RESPONSES

**Identification of a memory drug target**

ISRIB is a potent inhibitor of the integrated stress response (ISR), which involves the activation of eIF2 $\alpha$ -specific kinases, phosphorylation of eIF2 $\alpha$ , and consequent down-regulation of global translation levels. ISRIB is also a candidate drug for treating certain memory disorders. ISRIB does not prevent eIF2 $\alpha$  phosphorylation and must therefore act downstream of this step. Sekine *et al.* now report that ISRIB reverses the inhibitory effect of eIF2 $\alpha$  phosphorylation on the activity of eIF2B, a dedicated guanine nucleotide exchange factor, enhancing its activity independently of phosphorylation (see the Perspective by Hinnebusch). The authors isolated ISRIB-resistant cells and identified a genetic lesion in a short N-terminal region of eIF2B $\delta$  that appears to be responsible for the observed phenotype. — SMH

*Science*, this issue p. 1027;  
see also p. 967

## CELL ADHESION

**Stretching cell sheets promotes proliferation**

Mechanical strain regulates the development, organization, and function of multicellular tissues. But how? Cadherins mechanically couple neighboring epithelial cells through extracellular interactions and sequester the transcription factors  $\beta$ -catenin and Yap1. To find out more, Benham-Pyle *et al.* stretched epithelial cell sheets. This mechanical strain induced rapid cell cycle reentry, DNA synthesis by sequential nuclear accumulation, and transcriptional activation of Yap1 and  $\beta$ -catenin.

Thus, cell-cell junctions are mechanically responsive structural scaffolds providing signaling centers that coordinate transcriptional responses to externally applied force. — SMH

*Science*, this issue p. 1024

## INFECTIOUS DISEASES

**The battle against kinetoplastid diseases**

Diseases caused by protist parasites called kinetoplastids are endemic in many lower-income countries, infecting millions of people worldwide. The most widespread of these diseases is leishmaniasis, with 350 million people in 98 countries at risk of infection; another is Chagas disease, which infects an estimated 6 to 7 million people. Transmitted by insects, these diseases are often highly disfiguring and can be fatal. Many existing drug treatments, however, have serious side effects and are difficult to administer. In a Perspective, Bilbe outlines the challenges faced in developing drugs against these neglected diseases and highlights advances toward more effective, orally administered drug treatments. — JFU

*Science*, this issue p. 974

## CELL MIGRATION

**Moving to that electric feel**

Cell movement can be guided by chemical gradients (chemotaxis) or by electrical fields (electrotaxis), both of which contribute to wound healing. The mechanisms that control electrotaxis are not as well characterized as those controlling chemotaxis. The slime mold *Dictyostelium discoideum* has been widely used in chemotaxis studies. Gao *et al.* developed a high-throughput screening method to analyze electrotaxis in genetically modified *Dictyostelium* strains. Components of the TORC2 pathway, a pathway involved in chemotaxis, were also required for electrotaxis. — WW

*Sci. Signal.* **8**, ra50 (2015).

## REVIEW SUMMARY

## POROUS MATERIALS

## Function-led design of new porous materials

Anna G. Slater and Andrew I. Cooper\*

**BACKGROUND:** Porous materials are important in established processes such as catalysis and molecular separations and in emerging technologies for energy and health. Porous zeolites have made the largest contribution to society so far, and that field is still developing rapidly. Other porous solids have also entered the scene in the past two decades, such as metal-organic frameworks (MOFs), covalent organic frameworks (COFs), and porous organic polymers. No single class of porous material is ideal for all purposes. For example, crystallinity and long-range order might enhance selectivity for a molecular separation while also reducing mechanical

stability or processability with respect to less ordered structures. To have an impact on real applications, porous materials must be scalable and must satisfy multiple functional criteria such as long-term stability, selectivity, adsorption kinetics, and processability, all within a viable cost envelope. This presents a broad design challenge, and it requires us to be able to control structure and to understand multiple structure-property relationships at a detailed level.

**ADVANCES:** In addition to MOFs, COFs, and porous polymer networks, other classes of molecular porous solids have emerged in the

past 10 years, such as polymers of intrinsic microporosity and porous organic cages. The range of possible functions for porous solids is thus much broader than before. For example, conjugated microporous polymers and some COFs have extended, conjugated structures that are not present in zeolites or MOFs

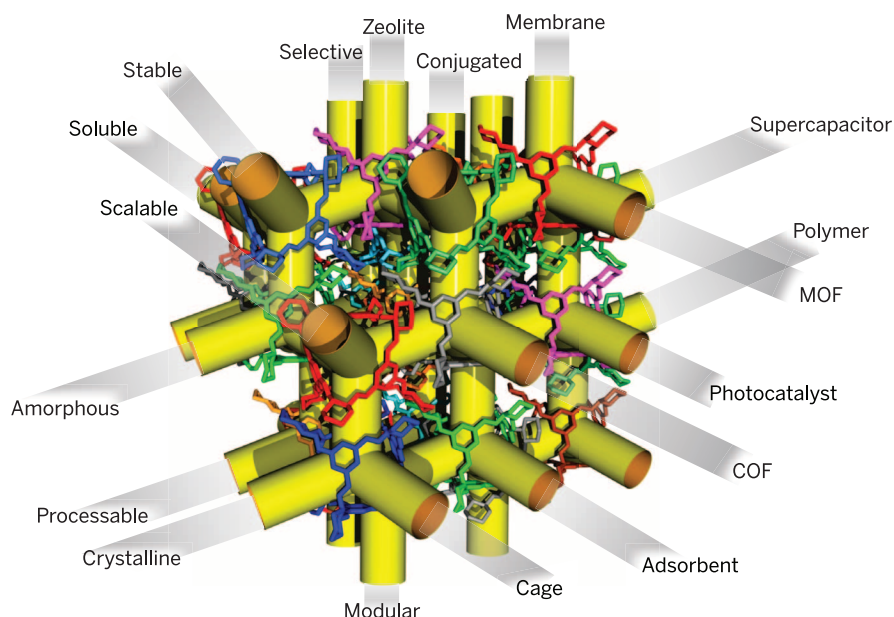
## ON OUR WEB SITE

Read the full article at <http://dx.doi.org/10.1126/science.aaa8075>

and have led to porous organic photocatalysts and electronic materials. The crystal engineering approaches developed for zeolites, MOFs, and COFs cannot be applied directly

to amorphous solids such as porous polymers, but analogous modular strategies have allowed functions such as porosity and electronic band gap to be controlled by choosing the appropriate molecular building blocks. Rapid advances in the computational prediction of structure and function offer a strategy for identifying the best porous materials for specific applications, for example, via large-scale screening of gas adsorption in hypothetical MOFs.

**OUTLOOK:** Advances in synthesis have produced new classes of functional porous solids as well as fundamental breakthroughs in areas such as selective carbon dioxide capture, molecular separations, and catalysis. As yet, these rapid developments in basic understanding are unmatched by large-scale commercial implementation, but enhanced functions (such as enzyme-like CO<sub>2</sub> selectivity) and new processing options (such as soluble porous solids) present exciting opportunities. A general challenge will be to re-engineer porous materials where scale-up is prohibited by cost, retaining the advanced function but using cheaper and more sustainable building blocks. It is therefore important to develop structure-property relationships to understand how promising materials work. Not all future opportunities for porous solids involve improving on existing materials or the development of more scalable preparation routes. For example, porous photocatalysts that can perform direct solar water splitting might provide a completely new platform for energy production. As we seek increasingly complex functions for porous materials, the use of *in silico* computational design to guide experiment will become more important. ■



**Porous materials can be defined by type or by function, but it is function that will determine the scope for practical applications.** Our ability to design functions in porous solids has advanced markedly in the past two decades as a result of developments in modular synthesis, materials characterization, and (more recently) computational structure-property predictions. This figure is based on the pore channels, shown in yellow, for an organic cage molecule, a new type of solution-processable porous solid developed over the past 6 years.

Department of Chemistry and Centre for Materials Discovery, University of Liverpool, Liverpool L69 7ZD, UK.

\*Corresponding author. E-mail: [aicooper@liv.ac.uk](mailto:aicooper@liv.ac.uk)

Cite this article as A. G. Slater *et al.*, *Science* **348**, aaa8075 (2015). DOI: 10.1126/science.aaa8075



## REVIEW

## POROUS MATERIALS

# Function-led design of new porous materials

Anna G. Slater and Andrew I. Cooper\*

Porous solids are important as membranes, adsorbents, catalysts, and in other chemical applications. But for these materials to find greater use at an industrial scale, it is necessary to optimize multiple functions in addition to pore structure and surface area, such as stability, sorption kinetics, processability, mechanical properties, and thermal properties. Several different classes of porous solids exist, and there is no one-size-fits-all solution; it can therefore be challenging to choose the right type of porous material for a given job. Computational prediction of structure and properties has growing potential to complement experiment to identify the best porous materials for specific applications.

Porous materials such as zeolites (1), metal-organic frameworks (MOFs) (2–4), covalent organic frameworks (COFs) (5), and porous polymers (6) have widespread uses in adsorption, catalysis, separation, purification, and energy storage and production. Moreover, the use of porous solids is set to grow in the future—for example, in membranes for water purification. Improving upon commercially established materials, such as zeolites or activated carbons, is a big challenge because they have been optimized over many years to fulfill multiple, combined functions; they not only act as catalysts or adsorbents but can also be processed into a usable form, such as pellets. Efficient manufacturing infrastructure with inexpensive raw materials also makes purely inorganic systems such as zeolites economically attractive. However, not all functions are satisfied by commercial materials. For example, there are as yet no commercial adsorbents that look poised to compete with aqueous amine technologies for carbon dioxide capture, despite the numerous disadvantages of liquid amines (7). Also, porous materials are not solely of interest in adsorption and catalysis: They also have potential as electronic materials, in light harvesting and energy transduction, as proton conductors, and in applications such as molecular sensing. There are hence many motivations to explore new porous materials.

In the past 20 years, the philosophy of molecular design has become increasingly prevalent in porous solids, driven by the framework design principles outlined for MOFs (2–4, 8), which in turn build on the rules developed for zeolites (1). Design-led approaches have been enabled by advances in synthetic control and by new computational techniques, as well as by developments in physical measurement. For example, structure-property relationships for multivariate MOFs

(9)—that is, structural families of MOFs with more than one organic linker—were explored using both solid-state nuclear magnetic resonance measurements and molecular simulations to rationalize properties (10). The properties of multivariate MOFs arise, or “emerge,” from the combination of the constituent molecular building units; in other porous solids, such as organic cages (11), the solid-state function can be intrinsic to the molecular building unit itself. The degree to which function is emergent or intrinsic is a central design question for porous solids, and computational prediction techniques become particularly attractive when function is emergent, and hence less intuitively linked to the isolated molecular building blocks.

Here, we survey some of the advantages and disadvantages of different types of porous solids. We also take a critical look at our ability to design new porous solids at the atomistic level, as considered from the viewpoint of individual functions. An important challenge is to apply these design approaches to real, practical systems, where it is invariably necessary to optimize more than one property, and also to mitigate undesirable properties, either through materials or systems design. For some new metal-organic and organic materials, this may require engineering around their more modest thermal and chemical stability relative to porous inorganic solids.

## Functional property drivers

For industrial applications, the primary concerns are functionality and operational costs rather than materials classification. However, porous solids are often grouped into, and reviewed as, separate classes of materials. These classes are themselves diverse in structure and function, but they nonetheless have some general advantages and disadvantages (Fig. 1). For example, porous metal-organic and organic solids have enormous structural diversity but do not exhibit the high-temperature stability of some purely inorganic materials, such as zeolites.

Porous materials can also be classified by their degree of long-range order and by the relative strength of the bonds between the atomic or molecular building blocks. Again, although each class is diverse, some broad groupings are possible (Fig. 2). For instance, porous polymer networks are typically amorphous but robust (12), being composed of strong covalent bonds, whereas MOFs are generally crystalline but the metal-ligand bonding is unstable to water in some cases. Long-range order is not always an advantage; for example, crystallinity is desirable for molecular sieving, where uniform pores are important, but amorphous materials with a hierarchy of pore sizes might be superior for heterogeneous catalysis (13).

Stability issues notwithstanding, weak intermolecular bonds can be useful in some cases. Three-dimensional networks and frameworks are, by definition, insoluble, whereas linear polymers of intrinsic microporosity (PIMs) (14) and porous molecular materials (15) have no formal intermolecular bonds and can therefore be processed as molecular solutions—for example, to form gas separation membranes (14, 16). In metal-organic materials, the intermolecular bond strength is tunable over a broad range, and some crystalline porous coordination polymers can be melt-processed (17).

Choosing the best porous solid for an application is challenging because success can rarely be gauged from one figure of merit alone, such as surface area or catalytic turnover number. As well as achieving its core target function, a porous material must also meet various other requirements such as stability (e.g., thermal, mechanical, hydrolytic, chemical, or photolytic stability), processability, ease of handling, adsorption/desorption kinetics, and thermal transport behavior. The use of expensive, rare, or toxic elements or reagents, either in the material itself or in its synthesis, is also to be avoided if possible. Ultimately, industry deals less in individual classes of materials and more in processes, or unit operations, that must deliver an integrated function within an acceptable life cycle and cost. As such, the relative merits of a new porous polymer, for example, should be considered alongside MOFs, COFs, porous molecular solids, and existing materials such as zeolites and activated carbon (Figs. 1 and 2).

## Modular design of function

Some important advances in functional porous solids, selected from the past 10 years, are shown in Fig. 3. In principle, it is possible to “dial in” almost any function in a porous material by combining atomic-level control over structure and composition with an adequate understanding of structure-property relationships. In practice there are major challenges, both in attaining structural control in solid-state materials and in predicting function from structure, even for materials where the structure is well established. For this reason, some of the materials shown in Fig. 3 were “designed” whereas others were “discovered.” Effective material design becomes

Department of Chemistry and Centre for Materials Discovery, University of Liverpool, Liverpool L69 7ZD, UK.

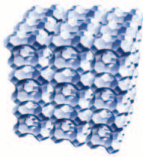
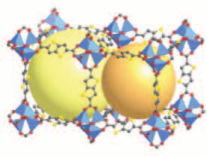
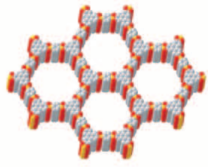
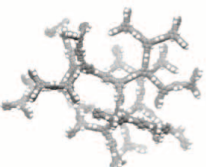
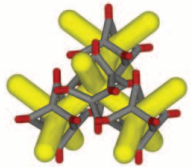
\*Corresponding author. E-mail: aicooper@liv.ac.uk

particularly difficult when the porous material must satisfy a diverse range of different and sometimes orthogonal functional criteria. For example, crystallinity provides order but can also lead to brittleness; high pore volumes can provide good gravimetric sorption capacity but might also reduce volumetric sorption capacity, heat transport, and mechanical strength, both for crystalline and amorphous solids.

MOFs have an inherent design advantage because the rigid node-strut topology and coordination bonding can be used to control both structure and composition (4, 8) (Fig. 1). Like-

wise, it is possible to control structure and composition in crystalline porous molecular solids, such as porous organic cages (15, 18), by exploiting strong noncovalent intermolecular interactions. COFs have similar structure-property design advantages. Their long-range order has often been more restricted, although single-crystalline COFs have also been prepared (19, 20). However, programming of structure and composition is not limited to ordered, crystalline solids; this has also been achieved in a modular way for a diverse range of amorphous porous polymers (6, 14, 21, 22). In certain cases, the molecular repeat unit in the

material can dominate properties, which allows function to be programmed without any long-range structural order. For example, pore volume and surface area is closely linked to the length of the rigid organic linker in conjugated microporous polymers (CMPs) (22, 23), even though they are amorphous, because short linkers avoid network interpenetration, as in some crystalline MOFs. Another well-established design principle in amorphous porous solids is the requirement for structural rigidity and sites of contortion in PIMs (14, 21) (Fig. 4A). Molecular cages can also have intrinsic porosity: The shape selectivity for

	<b>Zeolites</b>	<b>Metal-organic frameworks<sup>i</sup></b>	<b>Covalent-organic frameworks</b>	<b>Porous organic polymers</b>	<b>Porous molecular solids</b>
					
<b>Porosity</b>	Microporous or mesoporous <sup>ii</sup> ; narrow pore size distributions	Can be ultraporous <sup>iii</sup> /mesoporous; narrow pore size distributions	Can be ultraporous/mesoporous; narrow pore size distributions	Can be ultraporous/mostly microporous; broader pore sizes	Can be ultraporous/mesoporous, but this is rare so far
<b>Crystallinity</b>	Typically high; can also be amorphous	Typically high	Modest to high	Amorphous	High, but amorphous examples, too
<b>Stability</b>	Thermal stability generally excellent; can be acid/base sensitive	Poor to good; growing number of water-stable MOFs	Boronates <sup>iv</sup> generally poor; imines <sup>v</sup> generally good	Good to excellent, especially hydrothermal	Generally poor, though isolated examples of hydrothermal stability
<b>Modularity/diversity</b>	High; new structures can be based on known zeotypes <sup>vi</sup>	Very high even for single-linker MOFs; also multivariate MOFs <sup>vii</sup>	In principle high; less developed than MOFs	Very high; multiple linkers and linker functions possible <sup>viii</sup>	Cocrystals possible <sup>x</sup> ; not widely exemplified yet
<b>Processing</b>	Insoluble, but technologies for films, composites and pellets are well developed	Insoluble, though many recent examples of composite and films	Insoluble, but examples of surface growth	Modest processability, with exception of soluble PIMs <sup>x</sup>	Soluble, as for PIMs could be advantage or disadvantage, depending on function
<b>Designability</b>	Excellent, though design of organic templates can still be challenging <sup>xi</sup>	Excellent; isorecticular principles of node/strut metal-organic bonding are well developed <sup>xiii</sup>	In principle good, as for MOFs; isorecticular approach possible	Composition control good; 3-D structure control more challenging	Isolated cage can encode functions, <sup>xiii</sup> but no general isorecticular strategy
<b>Unique selling points</b>	Stability; low cost, commercially proven technology	Structural and chemical control for diverse range of materials	Electronic properties	Extended conjugation for CMPs <sup>xiv</sup> ; solution-processing for PIMs	Solution processing; physical properties intrinsic to cages
<b>Summary</b>	Developed but still actively growing area; zeolites have major commercial importance	Established and highly active field; as yet, no large-scale applications	Much less developed than MOFs, but early promise for organic electronics	Rapidly growing in number; diverse chemistry; commercial application for PIMs <sup>xv</sup>	New area with fewer examples, but early promise for specific molecular separations

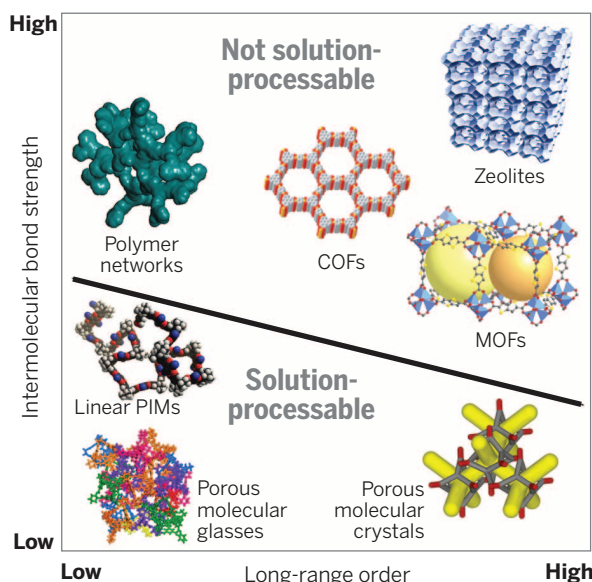
**Fig. 1. Classes of porous solids and selected functions.** The relative practical advantages of these materials will depend on the specific application, and all will be compared with established materials, such as porous zeolites (first column). Activated carbon is another important porous solid, not included here. Notes: (i) Metal-organic frameworks, or MOFs, are also known as porous coordination polymers (PCPs) (2). (ii) Microporous materials have pores smaller than 2 nm; mesoporous materials have pores in the size range 2 to 50 nm. (iii) "Ultraporous" refers here to a material with high pore volume and surface area, whether comprising micropores or mesopores [e.g., (40–43) and (12)]. (iv) Covalent organic frameworks, or COFs, with boronate ester linkages [e.g., (5)]. (v) COFs with imine linkages [e.g., (86)]. (vi) A zeotype is a

framework that is based on a known zeolite topology. (vii) "Multivariate" MOFs comprise more than one organic linker in a single framework [e.g., (9)]. (viii) For example, the combination of three different aromatic linkers allowed band gap tuning over a wide range for porous polymeric water-splitting catalysts (25). (ix) A cocrystal is a molecular crystal containing more than one molecular building unit [see (18, 38)]. (x) PIMs are polymers of intrinsic microporosity [e.g., (14, 21)]. (xi) Most inorganic zeolites are synthesized using an organic template, often an organic amine salt. (xii) See recent review (4). (xiii) See (11, 34). (xiv) Conjugated microporous polymers (22). (xv) PIM-1 (14) is used in a vapor sensor device (<http://umip.com/manchester-polymer-helps-protect-people-work>).



**Fig. 2. Functional classification**

**of porous solids.** One way to classify porous materials is by their degree of long-range order and their intermolecular bond strengths. These parameters affect function; for example, long-range order may be useful in molecular sieving applications, and strong intermolecular bonds may promote chemical or thermal stability. Only molecular porous solids can be processed as true solutions.



aromatic hydrocarbon isomers in a porous organic cage molecule was found to be defined by the shape of the cage itself (11) (Fig. 4B), which showed the same shape selectivity both in the solid state and in molecular solutions. Here, function is intrinsic to the molecular building unit, in contrast with MOFs where the isolated organic building units typically show none of the physical properties of the self-assembled framework. This modular philosophy, where the molecular building blocks encode the target function, also applies to electronic properties. For instance, electronic structure calculations for photocatalytic CMPs (24, 25) showed that the electronic properties of the polymer can be represented by small clusters of just a few monomer units (26).

Amorphous porous materials present particular difficulties for functional design because it is laborious to create an unambiguous model for the extended three-dimensional structure. As a result, of the several hundred recent papers on porous organic polymers (27), only a handful give extended structural models. Automated computational tools that can grow amorphous structures *in silico* offer a way forward (28, 29). Even for crystalline porous solids, our capacity for *de novo* design of function is still limited. The intuitive, topological assembly rules for MOFs, where families of metals and ligands assemble to give the same general framework topology (8), are not generic: Not all metal-ligand combinations lead to broad, structurally related families, and framework interpenetration (where one framework grows within another) can be difficult to anticipate by chemical insight alone. Exploratory syntheses, rather than more linear design strategies, are still therefore dominant. One can contrast the large number of hypothetical MOFs that we can enumerate computationally (30, 31) versus our current ability to identify their relative thermodynamic stabilities, and then to synthesize specific, desirable frameworks in a targeted way. For porous organic cage molecules, it is possible to compute the most thermodynamically stable crys-

tal packings from knowledge of the constituent molecules alone (18)—that is, assuming no underlying topology. If these methods can be made less computationally expensive, this offers a future strategy for the unconstrained *in silico* prediction of structure and function.

The prediction of physical properties from structure is also challenging, even when the structure of the porous material is known. The computational prediction of gas adsorption behavior is the best-developed area, and there are many examples where gas sorption isotherms have been computed for single-component gas systems (32, 33). Most studies make use of the rigid framework approximation, which becomes increasingly unreliable for flexible structures and for structures where the pores are of similar dimensions to the sorbate, although a growing number of studies have tackled adsorption selectivity in porous materials using methods that account for flexibility and molecular dynamics (11, 34, 35). Other physical properties are more difficult to predict from structure alone, and these include important functions such as catalytic activity and proton conductivity. Also, most variants of stability, such as mechanical stability (36), and even basic properties such as melting point, are relatively difficult to predict *de novo* from knowledge of atomic structure.

In summary, our ability to design function in porous materials a modular way has evolved markedly in the past 20 years, both for crystalline and amorphous porous solids. For example, crystalline MOFs (9), amorphous CMPs (37), and porous organic cage molecules (38) all constitute modular organic building blocks that may be combined interchangeably to produce more complex functional materials. Recently, but still uncommonly, computation has been used to guide rather than to post-rationalize experiments (39).

### Porosity and surface area

Extraordinary surface area (4, 40–42) and pore volume have been achieved in MOFs and COFs, including mesoporous frameworks with pores

sizes up to 9.8 nm (43), but the stability of these ultralow-density structures is as yet unproven for practical applications. For applications such as gas storage, surface area *per se*, as calculated from nitrogen adsorption isotherms, may not be the defining property (39, 44, 45). The design principles for achieving “ultraporosity” in crystalline MOFs were reviewed quite recently (4). High levels of porosity are not, however, limited to crystalline frameworks. Amorphous polymers can have surface areas of more than 5600 m<sup>2</sup>/g (12) through the use of rigid tetrahedral organic nodes and short, rigid linkers to avoid framework interpenetration (46). These covalently bonded networks are also stable to boiling water. Extremely high surface areas do not necessarily translate into direct advantages for applications such as CO<sub>2</sub> capture or molecular separations, but high pore volumes do provide other opportunities for diversification of function. Postsynthetic modification of robust, high-surface area polymers can introduce functionality such as acids (47) and amines (48). Even highly derivatized polymers could retain substantial surface area and adsorption capacity because the native, unfunctionalized framework started with such a high pore volume. Until recently, molecular solids have exhibited very low pore volumes and surface areas (49), but recent studies revealed molecular organic solids with surface areas in excess of 3700 m<sup>2</sup>/g (50). Here, the design principle is protected free volume within a porous organic cage; by contrast, most crystalline molecular materials with cavities are not stable to desolvation. Several design approaches have been used to preserve porosity in molecular crystals, such as strong intermolecular hydrogen bonding (51), the computational prediction of shape persistence in cage molecules (52), and the use of metal-coordination bonding to create “wall ties” (53) that stabilize an otherwise unstable, low-density crystal structure.

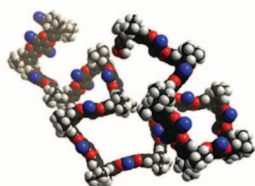
### Selectivity

Porous solids are an energy-efficient alternative for molecular separation processes that are currently performed by cryogenic distillation or by selective liquid solvents. The major formats are porous adsorbents and membranes (54). MOFs can be highly effective in molecular separations because the pore channel size, shape, and functionality can be controlled, much as for crystalline zeolites. An iron MOF, Fe<sub>2</sub>(dobdc) (dobdc: 2,5-dioxido-1,4-benzenedicarboxylate) (55), selectively adsorbed alkenes because of open iron(II) sites that can coordinate unsaturated species, thus allowing the separation of alkenes from alkanes. Likewise, affinity separations using metal-organic coordination were achieved in metallated amorphous porous solids (56, 57). Hydrocarbons can also be separated by MOFs using a summation of weaker supramolecular interactions (58). A porous framework was used to separate carbon monoxide (CO) and nitrogen by exploiting a unique structural transformation that occurs upon CO binding, thus giving rise to “self-accelerating” CO sorption (59).

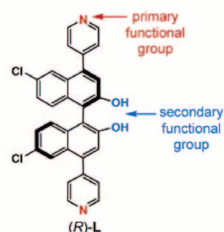
The separation of branched and linear C<sub>6</sub>, C<sub>7</sub>, and C<sub>8</sub> hydrocarbons is another important process

**2004**

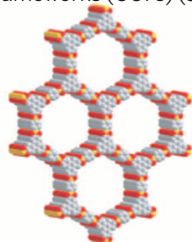
Polymers of intrinsic microporosity (PIMs) (14)

**2005**

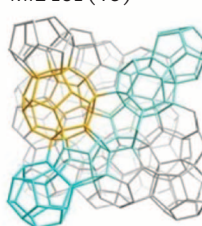
Chiral MOF for enantio-selective catalysis (94)



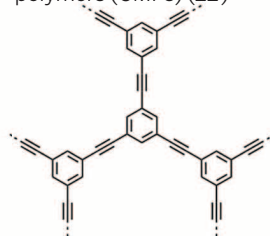
Covalent organic frameworks (COFs) (5)



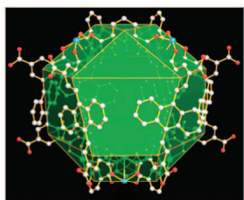
High pore volume MOF, MIL-101 (40)

**2007**

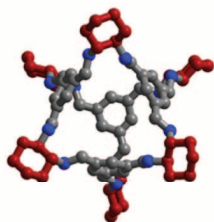
Conjugated microporous polymers (CMPs) (22)

**2008**

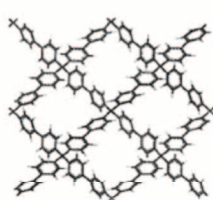
MOFs with high methane capacity (45)

**2009**

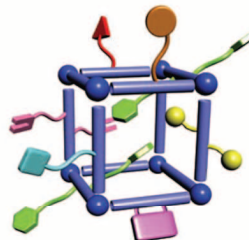
Porous organic cages (15)



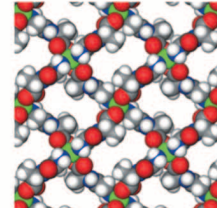
Porous aromatic frameworks (PAFs) (12)

**2010**

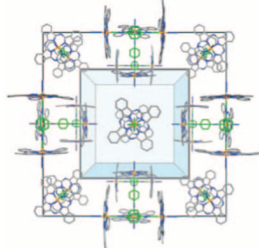
Multivariate MOFs (9)



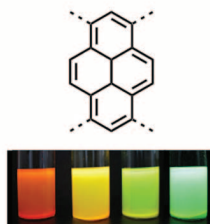
Adaptable peptide-based framework (35)

**2010**

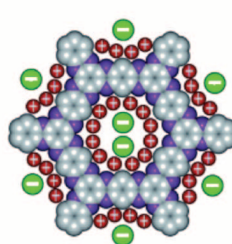
Heme-like porous molecular crystals (53)

**2011**

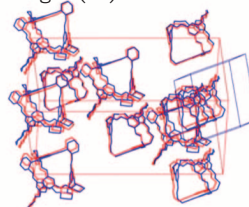
Band-gap engineering, CMPs (24, 25)



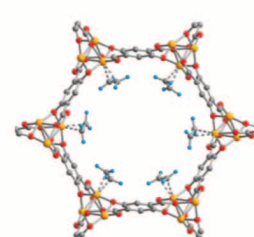
CMP supercapacitor (114)



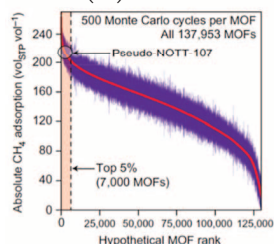
Crystal structure prediction, porous cages (18)

**2012**

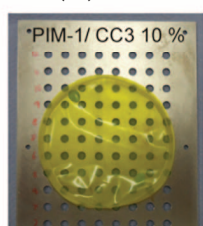
Alkane/alkene separation by a MOF (55)

**2012**

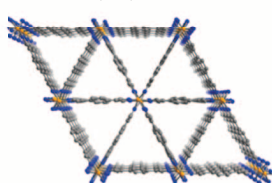
Computational screening of MOFs (31)



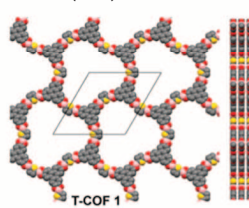
Organic-organic MMMs (16)

**2013**

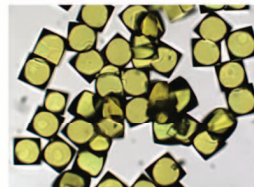
Hexane isomer separation by a MOF (60)



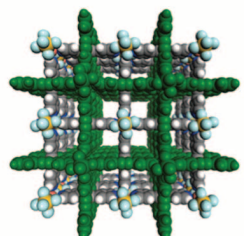
Electroactive thiophene COF (107)



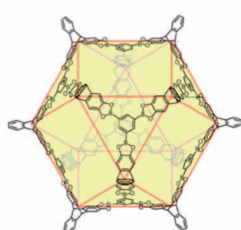
Single-crystalline COFs (19, 20)

**2013**

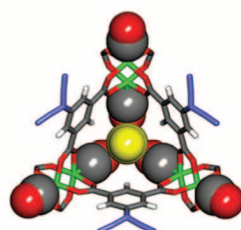
MOFs with extreme CO<sub>2</sub> selectivity (62)



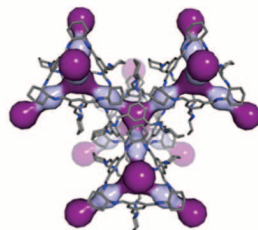
Mesoporous organic cage (50)

**2014**

Self-accelerating CO sorption (59)



Rare gas separation using porous cages (34)

**2015**

Cooperative CO<sub>2</sub> capture in a MOF (61)

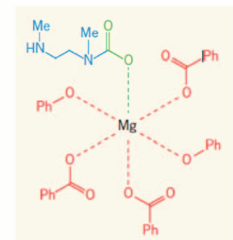


**Fig. 3. Selected advances in functional porous solids.** Both experimental and computational methods have progressed rapidly in the past decade to yield a range of materials with new or improved functions. Numbers in parentheses denote relevant references.



in industry, currently performed using zeolites. Here there is no metal coordination strategy because these hydrocarbons are saturated. An iron MOF,  $\text{Fe}_2(\text{BDP})_3$  (BDP: 1,4-benzenedipyrazolate), was shown to discriminate between linear and branched hexane isomers at industrially relevant temperatures (60). It was hypothesized that linear *n*-hexane has stronger van der Waals interactions with the triangular channel walls in the MOF.

Selectivity is a defining function in adsorbents for postcombustion carbon capture (7) where it is necessary to adsorb  $\text{CO}_2$  in preference to other gases, such as nitrogen. Selective  $\text{CO}_2$  adsorption has been demonstrated in MOFs where the  $\text{CO}_2$  inserts into the metal-ligand bonds, which suggests that the function of  $\text{CO}_2$ -fixation enzymes might give clues to designing better synthetic  $\text{CO}_2$  adsorbents in the future (61). In this system, crystallinity is probably essential for the resulting function: The energy-efficient adsorption and desorption of  $\text{CO}_2$  over a very narrow pressure range occurs because of cooperative effects between neighboring functional groups in the crystalline lattice. Amorphous porous polymers, for example, might not give similar cooperative behavior, even if suitably metallated (56, 57). Excellent selectivity and  $\text{CO}_2$  capacity have also been demonstrated for water-tolerant metal-organic materials based on the hexafluorosilicate anion (62). Hydrophobicity is a useful qualitative design principle for  $\text{CO}_2/\text{H}_2\text{O}$  selectivity. Recent studies on hydrophobic hyper-cross-linked polymers show that these materials swell in  $\text{CO}_2$  at pressures relevant

to precombustion  $\text{CO}_2$  capture and that they adsorb very little water, outperforming materials such as MOFs, zinc imidazolate frameworks (ZIFs), zeolites, and activated carbons under these conditions in terms of both  $\text{CO}_2$  capacity and  $\text{CO}_2/\text{H}_2\text{O}$  selectivity (63). The rational, atomistic design of more selective materials here is doubly complex, both because the materials are amorphous and because swelling is not easily captured in molecular simulations. Sorbent swelling could present an engineering problem in packed adsorbent beds, especially in postcombustion carbon capture where close-to-zero pressure drops are required. Fascinatingly, it seems that framework flexibility can be strongly influenced by crystal size (64), thus suggesting the scope to modulate such effects.

For polymer membranes, selectivity is a complex function of both solubility and diffusion terms. Design of function in amorphous polymer materials has so far been largely empirical, but this has yielded many successes. In particular, PIMs with extreme rigidity, which are nonetheless solution-processable, can combine excellent gas selectivity and gas permeability (21). The one-step synthesis of these rigid polymers is simple and elegant (Fig. 4A).

### Kinetics

Applications such as molecular separations, heterogeneous catalysis, and proton conductivity using porous materials are all critically dependent on diffusion kinetics (65). The actual regime

of diffusion limitation is specific to a given application. For instance, the principal diffusion resistance may not be in the nanopore size range and may actually be in the mesopore or macropore region, and then the engineered form and shape of the sorbent material may become more important. For membranes, there is a compromise between selectivity and permeability (66), and there is a major drive to discover new materials that maximize both of these parameters (21, 54). Physical aging of membranes is a problem that needs to be addressed, because initial permeabilities in PIMs can decrease drastically over quite short periods of time (67). The use of mixed-matrix membranes is one possible solution (16, 68), where a second, rigid filler material is blended with the polymer to stabilize the porosity over time, although this also introduces various processing challenges.

In  $\text{CO}_2$  capture from flue gas, the amount of  $\text{CO}_2$  that can be captured at a given gas flow rate is determined by the adsorption kinetics. Materials with high equilibrium  $\text{CO}_2$  uptakes but slow kinetics may not be useful because these equilibrium values might not be achieved in a dynamic flow situation. Hence, for gas separations, the working capacity defines the quantity of gas that can be adsorbed and desorbed by the sorbent within a given pressure- or temperature-swing time cycle (7). A general challenge is that adsorbents with excellent selectivity might often have poor kinetics and hence poor working capacities because the pore channels are, by definition, close in size to the dimensions of the guests (11). One promising strategy is the hierarchical structuring of materials to contain interconnected large and small pores, again highlighting the importance of processability.

### Processability

It is uncommon for porous materials to be usable in applications as synthesized; they are typically processed into a specific form, such as a pellet, a thin polymer membrane (54), or a surface-deposited MOF or zeolite film (69–73). Processability is therefore an important functional property that is often ignored, at least in the early discovery phase for new materials.

Mixed-matrix membranes (MMMs) are promising composite materials for gas separations (68), but processing challenges arise where the constituent materials in the MMM are incompatible. This can lead to nonselective channels at the phase interfaces between the organic polymer and the filler, which is typically an inorganic material such as silica or zeolite. An important development here is the use of porous organic fillers, such as organic cage molecules (16) or porous polymers (74), which in principle can form a more stable interface with the surrounding organic polymer phase. A key advantage of the organic cage MMM approach is that both the cage and the membrane polymer are soluble in common organic solvents, thus avoiding potential processing issues associated with colloidal particulate fillers. Insoluble materials (Fig. 2) can nonetheless be processed, as illustrated by the development of

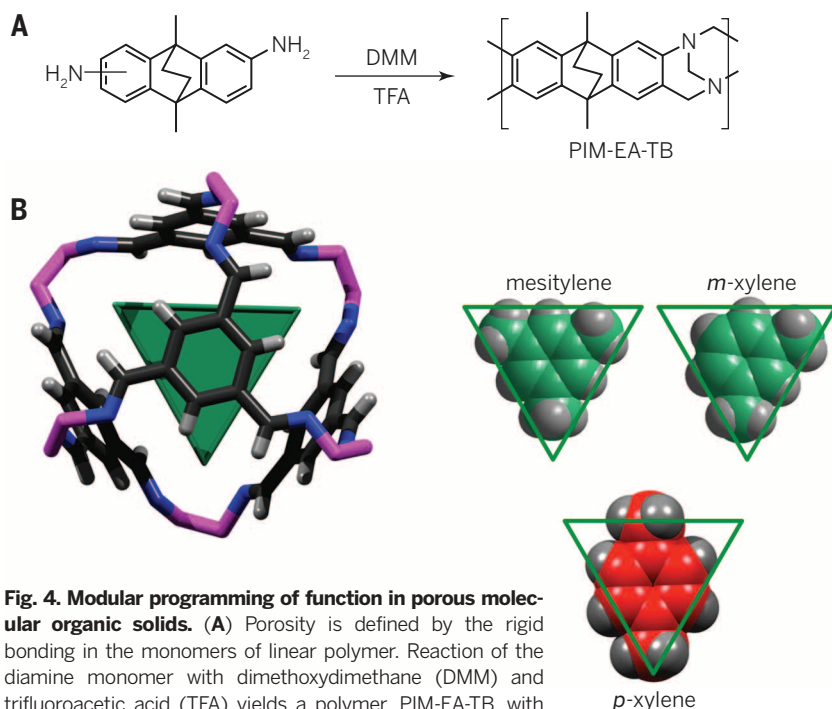


**Fig. 4. Modular programming of function in porous molecular organic solids.** (A) Porosity is defined by the rigid bonding in the monomers of linear polymer. Reaction of the diamine monomer with dimethoxydimethane (DMM) and trifluoroacetic acid (TFA) yields a polymer, PIM-EA-TB, with extreme rigidity that combines excellent gas selectivity and gas permeability. (B) Molecular selectivity for hydrocarbons is defined by an isolated organic cage molecule. The triangular cavity in the cage (highlighted in green) is a good shape match for mesitylene, which can be entrapped by the cage, and also for *m*-xylene, but not for *p*-xylene. PIM-EA-TB is amorphous while the cage molecule is crystalline, but the organic building blocks encode solid-state function in both cases.

large-scale pervaporation modules based on zeolite membranes grown on tubular supports (73).

Processability can also have a strong influence on cost, including that of the constituent feedstocks for the material and of any steps needed to render the material into a usable form. Simple, scalable processing routes with few steps are therefore desirable, irrespective of material type.

### Mechanical properties

The success of porous materials in industrial processes depends on their stability to stresses such as tension, compression, shear, bending, torsion, and impact (75). There are comparatively few studies on this important subject. Nano-indentation studies on MOF-5 concluded that inert atmospheres and low applied stresses would be needed to maintain structural integrity (76). The mechanical properties of “soft porous crystals,” a subclass of MOFs (77), were found to be low, particularly with respect to shear stresses and fracture propagation, although their synthetic variability allows scope to design new materials with improved strength. To maximize the strength of MOFs, it was suggested that framework connectivity should be as high as possible, as in the case of UiO-66 with 12-coordinate Zr, while the organic linkers should be short in length. Porous amorphous organic polymers show a similar trend of decreasing mechanical stability with increasing linker length (78); boron-based COFs were calculated to have similar mechanical properties to porous aromatic frameworks (79). There are hence some general design rules that transcend material subclass, and calculations here can show good agreement with experiment (36).

### Stability

Stability can mean many things in addition to mechanical stability, and it is an important, general challenge for porous materials in the future. Most applications for porous solids will require stability in air as a minimum. Other applications, such as post-combustion CO<sub>2</sub> capture, also require stability under humid, acidic conditions (63). For photocatalysts, long-term stability under intense irradiation is a requirement (25). In terms of thermal stability, high-temperature heterogeneous catalysis is likely to remain the preserve of inorganic materials, because the operating temperatures effectively rule out most of the newer porous organic and metal-organic materials. For lower-temperature processes, there is a growing body of work that shows that new materials might have adequate thermal stability.

The first generation of porous MOFs and boronate ester COFs had reasonable thermal stability, but they were rather unstable to moisture. The hydrolytic stability of MOFs has since been greatly improved using design strategies such as hydrophobic organic linkers (80) or postsynthetic modification with diazo groups (81). UiO-66 and its derivatives were shown to retain their structural stability after immersion in water and 0.1 M HCl solutions; HKUST-1 (Cu-BTC) is water-stable under certain conditions but degrades at higher relative humidities and/or temperatures

[90% relative humidity (RH) at 298 K] (82). MOFs have also been studied for their water adsorption and dehumidification properties (83, 84). To be useful in practical applications such as CO<sub>2</sub> capture, porous materials must be stable to the components in flue gas, not least to CO<sub>2</sub> itself and acidic components such as SO<sub>2</sub>, which is difficult to scrub. Recent studies cast doubt on the long-term stability of some ZIFs under humid conditions: A carbonate decomposition product was observed upon exposure of ZIF-8, *dia*-Zn(MeIm)<sub>2</sub> (MeIm: methylimidazole), or ZIF-67 to either gaseous CO<sub>2</sub> in 100% RH or CO<sub>2</sub> dissolved in water (85). Porous organic polymers can have excellent hydrolytic stability as well as stability toward acids and bases, although long-term oxidative stability is less well studied. Crystalline or semicrystalline COFs that are formed from less labile covalent linkages (86, 87) should have good chemical stability. Surprisingly, porous molecular crystals can also show high stability to water (88), or even to acids and bases (pH = 2 to 12), so long as reversible imine linkages are not present (89).

### Thermal properties

Heat management is a fundamental issue both in adsorption processes, such as gas storage or separation, and in heterogeneous catalysis. There are two related parameters to consider: (i) how much heat is released upon adsorption or by a catalytic reaction, and (ii) how readily that heat is dissipated in the material. Poor heat dissipation would be a problem for large adsorbent or catalyst beds. The degree of heat released is a function of the pore size and pore chemistry, and for catalysts it is also a function of the nature of the chemical reaction. Heat dissipation is a function of the thermal conductivity of the material, its specific heat capacity, and its physical form. A high specific heat capacity is not necessarily advantageous; for example, in temperature-swing adsorption and desorption, this may increase the amount of thermal energy that is required to regenerate the adsorbent. By contrast, good thermal conductivity is generally an advantage because it allows heat to be removed from or added to the porous material.

MOF-5 has poor thermal conductivity: 0.31 W m<sup>-1</sup> K<sup>-1</sup>, which is similar to concrete (90) and around an order of magnitude lower than other porous solids such as the zeolites sodalite and faujasite. ZIF-8 was predicted to have an even lower thermal conductivity of 0.165 to 0.190 W m<sup>-1</sup> K<sup>-1</sup> (91). These low values are not surprising given the low atomic number density for the materials, and comparable values might be expected for many of the material types summarized in Fig. 1. Recent computational studies suggest that there is some scope for designing higher thermal conductivities in MOFs, and by implication other porous solids, by considering the framework topology (92).

### Catalytic activity

Porous frameworks offer many advantages over both homogeneous and nonporous heterogeneous catalysts, for example, in terms of ease of recovery and shape and size selectivity. Zeolites

have by far the most widespread use in industrial catalysis, especially in the area of size-selective heterogeneous catalysis (93). Catalytic activity has also been demonstrated in a wide range of MOFs (94–96), COFs (97) and porous polymers (98), in principle addressing problems that zeolites cannot tackle. For example, one recent strategy is “defect engineering” to yield MOFs with coordinatively unsaturated metal centers, allowing unusual reactivity (99). In addition to more traditional thermal catalysis, heterogeneous photocatalysts are of interest in applications such as wastewater treatment, hydrogen production, artificial photosynthesis, and degradation of pollutants (100). In this regard, the growing number of metal-free porous polymer organocatalysts is of interest (98, 101, 102). In particular, carbon nitride (103) and carbon nitride composite materials (104) show promise as metal-free catalysts for the photochemical splitting of water, although those materials are not inherently porous. Extended conjugation is not a typical property of zeolites or MOFs, but this can be achieved in conjugated microporous polymers (22) and in some COFs (105–107). The modular design of improved porous organic photocatalysts—for example, by using “band gap engineering” strategies (24) to allow more effective adsorption of the available solar spectrum—is a design strategy for the future, as exemplified recently for porous polypyrene materials for photochemical hydrogen evolution (25). The introduction of high levels of porosity should allow faster and more efficient mass transport of water to the photogenerated charges in the catalyst.

### Other specific functions

Porous frameworks (108–110), porous molecular solids (111), and zeolites (112) all show promise as proton conductors. Porous COFs (105–107) and MOFs (113) have potential in organic electronics, and porous conjugated microporous polymers are promising supercapacitors (114). Solution-processable porous organic solids have been incorporated into sensors (115). The degree to which function can be designed into these various applications depends upon the property of interest. For example, the design of new proton conductors and supercapacitors is, at this stage, somewhat more empirical, not least because there is no single mechanism for proton transport or for charge storage.

### De novo computational design

Although we are still some way from the routine de novo design of even individual functions for porous solids, there have been major recent advances in this direction. Large-scale computational screening was applied to MOFs, where 102 building blocks were used to generate 137,953 hypothetical frameworks (31). This initial example was limited to rigid frameworks, and candidate structures were restricted to no more than four unique building blocks per MOF. Monte Carlo simulations suggested a large number of hypothetical materials with methane adsorption capacities that were greater than the record material at the time (230 vol<sub>STP</sub> vol<sup>-1</sup>), and one of



these predicted materials was found to be related to an experimental MOF that did indeed have excellent methane capacity that was close to the predicted value. In a more recent study, the same team explored the limits of practical methane storage in MOFs, and in particular the feasibility of reaching the Advanced Research Projects Agency–Energy target methane delivery capacity of  $315 \text{ cm}^3(\text{STP})/\text{cm}^3$  (39). A computational survey of 122,835 hypothetical frameworks considered how properties such as void fraction, volumetric surface area, and heat of adsorption affect the deliverable methane capacity (Fig. 5A). The results indicated that the best delivery capacity for any of the hypothetical frameworks was substantially lower than the  $315 \text{ cm}^3(\text{STP})/\text{cm}^3$  target (Fig. 5B). Only an artificial factor of 4 increase in the Lennard-Jones  $\epsilon$  parameters in the simulations, combined with an increase in the delivery temperature to 398 K, allowed this target to be attained (Fig. 5C). This illustrates the difficulty in designing adsorption sites in frameworks that interact strongly enough with methane, and it is an excellent example of the use of computation to guide rather than simply rationalize the design of porous solids. Recently, a “computation ready” (116) database of MOF structures has been made publicly available, thus allowing a broader computational community to participate in such property predictions for large libraries of materials (116, 117). Computational screening has also been applied to identify zeolites for ethanol/water separations (118) and for natural gas purification (119); in the latter case, a hierarchical approach was applied that included process cost analysis as the final ranking step.

These high-throughput property predictions for libraries of hypothetical frameworks are a potentially enabling development for experimentalists, but there are also limitations. The frameworks were treated as rigid to reduce computational cost, although computational methods do exist that can

treat framework flexibility for smaller numbers of frameworks (35, 120, 121). These high-throughput methods also do not provide a synthesis protocol for the computer-generated MOFs, nor do they ensure their thermodynamic stability. Indeed, such methods will tend to generate a large number of structures that are insufficiently thermodynamically stable to be accessed by experiment. Calculations have been used to assess the relative stabilities of different framework topologies, both for crystalline MOFs (122, 123) and for amorphous porous polymers (46), but these methods are not yet computationally affordable or sufficiently generalized to be used for the routine selection of promising synthetic targets, even when composition is fixed or constrained. The unconstrained prediction of the most thermodynamically stable compositions from a range of possible hypothetical phases is extremely challenging.

Is it possible, then, to predict structure, thermodynamic stability, and functional properties for porous materials from their constituent molecular building blocks without any input from experiment? There are no single studies that demonstrate such a *de novo* computational approach in its entirety, but there is potential to do this in the future—for example, by introducing energy ranking steps into the aforementioned large-scale computational screening of hypothetical MOFs. The strategy can also be illustrated for molecular organic crystals. The most stable organic cage compound for a given combination of organic linkers can be computed (Fig. 6, step 1) (124), along with the potential of the isolated cage to be shape-persistent and porous (52). Using the most stable computed cage structure, the lowest-energy crystal packing can then be computed using crystal structure prediction (step 2) (18). This computed crystal structure then feeds molecular dynamics simulations to probe gas diffusion and the dynamic pore size envelope (step 3) (125) and Monte Carlo simulations to evaluate gas sorption prop-

erties and gas selectivities (step 4) (34), much as for large-scale computational MOF screening. Hence we could compute, without any physical experiments, that reaction of 1,3,5-triformylbenzene and (*R,R*)-cyclohexanediamine should form a flexible, porous molecular solid with a remarkably high selectivity for xenon adsorption, as found by experiment (34).

We stress that this is a retrospective example; in reality, steps 1 to 4 were carried out in a series of studies over the course of about 5 years (18, 34, 52, 124), with experimental validations interspersed between the steps. However, with suitable advances in methodology and hardware, virtual screening methods could become a competitive reality. The largest single challenge here is perhaps the structure prediction and lattice energy calculation (step 2), which are not yet generic, especially if less rigid building blocks or the *de novo* prediction of the most likely compositions for multicomponent solids are considered.

The cages illustrated in Fig. 5 are quite large, prefabricated modules. By contrast, most MOFs, COFs, and polymers are prepared from smaller building blocks, which increases computational expense for unconstrained structure-composition searches. It is possible that a strategy of “extended modules,” as used to predict function for inorganic oxides (126), might also be adapted to porous framework solids so that the structure and function of complex materials could be predicted in a more granular way.

## Outlook

The field of porous materials is at an exciting stage in its evolution. Compared to 20 years ago, there are many more types of functional porous solids to choose from, and zeolites, while mature and commercially established, are still developing rapidly. For example, two-dimensional zeolites (72) open up new possibilities for what were hitherto thought of as three-dimensional materials.

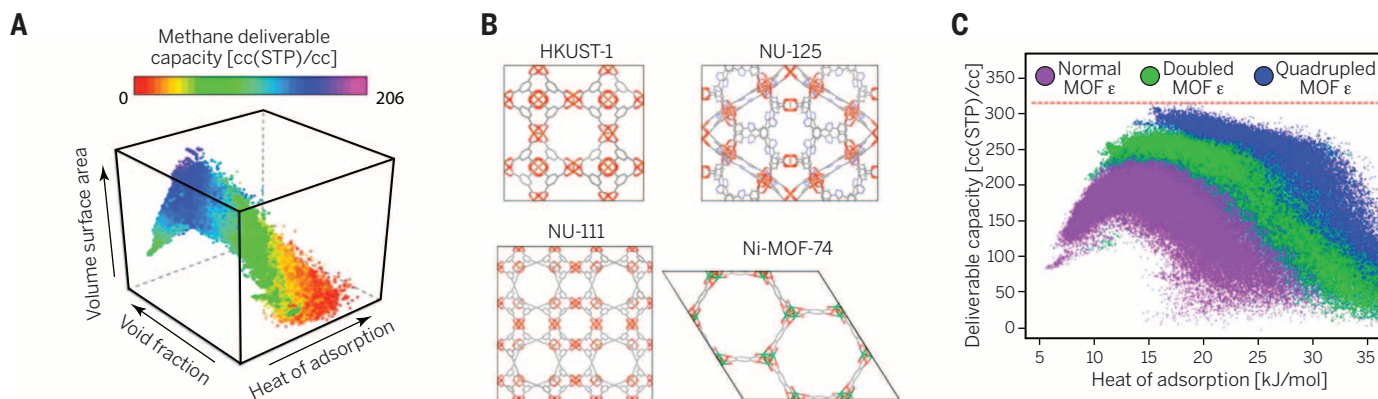


**Fig. 5. Exploring the limits of methane storage and delivery using high-throughput computation.** (A) Molecular simulations for 122,835 hypothetical MOFs and 39 idealized carbon-based porous materials yield a map of methane deliverable capacity for the materials, as relevant to natural gas storage applications. The relative thermodynamic stabilities of the various hypothetical frameworks were not considered. (B) Structures of HKUST-1, NU-125, and NU-111, the three best MOFs in terms of deliverable capacity between 65 and 5 bar, and Ni-MOF-74, the best MOF for methane storage at 35 bar. (C) Methane delivery

capacity (between 65 bar/298 K and 5.8 bar/398 K) for 48,000 hypothetical MOFs where the Lennard-Jones interaction parameter, which describes the interaction between methane and the MOF, is normal (purple), artificially doubled (green), and quadrupled (blue). A quadrupling of this parameter is needed to approach the ARPA-E target of  $315 \text{ cm}^3(\text{STP})/\text{cm}^3$  deliverable methane capacity, illustrating that even a wide range of hypothetical MOF structures do not interact strongly enough with methane to be practical, even though there is, in principle, sufficient surface area available in some of these materials.

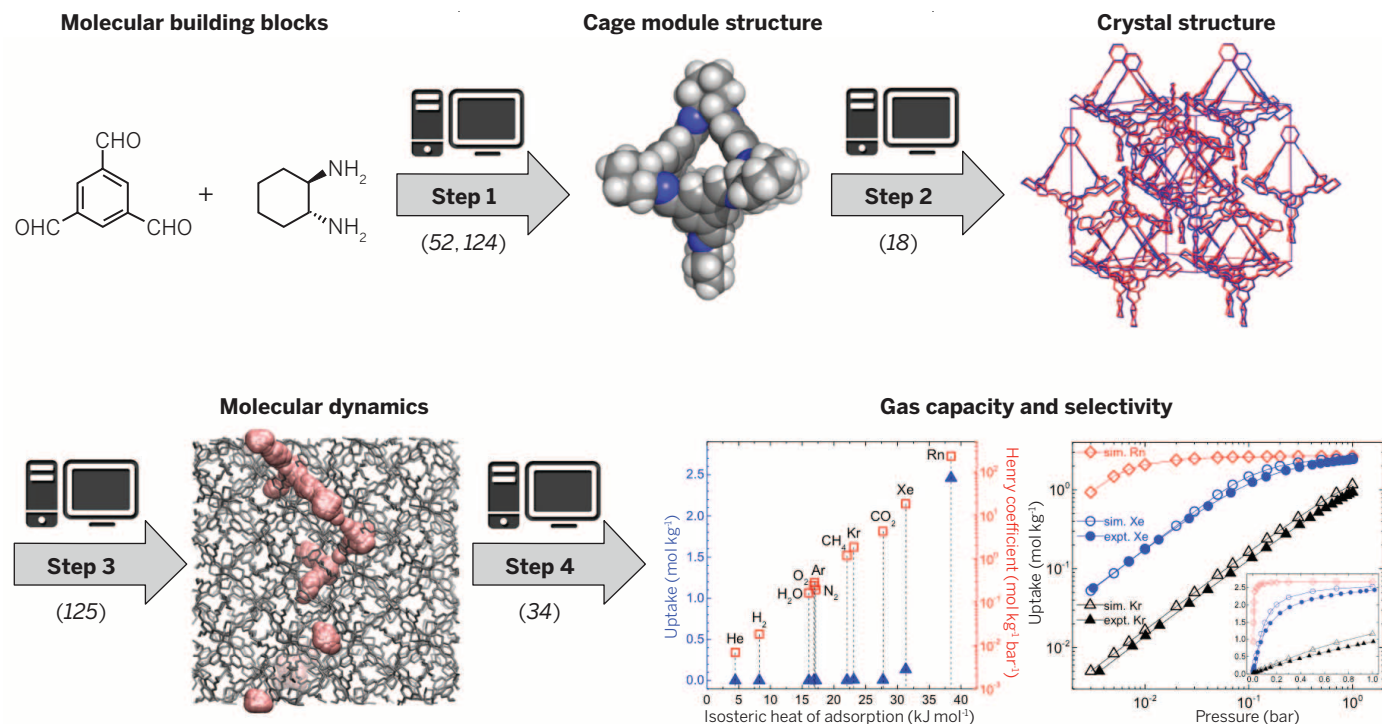


**Fig. 6. In silico prediction of function from molecular building blocks.** As computational methods evolve, it will become increasingly possible to predict structure and function for porous materials from knowledge of the primary building blocks alone. In this example, the most stable organic cage structure can be predicted from the aldehyde and amine building blocks (step 1) and the crystal structure can then be predicted from the structure of the cage

module (step 2). Molecular dynamics simulations (step 3) give information about gas diffusion rates, and grand canonical Monte Carlo simulations (step 4) predict both gas capacity and gas selectivity. This workflow could be applied in the future to hypothetical molecules, which would then allow the true in silico design of function for porous solids. Numbers in parentheses denote references relevant to the individual steps.

This new diversity can, however, make it hard to select the best material for a specific purpose. The qualitative criteria presented in Figs. 1 and 2 offer some guidance, but we suggest that the long-term solution is to develop computational structure/property prediction tools to augment experiment, ultimately to allow the de novo design of new porous solids. This would have strong translational benefit because the same prediction challenges exist for a wide range of nonporous solid-state materials; steps 1 to 3 in Fig. 6, for example, could be applied to any crystalline organic solid, whether porous or not.

Pending development and generalization of these predictive tools, materials design will proceed mainly via more qualitative, empirical rules, iterated with synthesis and property measurements. In this respect, some general opportunities and challenges can be identified. Carbon dioxide capture is an important unsolved problem where porous materials could be the solution, but the barriers to commercialization are daunting, not least because of the enormous scale: A single power plant can produce more than 20 billion kg of CO<sub>2</sub> annually. Candidate materials must therefore have low cost and long service lifetimes (i.e., good stability). Although substantial progress has been made on selectivity, both for adsorbents (61–63) and for membranes (21), scale-up potential will equally depend on kinetics. For membranes, selectivity and permeability are usually studied together, but for adsorbents, kinetics are

less commonly investigated, and this is an area that requires more attention. In order for PIM membranes (14, 21) to displace commercial high-free volume polymers in large scale separations, or to establish entirely new separation processes, it will be important to solve the physical aging problems associated with these materials (67). Improved water purification and water recovery (83, 84) technologies are also of growing importance worldwide. In principle, many of the material classes outlined in Fig. 1 could translate into water purification technologies, and this will likely be a future growth area, although again the scale of these processes necessitates improved performance, low cost, and high durability to compete, for example, with commercial desalination membranes. Heterogeneous catalysis is a mature field, and new porous solids must show specific advantages over established catalysts and catalyst supports such as zeolites, alumina, silica, or simple polymer resin technologies. So far, many heterogeneous MOF catalysts are simply variants of these more classical materials. However, a range of new opportunities exists; for example, the rise of asymmetric molecular organocatalysis (127) predates the rapid expansion in porous organic polymers (6, 22, 27) by just a few years. It is likely, therefore, that a range of metal-free porous heterogeneous polymer organocatalysts will soon follow (98, 101, 102), especially given the enormous synthetic versatility in porous polymers, which is perhaps their key advantage (Fig. 1). More spe-

cifically, CMP photocatalysts (25) have extended, conjugated chromophores that are not present in more traditional heterogeneous catalysts. The recent discovery of an organic, metal-free photocatalyst that performs photochemical water splitting for 200 days without a reduction in activity (104) suggests that for at least some organic materials, long-term photostability can be achieved that matches or exceeds that of traditional inorganic semiconductors. More active polymer photocatalysts for water splitting could in turn stimulate the search for improved porous separation media for the hydrogen and oxygen gas streams that would be produced. Alternatively, it might be possible to design a porous membrane material that not only produces hydrogen and oxygen gas but also separates them—for example, by tailoring the pore size.

Separation, adsorption, and heterogeneous catalysis are what might be called “traditional” areas for porous materials. There are also recent studies that demonstrate new possibilities for porous solids (105–115) where the advantages over materials such as zeolites are perhaps more clear-cut. For example, in battery and supercapacitor technologies, new porous solids (114) will be competing instead with materials such as graphite and graphene. New porous electronic materials have developed rapidly in recent years, where crystalline porosity in COFs, for example, has been used to position functional units with respect to one another in space (105–107) more



than to achieve porosity per se. Dopable, solution-processable porous molecular solids (15), perhaps designed using crystal structure prediction methods (18), would be a logical future development here.

## REFERENCES AND NOTES

- P. A. Wright, *Microporous Framework Solids* (Royal Society of Chemistry, Cambridge, 2008).
- M. Kondo, T. Yoshitomi, H. Matsuzaka, S. Kitagawa, K. Seki, Three-dimensional framework with channeling cavities for small molecules:  $[M-2(4,4'-bpy)_3(NO_3)_4] \cdot xH_2O_n$  ( $M = Co, Ni, Zn$ ). *Angew. Chem. Int. Ed. Engl.* **36**, 1725–1727 (1997). doi: [10.1002/anie.199717251](#)
- A. K. Cheetham, G. Férey, T. Loiseau, Open-framework inorganic materials. *Angew. Chem. Int. Ed.* **38**, 3268–3292 (1999). doi: [10.1002/\(SICI\)1521-3773\(199911\)38:22<3268::AID-ANIE3268>3.0.CO;2-U](#); pmid: 10602176
- H. Furukawa, K. E. Cordova, M. O'Keeffe, O. M. Yaghi, The chemistry and applications of metal-organic frameworks. *Science* **341**, 1230444 (2013). pmid: 23990564
- A. P. Côté et al., Porous, crystalline, covalent organic frameworks. *Science* **310**, 1166–1170 (2005). doi: [10.1126/science.1120411](#); pmid: 16293756
- A. Thomas, Functional materials: From hard to soft porous frameworks. *Angew. Chem. Int. Ed.* **49**, 8328–8344 (2010). doi: [10.1002/anie.201000167](#); pmid: 20949565
- K. Sumida et al., Carbon dioxide capture in metal-organic frameworks. *Chem. Rev.* **112**, 724–781 (2012). doi: [10.1021/cr2003272](#); pmid: 22204561
- O. M. Yaghi et al., Reticular synthesis and the design of new materials. *Nature* **423**, 705–714 (2003). doi: [10.1038/nature01650](#); pmid: 12802375
- H. Deng et al., Multiple functional groups of varying ratios in metal-organic frameworks. *Science* **327**, 846–850 (2010). doi: [10.1126/science.1181761](#); pmid: 20150497
- X. Kong et al., Mapping of functional groups in metal-organic frameworks. *Science* **341**, 882–885 (2013). doi: [10.1126/science.1238339](#); pmid: 23887875
- T. Mitra et al., Molecular shape sorting using molecular organic cages. *Nat. Chem.* **5**, 276–281 (2013). doi: [10.1038/nchem.1550](#); pmid: 23511415
- T. Ben et al., Targeted synthesis of a porous aromatic framework with high stability and exceptionally high surface area. *Angew. Chem. Int. Ed.* **48**, 9457–9460 (2009). doi: [10.1002/anie.200904637](#); pmid: 19921728
- D. R. Rolison, Catalytic nanoarchitectures—the importance of nothing and the unimportance of periodicity. *Science* **299**, 1698–1701 (2003). doi: [10.1126/science.1082332](#); pmid: 12637736
- P. M. Budd et al., Polymers of intrinsic microporosity (PIMs): Robust, solution-processable, organic nanoporous materials. *Chem. Commun.* **2004**, 230–231 (2004). doi: [10.1039/b311764b](#); pmid: 14737563
- T. Tozawa et al., Porous organic cages. *Nat. Mater.* **8**, 973–978 (2009). doi: [10.1038/nmat2545](#); pmid: 19855385
- A. F. Bushell et al., Nanoporous organic polymer/cage composite membranes. *Angew. Chem. Int. Ed.* **52**, 1253–1256 (2013). doi: [10.1002/anie.201206339](#); pmid: 23225333
- D. Uemeyama, S. Horike, M. Inukai, T. Itakura, S. Kitagawa, Reversible solid-to-liquid phase transition of coordination polymer crystals. *J. Am. Chem. Soc.* **137**, 864–870 (2015). doi: [10.1021/ja511019u](#); pmid: 25530162
- J. T. A. Jones et al., Modular and predictable assembly of porous organic molecular crystals. *Nature* **474**, 367–371 (2011). doi: [10.1038/nature10125](#); pmid: 21677756
- D. Beaudoin, T. Maris, J. D. Wuest, Constructing monocryalline covalent organic networks by polymerization. *Nat. Chem.* **5**, 830–834 (2013). doi: [10.1038/nchem.1730](#); pmid: 24056338
- Y. B. Zhang et al., Single-crystal structure of a covalent organic framework. *J. Am. Chem. Soc.* **135**, 16336–16339 (2013). doi: [10.1021/ja409033p](#); pmid: 24143961
- M. Carta et al., An efficient polymer molecular sieve for membrane gas separations. *Science* **339**, 303–307 (2013). doi: [10.1126/science.1228032](#); pmid: 23329042
- J.-X. Jiang et al., Conjugated microporous poly (aryleneethynylene) networks. *Angew. Chem. Int. Ed.* **46**, 8574–8578 (2007). doi: [10.1002/anie.200701595](#); pmid: 17899616
- J.-X. Jiang et al., Synthetic control of the pore dimension and surface area in conjugated microporous polymer and copolymer networks. *J. Am. Chem. Soc.* **130**, 7710–7720 (2008). doi: [10.1021/ja8010176](#); pmid: 18500800
- J. X. Jiang, A. Trewin, D. J. Adams, A. I. Cooper, Band gap engineering in fluorescent conjugated microporous polymers. *Chem. Sci.* **2**, 1777 (2011). doi: [10.1039/c1sc00329a](#)
- R. S. Sprick et al., Tunable organic photocatalysts for visible-light-driven hydrogen evolution. *J. Am. Chem. Soc.* **137**, 3265–3270 (2015). doi: [10.1021/ja511552k](#); pmid: 25643993
- M. A. Wijnenburg et al., Shedding light on structure-property relationships for conjugated microporous polymers: The importance of rings and strain. *Macromolecules* **46**, 7696–7704 (2013). doi: [10.1021/ma401311s](#); pmid: 24159243
- R. Dawson, A. I. Cooper, D. J. Adams, Nanoporous organic polymer networks. *Prog. Polym. Sci.* **37**, 530–563 (2012). doi: [10.1016/j.progpolymsci.2011.09.002](#)
- L. J. Abbott, C. M. Colina, Atomistic structure generation and gas adsorption simulations of microporous polymer networks. *Macromolecules* **44**, 4511–4519 (2011). doi: [10.1021/ma200303p](#)
- S. Jiang et al., Molecular dynamics simulations of gas selectivity in amorphous porous molecular solids. *J. Am. Chem. Soc.* **135**, 17818–17830 (2013). doi: [10.1021/ja407374k](#); pmid: 24156758
- T. Watanabe, D. S. Sholl, Accelerating applications of metal-organic frameworks for gas adsorption and separation by computational screening of materials. *Langmuir* **28**, 14114–14128 (2012). doi: [10.1021/la301915s](#); pmid: 22783907
- C. E. Wilmer et al., Large-scale screening of hypothetical metal-organic frameworks. *Nat. Chem.* **4**, 83–89 (2012). doi: [10.1038/nchem.1192](#); pmid: 22270624
- T. Dören, Y. S. Bae, R. Q. Snurr, Using molecular simulation to characterise metal-organic frameworks for adsorption applications. *Chem. Soc. Rev.* **38**, 1237–1247 (2009). doi: [10.1039/b803498m](#); pmid: 19384435
- Q. Yang, D. Liu, C. Zhong, J. R. Li, Development of computational methodologies for metal-organic frameworks and their application in gas separations. *Chem. Rev.* **113**, 8261–8323 (2013). doi: [10.1021/cr400005f](#); pmid: 23826973
- L. Chen et al., Separation of rare gases and chiral molecules by selective binding in porous organic cages. *Nat. Mater.* **13**, 954–960 (2014). doi: [10.1038/nmat4035](#); pmid: 25038731
- J. Rabone et al., An adaptable peptide-based porous material. *Science* **329**, 1053–1057 (2010). pmid: 20798314
- B. Lukose et al., Structural properties of metal-organic frameworks within the density-functional based tight-binding method. *Phys. Status Solidi B* **249**, 335–342 (2012). doi: [10.1002/pssb.201100634](#)
- R. Dawson et al., Functionalized conjugated microporous polymers. *Macromolecules* **42**, 8809–8816 (2009). doi: [10.1021/ma901801s](#)
- T. Hasell, S. Y. Chong, M. Schmidtman, D. J. Adams, A. I. Cooper, Porous organic alloys. *Angew. Chem. Int. Ed.* **51**, 7154–7157 (2012). doi: [10.1002/anie.201202849](#); pmid: 22684980
- D. A. Gómez-Gualdrón, C. E. Wilmer, O. K. Farha, J. T. Hupp, R. Q. Snurr, Exploring the limits of methane storage and delivery in nanoporous materials. *J. Phys. Chem. C* **118**, 6941–6951 (2014). doi: [10.1021/jp502359q](#)
- G. Férey et al., A chromium terephthalate-based solid with unusually large pore volumes and surface area. *Science* **309**, 2040–2042 (2005). doi: [10.1126/science.1116275](#); pmid: 16179475
- H. Furukawa et al., Ultrahigh porosity in metal-organic frameworks. *Science* **329**, 424–428 (2010). doi: [10.1126/science.1192160](#); pmid: 20595583
- O. K. Farha et al., Metal-organic framework materials with ultrahigh surface areas: Is the sky the limit? *J. Am. Chem. Soc.* **134**, 15016–15021 (2012). doi: [10.1021/ja3055639](#); pmid: 22906112
- H. Deng et al., Large-pore apertures in a series of metal-organic frameworks. *Science* **336**, 1018–1023 (2012). doi: [10.1126/science.1220131](#); pmid: 22628651
- X. Lin et al., High H<sub>2</sub> adsorption by coordination-framework materials. *Angew. Chem. Int. Ed.* **45**, 7358–7364 (2006). doi: [10.1002/anie.200601991](#); pmid: 16927440
- S. Ma et al., Metal-organic framework from an anthracene derivative containing nanoscopic cages exhibiting high methane uptake. *J. Am. Chem. Soc.* **130**, 1012–1016 (2008). doi: [10.1021/ja0771639](#); pmid: 18163628
- J. M. H. Thomas, A. Trewin, Amorphous PAF-1: Guiding the rational design of ultraporous materials. *J. Phys. Chem. C* **118**, 19712–19722 (2014). doi: [10.1021/jp502336a](#)
- W. Lu et al., Sulfonate-grafted porous polymer networks for preferential CO<sub>2</sub> adsorption at low pressure. *J. Am. Chem. Soc.* **133**, 18126–18129 (2011). doi: [10.1021/ja2087773](#); pmid: 22007926
- W. Lu et al., Polyamine-tethered porous polymer networks for carbon dioxide capture from flue gas. *Angew. Chem. Int. Ed.* **51**, 7480–7484 (2012). doi: [10.1002/anie.201201716](#); pmid: 22151527
- N. B. McKeown, Nanoporous molecular crystals. *J. Mater. Chem.* **20**, 10588 (2010). doi: [10.1039/c0jm01867h](#)
- G. Zhang, O. Presly, F. White, I. M. Oppel, M. Mastalerz, A permanent mesoporous organic cage with an exceptionally high surface area. *Angew. Chem. Int. Ed.* **53**, 1516–1520 (2014). doi: [10.1002/anie.201308924](#); pmid: 24403008
- M. Mastalerz, I. M. Oppel, Rational construction of an extrinsic porous molecular crystal with an extraordinary high specific surface area. *Angew. Chem. Int. Ed.* **51**, 5252–5255 (2012). doi: [10.1002/anie.201201174](#); pmid: 22473702
- K. E. Jelfs et al., Large self-assembled chiral organic cages: Synthesis, structure, and shape persistence. *Angew. Chem. Int. Ed.* **50**, 10653–10656 (2011). doi: [10.1002/anie.201105104](#); pmid: 21928449
- C. G. Bezzu, M. Helliwell, J. E. Warren, D. R. Allan, N. B. McKeown, Heme-like coordination chemistry within nanoporous molecular crystals. *Science* **327**, 1627–1630 (2010). doi: [10.1126/science.1184228](#); pmid: 20339069
- D. E. Sanders et al., Energy-efficient polymeric gas separation membranes for a sustainable future: A review. *Polymer* **54**, 4729–4761 (2013). doi: [10.1016/j.polymer.2013.05.075](#)
- E. D. Bloch et al., Hydrocarbon separations in a metal-organic framework with open iron(II) coordination sites. *Science* **335**, 1606–1610 (2012). doi: [10.1126/science.1217544](#); pmid: 22461607
- J.-X. Jiang et al., Metal-organic conjugated microporous polymers. *Angew. Chem. Int. Ed.* **50**, 1072–1075 (2011). doi: [10.1002/anie.201005864](#); pmid: 21268197
- B. Li et al., Introduction of  $\pi$ -complexation into porous aromatic framework for highly selective adsorption of ethylene over ethane. *J. Am. Chem. Soc.* **136**, 8654–8660 (2014). doi: [10.1021/ja502119z](#); pmid: 24901372
- S. Yang et al., Supramolecular binding and separation of hydrocarbons within a functionalized porous metal-organic framework. *Nat. Chem.* **7**, 121–129 (2014). doi: [10.1038/nchem.2114](#); pmid: 25615665
- H. Sato et al., Self-accelerating CO sorption in a soft nanoporous crystal. *Science* **343**, 167–170 (2014). doi: [10.1126/science.1246423](#); pmid: 24336572
- Z. R. Herm et al., Separation of hexane isomers in a metal-organic framework with triangular channels. *Science* **340**, 960–964 (2013). doi: [10.1126/science.1234071](#); pmid: 23704568
- T. M. McDonald et al., Cooperative insertion of CO<sub>2</sub> in diamine-appended metal-organic frameworks. *Nature* **519**, 303–308 (2015). doi: [10.1038/nature14327](#); pmid: 25762144
- P. Nugent et al., Porous materials with optimal adsorption thermodynamics and kinetics for CO<sub>2</sub> separation. *Nature* **495**, 80–84 (2013). doi: [10.1038/nature11893](#); pmid: 23446349
- R. T. Woodward et al., Swellable, water- and acid-tolerant polymer sponges for chemoselective carbon dioxide capture. *J. Am. Chem. Soc.* **136**, 9028–9035 (2014). doi: [10.1021/ja503196h](#); pmid: 24874971
- Y. Sakata et al., Shape-memory nanopores induced in coordination frameworks by crystal downsizing. *Science* **339**, 193–196 (2013). doi: [10.1126/science.1231451](#); pmid: 23307740
- J. Karger, D. M. Ruthven, D. N. Theodorou, *Diffusion in Nanoporous Materials* (Wiley, New York, 2012).
- L. M. Robeson, The upper bound revisited. *J. Membr. Sci.* **320**, 390–400 (2008). doi: [10.1016/j.memsci.2008.04.030](#)
- A. G. McDermott, P. M. Budd, N. B. McKeown, C. M. Colina, R.unt, Physical aging of polymers of intrinsic microporosity: A SAXS/WAXS study. *J. Mater. Chem. A* **2**, 11742 (2014). doi: [10.1039/C4TA02165G](#)
- M. Rezakazemi, A. E. Amooghin, M. M. Montazer-Rahmati, A. F. Ismail, T. Matsuura, State-of-the-art membrane based CO<sub>2</sub> separation using mixed matrix membranes (MMMs): An overview on current status and future directions. *Prog. Polym. Sci.* **39**, 817–861 (2014). doi: [10.1016/j.progpolymsci.2014.01.003](#)
- R. Ranjan, M. Tsapatsis, Microporous metal organic framework membrane on porous support using the seeded

- growth method. *Chem. Mater.* **21**, 4920–4924 (2009). doi: [10.1021/cm902032y](https://doi.org/10.1021/cm902032y)
70. H. Bux *et al.*, Zeolitic imidazolate framework membrane with molecular sieving properties by microwave-assisted solvothermal synthesis. *J. Am. Chem. Soc.* **131**, 16000–16001 (2009). doi: [10.1021/ja907359t](https://doi.org/10.1021/ja907359t); pmid: [19842668](https://pubmed.ncbi.nlm.nih.gov/19842668/)
  71. R. Makiura *et al.*, Surface nano-architecture of a metal-organic framework. *Nat. Mater.* **9**, 565–571 (2010). doi: [10.1038/nmat2769](https://doi.org/10.1038/nmat2769); pmid: [20512155](https://pubmed.ncbi.nlm.nih.gov/20512155/)
  72. W. J. Roth, P. Nachtigall, R. E. Morris, J. Čejka, Two-dimensional zeolites: Current status and perspectives. *Chem. Rev.* **114**, 4807–4837 (2014). doi: [10.1021/cr400600f](https://doi.org/10.1021/cr400600f); pmid: [24555638](https://pubmed.ncbi.nlm.nih.gov/24555638/)
  73. Y. Morigami, M. Kondo, J. Abe, H. Kita, K. Okamoto, The first large-scale pervaporation plant using tubular-type module with zeolite NaA membrane. *Separ. Purif. Tech.* **25**, 251–260 (2001). doi: [10.1016/S1383-5866\(01\)00109-5](https://doi.org/10.1016/S1383-5866(01)00109-5)
  74. C. H. Lau *et al.*, Ending aging in super glassy polymer membranes. *Angew. Chem. Int. Ed.* **53**, 5322–5326 (2014). doi: [10.1002/anie.201402234](https://doi.org/10.1002/anie.201402234); pmid: [24740816](https://pubmed.ncbi.nlm.nih.gov/24740816/)
  75. J. C. Tan, A. K. Cheetham, Mechanical properties of hybrid inorganic-organic framework materials: Establishing fundamental structure-property relationships. *Chem. Soc. Rev.* **40**, 1059–1080 (2011). doi: [10.1039/c0cs00163e](https://doi.org/10.1039/c0cs00163e); pmid: [21221446](https://pubmed.ncbi.nlm.nih.gov/21221446/)
  76. D. F. Bahr *et al.*, Mechanical properties of cubic zinc carboxylate IRMOF-1 metal-organic framework crystals. *Phys. Rev. B* **76**, 184106 (2007). doi: [10.1103/PhysRevB.76.184106](https://doi.org/10.1103/PhysRevB.76.184106)
  77. S. Henke, W. Li, A. K. Cheetham, Guest-dependent mechanical anisotropy in pillared-layered soft porous crystals—a nanoindentation study. *Chem. Sci.* **5**, 2392–2397 (2014). doi: [10.1039/c4sc00497c](https://doi.org/10.1039/c4sc00497c)
  78. B. Lukose, M. Wahiduzzaman, A. Kuc, T. Heine, Mechanical, electronic, and adsorption properties of porous aromatic frameworks. *J. Phys. Chem. C* **116**, 22878–22884 (2012). doi: [10.1021/jp3067102](https://doi.org/10.1021/jp3067102)
  79. S. Amirjalayer, R. Q. Snurr, R. Schmid, Prediction of structure and properties of boron-based covalent organic frameworks by a first-principles derived force field. *J. Phys. Chem. C* **116**, 4921–4929 (2012). doi: [10.1021/jp21280m](https://doi.org/10.1021/jp21280m)
  80. T. Wu *et al.*, Enhancing the stability of metal-organic frameworks in humid air by incorporating water repellent functional groups. *Chem. Commun.* **46**, 6120–6122 (2010). doi: [10.1039/c0cc01170c](https://doi.org/10.1039/c0cc01170c); pmid: [20672162](https://pubmed.ncbi.nlm.nih.gov/20672162/)
  81. J. Aguilera-Sigalat, D. Bradshaw, A colloidal water-stable MOF as a broad-range fluorescent pH sensor via post-synthetic modification. *Chem. Commun.* **50**, 4711–4713 (2014). doi: [10.1039/c4cc00659c](https://doi.org/10.1039/c4cc00659c); pmid: [24675992](https://pubmed.ncbi.nlm.nih.gov/24675992/)
  82. J. B. DeCoste *et al.*, The effect of water adsorption on the structure of the carboxylate containing metal-organic frameworks Cu-BTC, Mg-MOF-74, and UiO-66. *J. Mater. Chem. A* **1**, 11922 (2013). doi: [10.1039/c3ta12497e](https://doi.org/10.1039/c3ta12497e)
  83. Y. K. Seo *et al.*, Energy-efficient dehumidification over hierarchically porous metal-organic frameworks as advanced water adsorbents. *Adv. Mater.* **24**, 806–810 (2012). doi: [10.1002/adma.201104084](https://doi.org/10.1002/adma.201104084); pmid: [22162212](https://pubmed.ncbi.nlm.nih.gov/22162212/)
  84. H. Furukawa *et al.*, Water adsorption in porous metal-organic frameworks and related materials. *J. Am. Chem. Soc.* **136**, 4369–4381 (2014). doi: [10.1021/ja500330a](https://doi.org/10.1021/ja500330a); pmid: [24588307](https://pubmed.ncbi.nlm.nih.gov/24588307/)
  85. C. Mottlillo, T. Friščić, Carbon dioxide sensitivity of zeolitic imidazolate frameworks. *Angew. Chem. Int. Ed.* **53**, 7471–7474 (2014). doi: [10.1002/anie.201402082](https://doi.org/10.1002/anie.201402082); pmid: [24889776](https://pubmed.ncbi.nlm.nih.gov/24889776/)
  86. F. J. Uribe-Romo *et al.*, A crystalline imine-linked 3-D porous covalent organic framework. *J. Am. Chem. Soc.* **131**, 4570–4571 (2009). doi: [10.1021/ja8096256](https://doi.org/10.1021/ja8096256); pmid: [19281246](https://pubmed.ncbi.nlm.nih.gov/19281246/)
  87. P. Kuhn, M. Antonietti, A. Thomas, Porous, covalent triazine-based frameworks prepared by ionothermal synthesis. *Angew. Chem. Int. Ed.* **47**, 3450–3453 (2008). doi: [10.1002/anie.200705710](https://doi.org/10.1002/anie.200705710); pmid: [18330878](https://pubmed.ncbi.nlm.nih.gov/18330878/)
  88. T. Hasell, M. Schmidtman, C. A. Stone, M. W. Smith, A. I. Cooper, Reversible water uptake by a stable imine-based porous organic cage. *Chem. Commun.* **48**, 4689–4691 (2012). doi: [10.1039/c2cc31212c](https://doi.org/10.1039/c2cc31212c); pmid: [22476323](https://pubmed.ncbi.nlm.nih.gov/22476323/)
  89. M. Liu *et al.*, Acid- and base-stable porous organic cages: Shape persistence and pH stability via post-synthetic “tying” of a flexible amine cage. *J. Am. Chem. Soc.* **136**, 7583–7586 (2014). doi: [10.1021/ja503223j](https://doi.org/10.1021/ja503223j); pmid: [24785267](https://pubmed.ncbi.nlm.nih.gov/24785267/)
  90. B. L. Huang *et al.*, Thermal conductivity of a metal-organic framework (MOF-5): Part II. Measurement. *Int. J. Heat Mass Transfer* **50**, 405–411 (2007). doi: [10.1016/j.jheatmasstransfer.2006.10.001](https://doi.org/10.1016/j.jheatmasstransfer.2006.10.001)
  91. X. L. Zhang, J. W. Jiang, Thermal conductivity of zeolitic imidazolate framework-8: A molecular simulation study. *J. Phys. Chem. C* **117**, 18441–18447 (2013). doi: [10.1021/jp405156y](https://doi.org/10.1021/jp405156y)
  92. L. P. Han, M. Budge, P. A. Greaney, Relationship between thermal conductivity and framework architecture in MOF-5. *Comput. Mater. Sci.* **94**, 292–297 (2014). doi: [10.1016/j.comatsci.2014.06.008](https://doi.org/10.1016/j.comatsci.2014.06.008)
  93. J. Čejka, G. Centi, J. Perez-Pariente, W. J. Roth, Zeolite-based materials for novel catalytic applications: Opportunities, perspectives and open problems. *Catal. Today* **179**, 2–15 (2012). doi: [10.1016/j.cattod.2011.10.006](https://doi.org/10.1016/j.cattod.2011.10.006)
  94. C. D. Wu, A. Hu, L. Zhang, W. Lin, A homochiral porous metal-organic framework for highly enantioselective heterogeneous asymmetric catalysis. *J. Am. Chem. Soc.* **127**, 8940–8941 (2005). doi: [10.1021/ja052431t](https://doi.org/10.1021/ja052431t); pmid: [15969557](https://pubmed.ncbi.nlm.nih.gov/15969557/)
  95. A. Corma, H. García, F. X. Labrés i Xamena, Engineering metal organic frameworks for heterogeneous catalysis. *Chem. Rev.* **110**, 4606–4655 (2010). doi: [10.1021/cr9003924](https://doi.org/10.1021/cr9003924); pmid: [20359232](https://pubmed.ncbi.nlm.nih.gov/20359232/)
  96. J. Liu *et al.*, Applications of metal-organic frameworks in heterogeneous supramolecular catalysis. *Chem. Soc. Rev.* **43**, 6011–6061 (2014). doi: [10.1039/C4CS00094C](https://doi.org/10.1039/C4CS00094C); pmid: [24871268](https://pubmed.ncbi.nlm.nih.gov/24871268/)
  97. H. Xu *et al.*, Catalytic covalent organic frameworks via pore surface engineering. *Chem. Commun.* **50**, 1292–1294 (2014). doi: [10.1039/C3CC48813F](https://doi.org/10.1039/C3CC48813F); pmid: [24352109](https://pubmed.ncbi.nlm.nih.gov/24352109/)
  98. D. S. Kundu, J. Schmidt, C. Bleschke, A. Thomas, S. Bleichert, A microporous binol-derived phosphoric acid. *Angew. Chem. Int. Ed.* **51**, 5456–5459 (2012). doi: [10.1002/anie.201109072](https://doi.org/10.1002/anie.201109072); pmid: [22499549](https://pubmed.ncbi.nlm.nih.gov/22499549/)
  99. Z. Fang *et al.*, Structural complexity in metal-organic frameworks: Simultaneous modification of open metal sites and hierarchical porosity by systematic doping with defective linkers. *J. Am. Chem. Soc.* **136**, 9627–9636 (2014). doi: [10.1021/ja503218j](https://doi.org/10.1021/ja503218j); pmid: [24915512](https://pubmed.ncbi.nlm.nih.gov/24915512/)
  100. Y. Qu, X. Duan, Progress, challenge and perspective of heterogeneous photocatalysts. *Chem. Soc. Rev.* **42**, 2568–2580 (2013). doi: [10.1039/C2CS35355E](https://doi.org/10.1039/C2CS35355E); pmid: [23192101](https://pubmed.ncbi.nlm.nih.gov/23192101/)
  101. J.-X. Jiang *et al.*, Conjugated microporous polymers with Rose Bengal dye for highly efficient heterogeneous organophotocatalysis. *Macromolecules* **46**, 8779–8783 (2013). doi: [10.1021/ma402104h](https://doi.org/10.1021/ma402104h)
  102. J. Luo, X. Zhang, J. Zhang, Carbazolic porous organic framework as an efficient, metal-free visible-light photocatalyst for organic synthesis. *ACS Catal.* **5**, 2250–2254 (2015). doi: [10.1021/acscatal.5b00025](https://doi.org/10.1021/acscatal.5b00025)
  103. X. Wang *et al.*, A metal-free polymeric photocatalyst for hydrogen production from water under visible light. *Nat. Mater.* **8**, 76–80 (2009). doi: [10.1038/nmat2317](https://doi.org/10.1038/nmat2317); pmid: [18997776](https://pubmed.ncbi.nlm.nih.gov/18997776/)
  104. J. Liu *et al.*, Metal-free efficient photocatalyst for stable visible water splitting via a two-electron pathway. *Science* **347**, 970–974 (2015). doi: [10.1126/science.1234145](https://doi.org/10.1126/science.1234145); pmid: [25722405](https://pubmed.ncbi.nlm.nih.gov/25722405/)
  105. S. Wan, J. Guo, J. Kim, H. Ihee, D. Jiang, A belt-shaped, blue luminescent, and semiconducting covalent organic framework. *Angew. Chem. Int. Ed.* **47**, 8826–8830 (2008). doi: [10.1002/anie.200803826](https://doi.org/10.1002/anie.200803826); pmid: [18830952](https://pubmed.ncbi.nlm.nih.gov/18830952/)
  106. J. W. Colson *et al.*, Oriented 2D covalent organic framework thin films on single-layer graphene. *Science* **332**, 228–231 (2011). doi: [10.1126/science.1202747](https://doi.org/10.1126/science.1202747); pmid: [21474758](https://pubmed.ncbi.nlm.nih.gov/21474758/)
  107. G. H. V. Bertrand, V. K. Michaelis, T. C. Ong, R. G. Griffin, M. Dincă, Thiophene-based covalent organic frameworks. *Proc. Natl. Acad. Sci. U.S.A.* **110**, 4923–4928 (2013). doi: [10.1073/pnas.1218241110](https://doi.org/10.1073/pnas.1218241110); pmid: [23479656](https://pubmed.ncbi.nlm.nih.gov/23479656/)
  108. M. Yoon, K. Suh, S. Natarajan, K. Kim, Proton conduction in metal-organic frameworks and related modularly built porous solids. *Angew. Chem. Int. Ed.* **52**, 2688–2700 (2013). doi: [10.1002/anie.201206410](https://doi.org/10.1002/anie.201206410); pmid: [23345157](https://pubmed.ncbi.nlm.nih.gov/23345157/)
  109. S. Burekaew *et al.*, One-dimensional imidazole aggregate in aluminum porous coordination polymers with high proton conductivity. *Nat. Mater.* **8**, 831–836 (2009). doi: [10.1038/nmat2526](https://doi.org/10.1038/nmat2526); pmid: [19734885](https://pubmed.ncbi.nlm.nih.gov/19734885/)
  110. J. M. Taylor, K. W. Dawson, G. K. H. Shimizu, A water-stable metal-organic framework with highly acidic pores for proton-conducting applications. *J. Am. Chem. Soc.* **135**, 1193–1196 (2013). doi: [10.1021/ja310435e](https://doi.org/10.1021/ja310435e); pmid: [23305324](https://pubmed.ncbi.nlm.nih.gov/23305324/)
  111. M. Yoon *et al.*, High and highly anisotropic proton conductivity in organic molecular porous materials. *Angew. Chem. Int. Ed.* **50**, 7870–7873 (2011). doi: [10.1002/anie.201101777](https://doi.org/10.1002/anie.201101777); pmid: [21721085](https://pubmed.ncbi.nlm.nih.gov/21721085/)
  112. C. Laberty-Robert, K. Vallé, F. Pereira, C. Sanchez, Design and properties of functional hybrid organic-inorganic membranes for fuel cells. *Chem. Soc. Rev.* **40**, 961–1005 (2011). doi: [10.1039/c0cs00144a](https://doi.org/10.1039/c0cs00144a); pmid: [21218233](https://pubmed.ncbi.nlm.nih.gov/21218233/)
  113. D. Sheberla *et al.*, High electrical conductivity in Ni<sub>3</sub>(2,3,6,7,10,11-hexaminitrotriphenylene)<sub>2</sub>, a semiconducting metal-organic graphene analogue. *J. Am. Chem. Soc.* **136**, 8859–8862 (2014). doi: [10.1021/ja502765n](https://doi.org/10.1021/ja502765n); pmid: [24750124](https://pubmed.ncbi.nlm.nih.gov/24750124/)
  114. Y. Kou, Y. Xu, Z. Guo, D. Jiang, Supercapacitive energy storage and electric power supply using an aza-fused  $\pi$ -conjugated microporous framework. *Angew. Chem. Int. Ed.* **50**, 8753–8757 (2011). doi: [10.1002/anie.201103493](https://doi.org/10.1002/anie.201103493); pmid: [21842523](https://pubmed.ncbi.nlm.nih.gov/21842523/)
  115. M. Brutschy, M. W. Schneider, M. Mastalerz, S. R. Waldvogel, Porous organic cage compounds as highly potent affinity materials for sensing by quartz crystal microbalances. *Adv. Mater.* **24**, 6049–6052 (2012). doi: [10.1002/adma.201202786](https://doi.org/10.1002/adma.201202786); pmid: [22941901](https://pubmed.ncbi.nlm.nih.gov/22941901/)
  116. Y. G. Chung *et al.*, Computation-ready, experimental metal-organic frameworks: A tool to enable high-throughput screening of nanoporous crystals. *Chem. Mater.* **26**, 6185–6192 (2014). doi: [10.1021/cm502594j](https://doi.org/10.1021/cm502594j)
  117. E. L. First, C. A. Floudas, MOFomics: Computational pore characterization of metal-organic frameworks. *Micropor. Mesopor. Mater.* **165**, 32–39 (2013). doi: [10.1016/j.micromeso.2012.07.049](https://doi.org/10.1016/j.micromeso.2012.07.049)
  118. P. Bai *et al.*, Discovery of optimal zeolites for challenging separations and chemical transformations using predictive materials modeling. *Nat. Commun.* **6**, 5912 (2015). doi: [10.1038/ncomms6912](https://doi.org/10.1038/ncomms6912); pmid: [25607776](https://pubmed.ncbi.nlm.nih.gov/25607776/)
  119. E. L. First, M. M. F. Hasan, C. A. Floudas, Discovery of novel zeolites for natural gas purification through combined material screening and process optimization. *AIChE J.* **60**, 1767–1785 (2014). doi: [10.1002/aic.14441](https://doi.org/10.1002/aic.14441)
  120. F. X. Coudert, C. Mellot-Draznieks, A. H. Fuchs, A. Boutin, Prediction of breathing and gate-opening transitions upon binary mixture adsorption in metal-organic frameworks. *J. Am. Chem. Soc.* **131**, 11329–11331 (2009). doi: [10.1021/ja904123f](https://doi.org/10.1021/ja904123f); pmid: [19637918](https://pubmed.ncbi.nlm.nih.gov/19637918/)
  121. L. Chen *et al.*, Elucidating the breathing of the metal-organic framework MIL-53(Sc) with ab initio molecular dynamics simulations and in situ X-ray powder diffraction experiments. *J. Am. Chem. Soc.* **135**, 15763–15773 (2013). doi: [10.1021/ja403453g](https://doi.org/10.1021/ja403453g); pmid: [23731240](https://pubmed.ncbi.nlm.nih.gov/23731240/)
  122. L. M. Rodriguez-Albelo *et al.*, Zeolitic polyoxometalate-based metal-organic frameworks (Z-POMOFs): Computational evaluation of hypothetical polymorphs and the successful targeted synthesis of the redox-active Z-POMOF1. *J. Am. Chem. Soc.* **131**, 16078–16087 (2009). doi: [10.1021/ja905009e](https://doi.org/10.1021/ja905009e); pmid: [19842657](https://pubmed.ncbi.nlm.nih.gov/19842657/)
  123. C. Mellot-Draznieks, J. Dutoir, G. Férey, Hybrid organic-inorganic frameworks: Routes for computational design and structure prediction. *Angew. Chem. Int. Ed.* **43**, 6290–6296 (2004). doi: [10.1002/anie.200454251](https://doi.org/10.1002/anie.200454251); pmid: [15372642](https://pubmed.ncbi.nlm.nih.gov/15372642/)
  124. K. E. Jelfs *et al.*, In silico design of supramolecules from their precursors: Odd-even effects in cage-forming reactions. *J. Am. Chem. Soc.* **135**, 9307–9310 (2013). doi: [10.1021/ja404253j](https://doi.org/10.1021/ja404253j); pmid: [23745577](https://pubmed.ncbi.nlm.nih.gov/23745577/)
  125. D. Holden *et al.*, Gas diffusion in a porous organic cage: Analysis of dynamic pore connectivity using molecular dynamics simulations. *J. Phys. Chem. C* **118**, 12734–12743 (2014). doi: [10.1021/jp500293s](https://doi.org/10.1021/jp500293s)
  126. M. S. Dyer *et al.*, Computationally assisted identification of functional inorganic materials. *Science* **340**, 847–852 (2013). doi: [10.1126/science.1226558](https://doi.org/10.1126/science.1226558); pmid: [23579498](https://pubmed.ncbi.nlm.nih.gov/23579498/)
  127. D. W. C. MacMillan, The advent and development of organocatalysis. *Nature* **455**, 304–308 (2008). doi: [10.1038/nature07367](https://doi.org/10.1038/nature07367); pmid: [18800128](https://pubmed.ncbi.nlm.nih.gov/18800128/)

## ACKNOWLEDGMENTS

We thank R. L. Bedard for his advice and for discussions that led to the original concept of this review and T. Hasell, K. E. Jelfs, M. A. Little, L. Chen, and M. Zwiernburg for input. Supported by the Engineering and Physical Sciences Research Council (EP/H000925/1) and European Research Council under the European Union's Seventh Framework Programme/ERC Grant Agreement no. 321156.

10.1126/science.aaa8075



## RESEARCH ARTICLES

## PHOTOSYNTHESIS

# Structural basis for energy transfer pathways in the plant PSI-LHCI supercomplex

Xiaochun Qin,<sup>1,2\*</sup> Michihiro Suga,<sup>2\*</sup> Tingyun Kuang,<sup>1†</sup> Jian-Ren Shen<sup>1,2‡</sup>

Photosynthesis converts solar energy to chemical energy by means of two large pigment-protein complexes: photosystem I (PSI) and photosystem II (PSII). In higher plants, the PSI core is surrounded by a large light-harvesting complex I (LHCI) that captures sunlight and transfers the excitation energy to the core with extremely high efficiency. We report the structure of PSI-LHCI, a 600-kilodalton membrane protein supercomplex, from *Pisum sativum* (pea) at a resolution of 2.8 angstroms. The structure reveals the detailed arrangement of pigments and other cofactors—especially within LHCI—as well as numerous specific interactions between the PSI core and LHCI. These results provide a firm structural basis for our understanding on the energy transfer and photoprotection mechanisms within the PSI-LHCI supercomplex.

Photosynthesis uses light energy from the Sun to convert CO<sub>2</sub> and water into carbohydrates and oxygen, thus sustaining all aerobic life forms on Earth. In oxygenic photosynthesis, photosystem II (PSII) uses light energy to split water into oxygen, protons, and electrons, whereas photosystem I (PSI) is responsible for the reduction of nicotinamide adenine dinucleotide phosphate (NADP<sup>+</sup>) into NADPH. In higher plants, the PSI core is surrounded by the light-harvesting complex I (LHCI), forming a PSI-LHCI supercomplex, to facilitate efficient energy harvesting while avoiding concentration quenching (1). The energy absorbed by LHCI is transferred to the PSI core, where it is converted into chemical energy with a quantum efficiency close to 100% (2).

The PSI core exists as a homotrimer in cyanobacteria, and its structure has been determined at 2.5 Å resolution (3). Each monomer contains 12 protein subunits, 128 cofactors [96 chlorophylls (Chls), two phylloquinones, three Fe<sub>4</sub>S<sub>4</sub> clusters, 22 carotenoids, four lipids, and a Ca<sup>2+</sup> ion]. By contrast, the higher plant PSI-LHCI supercomplex exists in a monomeric form and contains four unique subunits (PsaG, PsaH, PsaN, and PsaO) in the core, as well as subunits homologous to cyanobacterial PSI (4) and four Lhca subunits (Lhca1 to Lhca4) in the LHCI complex. The structure of the higher plant PSI-LHCI supercomplex has been solved at 4.4 Å to 3.3 Å resolutions from *P. sativum* var. Alaska (5–7), which

revealed the presence of 17 protein subunits (13 core subunits and four Lhcas) and 199 cofactors [174 chlorophyll a molecules (Chls a), 19 carotenoids, two phylloquinones, three Fe<sub>4</sub>S<sub>4</sub> clusters, and one lipid] (PDB ID: 3LW5) with a total molecular mass of 600 kD (7). However, the resolutions achieved so far were not high enough to reveal the detailed structure of PSI-LHCI, especially with respect to the position and number of cofactors associated with LHCI.

We crystallized PSI-LHCI from *P. sativum* var. Alaska and analyzed its structure at 2.8 Å resolution (figs. S1 to S5 and table S1) (8). This improved resolution reveals the detailed organization of protein subunits and cofactors, enabling the mechanisms of energy transfer, regulation, and photoprotection within the PSI-LHCI supercomplex to be examined on a more robust structural basis.

## Architecture of the PSI-LHCI supercomplex

The overall structure of PSI-LHCI resembles a semispherical shape similar to that reported previously, with a dimension of 140 Å × 40 Å (Fig. 1, A and C). The supercomplex contains 16 subunits but does not include PsaN and PsaO, which suggests that these two subunits were lost during purification or crystallization owing to their loose association with the PSI core (9, 10). Four LHCI subunits, Lhca1 to Lhca4, are arranged in the form of a heterodimer of two heterodimers (Lhca1-Lhca4 and Lhca2-Lhca3) and are attached to one side of the PSI core where PsaG, PsaF, PsaJ, and PsaK are located (Fig. 1A).

In addition to the protein subunits, we assigned 155 Chls (143 Chls a and 12 Chls b), 35 carotenoids [26 β-carotenes (BCRs), five luteins (Luts), and four violaxanthins (Vios)], 10 lipids [six phosphatidylglycerols (PGs), three monoga-

lactosyldiacylglycerols (MGDGs), and one digalactosyldiacylglycerol (DGDG)], three Fe<sub>4</sub>S<sub>4</sub> clusters, two phylloquinones, and several water molecules (Fig. 1B and table S2). We identified fewer Chls than in the previous study (155 versus 174) (7), which may be due to ambiguities in the electron density of the previous lower-resolution structure. The composition of the pigments we assigned in the crystal structure largely agrees with the results of our chemical analysis by high-performance liquid chromatography (HPLC) (table S3). [For a detailed assignment of these cofactors and comparison with the previous structure (6, 7), see table S2 and fig. S6.] There are two monomers in the crystallographic asymmetric unit; because the monomers are identical, we describe the PSI-LHCI structure of the monomer whose chains are labeled by capital letters in the PDB file.

## Structure of the Lhca apoproteins

All of the Lhca proteins have three major transmembrane (TM) helices, A, B, and C, and an amphipathic helix D at the luminal side (Fig. 2, A and B, and fig. S7), similar to the structures of light-harvesting complex II (LHCII) and the minor antenna protein CP29 (fig. S8, A to D) [for LHCI we followed the nomenclature used in LHCII (11) and CP29 (12), whereas for the PSI core we followed the nomenclature used in cyanobacterial PSI (3)]. However, there are notable differences among the structures of the four Lhcas, and between Lhcas and LHCII and CP29, in the two loop regions AC and BC as well as the N-terminal region, which are the least conserved regions in the sequences (Fig. 2 and fig. S8E). In loop AC, the length of Lhca1 resembles that of LHCII and CP29 (fig. S8, A to D) but is much shorter than that of Lhca2, Lhca3, and Lhca4 (Fig. 2C). In loop BC, the short amphipathic helix E found in both LHCII and CP29 structures becomes shorter and locates closer to helix B in Lhca1, and no longer exists in Lhca2, Lhca3, and Lhca4 (Fig. 2D). In the N-terminal region, three Lhcas (Lhca1, Lhca2, and Lhca4) have a similar folding containing Chl601, whereas Lhca3 has a short “helix F” (Ser<sup>55</sup>-Tyr<sup>61</sup>) and does not have Chl at the equivalent position (Fig. 2, E to G).

In addition, helix B of Lhca3 is one turn shorter than other Lhcas at the stromal side (Fig. 2, B and E), allowing the forward loop region (Leu<sup>75</sup>-Glu<sup>88</sup>), which interacts with the PSI core in all Lhca proteins, to maximize interactions with PsaA. Helix C of Lhca1 is one turn shorter than other Lhcas at the stromal side, making it more similar to LHCII and CP29 (Fig. 2, A and C, and fig. S8, A and B). Taken together, the middle Lhcas (Lhca2 and Lhca4) in the “LHCI belt” are very similar, whereas Lhcas residing in the two sides (Lhca1 and Lhca3) have notable differences. These differences may be responsible for the variations in their pigment composition and spatial arrangement, and for their association with other subunits.

LHCI was often separated into two fractions upon isolation: one enriched in the Lhca1-Lhca4 dimer (13, 14) and the other enriched in the

<sup>1</sup>Photosynthesis Research Center, Key Laboratory of Photobiology, Institute of Botany, Chinese Academy of Sciences, Beijing 100093, China. <sup>2</sup>Photosynthesis Research Center, Graduate School of Natural Science and Technology, Okayama University, Tsushima Naka 3-1-1, Okayama 700-8530, Japan.

\*These authors contributed equally to this work. †Corresponding author. E-mail: kuangty@ibcas.ac.cn (T.K.); shen@cc.okayama-u.ac.jp (J.-R.S.)

Lhca2-Lhca3 dimer (15). From our structure, the Lhca-Lhca intersubunit interactions can be categorized into two types: (i) hydrophilic interactions between the N- and C-terminal regions of one Lhca with helix C of the adjacent Lhca, and (ii) hydrophobic interactions between Chls and carotenoids from helix A of one Lhca with those from helix C of the adjacent Lhca (Fig. 3). Our structure indicates that both types of interactions are stronger between Lhca1 and Lhca4, slightly weaker between Lhca2 and Lhca3, and much weaker between Lhca2 and Lhca4. In particular, two bridging carotenoids, BCR623 and Lut624, were found in the region between Lhca1 and Lhca4, maximizing their interactions (Fig. 3, A and D), whereas only BCR623 was found between Lhca2 and Lhca4 (Fig. 3, B and E) and between Lhca2 and Lhca3 (Fig. 3, C and F), leading to weaker interactions between them.

### Arrangement and functions of Chls in LHCI

We identified 75 cofactors in the four Lhca subunits: 45 Chls a, 12 Chls b, four BCRs, five Luts, four Vios, three PGs, and two MGDGs (Fig. 1B, figs. S9 and S10, and tables S2 and S4). The numbers of Chls b and carotenoids assigned are very similar to those determined chemically (table S3), which gives rise to a Chl a/b ratio of 3.75, consistent with that of 3.71 from previous biochemical analysis (15). The Chls in LHCI are

distributed into two layers, one close to the stromal and the other one close to the luminal surface (Fig. 4). The stromal-side Chl layer contains 36 Chls (29 Chls a and 7 Chls b) with an average Mg-to-Mg distance of 11.3 Å (Fig. 4B). The luminal-side Chl layer has a less dense packing composed of 16 Chls a and 5 Chls b, which are separated into two clusters in each Lhca (Fig. 4C) with an average Mg-to-Mg distance of 10.6 Å within each cluster and 19.7 Å between the clusters. The shortest distance between the stromal- and luminal-side layers is 11.6 Å, from Chl a607 to Chl a619 in Lhca3.

In comparison with LHCI, there are unique Chls found in LHCI with either different orientations or positions, most of which are located at the gap region between LHCI and the PSI core, or in connecting regions between adjacent Lhcas (Fig. 4, fig. S8, C and D, and table S4). Among them, Chls 601 in Lhca1, Lhca2, and Lhca4 have similar  $Q_x$  and  $Q_y$  transition dipole moments (Fig. 2, F and G, and table S4), but different from the ones in LHCI. Chl a607 in Lhca3 is unusual because other Lhcas bind Chl b at this site, and it is also closer to the PSI core than is Chl b607, which suggests that Chl a607 may promote energy transfer from Lhca3 to the PSI core. In addition, Chl a616 in Lhca1, Chl a617 in Lhca3 and Lhca4, Chl b618 in Lhca2 and Lhca4, and Chl a619 in Lhca4 were not found in LHCI (Fig. 2, F and G, Fig. 4, fig. S8, C and D, and table S4).

Among the 12 Chls b in LHCI, two (b601, b607) are bound to Lhca1, five (b601, b606, b607, b608, and b618) to Lhca2, one (b608) to Lhca3, and four (b606, b607, b608, and b618) to Lhca4 (Fig. 4). The uneven distribution of Chl b indicates that Lhca2 and Lhca4 have a higher affinity for Chl b than do Lhca1 and Lhca3, in agreement with results from *in vitro* reconstitution experiments (16, 17). Nearly all Chls b are located in helix C or the N-terminal loop, both of which form the interfacial regions of two adjacent Lhca proteins (Figs. 1 and 4), which suggests that they may be important in mediating energy transfer and/or interactions between adjacent Lhca subunits.

A striking feature of Lhcas is the presence of red forms of several Chls a that are important for energy transfer and trapping in the whole PSI complex (18), through which most of harvested energy is transferred to the reaction center with high efficiencies (19–21). The a603-a609 dimers in each Lhca (Fig. 5) have a close distance and some overlap between their C and E rings, reflecting their nature as red Chls. All four Chl 603-609 dimers are bound at the inside of LHCI, with their phytol tails protruding into the gap region between LHCI and the PSI core, in good agreement with their roles of mediating energy transfer from LHCI to the PSI core. The interactions between the PSI core and LHCI may affect the conformation of the red dimers, especially through the interactions with the hydrophobic

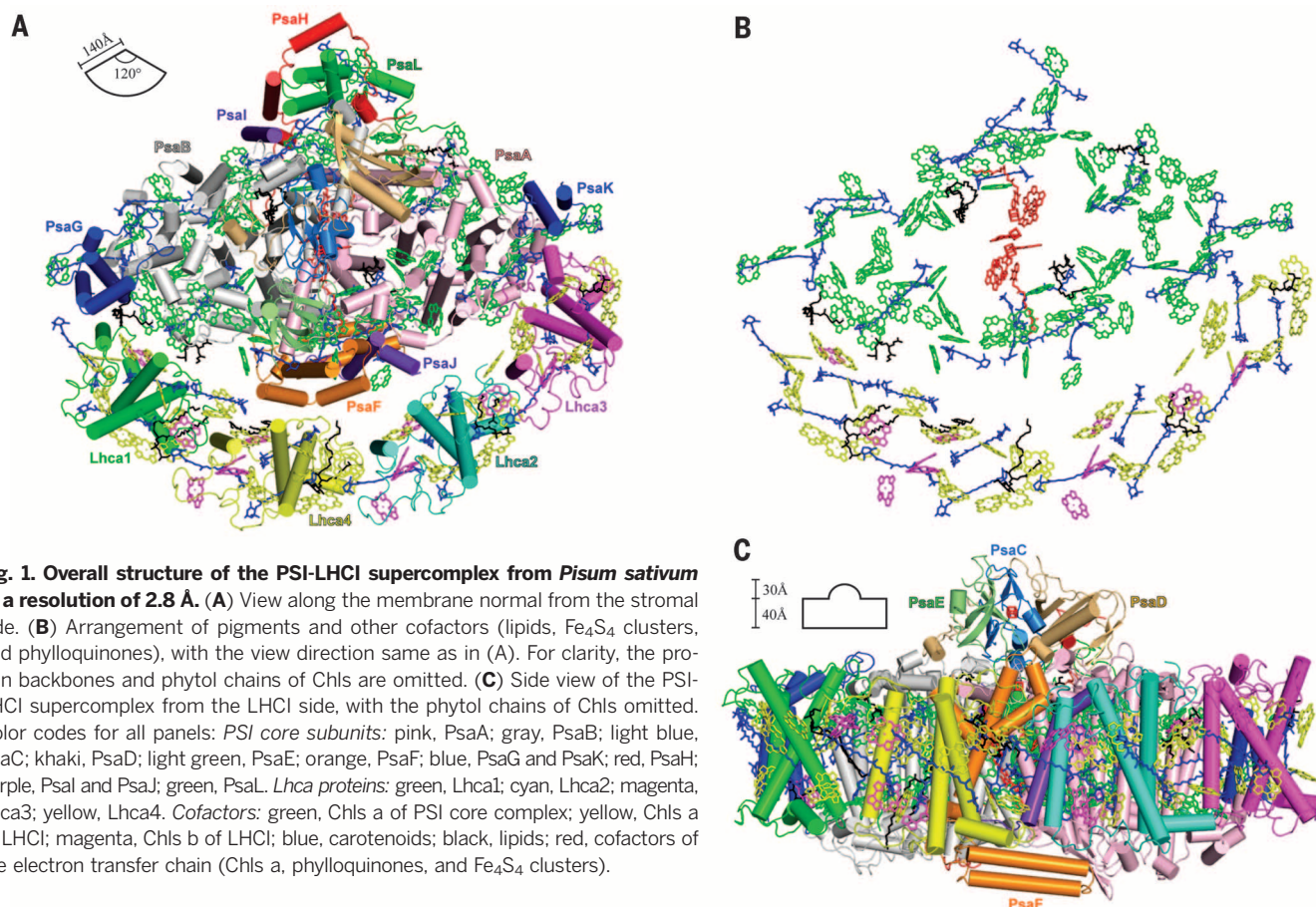


**Fig. 1. Overall structure of the PSI-LHCI supercomplex from *Pisum sativum* at a resolution of 2.8 Å. (A)** View along the membrane normal from the stromal side. **(B)** Arrangement of pigments and other cofactors (lipids,  $Fe_4S_4$  clusters, and phylloquinones), with the view direction same as in (A). For clarity, the protein backbones and phytol chains of Chls are omitted. **(C)** Side view of the PSI-LHCI supercomplex from the LHCI side, with the phytol chains of Chls omitted. Color codes for all panels: *PSI core subunits*: pink, PsaA; gray, PsaB; light blue, PsaC; khaki, PsaD; light green, PsaE; orange, PsaF; blue, PsaG and PsaK; red, PsaH; purple, PsaI and PsaJ; green, PsaL. *Lhca proteins*: green, Lhca1; cyan, Lhca2; magenta, Lhca3; yellow, Lhca4. *Cofactors*: green, Chls a of PSI core complex; yellow, Chls a of LHCI; magenta, Chls b of LHCI; blue, carotenoids; black, lipids; red, cofactors of the electron transfer chain (Chls a, phylloquinones, and  $Fe_4S_4$  clusters).



phytol tails (22), which agrees with the enhancement of the red forms in LHCI upon its binding to the PSI core (23). In Lhca1 and Lhca2, the central ligand of Chl a603 is His (Fig. 5, A and

B, and table S4), whereas it is Asn in Lhca3 and Lhca4 (Fig. 5, C and D, and table S4). Chl a603 is connected with a609 by the His or Asn residue through hydrogen bonds, and Chl a609 is

further hydrogen-bonded with an Arg residue (Fig. 5). The multiple interactions of Chl a609 suggest that its porphyrin head is more stable geometrically than Chl a603, implying that Chl

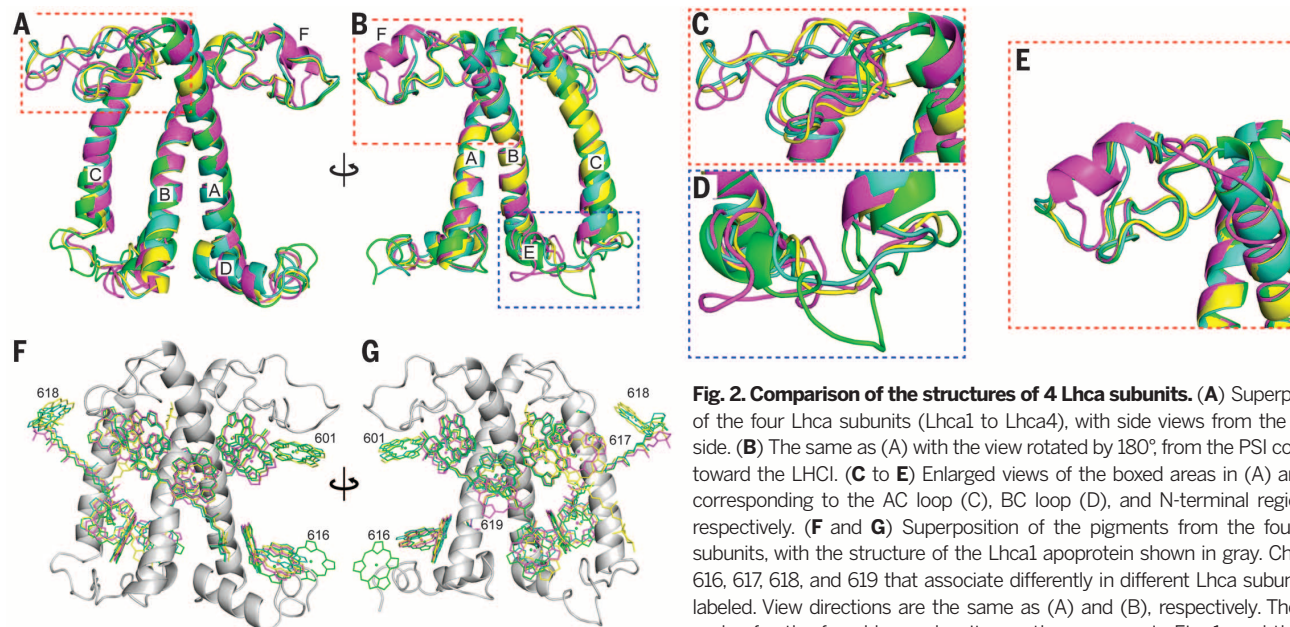


**Fig. 2. Comparison of the structures of 4 Lhca subunits.** (A) Superposition of the four Lhca subunits (Lhca1 to Lhca4), with side views from the Lhcas' side. (B) The same as (A) with the view rotated by 180°, from the PSI core side toward the LHCI. (C to E) Enlarged views of the boxed areas in (A) and (B), corresponding to the AC loop (C), BC loop (D), and N-terminal region (E), respectively. (F and G) Superposition of the pigments from the four Lhca subunits, with the structure of the Lhca1 apoprotein shown in gray. Chls 601, 616, 617, 618, and 619 that associate differently in different Lhca subunits are labeled. View directions are the same as (A) and (B), respectively. The color codes for the four Lhca subunits are the same as in Fig. 1, and those of pigments the same as the Lhca subunits they are associated with.

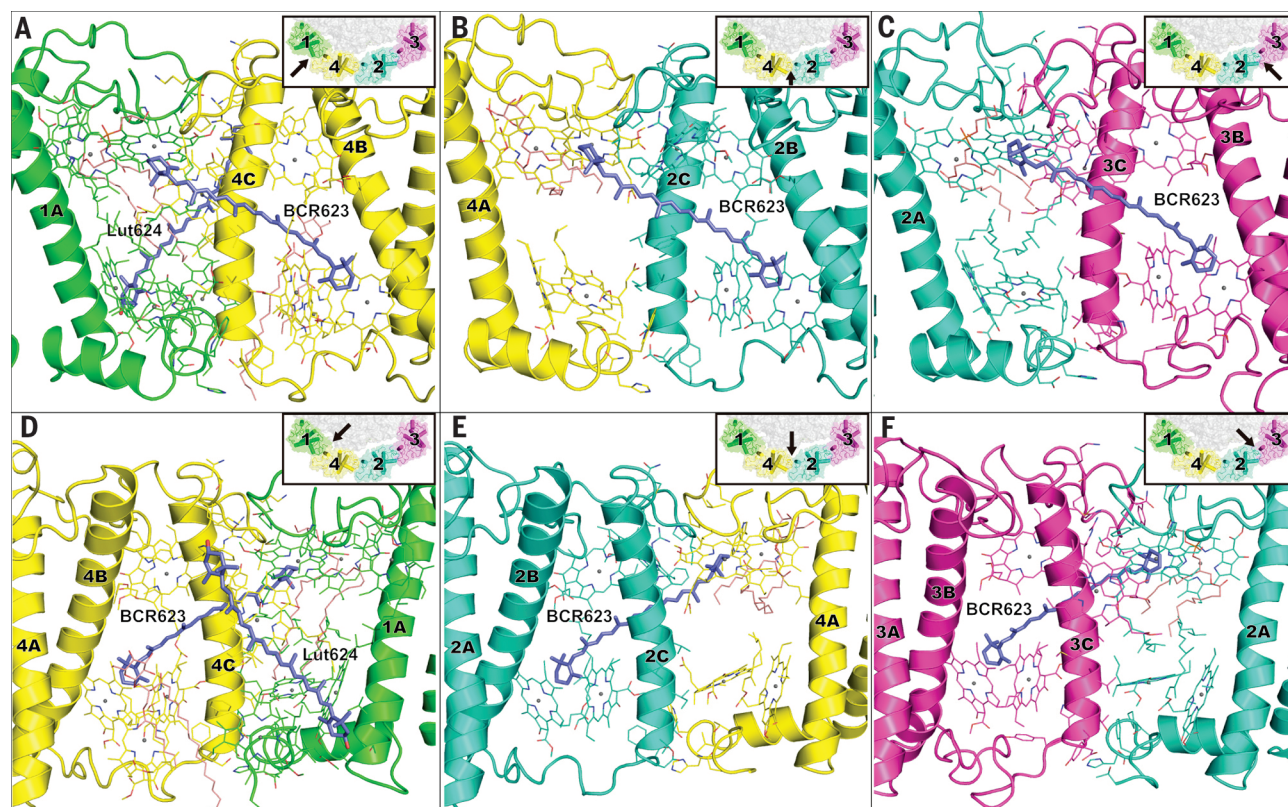


**Fig. 3. Interactions between adjacent Lhca subunits.** (A to C) Side view, from LHCI to the PSI core side, of interactions between Lhca1 and Lhca4, between Lhca4 and Lhca2, and between Lhca2 and Lhca3, respectively. (D to F) Views of (A) to (C), respectively, from the PSI core to the LHCI side. Carotenoids bridging two adjacent Lhca subunits are shown as blue sticks. Adjacent TM helices are labeled by Lhca number and TM helix name; thus, 1A represents helix A of Lhca1.



a603 may be more likely to undergo conformational modulation. This suggests a functional difference between the individual Chls in the red dimer.

### Arrangement and function of carotenoids in LHCI

Our structure reveals that each Lhca binds three carotenoids (one Lut, one Vio, and one BCR) at three sites (L1, L2, and N1, respectively), and another lutein (Lut624) is bound between Lhca1 and Lhca4, giving rise to a total of 13 carotenoids in the four Lhcas (Fig. 1B, Fig. 4, fig. S9, and table S4). Lut620 (L1 site) and Vio621 (L2 site) are in all-trans configurations and are located in the two elongated grooves on the two sides of helices A and B. The third carotenoid is an all-trans  $\beta$ -carotene, BCR623, located at the N1 site. The presence of these three kinds of carotenoids is consistent with previous and present biochemical analysis (15, 16, 24, 25) (table S3), and the Lhcas do not bind any carotenoids at the V1 site found in LHCI (although the V1 site may be partially occupied by a BCR from an adjacent Lhca). Among the three carotenoid-binding sites of Lhca, the L1 site is conserved also in LHCI and CP29 (fig. S8, C and D, and table S4), where it has been suggested to function as a nonphotochemical quencher to promote energy dissipation from the nearby, lowest excited energy-bearing Chl a610-a611-a612 cluster in both major (26) and minor LHCIIs (27). We observed the same orientation of Lut620 and the surrounding Chl a610-a611-a612 cluster in Lhcas; however, because the Chl a610-a611-a612 cluster is not the site with the lowest energy level in LHCI (the lowest energy level is located in the red Chls), the efficiency of quenching through this pathway would be lower in LHCI than that in LHCIIs.

The occupancy of the L2 site is variable depending on different proteins (i.e., Lut in LHCI, Vio in minor LHCIIs and LHCI) (table S4). Vio in LHCIIs may be changed to zeaxanthin (Zea) by Vio de-epoxidase, which is important for photoprotection by quenching the  $^1\text{Chl}^*$  states (28–30). In LHCI, *in vivo* studies also suggested the possible conversion of Vio to Zea (31–33), and indeed a Zea-dependent quenching of the excitation energy in LHCI has been observed recently (33). However, the extent and role of the xanthophyll cycle in PSI are not clear, and the de-epoxidation of LHCI may depend on affinities of the Vio binding sites, as well as the interaction between LHCI and the PSI core. Our structure revealed possible functional differences between the L2 sites of different Lhcas, as the Chls (a/b606, a/b607) surrounding this site are involved in a different hydrogen-bond network. In Lhca2 and Lhca4, the central ligand for both Chl b606 and Chl b607 is water (Fig. 5, B, D, F, and H), and the C7-formyl group of Chl b606 forms a hydrogen bond to the coordinated water of Chl b607, similar to the arrangement seen in LHCI and CP29. On the other hand, the central ligand of Chl a/b607 is Gln<sup>105</sup> in Lhca1 (Fig. 5, A and E) and Val<sup>135</sup> in Lhca3 (Fig. 5, C and G), neither of which forms hydrogen bonds with Chl a606.

Furthermore, a Glu residue located at helix C close to the luminal side in all Lhcas and CP29 interacts with both Chl 607 and/or Chl 606 by hydrogen bonds (Fig. 5). The differences in their coordination pattern may suggest a different role of these pigments in energy absorption or quenching.

### Structure of the PSI core

The PSI core contains 98 Chls a, 22 BCRs, five lipids (three PGs, one MGDG, and one DGDG), three Fe<sub>4</sub>S<sub>4</sub> clusters, and two phyloquinones (Fig. 1B, fig. S10, and tables S2 and S5). Of the 22 BCRs, 17 have an all-trans configuration and 5 contain

one or two cis bonds (two 9-cis, one 9,9'-cis, one 9,13'-cis, and one 13-cis) (table S5). Most of the BCRs were located in the same position as those observed in the cyanobacterial PSI, and the cis and trans conformations of carotenoids are identical in the cyanobacterial and plant PSI cores (table S5), indicating that they have been conserved over 1.5 billion years of evolution. However, several changes were observed in the position of carotenoids between the two species. BCR4022, bound at the outside of TM helices PsaL-e, PsaL-g, and PsaI in the cyanobacterial PSI core, is not present in the plant PSI core; this may be related to the distinctly different environment of PsaI between

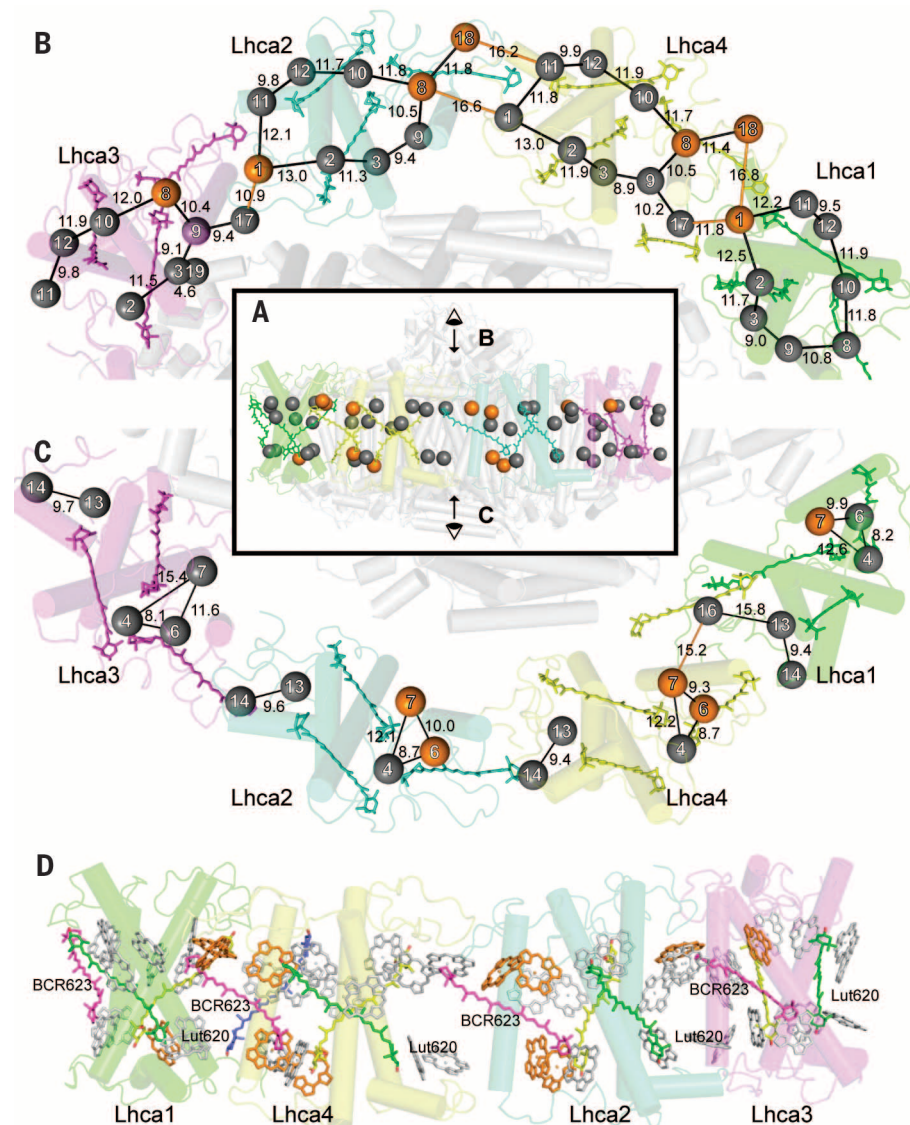


**Fig. 4. Arrangements of pigments within LHCI.** (A and D) Side view, from the LHCI side, of the overall arrangement of pigments in the four Lhcas. (B and C) View of the pigment arrangements along the membrane normal from the stromal and luminal sides, respectively [view directions indicated by arrow-heads in (A)]. In (A) to (C), Chls a and Chls b are represented by gray and orange spheres, respectively, at the positions of their Mg<sup>2+</sup> ions, with Mg-to-Mg distances of adjacent Chls given in Å. The numbers of Chls are labeled with the last one or two digits. Lhca subunits are depicted in the same colors as in Fig. 1, and carotenoids are depicted in the same color as the Lhca subunits they are associated with. In (D), the three carotenoid binding sites L1 (Lut620), L2 (Vio621), and N1 (BCR623) are shown in green, yellow, and magenta, respectively. Lut624 in the L3 site of Lhca4 is shown in light blue.



cyanobacterial and plant PSIs, as PsaI is located at the monomer-monomer interface between the subunits of the cyanobacterial trimer. On the other hand, PsaL bound an additional BCR4025 at the outside of TM helices PsaL-d and PsaL-g (Fig. 1, A and B) toward the suggested LHCII binding site (34). Two BCRs present in the cyanobacterial PSI core, BCR4015 (located between TM helices of PsaF and PsaJ) and BCR4021 (bound to PsaM), were also not present in the plant PSI core, whereas PsaG and PsaK bound two additional BCRs, BCR4023 and BCR4024, respectively (Fig. 1, A and B, and fig. S11, A and C).

These discrepancies may imply possible functional differences of BCRs between plant and cyanobacterial PSI cores.

Notable differences were found in the structures of PsaG, PsaK, and PsaH between our results and previous structures (5–7) (fig. S11). In our structure, the direction of the PsaG polypeptide was reversed, resulting in a completely reversed location of the two TM helices PsaG-a and PsaG-b (fig. S11, A and B). A short helix was found between PsaG-a and PsaG-b, and a large extramembrane loop in the luminal side found in the previous structure was not found in our

structure. PsaG-a has extensive interactions with Lhca1 that may contribute to stabilizing the supercomplex, whereas PsaG-b has interactions with PsaB, and the C-terminal region of PsaG has interactions with both PsaB and Lhca1 (fig. S12D). Two Chls a, one BCR, and one MGDG were found in PsaG, whereas the previous structure revealed only one Chl a (fig. S11, A and B).

Previously, the structure of PsaK from cyanobacteria could only be built partially with its TM helices as polyalanines (3). In our structure, all of the TM residues together with three Chls a and one BCR were built unambiguously, although

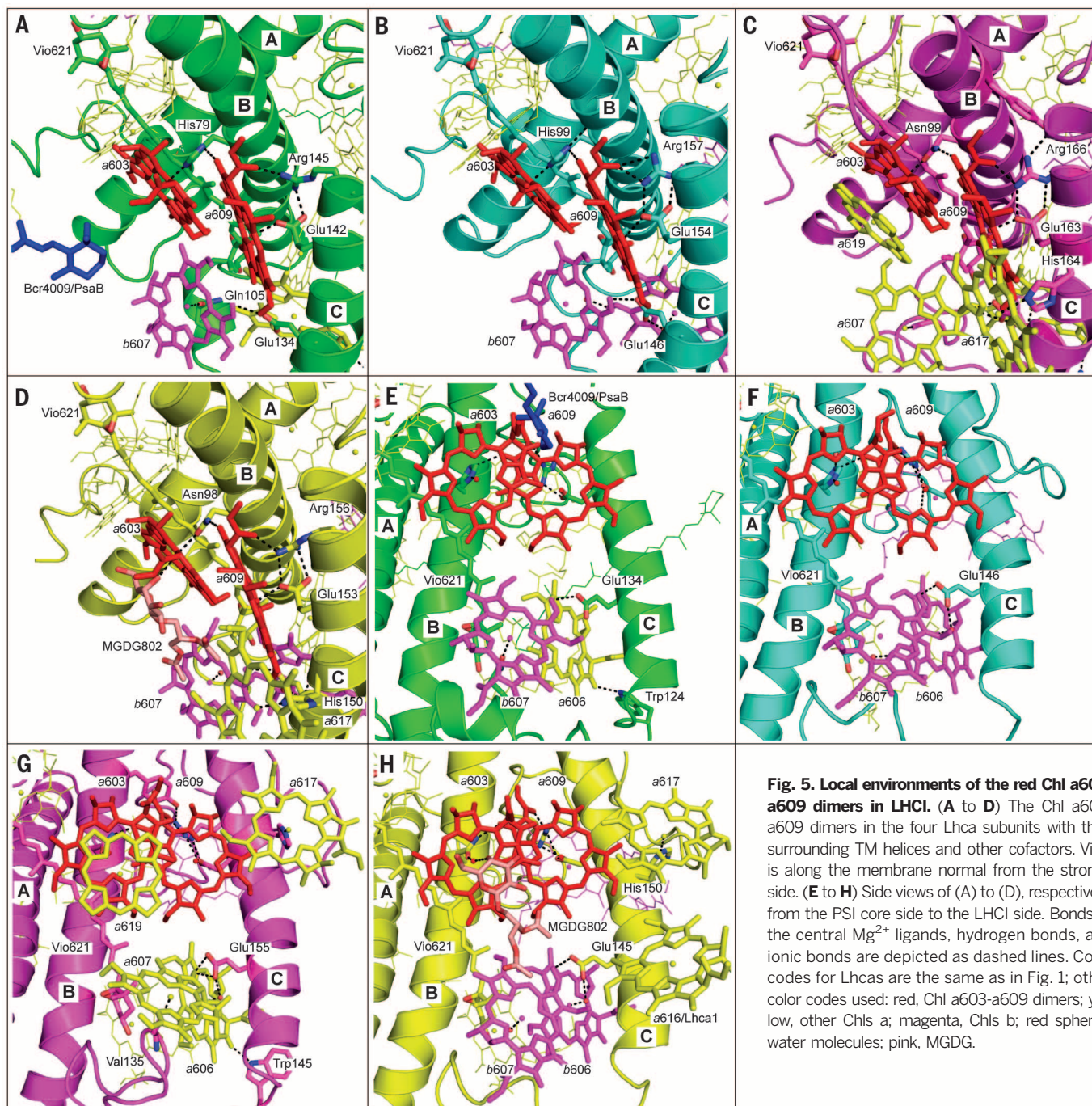


**Fig. 5. Local environments of the red Chl a603-a609 dimers in LHCI.** (A to D) The Chl a603-a609 dimers in the four Lhca subunits with their surrounding TM helices and other cofactors. View is along the membrane normal from the stromal side. (E to H) Side views of (A) to (D), respectively, from the PSI core side to the LHCI side. Bonds to the central  $Mg^{2+}$  ligands, hydrogen bonds, and ionic bonds are depicted as dashed lines. Color codes for Lhcas are the same as in Fig. 1; other color codes used: red, Chl a603-a609 dimers; yellow, other Chls a; magenta, Chls b; red spheres, water molecules; pink, MGDG.



the loop region connecting the two helices could not be built because of the relatively poor electron density around this region (fig. S11C). Although the structure of helix PsaK-a was similar to that reported previously for plant PSI (6, 7), the locations of PsaK-b, together with Chls, were completely different, and no BCR was found in PsaK in the previous structure (6, 7) (fig. S11D). Because the sequences of plant PsaK and PsaG are similar to that of cyanobacterial PsaK, PsaG has been suggested to arise from PsaK via gene duplication (35). Our structure shows that PsaK indeed has a structure similar to that of PsaG (fig. S11, E and F), which suggests that they may have similar functions. Because both subunits are required to enable energy transfer from

LHCI to the PSI core, the common structural features may reflect the prerequisites for such functions.

The structure of PsaH differs from the previous model (6, 7), especially in the N-terminal region (fig. S11G). In our structure, PsaH extensively interacts with PsaL as well as PsaD and PsaB in the stromal side. On the luminal side, PsaH interacts with PsaB, PsaI, and PsaL (fig. S11, H and I). The interactions with PsaB, PsaD, PsaI, and PsaL are in agreement with previous cross-linking results (36) and also explain PsaH's function in stabilizing PSI (37). The interaction with PsaD may explain why PsaH is essential for efficient electron transfer in PSI (37) because PsaC, PsaD, and PsaE form the docking site for ferredoxin (38) and

PsaC carries the terminal  $\text{Fe}_4\text{S}_4$  clusters. These structural features illustrate the importance of PsaH in stabilizing the PSI monomer and maintaining the function of plant PSI.

### Interactions and possible energy transfer pathways between LHCI and the PSI core

Our structure reveals extensive and specific protein-protein and pigment-pigment interactions between each Lhca and PSI core subunits (Fig. 1, A and B, and fig. S12). At the stromal side, the region between the N-terminal loop and the beginning of helix B in Lhca1, Lhca2, and Lhca4 interacts with PsaB-Pro<sup>311</sup> and several cofactors, the N-terminal region of PsaJ, and the region around Phe<sup>207</sup>-Asn<sup>222</sup> of PsaF, respectively,

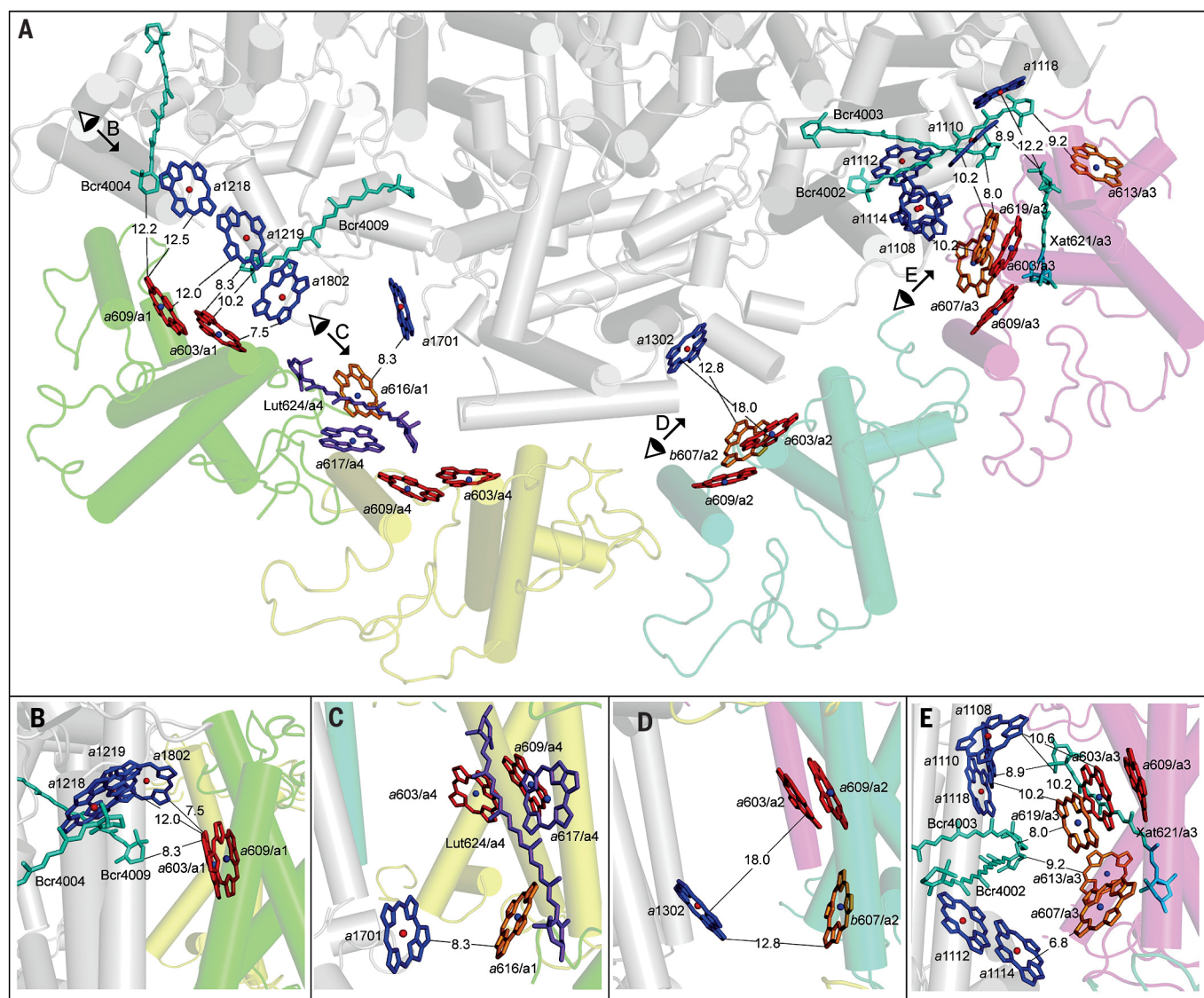


**Fig. 6. Plausible energy transfer pathways from LHCI to the PSI core.**

(A) Overall location of pigments involved in energy transfer from LHCI to the PSI core, with eye symbols and arrowheads indicating view directions shown in the following panels. (B) Stromal-side energy transfer pathway 1Bs from Lhca1 to PSI core. (C) Luminal-side pathway 1FI from Lhca1 to PSI core. (D) Pathways 2Js and 2Jl from Lhca2 to PSI core. (E) Pathways

3As and 3Al from Lhca3 to PSI core. View directions are from the stromal side for (A) and perpendicular to the membrane normal for (B) to (E), respectively. The nomenclature of the core subunits follows the cyanobacterial one (3). Color codes: blue, Chls a in PSI core; red, Chl a603-a609 dimers; purple, Chl a617 and Lut624 in Lhca4; orange, other Chls close to PSI core; cyan, carotenoids.



whereas Gln<sup>57</sup> in helix F and residues Pro<sup>74</sup> to Ile<sup>87</sup> at the N-terminal loop of Lhca3 interact with several regions of PsAa (fig. S12, B to E). In addition, BCR623 and helix C at the peripheral region of Lhca1 interact with MGDG and TM helix PsAa-G (fig. S12D), and residues Ile<sup>237</sup>, Leu<sup>240</sup>, Val<sup>241</sup>, Leu<sup>266</sup>, and Chl a607 at the peripheral region of Lhca3 interact with PsAa at the luminal side (fig. S12, E and F).

Examination of nearest-neighbor relationships between pigments revealed a number of possible energy transfer pathways from Lhcas to the PSI core (table S6), among which four appear to be most plausible; these were designated 1Bs, 1Fl, 2Js, and 3As/3Al (according to Lhca number, PSI core subunit, and stromal or luminal side) (Fig. 6 and table S6). The 1Bs pathway indicates possible energy transfer from the Chl dimer a603-a609 of Lhca1 to three Chls (a1218, a1219, and a1802) of PsAa at the stromal side, with the shortest edge-to-edge distance of 7.5 Å (Fig. 6, A and B). Chl a616 of Lhca1 may also guide energy to Chl a1701 of PsAa at the luminal side, providing the 1Fl pathway (Fig. 6, A and C). Because of the large gap between Lhca4 and the PSI core, a direct energy transfer from Lhca4 to the PSI core would be difficult, and Lhca4 may guide its energy to the PSI core via its red forms Chl a603-a609 through the 1Fl pathway. Chl a603 of Lhca2 is slightly distant to accomplish a direct energy transfer to Chl a1302 of PsAa (Fig. 6, A and D), which suggests that the 2Js pathway may not be highly efficient. The Chl trimer (a603-a609-a619) of Lhca3 is close to Chl a1108 and the a1110-a1118 dimer of PsAa at the stromal side, forming the 3As pathway (Fig. 6, A and E). Because of the strong coupling between Chl a1110-a1118, this pathway suggests energy transfer from red forms of Lhca3 to this Chl pair in the PSI core. At the luminal side, Chl a607 of Lhca3 is close to another Chl a1112-a1114 dimer of PsAa, providing the 3Al pathway (Fig. 6, A and E). In addition, Chls a613 and a614 of Lhca3 are close to Chl a1002 of PsAa (3Kl pathway), which may also facilitate energy transfer from Lhca3 to the PSI core.

## REFERENCES AND NOTES

- G. D. Scholes, G. R. Fleming, A. Olaya-Castro, R. van Grondelle, *Nat. Chem.* **3**, 763–774 (2011).
- N. Nelson, *J. Nanosci. Nanotechnol.* **9**, 1709–1713 (2009).
- P. Jordan et al., *Nature* **411**, 909–917 (2001).
- H. V. Scheller, P. E. Jensen, A. Haldrup, C. Lund, J. Knoetzel, *Biochim. Biophys. Acta* **1507**, 41–60 (2001).
- A. Ben-Shem, F. Frolov, N. Nelson, *Nature* **426**, 630–635 (2003).
- A. Amunts, O. Drory, N. Nelson, *Nature* **447**, 58–63 (2007).
- A. Amunts, H. Toporik, A. Borovikova, N. Nelson, *J. Biol. Chem.* **285**, 3478–3486 (2010).
- See supplementary materials on Science Online.
- W. Z. He, R. Malkin, *FEBS Lett.* **308**, 298–300 (1992).
- P. E. Jensen, A. Haldrup, S. Zhang, H. V. Scheller, *J. Biol. Chem.* **279**, 24212–24217 (2004).
- Z. Liu et al., *Nature* **428**, 287–292 (2004).
- X. Pan et al., *Nat. Struct. Mol. Biol.* **18**, 309–315 (2011).
- T. Y. Kuang, J. H. Argyroudi-Akoyunoglou, H. Y. Nakatani, J. Watson, C. J. Arritzen, *Arch. Biochem. Biophys.* **235**, 618–627 (1984).
- E. Lam, W. Ortiz, R. Malkin, *FEBS Lett.* **168**, 10–14 (1984).
- E. Wientjes, R. Croce, *Biochem. J.* **433**, 477–485 (2011).
- R. Croce, T. Morosinotto, S. Castelletti, J. Breton, R. Bassi, *Biochim. Biophys. Acta* **1556**, 29–40 (2002).
- S. Castelletti et al., *Biochemistry* **42**, 4226–4234 (2003).
- B. Gobets, R. van Grondelle, *Biochim. Biophys. Acta* **1507**, 80–99 (2001).

- T. Morosinotto, J. Breton, R. Bassi, R. Croce, *J. Biol. Chem.* **278**, 49223–49229 (2003).
- T. Morosinotto, M. Mozzo, R. Bassi, R. Croce, *J. Biol. Chem.* **280**, 20612–20619 (2005).
- R. Croce, H. van Amerongen, *Photosynth. Res.* **116**, 153–166 (2013).
- L. Fiedor, A. Kania, B. Myśliwa-Kurczel, Ł. Orzeł, G. Stochel, *Biochim. Biophys. Acta* **1777**, 1491–1500 (2008).
- T. Morosinotto, M. Ballottari, F. Klimmek, S. Jansson, R. Bassi, *J. Biol. Chem.* **280**, 31050–31058 (2005).
- V. H. R. Schmid et al., *J. Biol. Chem.* **277**, 37307–37314 (2002).
- X. Qin et al., *Photosynth. Res.* **90**, 195–204 (2006).
- A. V. Ruban et al., *Nature* **450**, 575–578 (2007).
- M. Mozzo, F. Passarini, R. Bassi, H. van Amerongen, R. Croce, *Biochim. Biophys. Acta* **1777**, 1263–1267 (2008).
- B. Demmig, K. Winter, A. Krüger, F. C. Czygan, *Plant Physiol.* **84**, 218–224 (1987).
- A. M. Gilmore, H. Y. Yamamoto, *Plant Physiol.* **96**, 635–643 (1991).
- K. K. Niyogi, A. R. Grossman, O. Björkman, *Plant Cell* **10**, 1121–1134 (1998).
- A. Wehner, S. Storf, P. Jahns, V. H. R. Schmid, *J. Biol. Chem.* **279**, 26823–26829 (2004).
- T. Morosinotto, S. Caffarri, L. Dall'Osto, R. Bassi, *Physiol. Plant.* **119**, 347–354 (2003).
- M. Ballottari et al., *Proc. Natl. Acad. Sci. U.S.A.* **111**, E2431–E2438 (2014).
- R. Kouřil et al., *Biochemistry* **44**, 10935–10940 (2005).
- S. Kjaerulf, B. Andersen, V. S. Nielsen, B. L. Møller, J. S. Okkels, *J. Biol. Chem.* **268**, 18912–18916 (1993).
- S. Jansson, B. Andersen, H. V. Scheller, *Plant Physiol.* **112**, 409–420 (1996).
- H. Naver, A. Haldrup, H. V. Scheller, *J. Biol. Chem.* **274**, 10784–10789 (1999).
- N. Nelson, C. F. Yocum, *Annu. Rev. Plant Biol.* **57**, 521–565 (2006).

## ACKNOWLEDGMENTS

We thank C. Lu, W. Wang, and G. Han for discussions and help during sample preparation and K. Wang and C. Yang for HPLC analysis. X-ray data were collected at beamlines BL41XU and BL44XU of SPring-8, Japan, and we thank the staff members of these beamlines for their extensive support. This work was supported by National Basic Research Program of China grants 2011CBA00901 and 2015CB150101, Chinese Academy of Sciences grant KGZD-EW-T05, and JSPS KAKENHI grants 24000018 (J.-R.S.) and 26840023 (M.S.) from MEXT, Japan. The atomic coordinates have been deposited in the Protein Data Bank with accession code 4XK8. Author contributions: T.K. and J.-R.S. conceived the project; X.Q. prepared the sample and made the crystals; M.S. and X.Q. conducted the diffraction experiments; M.S. analyzed the structure; X.Q., M.S., and J.-R.S. wrote the manuscript; and all authors discussed and commented on the results and the manuscript.

## SUPPLEMENTARY MATERIALS

www.sciencemag.org/content/348/6238/989/suppl/DC1  
Materials and Methods  
Figs. S1 to S12  
Tables S1 to S6  
References (39–45)

1 March 2015; accepted 28 April 2015  
10.1126/science.aab0214

## T CELL METABOLISM

# The protein LEM promotes CD8<sup>+</sup> T cell immunity through effects on mitochondrial respiration

Isobel Okoye,<sup>1,\*</sup> Lihui Wang,<sup>1,\*</sup> Katharina Pallmer,<sup>2,†</sup> Kirsten Richter,<sup>2,†</sup> Takaharu Ichimura,<sup>3</sup> Robert Haas,<sup>4</sup> Josh Crouse,<sup>2</sup> Onjee Choi,<sup>1</sup> Dean Heathcote,<sup>1</sup> Elena Lovo,<sup>1</sup> Claudio Mauro,<sup>4</sup> Reza Abdi,<sup>3</sup> Annette Oxenius,<sup>2</sup> Sophie Rutschmann,<sup>1,‡</sup> Philip G. Ashton-Rickardt<sup>1,§</sup>

Protective CD8<sup>+</sup> T cell-mediated immunity requires a massive expansion in cell number and the development of long-lived memory cells. Using forward genetics in mice, we identified an orphan protein named lymphocyte expansion molecule (LEM) that promoted antigen-dependent CD8<sup>+</sup> T cell proliferation, effector function, and memory cell generation in response to infection with lymphocytic choriomeningitis virus. Generation of LEM-deficient mice confirmed these results. Through interaction with CR6 interacting factor (CRIF1), LEM controlled the levels of oxidative phosphorylation (OXPHOS) complexes and respiration, resulting in the production of pro-proliferative mitochondrial reactive oxygen species (mROS). LEM provides a link between immune activation and the expansion of protective CD8<sup>+</sup> T cells driven by OXPHOS and represents a pathway for the restoration of long-term protective immunity based on metabolically modified cytotoxic CD8<sup>+</sup> T cells.

Cytotoxic CD8<sup>+</sup> T cells (CTLs) are a central arm of the immune system responsible for protection from intracellular viruses and cancer because they kill infected or transformed cells (1). Because chronic virus infection (2) and cancer (3) are widespread diseases, it is clear that CTL immunity often fails. A major reason for this failure is that high viral (4, 5) or tumor (6–8) load results in either deletion or functional inactivation (known as immune exhaustion) of CTLs. The result is failure in both short-term CTL immunity and immunological memory because memory CD8 T cell develop-

ment is blocked (9). Impaired expansion is an important cause of deletion and immune exhaustion and results in failure to produce sufficient numbers of protective CTLs and memory cells (5).

## Retro mutant mice have increased immunity to chronic viral infection

Infection of wild-type C57BL/6 mice with the clone 13 variant of lymphocytic choriomeningitis virus (LCMV C13) is an established model for human chronic viral infection resulting in a massive viral load that causes both deletion and immune

exhaustion of CTLs and a block in memory CD8 T cell development (10).

We examined the CTL response to LCMV C13 infection after germline mutagenesis to identify

mutants with enhanced immunity. To this end, 430 third-generation (G3) ethyl-N-nitrosourea (ENU)-induced germline mutants were produced in a C57BL/6J background (11). G3 mice were infected with LCMV C13, and after 8 days the level of LCMV-specific CD8 T cells was measured in the spleen by staining with a tetramer for the np396 LCMV peptide and by flow cytometry (12). Three independent germline transmissible modifications, which resulted in increased levels of LCMV-specific CD8 T cells, were isolated, of which one (a semidominant) was bred to homozygosity (fig. S1A). We named this strain *Retro*.

Homozygous *Retro* mutant mice showed a 10-fold increase in CD8 T cells specific for LCMV np396 peptide compared with wild-type (WT) and a smaller but significant increase in the number of CTLs specific for the gp33-LCMV peptide (Fig. 1, A and B). Compared with WT mice, a

smaller percentage of *Retro* mutant CTLs expressed the programmed cell death-1 (PD-1) immune exhaustion marker (5) (Fig. 1C). However, *Retro* mutant mice still harbored increased numbers of PD-1<sup>+</sup> np396<sup>+</sup> CD8<sup>+</sup> cells compared with WT (Fig. 1D). In addition, *Retro* mutant CTLs exhibited increased functionality: There was increased CTL activity in ex vivo killing experiments (Fig. 1E), increased exocytosis of cytotoxic granules (17) (Fig. 1F), and increased production of the cytokine interferon (IFN)- $\gamma$  (fig. S1B). The increase in CTL immunity resulted in a 10<sup>6</sup>-fold decrease in LCMV C13 titer in the spleens of *Retro* mutant mice on day 8 after infection compared with WT (Fig. 1G). The increase in CTL activity was a function of cell number (fig. S1C).

All *Retro* mutant mice succumbed to LCMV C13 infection after 14 days, whereas all WT mice had survived (Fig. 1H). *Retro* mutant death is

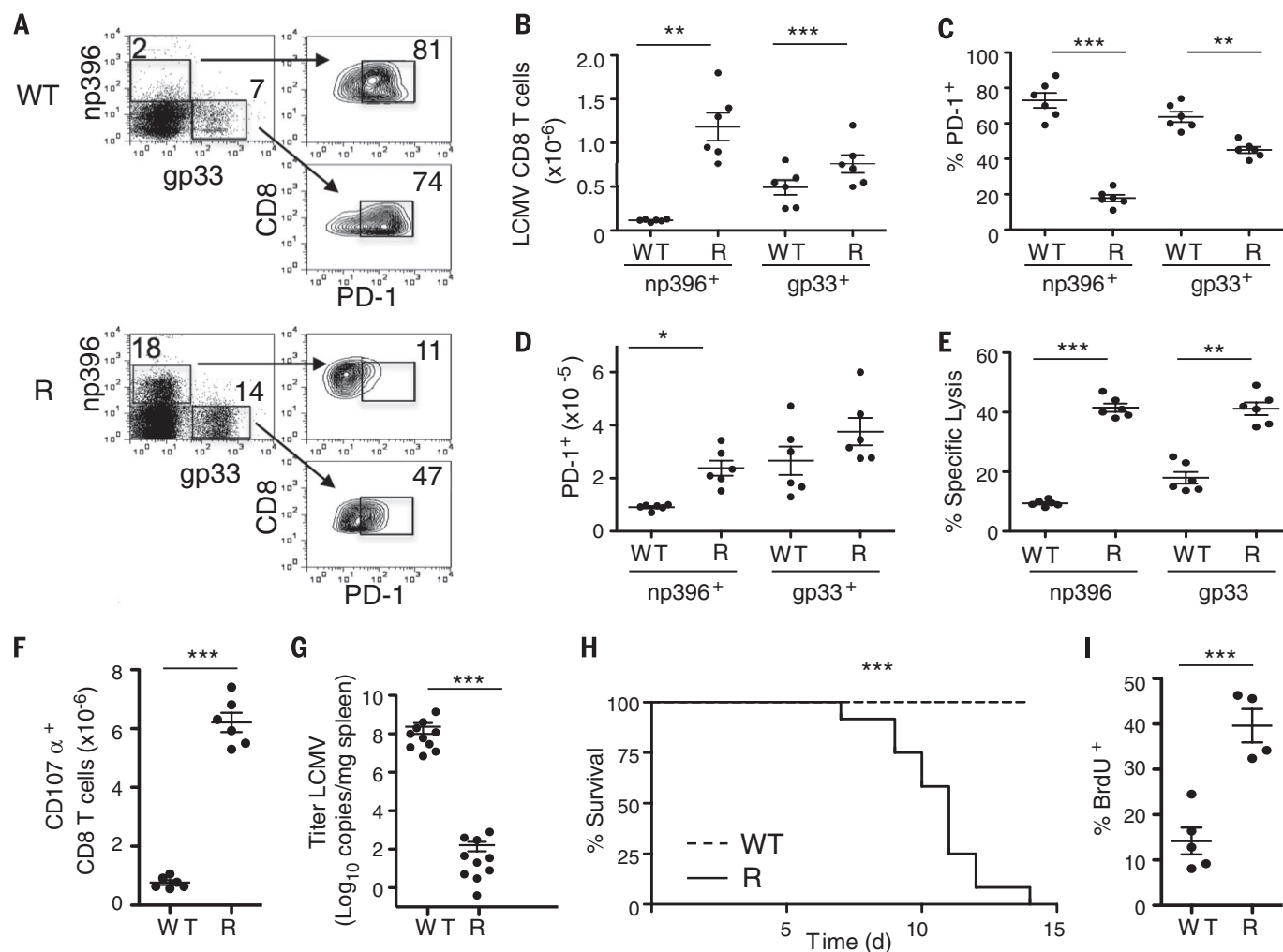


**Fig. 1. *Retro* mutant mice exhibit enhanced CD8 T cell responses to chronic LCMV infection.** (A) Flow cytometry on spleen cells from day 8 post infection (p.i.) with LCMV C13 of WT and *Retro* homozygous mutant (R) mice. Staining with tetramers, refolded with either np396 or gp33 peptides, and PD-1 is shown (percentage next to gate) on CD8<sup>+</sup> gated cells. (B) Number of tetramer<sup>+</sup> CD8<sup>+</sup> splenocytes on day 8 p.i. (C) Percentage of PD-1<sup>+</sup> of tetramer<sup>+</sup> CD8<sup>+</sup> splenocytes on day 8 p.i. (D) Number of PD-1<sup>+</sup> tetramer<sup>+</sup> CD8<sup>+</sup> splenocytes on day 8 p.i. (E) Percentage of specific CTL lysis from Cr<sup>51</sup>-

release assays for splenocytes on day 8 p.i. (F) Number of CD107a<sup>+</sup> CD8<sup>+</sup> splenocytes on day 8 p.i. (G) Titer of LCMV C13 in the spleen on day 8 p.i. (H) Kaplan-Meier survival graph after LCMV C13 infection. (I) Percentage of BrdU<sup>+</sup> of np396<sup>+</sup> CD8<sup>+</sup> splenocytes on day 8 p.i. Mean  $\pm$  SEM;  $N = 6$  to 12 mice. \*\*\* $P < 0.0001$ ; \*\* $P < 0.0005$ ; \* $P < 0.001$ . Two-tailed Student's  $t$  tests were used for all, except that Gehan-Breslow-Wilcoxon tests were used for survival curves. Each data set is representative of at least three individual experiments.



presumably a consequence of elevated CTL-mediated cytotoxicity resulting in the fatal loss of vascular integrity (13). Despite an increase in activated phenotype T cells (fig. S2), viability, blood development, and autoimmunity in *Retro* mutant mice was normal (fig. S3 and tables S1 to S3). In vivo bromodeoxyuridine (BrdU) labeling indicated that np396<sup>+</sup> CD8<sup>+</sup> cells underwent increased proliferation after LCMV C13 infection of

*Retro* mutant mice (Fig. 1I). The increased number of antigen-specific CD8 T cells in LCMV C13-infected *Retro* mutant mice is likely due to increased proliferation of these cells.

Adoptive transfer of *Retro* mutant CD8 T cells (14) showed that the phenotype of increased CTL immunity resides in the CD8 T cell compartment (fig. S4, A to D). The phenotype of *Retro* mutant mice also extended to antitumor responses. After chal-

lenge with B16 F10 melanoma cells, *Retro* mutant mice harbored three times as many CTLs (Fig. 2A) and one-fourth as many tumors (Fig. 2, B and C).

### *Retro* mutant mice have increased memory T cell development

After acute infection of *Retro* mutant mice with LCMV Armstrong, there was an increase in the clonal burst size of both np396<sup>+</sup> CD8<sup>+</sup> and gp33<sup>+</sup>

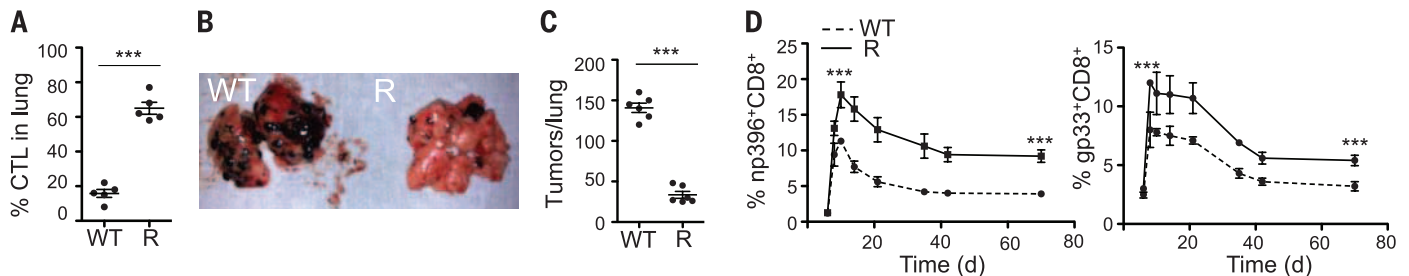


**Fig. 2. *Retro* improves immunity against tumors and acute viral infections.** Mice were injected intravenously with B16 F10 melanoma cells. (A) Percentage of CD3<sup>+</sup> CD8<sup>+</sup> CD44<sup>hi</sup> cells from lungs, day 35 p.i. (B) Foci of melanomas in the lung on day 35 p.i. (C) Number of melanomas per lung on day 35 p.i. Mice were infected with LCMV Armstrong. (D) Mean percentage of (left) np396<sup>+</sup> and (right) gp33<sup>+</sup> CD8<sup>+</sup> peripheral blood leukocytes (PBL). Mean  $\pm$  SEM;  $N = 6$  to 10 mice; \*\*\* $P < 0.0001$ . Two-tailed Student's  $t$  tests were used for all. Each data set is representative of at least three individual experiments.

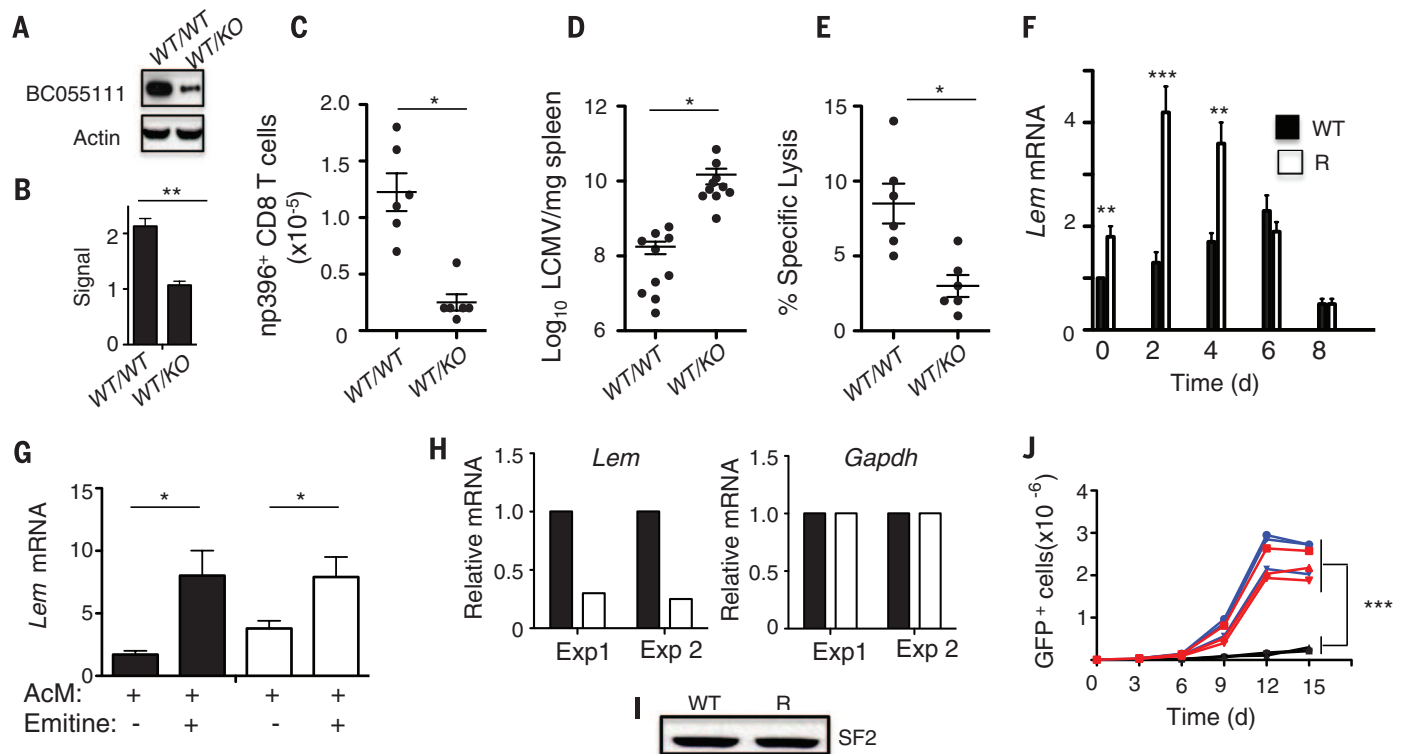


**Fig. 3. *Retro* mutation identifies LEM.** BC055111<sup>WT/WT</sup> and BC055111<sup>WT/KO</sup> mice were infected with LCMV C13. (A) Western blot on CTLs for BC055111 (49 kD) on total CD8 T cells from the spleen on day 4 p.i. (B) Bar graph of BC055111 signal strength from (A). BC055111<sup>WT/WT</sup> and BC055111<sup>WT/KO</sup> mice were infected with LCMV C13. (C) Number of np396<sup>+</sup> CD8<sup>+</sup> splenocytes on day 8 p.i. (D) LCMV titer in the spleen on day 8 p.i. (E) Percentage of specific CTL lysis from Cr<sup>51</sup>-release assays for splenocytes on day 8 p.i. (F) Bar graph for mean *Lem* mRNA in total CD8 T cells from the spleens of WT or R mice after infection with LCMV C13. Level of mRNA normalized to the  $t = 0$  WT level. (G) Bar graphs for mean *Lem* mRNA in CD8 T cells cultured for 3 days in cytokines, then incubated with actinomycin D or emitine. Level of mRNA

normalized to the  $t = 0$  WT level. [(A) to (G)] Mean  $\pm$  SEM;  $N = 6$  mice. Each data set is representative of at least three individual experiments. (H) Bar graphs for mean relative *Lem* or *Gapdh* mRNA from two independent immunoprecipitation experiments performed on  $N = 2$  mice each time. mRNA levels are relative to WT and are from CD8 T cells cultured for 3 days in cytokines. (I) Western blot for SF2 (27 kD) after immunoprecipitation in (H). (J) Mean number of green fluorescent protein-positive (GFP<sup>+</sup>) CTLL-2 cells cultured in IL-2 ( $N = 4$  wells) from three independent transductions with MIGR1 alone (V-black), or MIGR1 encoded *Lem* ORF (WT, blue sequence; R, red sequence). \*\*\* $P < 0.005$ ; \*\* $P < 0.01$ ; \* $P < 0.05$ . Two-tailed Student's  $t$  tests were used.

CD8<sup>+</sup> cells (Fig. 2D) compared with WT. Longitudinal analysis in the blood revealed a corresponding increase in the number of LCMV-specific CD8 T cells during the memory phase in *Retro* mutant mice (15). After 70 days, there was a fourfold increase in the number of LCMV-specific central memory T CD8 cells (Tcm) in the spleen as identified by the CD62L<sup>+</sup> CD127<sup>+</sup> CD8<sup>+</sup> cell surface phenotype (16) (fig. S4, E and F).

We boosted mice with a second dose of LCMV Armstrong and measured the expansion of secondary CTLs during the memory response. The numbers of secondary CTLs were about 10 times as high compared with WT (fig. S4, G and H), indicating that *Retro* mutant mice have an enhanced memory phenotype. During acute immune responses the pool of CTLs contains not only short-lived effectors but also memory cell precursors (17, 18). The increase in the total number of CD8 T cells resulted in an increase in the number and percentage of both memory cell precursors and short-lived effectors in *Retro* mutants compared with WT (fig. S5). Therefore, the *Retro* mutation increases the level of both primary short-lived effectors and Tcm by facilitating a global increase in the expansion of antigen-activated CD8 T cells.

### The *Retro* mutation identifies lymphocyte expansion molecule

We used high-throughput exome sequencing (19) to identify the *Retro* mutation. Comparison with the reference C57BL/6J genome identified several homozygous single-nucleotide variants (SNV) in homozygous *Retro* mutant mice (fig. S6A). Upon re-sequencing and comparison with the Charles River substrain of C57BL/6J used for our ENU mutagenesis, four homozygous SNVs were identified as being associated with *Retro* homozygous mutant

mice. Only one homozygous SNV correlated with the *Retro* homozygous phenotype (fig. S6B). This was an A to G transition of nucleotide 1304 (A1304G) in exon 2 of the *BC055111* gene on chromosome 4 (fig. S7A). *BC055111* encodes an orphan protein with no substantial homology to any other mouse protein (BLASTP, *E* value > 0.38). The *BC055111<sup>Retro</sup>* allele (R) was semidominant for increased CTL immunity to LCMV C13 (fig. S7, B to D).

We generated C57BL/6 mice with a *BC055111* knock-out (KO) allele (20) (fig. S8). Homozygosity for the *BC055111* KO allele results in embryonic lethality, so we used heterozygous KO mice to validate the gene candidate (12). There was decreased *BC055111*-encoded protein in CTLs from heterozygous *BC055111* KO mice compared with WT (Fig. 3, A and B). We observed decreased np396<sup>+</sup> CD8<sup>+</sup> expansion (Fig. 3C), increased LCMV titer (Fig. 3D) and decreased CTL activity (Fig. 3E) in *BC055111<sup>WT/KO</sup>* compared with *BC055111<sup>WT/WT</sup>* mice. Therefore, *BC055111* directly controls CTL immunity to LCMV. We named the *BC055111* encoded orphan protein “lymphocyte expansion molecule” (LEM).

### The *Retro* mutation stabilizes *Lem* mRNA

The kinetics of *Lem* mRNA accumulation in *Retro* mutant CD8 T cells after LCMV C13 infection was increased compared with WT (Fig. 3F). The increased level of *Lem* mRNA was also observed when transcription was inhibited by actinomycin D, indicating that the *Retro* mutation stabilized *Lem* mRNA in CD8 T cells (Fig. 3G).

*Lem* mRNA contains introns in the 3' untranslated region (3'UTR), which may make it susceptible to nonsense-mediated decay (NMD) (21). This was confirmed when blockade of NMD by emetine increased the stability of wild-type

*Lem* mRNA (Fig. 3G). The *Retro* mutation is predicted to abolish an alternative splice factor/splice factor 2 (ASF/SF2) binding site in *Lem* (12), which is thought to be required for NMD (22). Immunoprecipitation (IP) confirmed decreased levels of SF2 associated with *Retro* mutant *Lem* message (Fig. 3H) in cells with normal SF2 levels (Fig. 3I). This suggests that the A1304G mutation in *Retro* mutant mice partially protects *Lem* mRNA from NMD, resulting in stabilization. The *Lem* open reading frame (ORF) harboring the *Retro* A1304G mutation was no better than WT ORF at driving interleukin-2 (IL-2)-induced proliferation of T cells (fig. S9 and Fig. 3J). Therefore, the increased expression of *Lem* rather than any qualitative alteration in protein activity is responsible for the phenotype of *Retro* mutant mice. We conclude that WT LEM is a positive modulator of CTL expansion that is up-regulated in *Retro* mutant mice.

### The *Retro* mutation increases LEM expression

LEM protein was up-regulated in total CD8 T cells after LCMV C13 infection with *Retro* mutant mice displaying increased kinetics compared with WT (Fig. 4, A and B). Intracellular staining (fig. S10) indicated that LEM expression was specific for activated CD8 T cells (CD44<sup>hi</sup> CD62L<sup>lo</sup> CD8<sup>+</sup>) and was elevated in *Retro* mutant cells (Fig. 4, C and D). LEM was up-regulated 2 days after LCMV C13 infection despite a low frequency of CD8 cells expressing LCMV-specific T cell receptors (TCRs) (fig. S11A and Fig. 4, A and C). In addition to stimulation through the TCR (via antibody to CD3) (Fig. 4E), treatment with either IL-2 (Fig. 4F) or IL-15 (Fig. 4G) resulted in LEM up-regulation, which was enhanced in

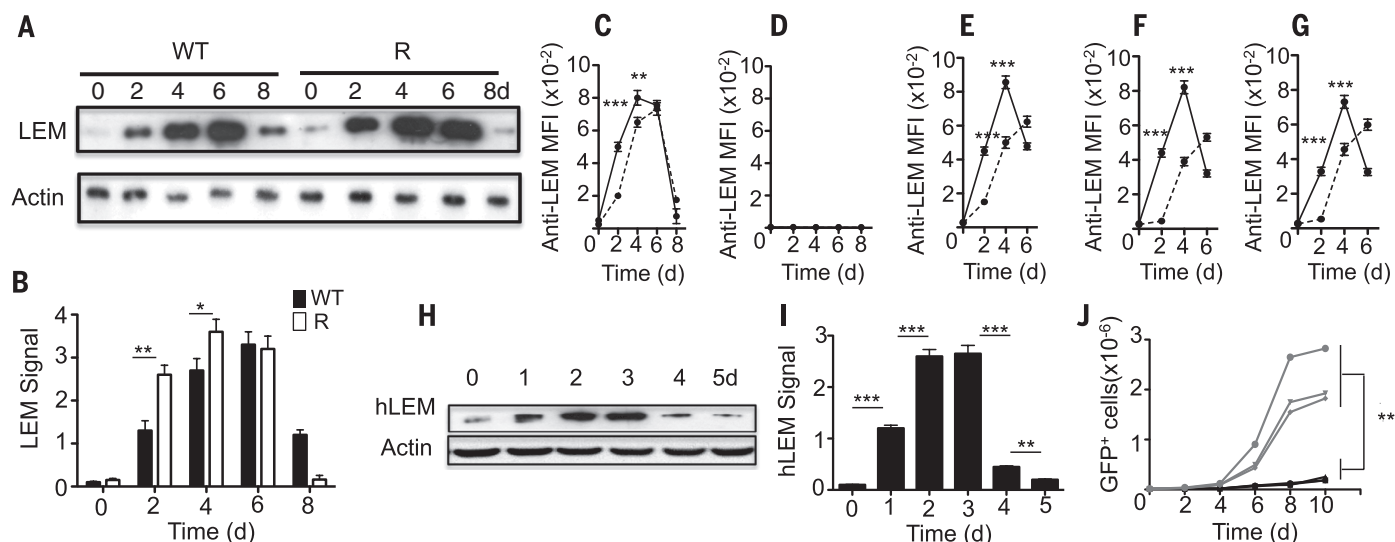


**Fig. 4. The *Retro* mutation increases LEM expression.** Mice were infected with LCMV C13. (A) Western blots for LEM (49 kD) on total CD8 T cells from the spleen. (B) Bar graph of signal strength from (A). (C to G) Mean fluorescence intensity (MFI) after staining with antibody to LEM in gated (C) CD44<sup>hi</sup> CD62L<sup>lo</sup> CD8<sup>+</sup> or (D) CD44<sup>lo</sup> CD62L<sup>hi</sup> CD8<sup>+</sup> splenocytes after infection with LCMV C13, or on total CD8 T cells that were activated in vitro with either (E) antibody to CD3/CD28, (F) IL-2, or (G) IL-15. [(A) to (G)] Mean

± SEM; N = 6 mice. (H) Western blots for human LEM, 49 kD on antibody to CD3/CD28-activated human CD8 T cells. (I) Bar graph of signal strength from (H). (J) Mean number of GFP<sup>+</sup> human CD8 T cell blasts (N = 4 wells) after three independent transductions with MIGR1 alone (V-black), or MIGR1 encoded *hLEM* ORF (gray). \*\*\**P* < 0.0001; \*\**P* < 0.0005; \**P* < 0.001. Two-tailed Student's *t* tests were used. Each data set is representative of at least three individual experiments.



*Retro* mutant CD8 T cells (Fig. 4, E to G). Therefore, LEM expression can be induced by bystander activation by pro-proliferative cytokines

as well as antigen-dependent TCR signals. The level of LEM controlled the levels of *Retro* mutant CD8 T cells both in vivo (fig. S11, B to E)

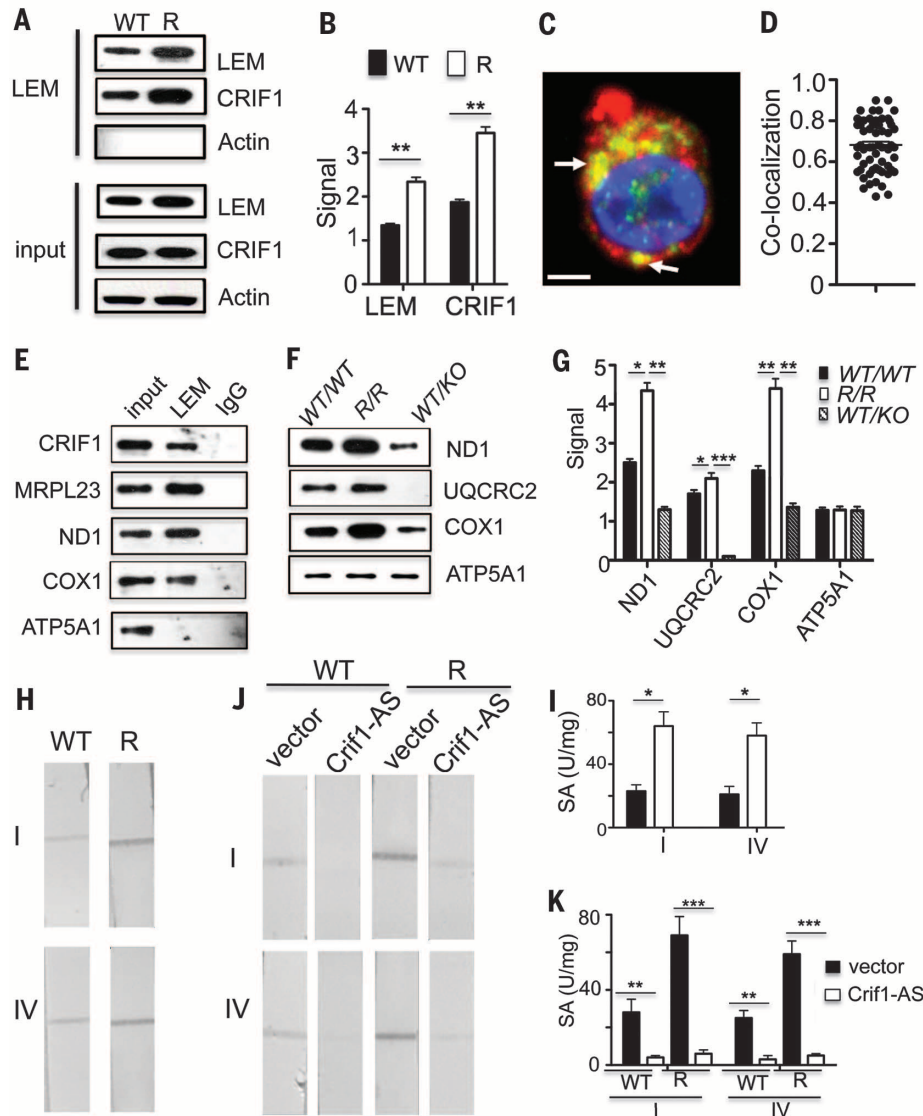


**Fig. 5. LEM interacts with CRIF1 to control the activity of OXPHOS proteins.** WT and R mice were infected with LCMV C13, and on day 4 p.i. total CD8 T cells were purified. **(A)** Western blots directly on cell extracts (input) or after immunoprecipitation for LEM (LEM, 49 kD; CRIF1, 25 kD;  $\beta$  actin, 42 kD). **(B)** Bar graph of signal strengths from (A). **(C)** CIM from staining with antibodies against LEM (red) or CRIF1 (green). Nuclei stained with 4',6-diamidino-2-phenylindole (blue). Examples of colocalization (yellow) are indicated by arrows. Scale bar, 2.5  $\mu$ m. **(D)** Colocalization of LEM and CRIF1 as measured by Pearson's correlation coefficient in multiple optical cell slices ( $N = 62$ ). Mean =  $0.68 \pm 0.11$ . WT mice were infected with LCMV C13, and on day 4 p.i. total CD8 T cells were purified. **(E)** Western blots directly on cell extracts (input) or after immunoprecipitation with LEM antibody or with control rabbit immunoglobulin G (MRPL23, 18 kD; ND1, 36 kD; COX1, 57 kD; ATP5A1, 60 kD). *Lem*<sup>WT/WT</sup>, *Lem*<sup>R/R</sup>, or *Lem*<sup>WT/KO</sup> mice were infected with LCMV C13, and on day 4 p.i. total CD8 T cells were purified. **(F)** Western blots for OXPHOS proteins (UQCRC2, 49 kD). **(G)** Bar graph of signal strength from (F). WT and R mice were infected with LCMV C13, and on day 4 p.i. total CD8 T cells were purified. **(H)** Immunocapture-enzyme assays for OXPHOS complexes I and IV. **(I)** Bar graphs for mean specific activity (signal strength per mg protein) from (H). Donor CD8 T cells harboring vector alone or Crif1-AS were purified from WT recipient mice on day 4 p.i. with LCMV C13. **(J)** Immunocapture-enzyme assays for OXPHOS complexes I and IV. **(K)** Bar graphs for mean specific activity from (J). Mean  $\pm$  SEM;  $N = 6$  mice. \*\*\* $P < 0.005$ ; \*\* $P < 0.01$ ; \* $P < 0.05$ . Two-tailed Student's  $t$  tests were used. Each data set is representative of at least three individual experiments.

and in vitro (fig. S12). PD-1 up-regulation by *Retro* mutant CTLs was unaffected in vitro after TCR stimulation, suggesting that LEM does not directly down-regulate PD-1 expression (fig. S11, F and G).

### Functional equivalence of human LEM

*C10orf177* encodes the human homolog of LEM (BLASTP, 72% of complete amino acid identity with mouse LEM;  $E$  value = 0), which is up-regulated in activated human CD8 T cells (Fig. 4, H and I). Ectopic expression of human LEM resulted in about a 15-fold increase in the expansion (Fig. 4J). Therefore, LEM can modulate CD8 T cell expansion in man as well as mice.

### LEM interacts with CRIF1 to control the activity of OXPHOS proteins

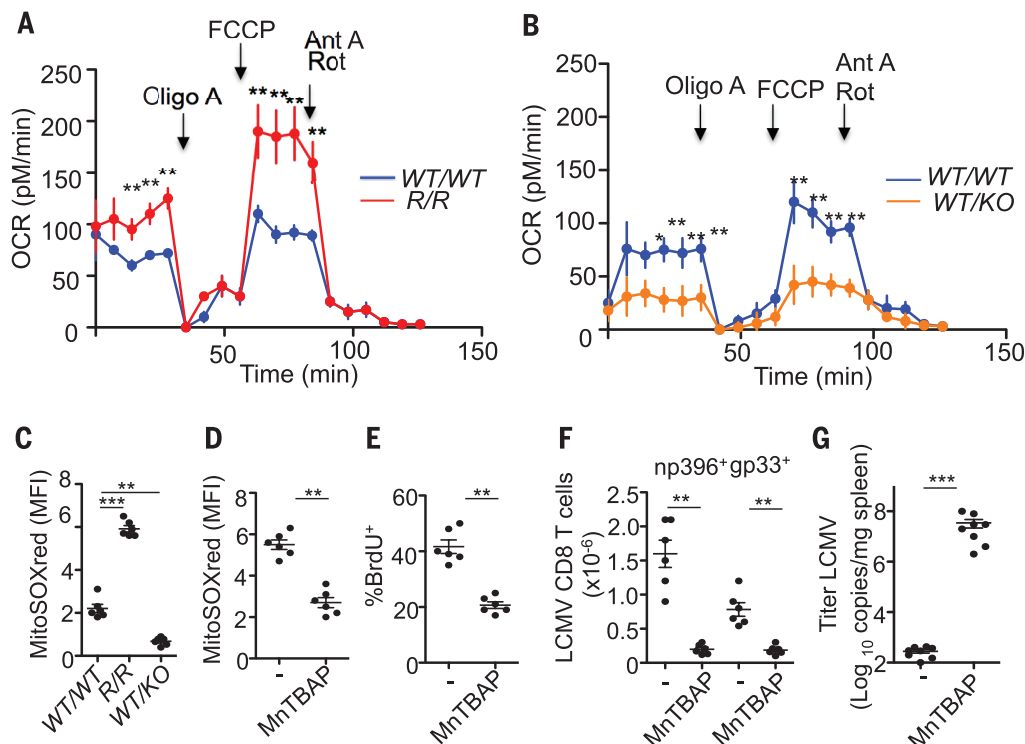
Analysis of LEM amino acid sequence predicts the presence of at least two intrinsically unstructured (IU) protein domains (12, 23). Therefore, we investigated whether LEM modulates CD8 T cell proliferation through specific protein: protein interactions. Yeast two-hybrid (Y2H) analysis identified nine different LEM-interacting proteins (24) (fig. S13). Coimmunoprecipitation (co-IP) with antibody to LEM (fig. S10) demonstrated that one target—CR6 interacting factor (CRIF1)—interacts with LEM in CTLs (Fig. 5, A and B).

CRIF1 is required for the translation and insertion of oxidative phosphorylation (OXPHOS) polypeptides into the inner membrane of mitochondria after they emerge from the 39S subunit of the mitoribosomes (25). Confocal immunofluorescence microscopy (CIM) revealed that LEM colocalizes with CRIF1 in CTLs (Fig. 5, C and D, and fig. S14). Both LEM and CRIF1 were localized to mitochondria by costaining with the mitoracker red dye (figs. S15 and S16). Co-IP localized LEM to the mitoribosome by revealing an association with the 39S subunit protein MRPL23 and several OXPHOS proteins such as NADH ubiquinone oxidoreductase chain 1 (ND1), ubiquinol cytochrome c oxidoreductase chain 2 (UQCRC2), and cytochrome c oxidoreductase chain 1 (COX1) (25) (Fig. 5E). The OXPHOS protein adenosine triphosphate (ATP) synthase  $\alpha$  subunit 1 (ATP5A1) does not require CRIF1 for translation and did not coimmunoprecipitate, suggesting that interaction of LEM with OXPHOS proteins is via CRIF1. Through its interaction with CRIF1, LEM is part of a complex that mediates the translation and insertion of OXPHOS proteins into the mitochondrial inner membrane.

*Retro* mutant CTLs harbored increased levels, and heterozygous LEM KO CTLs reduced levels of OXPHOS proteins (Fig. 5, F and G). Immunocapture confirmed that the specific activities of OXPHOS complexes were elevated in *Retro* mutant CTLs (Fig. 5, H and I), although LEM did not affect the expression of *Oxphos* genes or the number or mass of mitochondria (fig. S17, A to C). Therefore, LEM controlled the activity of OXPHOS complexes by most likely facilitating the production of subunit proteins.

As was observed in CRIF1 KO cells (25), when we knocked down *Crif1* mRNA (fig. S18, A to C),

**Fig. 6. LEM controls production of mitogenic mROS.** *Lem*<sup>WT/WT</sup>, *Lem*<sup>R/R</sup>, or *Lem*<sup>WT/KO</sup> mice were infected with LCMV C13, and on day 4 p.i. total CD8 T cells were purified from the spleen. (A and B) Oxygen consumption rate (OCR) after sequential injection of oligomycin, FCCP, and antimycin A/rotenone. (C) *Lem*<sup>WT/WT</sup>, *Lem*<sup>R/R</sup>, or *Lem*<sup>WT/KO</sup> mice were infected with LCMV C13, then on day 8 p.i. np 396<sup>+</sup> CD8<sup>+</sup> splenocytes were gated, then the MFI of MitoSOX red staining was determined. R mice were infected with LCMV C13, then over the course of 8 days were injected with MntBAP or not. Gated np 396<sup>+</sup> CD8<sup>+</sup> splenocytes were examined on day 8 p.i. for (D) MitoSOX red staining and (E) % BrdU-positive cells. In the same spleens: (F) Number of tetramer-positive cells and (G) Titer of LCMV. Mean ± SEM. For (A) to (F), *N* = 6 mice, and for (G), *N* = 9 mice. \*\*\**P* < 0.001; \*\**P* < 0.005; \**P* < 0.01. Two-tailed Student's *t* tests were used. Each data set is representative of at least three individual experiments.



OXPHOS-specific activity was reduced (Fig. 5, J and K). Knock-down of *Crif1* message in *Retro* mutant CTLs also abolished the increases in OXPHOS activity due to LEM up-regulation. We conclude that LEM interaction with CRIF1 within mitochondria determines OXPHOS activity.

CRIF1 is required for cell proliferation during embryo development (26). *Crif1* message knock-down resulted in the impaired proliferation and expansion of anti-LCMV CTLs (fig. S18, D and E). The increase in CTL expansion caused by LEM up-regulation required CRIF1 expression because *Crif1* message knock-down diminished the increased expansion of *Retro* mutant CTLs. We conclude that LEM requires interaction with CRIF1 to drive the expansion of CTLs.

### LEM is a positive modulator of mitochondrial ROS-driven proliferation

We examined the consequences of LEM control of OXPHOS activity on CTL metabolism and expansion. Oxygen consumption studies demonstrated that *Retro* mutant CTLs had significantly higher respiratory levels compared with WT (Fig. 6A) (27), but glycolysis was not increased (fig. S17D). Conversely, respiratory activity (Fig. 6B) of LEM heterozygous KO CTLs, but not glycolysis (fig. S17E), was decreased.

OXPHOS results in the production of ROS through stepwise reduction of O<sub>2</sub> (27). The modulation of OXPHOS by LEM resulted in altered production of mROS. Staining with the redox-sensitive dye MitoSOX red revealed that compared with WT, *Retro* mutant CTLs had increased levels of mROS and LEM heterozygous KO CTLs had decreased mROS (Fig. 6C). The production

of mROS is required for the activation and expansion of T lymphocytes (27). Injection of *Retro* mutant mice with the antioxidant MntBAP (28) reduced the level of mROS in CTLs (Fig. 6D), resulting in decreased proliferation (Fig. 6E) and expansion of CTLs (Fig. 6F) with a corresponding increase in LCMV C13 titer (Fig. 6G). We conclude that mROS resulting from OXPHOS activity drives expansion and CTL immunity in *Retro* mutant mice.

We have used unbiased forward genetics to discover LEM at the heart of a pathway that, when up-regulated, not only restores CTL immunity to chronic viral infection and tumor challenge but also increases memory cell development. Although other molecular interventions either restore primary CTL immunity (5) or divert development toward the memory lineage (29), the LEM pathway is important because it controls the expansion of both short-term effectors and memory cells (9). Up-regulation of LEM in *Retro* mutant mice increased both the overall number of CTLs and also the number of PD-1<sup>+</sup> CTLs. Therefore, LEM therapy has the potential both to globally expand CTLs and to increase the number of PD-1<sup>+</sup> CTLs available for derepression by antibodies to PD-1 (8).

At the peptide tunnel exit of 39S mitoribosomes, LEM is likely recruited by CRIF1 to facilitate the insertion of OXPHOS polypeptides into the inner mitochondrial membrane, thereby controlling OXPHOS activity (25) (fig. S19). We propose that CTL expansion and memory cell development are controlled by mROS produced after the up-regulation of LEM upon immune activation (27, 30)

### REFERENCES AND NOTES

1. J. H. Russell, T. J. Ley, *Annu. Rev. Immunol.* **20**, 323–370 (2002).
2. B. Autran, G. Carcelain, B. Combadiere, P. Debre, *Science* **305**, 205–208 (2004).
3. D. Pardoll, *Proc. Natl. Acad. Sci. U.S.A.* **99**, 15840–15842 (2002).
4. C. L. Day et al., *Nature* **443**, 350–354 (2006).
5. D. L. Barber et al., *Nature* **439**, 682–687 (2006).
6. M. A. Curran, W. Montalvo, H. Yagita, J. P. Allison, *Proc. Natl. Acad. Sci. U.S.A.* **107**, 4275–4280 (2010).
7. P. Georgel, X. Du, K. Hoebe, B. Beutler, *Methods Mol. Biol.* **415**, 1–16 (2008).
8. S. L. Topalian et al., *N. Engl. J. Med.* **366**, 2443–2454 (2012).
9. M. A. Williams, M. J. Bevan, *Annu. Rev. Immunol.* **25**, 171–192 (2007).
10. S. N. Mueller, R. Ahmed, *Proc. Natl. Acad. Sci. U.S.A.* **106**, 8623–8628 (2009).
11. O. Choi et al., *J. Immunol.* **188**, 3920–3927 (2012).
12. Materials and methods are available as supplementary materials on Science Online.
13. H. Frebel et al., *J. Exp. Med.* **209**, 2485–2499 (2012).
14. A. H. Rahman et al., *J. Immunol.* **181**, 3804–3810 (2008).
15. L. L. Lau, B. D. Jamieson, T. Somasundaram, R. Ahmed, *Nature* **369**, 648–652 (1994).
16. S. M. Byrne et al., *J. Immunol.* **189**, 1133–1143 (2012).
17. J. T. Opferman, B. T. Ober, P. G. Ashton-Rickardt, *Science* **283**, 1745–1748 (1999).
18. N. S. Joshi et al., *Immunity* **27**, 281–295 (2007).
19. H. Fairfield et al., *Genome Biol.* **12**, R86 (2011).
20. W. C. Skarnes et al., *Nature* **474**, 337–342 (2011).
21. I. Ivanov, K. C. Lo, L. Hawthorn, J. K. Cowell, Y. Ionov, *Oncogene* **26**, 2873–2884 (2007).
22. H. Sato, N. Hosoda, L. E. Maquat, *Mol. Cell* **29**, 255–262 (2008).
23. H. J. Dyson, P. E. Wright, *Nat. Rev. Mol. Cell Biol.* **6**, 197–208 (2005).
24. C. W. Xu, A. R. Mendelsohn, R. Brent, *Proc. Natl. Acad. Sci. U.S.A.* **94**, 12473–12478 (1997).
25. S. J. Kim et al., *Cell Metab.* **16**, 274–283 (2012).



26. M. C. Kwon *et al.*, *EMBO J.* **27**, 642–653 (2008).  
 27. L. A. Sena *et al.*, *Immunity* **38**, 225–236 (2013).  
 28. N. G. Laniewski, J. M. Grayson, *J. Virol.* **78**, 11246–11257 (2004).  
 29. K. Araki *et al.*, *Nature* **460**, 108–112 (2009).  
 30. G. J. van der Windt *et al.*, *Immunity* **36**, 68–78 (2012).

## ACKNOWLEDGMENTS

We thank C. Bangham and R. Shattock for helpful comments on the paper. The data reported in this manuscript are tabulated in the main paper and in the supplementary materials. The *Lem* gene sequence is deposited in GenBank accession KP939367. P.G.A.-R. is the inventor on international patent application PCT/GB2014/051603 (International Publication Number WO

2014/188220) A1. The patent covers the use of LEM nucleic acids and polypeptides to activate T cell immunity to cancer and viral infection and agents that down-regulate LEM for the treatment of autoimmune and inflammatory disease. Retro mutant mice are available from P.G.A.-R. under a material transfer agreement with Imperial College London. We thank J. Hehl and S. Stoma from the Scientific Center for Optical and Electron Microscopy ScopeM of the Swiss Federal Institute of Technology ETHZ for technical support. The research was supported by the ETH Zurich, the Swiss National Science Foundation (310030\_146140), Medical Research Council (MRC) grant G0700795, and NIH grant AI091930. I.O. and research were supported by a grant from the Wellcome Trust; L.W. and D.H. and research were supported by a grant from Cancer Research UK (A9995); O.C. and research were supported by NIH

grant AI45108. R.H. was supported by a MRC Ph.D. studentship, and C.M. was supported by a British Heart Foundation Fellowship (FS/12/38/29640).

## SUPPLEMENTARY MATERIALS

www.sciencemag.org/content/348/6238/995/suppl/DC1  
 Materials and Methods  
 Figs. S1 to 19  
 Tables S1 to S3  
 References (31–38)

23 January 2015; accepted 6 April 2015  
 Published online 16 April 2015;  
 10.1126/science.aaa7516

## REPORTS

## INORGANIC CHEMISTRY

# Synthesis and characterization of $P_2N_3^-$ : An aromatic ion composed of phosphorus and nitrogen

Alexandra Velian and Christopher C. Cummins\*

Aromaticity is predominantly associated with carbon-rich compounds but can also occur in all-inorganic ones. We report the synthesis of the diphosphatriazolate anion, a rare example of a planar aromatic inorganic species. Treatment of azide ( $N_3^-$ ) in tetrahydrofuran solution with  $P_2A_2$  ( $A = C_{14}H_{10}$ ), a source of  $P_2$ , produced  $P_2N_3^-$ , which we isolated as its [Na-kryptofix-221]<sup>+</sup> salt in 22% yield and characterized by single-crystal x-ray diffraction. Salts [Na-kryptofix-221] [ $P_2N_3$ ] and [Na-kryptofix-221] [ $P_2^{15}NN_2$ ] were analyzed by infrared and Raman spectroscopy,  $^{15}N$  and  $^{31}P$  nuclear magnetic resonance spectroscopy, and mass spectrometry. The formation of the  $P_2N_3^-$  anion was investigated using density functional theory, and its aromatic character was confirmed by NICS (nucleus-independent chemical shift) and QTAIM (quantum theory of atoms in molecules) methods.

In a chemical context, the term aromaticity refers to the special stability and electronic delocalization exhibited by planar hydrocarbons having  $4n + 2$   $\pi$  electrons, the most famous example of which is benzene ( $C_6H_6$ , six  $\pi$  electrons,  $n = 1$ ) (1, 2). The prevalence of aromatic hydrocarbons, many of which are naturally occurring in fossil fuel deposits, makes aromaticity largely the province of organic chemistry. Put forward as “inorganic benzene,” borazine ( $B_3N_3H_6$ ) is a colorless liquid and possesses high stability but is not deemed aromatic by the criterion of electronic delocalization (3–5). Aromaticity does not only occur in the case of six-membered planar rings; another instance is the pentagonal cyclopentadienide ion ( $C_5H_5^-$ , six  $\pi$  electrons). Theory suggests that an all-nitrogen pentagonal ion  $N_5^-$ , isoelectronic to cyclopentadienide, would be aromatic; however, pentazolate has so far been observed only as a gas-phase ion by tandem mass spectrometry experiments.

There, the pentazolate anion was generated from parahydroxyphenylpentazole by cleavage of the organic residue from the  $N_5^-$  unit using a high collision voltage (6).  $SN_2P_2$ , a sulfur-pnictogen ring with six  $\pi$  electrons, was recently identified in the gas phase by infrared (IR) spectroscopy as a product of the flash pyrolysis of  $SP(N_3)_3$  (7).

By contrast, the all-phosphorus aromatic five-membered anionic ring  $P_5^-$  was identified as a persistent species in solution (8); it could even be used in ensuing synthetic studies giving rise to metallocene analogs in which a  $P_5^-$  ring replaces a cyclopentadienide ligand, as exemplified by the ferrocene-analogous complex  $Cp^*Fe(P_5)$  ( $Cp^* = C_5Me_5$ ; Me = methyl) (9). The  $Cp^*Fe(P_5)$  complex has proven to be a valuable building block in supramolecular chemistry, assembling into nanometer-scale balls upon interaction with copper(I) halides (10).

Recently, we prepared a versatile, anthracene-based source of  $P_2$ ,  $P_2A_2$  ( $A = \text{anthracene or } C_{14}H_{10}$ ), shown to release anthracene and diphosphorus upon mild heating (11). In the context of accessing all-pnictogen heterocycles, we wondered whether the diphosphatriazolate anion

$P_2N_3^-$  (Fig. 1) could be prepared in a “click” reaction between diphosphorus (provided by  $P_2A_2$ ) and the azide anion  $N_3^-$ , similar to triazole formation in the [3+2] cyclization of azides with alkynes or phosphalkynes (12–15).

We found that  $P_2N_3^-$  formed in quantitative spectroscopic yield (along with anthracene) when a solution of  $P_2A_2$  (Fig. 2) in tetrahydrofuran (THF) was heated to 70°C for 3 hours in the presence of excess [TBA] [ $N_3$ ] (6.2 equiv; TBA = tetrabutylammonium). The  $P_2N_3^-$  anion displays a phosphorus chemical shift at +334 ppm and is readily detected by electrospray ionization (ESI) spectrometry (mass-charge ratio  $m/z = 104.9$ ). Similar solubility properties impeded the separation of the desired [TBA] [ $P_2N_3$ ] salt from excess [TBA] [ $N_3$ ] and anthracene, but when the reaction was repeated with a substoichiometric amount of [Na-kryptofix-221] [ $N_3$ ], pure [Na-kryptofix-221] [ $P_2N_3$ ] could be isolated by crystallization in 22% yield as colorless crystals sensitive to air and moisture.

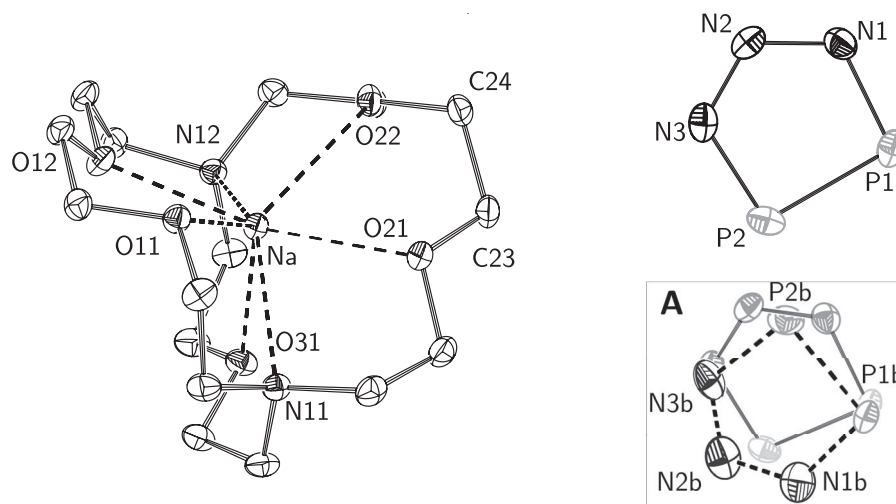
The identity of the [Na-kryptofix-221] [ $P_2N_3$ ] salt was confirmed by x-ray diffraction analysis (Fig. 1) (16). Of remarkable simplicity, the  $P_2N_3^-$  anion reveals itself as an essentially planar ring approximating  $C_{2v}$  point group symmetry, with metrical parameters that compare well to those predicted using density functional theory (DFT). The P-P and P-N interatomic distances [ $2.068 \pm 0.001$  Å and  $1.679$  (avg.) Å, respectively] fall in between typical single- and double-bond values (17, 18); this multiple bonding character is also reflected by the delocalization indices calculated for the P-P and P-N bonds (1.48 and 1.19, respectively) (19–21). The delocalized bonding present in the  $P_2N_3^-$  anion is best visualized by plotting the Laplacian of the calculated electronic charge density in the plane of the ring (Fig. 3) (22); here, the areas of local charge concentration are distributed over all atomic basins.

To probe the expected aromaticity of the diphosphatriazolate anion relative to other five-membered rings with six  $\pi$  electrons ( $N_5^-$ ,  $P_5^-$ ,  $C_5H_5^-$ , and  $N_2S_3^{2+}$ ) that are deemed aromatic (23, 24), we calculated its nucleus-independent chemical shift along the  $z$  axis (NICS<sub>zz</sub>) (24). Similar to the aforementioned rings, the NICS<sub>zz</sub> profile for the  $P_2N_3^-$  anion was found to be class I, with the highest absolute value for NICS at  $\sim 0.6$  Å above the ring critical point, diagnostic for a  $\pi$  aromatic system (Fig. 4) (25). Moreover, magnetic

Department of Chemistry, Massachusetts Institute of Technology, Cambridge, MA 02139, USA.

\*Corresponding author. E-mail: ccummins@mit.edu

**Fig. 1. Solid-state molecular structure of [Na-kryptofix-221]  $[P_2N_3]^-$ .** Hydrogen atoms are omitted for clarity; the ellipsoids are plotted at the 50% probability level. The  $P_2N_3^-$  unit is disordered over two positions with occupancies of 92% (major component) and 8% (minor component), respectively (inset **A**). Selected interatomic distances and angles: (major component) N2-N1,  $1.326 \pm 0.002$  Å; N1-P1,  $1.677 \pm 0.002$  Å; P1-P2,  $2.069 \pm 0.001$  Å; P2-N3,  $1.680 \pm 0.002$  Å; N3-N2,  $1.310 \pm 0.002$  Å; P1-P2-N3,  $93.17^\circ \pm 0.08^\circ$ ; P2-N3-N2,  $117.7^\circ \pm 0.2^\circ$ ; N1-N2-N3,  $118.5^\circ \pm 0.2^\circ$ ; (minor component) N3B-N2B,  $1.32 \pm 0.03$  Å; N2B-N1B,  $1.32 \pm 0.02$  Å; N1B-P1B,  $1.64 \pm 0.02$  Å; P1B-P2B,  $2.08 \pm 0.02$  Å; P2B-N3B,  $1.69 \pm 0.02$  Å. A model of  $P_2N_3^-$  anion was optimized using DFT methods (27,32); selected interatomic distances and angles: P-P, 2.07 Å; P-N, 1.69 Å; N-N, 1.31 Å; P-P-N,  $93^\circ$ ; P-N-N,  $117^\circ$ ; N-N-N,  $120^\circ$ .



susceptibility analysis by QTAIM (quantum theory of atoms in molecules) showed that  $\pi$  orbitals made the largest contribution (57%) to the total magnetic aromaticity of the  $P_2N_3^-$  anion (26, 27).

The downfield  $^{31}\text{P}$  nuclear magnetic resonance (NMR) shifts observed for the  $P_2N_3^-$  and  $P_5^-$  anions (+334 and +467 ppm, respectively) are characteristic for these aromatic, all-pnictogen anionic rings. The  $C_{2v}$  symmetry of  $P_2N_3^-$  observed in polar solvents such as THF and acetonitrile, where the anion appears to tumble freely, is broken in nonpolar solvents such as benzene, where the phosphorus atoms become inequivalent and two peaks in a 1:1 ratio are detected by  $^{31}\text{P}$  NMR spectroscopy. This desymmetrization is also observed in the solid-state structure, where N3 and N3b are preferentially oriented toward C23 of the cryptand (N3-C23 distance =  $3.329 \pm 0.002$  Å); this may be the effect of a weak donor-acceptor interaction (C23-H...N3) (28). Consistent with this hypothesis is the natural bond orbital (NBO) analysis of the diphosphatriazolate anion, which reveals N1 and N3 as the most basic sites of the  $P_2N_3^-$  ring, each bearing a partial  $-0.64$  charge (Fig. 3).

To access more information about the properties and formation of the  $P_2N_3^-$  ion, we used terminally labeled [Na-kryptofix-221]  $[^{15}\text{N}N_2]$  as a reaction partner together with  $P_2A_2$ , giving rise to the formation of [Na-kryptofix-221]  $[P_2^{15}NN_2]$  ( $^{15}\text{N}$  between P and  $^{14}\text{N}$ ; Fig. 2) (27). The IR and Raman vibrational spectra for the  $^{15}\text{N}$ -labeled diphosphatriazolate anion are predictably redshifted with respect to the unlabeled  $P_2N_3^-$  ion and are well reproduced computationally (table S2). Involving primarily the vibration of the P-P bond, the  $A_1$  Raman mode is largely unaffected by the incorporation of the  $^{15}\text{N}$  label and is detected at  $519\text{ cm}^{-1}$  for both the labeled and the unlabeled anion. For comparison, the breathing mode of the  $P_5^-$  ion was observed at  $463\text{ cm}^{-1}$  in solution (8), and the stretching frequency of the P-P bond in diphosphene  $\text{ArP}=\text{PAR}$  (Ar = 2,4,6-tri-*tert*-butylphenyl) was observed at  $610\text{ cm}^{-1}$  (29), which suggests that the P-P bond in  $P_2N_3^-$  is stronger than in its all-phosphorus analog but

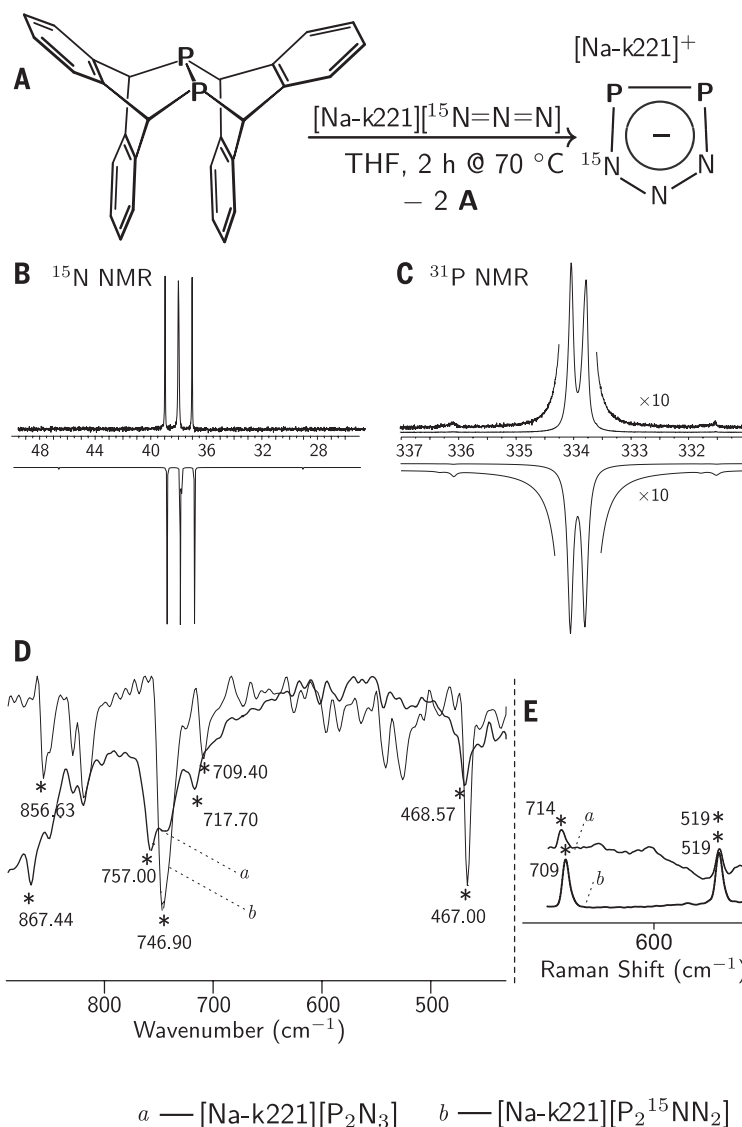


**Fig. 2. Characterization of the [Na-kryptofix-221]  $[P_2^{15}NN_2]^-$  salt.** (A) Preparation by thermolysis of  $P_2A_2$  in the presence of [Na-kryptofix-221]  $[^{15}\text{N}N_2]$ . (B and C) Experimental (up) and simulated (down)  $^{15}\text{N}$  NMR and  $^{31}\text{P}$  NMR spectra, respectively, of the  $[P_2^{15}NN_2]^-$  ion. (D and E) IR and Raman vibrational spectra, respectively, of solid [Na-kryptofix-221]  $[P_2N_3]$  and [Na-kryptofix-221]  $[P_2^{15}NN_2]$ .



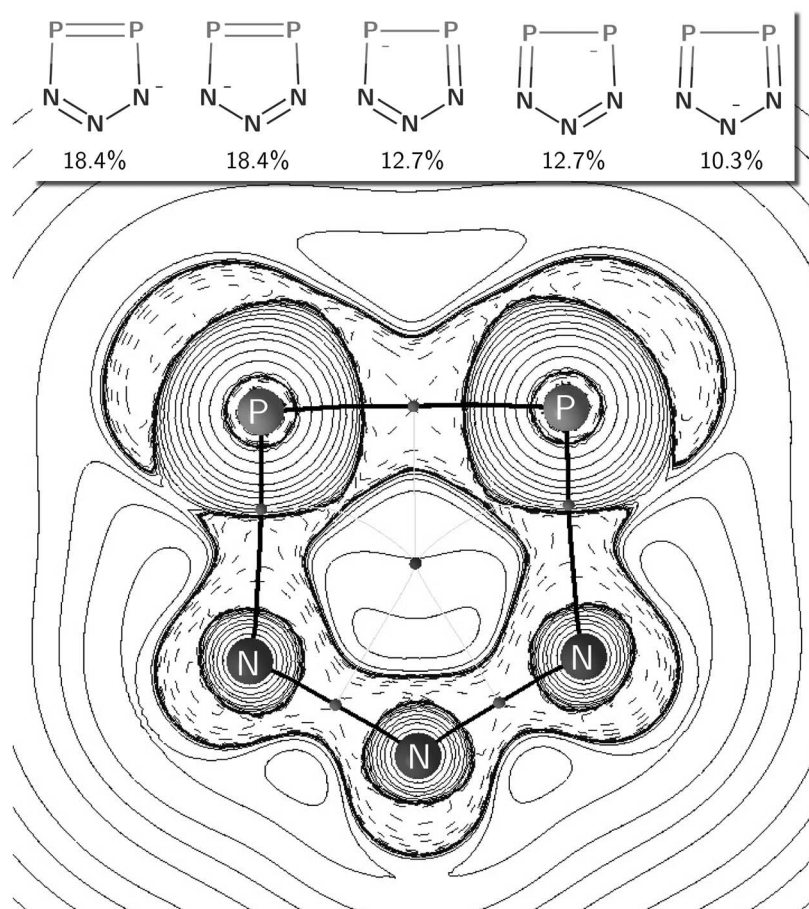
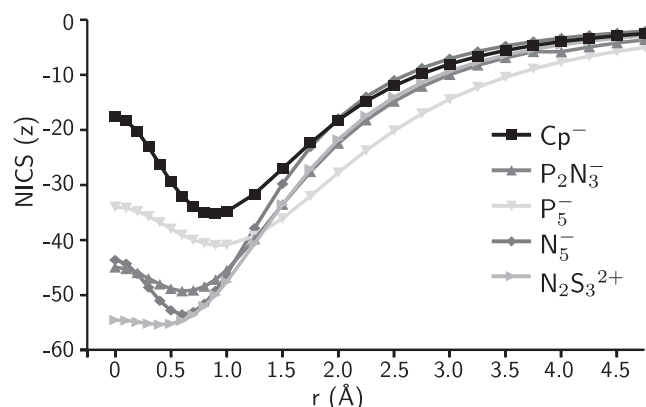


**Fig. 3. Theoretical bonding analysis.** Natural resonance theory (NRT) (33) resonance weights (top) calculated for the diphosphatriazolate anion,  $P_2N_3^-$  (34, 35). The topology of the Laplacian distribution of charge density (bottom) in the plane of the  $P_2N_3^-$  anion is shown with regions of charge depletion in solid curves and those of charge concentration in dashed curves. Bond paths, bond and ring critical points, and atomic basin paths are also depicted (21).

**Fig. 4. Probing aromaticity.** Plotted is NICS( $z$ ) versus  $r$  (Å) (27) for  $Cp^-$ ,  $P_2N_3^-$ ,  $P_5^-$ ,  $N_5^-$ , and  $N_2S_3^{2+}$ .



weaker than in the diphosphene. The  $B_1$  Raman vibration of the diphosphatriazolate anion, involving primarily the stretching and contracting of the P–N bonds, red-shifts from  $714\text{ cm}^{-1}$  for  $P_2N_3^-$  to  $709\text{ cm}^{-1}$  for  $P_2^{15}NN_2^-$ .

With three spin  $\frac{1}{2}$  nuclei, the  $P_2^{15}NN_2^-$  anion is an ABX spin system and displays second-order coupling (30, 31). The  $^{15}\text{N}$  NMR spectrum of  $P_2^{15}NN_2^-$  consists of an apparent doublet of

doublets centered at  $+38.0\text{ ppm}$ , while its  $^{31}\text{P}$  NMR spectrum reveals an apparent doublet ( $J_{\text{virtual}} = 52\text{ Hz}$ ) flanked by two sets of outer wings ( $\pm 460\text{ Hz}$ ; Fig. 2). With the aid of the Spin Simulation package of the MNova NMR program, we estimated  $^1J_{P1-P2}$ ,  $^1J_{P2-N3}$ ,  $^2J_{P1-N3}$ , and  $\Delta\nu_{P1P2}$  to be  $-460$ ,  $+102$ ,  $+2$ , and  $17\text{ Hz}$ , respectively (fig. S6 and table S1). The large P1–P2 coupling constant between the almost equivalent

phosphorus atoms effects a stronger coupling of the P1 atom to the  $^{15}\text{N}$  nucleus in position 3 than otherwise (31). The presence of the outer wings in the  $^{31}\text{P}$  NMR spectrum, centered at  $\pm 460\text{ Hz}$  from the center of the apparent doublet ( $J_{\text{virtual}} = 52\text{ Hz}$ ), is characteristic for the ABX spin system (31).  $^{15}\text{N}$  NMR spectroscopy data rule out the presence of the 1,3 isomer of the  $P_2^{15}NN_2^-$  ion in the reaction mixture, as the 1,3 isomer can incorporate the  $^{15}\text{N}$  atom in either position 2 or 4 of the heterocycle. This would give rise to two distinct signals in the  $^{15}\text{N}$  NMR spectrum, contrary to the experimental findings.

Using DFT methods [M06-2X, def2-TZVPP+, COSMO(THF)] (27), we investigated two routes through which  $P_2N_3^-$  could form: (i) an associative route in which the reactive intermediate  $P_2N_3A^-$  forms from  $P_2A$  and  $N_3^-$  and subsequently loses  $A$ , and (ii) a dissociative route in which  $P_2$ , formed in the fragmentation of  $P_2A$ , reacts directly with  $N_3^-$ . Similar to the  $P_2$  transfer from  $P_2A_2$  to 1,3-cyclohexadiene (17), we found the two routes to have comparable energetic profiles (fig. S13), likely both contributing to the formation of the  $P_2N_3^-$  anion.

This work shows that it is possible to synthesize, using an original  $P_2$  transfer reaction, a planar aromatic heterocycle composed exclusively of nitrogen and phosphorus. Until now, to render isolable a molecular entity having substantial  $P=P$  double-bond character, the approach has been to use an architecture with bulky adjacent substituents to block the site, thereby preventing access to the reactive moiety and attendant degradation (18). Here, the small title anion  $P_2N_3^-$  is entirely free of blocking groups and the observed stability must be attributed to electronic stabilization. Considering the data in aggregate, this stabilization is best construed as aromaticity—an effect traditionally reserved for the domain of organic chemistry.

## REFERENCES AND NOTES

1. M. Faraday, *Philos. Trans. R. Soc. London* **115**, 440–466 (1825).
2. P. R. Schleyer, *Chem. Rev.* **101**, 1115–1118 (2001).
3. A. Stock, E. Pohlend, *Ber. Deutsch. Chem. Ges. A/B* **59**, 2215–2223 (1926).
4. B. Kiran, A. K. Phukan, E. D. Jemmis, *Inorg. Chem.* **40**, 3615–3618 (2001).
5. R. Islas *et al.*, *Struct. Chem.* **18**, 833–839 (2007).
6. A. Vij, J. G. Pavlovich, W. W. Wilson, V. Vij, K. O. Christe, *Angew. Chem. Int. Ed.* **41**, 3051 (2002).
7. X. Zeng *et al.*, *Angew. Chem. Int. Ed.* **54**, 1327–1330 (2015).
8. M. Baudler *et al.*, *Angew. Chem. Int. Ed. Engl.* **27**, 280–281 (1988).
9. O. J. Scherer, T. Brück, G. Wolmershäuser, *Chem. Ber.* **121**, 935–938 (1988).
10. M. Scheer *et al.*, *J. Am. Chem. Soc.* **129**, 13386–13387 (2007).
11. A. Velian *et al.*, *J. Am. Chem. Soc.* **136**, 13586–13589 (2014).
12. R. Huisgen, *Angew. Chem. Int. Ed. Engl.* **2**, 565–598 (1963).
13. H. C. Kolb, M. G. Finn, K. B. Sharpless, *Angew. Chem. Int. Ed.* **40**, 2004–2021 (2001).
14. S. Herler *et al.*, *Angew. Chem. Int. Ed.* **44**, 7790–7793 (2005).
15. S. L. Choong, A. Nafady, A. Stasch, A. M. Bond, C. Jones, *Dalton Trans.* **42**, 7775–7780 (2013).
16. Metrical parameters for the structure of [Na-kryptofix-221] [ $P_2N_3$ ] are available free of charge from the Cambridge Crystallographic Data Centre under reference CCDC-1051576.
17. P. Pyrykkö, M. Atsumi, *Chem. Eur. J.* **15**, 12770–12779 (2009).
18. M. Yoshifuji, I. Shima, N. Inamoto, K. Hirotsu, T. Higuchi, *J. Am. Chem. Soc.* **103**, 4587–4589 (1981).
19. J. Poater, X. Fradera, M. Duran, M. Solà, *Chem. Eur. J.* **9**, 400–406 (2003).
20. C. L. Firme, O. Antunes, P. M. Esteves, *Chem. Phys. Lett.* **468**, 129–133 (2009).

21. AIMAll, Version 14.11.23; aim.tkgristmill.com.
22. R. F. W. Bader, *Chem. Rev.* **91**, 893–928 (1991).
23. W. V. F. Brooks, T. S. Cameron, S. Parsons, J. Passmore, M. J. Schriver, *Inorg. Chem.* **33**, 6230–6241 (1994).
24. Z. Chen, C. S. Wannere, C. Corminboeuf, R. Puchta, P. Schleyer, *Chem. Rev.* **105**, 3842–3888 (2005).
25. A. Stanger, *J. Org. Chem.* **71**, 883–893 (2006).
26. C. Foroutan-Nejad, *J. Phys. Chem. A* **115**, 12555–12560 (2011).
27. See supplementary materials on Science Online.
28. F. Weinhold, R. A. Klein, *Mol. Phys.* **110**, 565–579 (2012).
29. H. Hamaguchi, M. Tasumi, M. Yoshifuji, N. Inamoto, *J. Am. Chem. Soc.* **106**, 508–509 (1984).
30. J. Pople, W. G. Schneider, H. J. Bernstein, *High Resolution Nuclear Magnetic Resonance* (McGraw-Hill, New York, 1959).
31. W. H. Hersh, *J. Chem. Educ.* **74**, 1485 (1997).
32. F. Neese, *ORCA—an Ab Initio, Density Functional and Semiempirical Program Package*, Version 3.0.1 (University of Bonn, 2013).
33. E. D. Glendening, J. K. Badenhoop, F. Weinhold, *J. Comput. Chem.* **19**, 628–646 (1998).
34. NBO 5.0 (Theoretical Chemistry Institute, University of Wisconsin, 2001).
35. NBOView 2.0: NBO Orbital Graphics Plotter (University of Wisconsin, 2013).

## ACKNOWLEDGMENTS

This material is based on work supported by NSF grant CHE-1362118.

## SUPPLEMENTARY MATERIALS

www.sciencemag.org/content/348/6238/1001/suppl/DC1  
Materials and Methods  
Figs. S1 to S13  
Tables S1 to S15  
References (36–56)

1 March 2015; accepted 5 May 2015  
10.1126/science.aab0204

## SHAPE MEMORY ALLOYS

# Ultralow-fatigue shape memory alloy films

Christoph Chluba,<sup>1</sup> Wenwei Ge,<sup>2</sup> Rodrigo Lima de Miranda,<sup>1</sup> Julian Strobel,<sup>1</sup> Lorenz Kienle,<sup>1</sup> Eckhard Quandt,<sup>1\*</sup> Manfred Wuttig<sup>2\*</sup>

Functional shape memory alloys need to operate reversibly and repeatedly. Quantitative measures of reversibility include the relative volume change of the participating phases and compatibility matrices for twinning. But no similar argument is known for repeatability. This is especially crucial for many future applications, such as artificial heart valves or elastocaloric cooling, in which more than 10 million transformation cycles will be required. We report on the discovery of an ultralow-fatigue shape memory alloy film system based on TiNiCu that allows at least 10 million transformation cycles. We found that these films contain Ti<sub>2</sub>Cu precipitates embedded in the base alloy that serve as sentinels to ensure complete and reproducible transformation in the course of each memory cycle.

Shape memory alloys (SMAs) are attractive because of their distinct properties. The shape memory effect (1) is the basis in many modern solid-state actuators (2). Medical implants such as self-expanding stents (3) or orthodontic arch wires (4) take advantage of the superelasticity (1). This property also finds application in the emerging field of elastocaloric solid-state refrigerators (5). The basic principle of both features is the reversible martensite-austenite transformation, which is temperature-driven in the case of the shape memory effect and stress-driven in the case of the superelasticity. The corresponding large work output of SMAs is a consequence of a first-order structural phase transformation featuring a large eigenstrain and substantial enthalpy of transformation (6, 7). In apparent contradiction to its first-order characteristic, the property-controlling phase transformation of SMAs is reversible because the transforming phases are elastically compatible, meaning that the structural distortions arising from the transformation do not exceed the limits of reversibility (8). Nevertheless, a limiting factor for any high-cycle application of either

property is fatigue, both the integrity of the material (structural fatigue) as well as the change of their functional properties and their reversibility (functional fatigue). A general understanding of how often the transformation can be executed in polycrystals—its fatigue characteristics—is lacking, even though it currently constitutes the major obstacle to the implementation of the new technologies (9).

The most prominent SMAs are based on titanium-nickel, for which an equiatomic composition of the shape memory effect was uncovered in 1963 (10). The specific combination of their large effect sizes, tunability of the transformation temperatures by partial substitution of Ni or Ti with other elements (such as Cu, Pd, Pt, Co, Fe, and Hf), good mechanical properties, and excellent biocompatibility in case of binary TiNi (11) results in these alloys being the first choice for most solid-state shape memory and superelasticity applications. Despite the almost ubiquitous use of binary TiNi for superelastic implants (12), these alloys show a dramatic fatigue upon full cycling of the stress-induced martensitic transformation. Even for the first cycles, a change in the transformation temperature (13), a decrease of the superelastic plateau strain, and an accumulation of residual martensite are observed (14). Different fatigue investigations have revealed the fatigue endurance limit (maximum strain amplitude for run-out at 10 million cycles) for bulk superelastic TiNi to be between 0.4 and 0.6%, which is almost independent from the mean strain (3, 13). For example, the superelastic fatigue life in TiNi and TiNiCu wires by using a less-demanding rotary bending fatigue tester only reached 1 million cycles if the maximum stress at the outer surface was smaller than 0.8% (15). This behavior implies that only partial transformations can be used for any high-cycle applications,

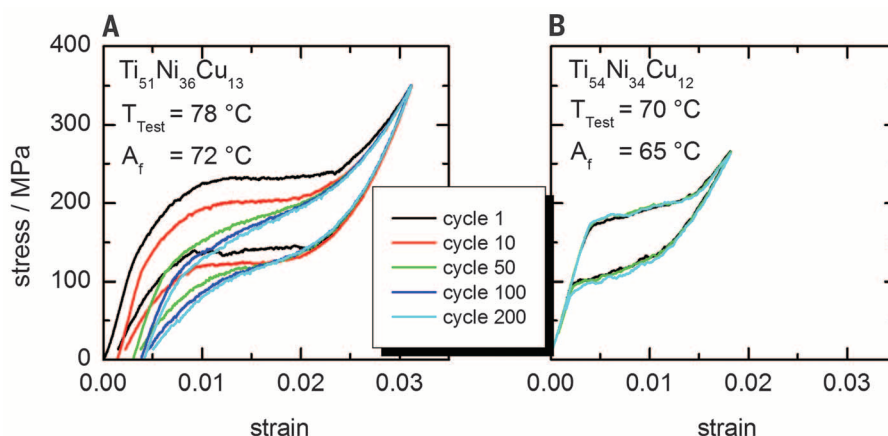


**Fig. 1. Evolution of fatigue in SMA films.** (A and B) Fatigue stress-strain curves of tensile fatigue tests performed up to 200 cycles at test temperatures ( $T_{\text{Test}}$ ) larger than austenite finish temperature ( $A_f$ ) noted in (A) and (B). Fatigue characteristics of near-equiatomic Ti<sub>51</sub>Ni<sub>36</sub>Cu<sub>13</sub> (sample 1) films with strong fatigue behavior and mechanically stable Ti-rich Ti<sub>54</sub>Ni<sub>34</sub>Cu<sub>12</sub> (sample 2) films are shown.

<sup>1</sup>Institute for Materials Science, Faculty of Engineering, University of Kiel, Kiel, Germany. <sup>2</sup>Department of Materials Science and Engineering, University of Maryland, College Park, MD, USA.

\*Corresponding author. E-mail: eq@tf.uni-kiel.de (E.Q.); wuttig@umd.edu (M.W.)



which is considered to be the major drawback of elastocaloric materials besides the observed pronounced functional fatigue (16). The behavior is related to the incompleteness of the transformation upon cycling (17), resulting in surface roughness, which is believed to be the origin of crack formation and subsequent mechanical failure of the material.

The obstacles described above demonstrate the connection between reversibility (functional fatigue) with structural fatigue. Essential for the reversibility are both the compatibility of the martensite-austenite and the twin/twin interfaces. The former and latter are perfect when the compatibility triplet—which consists of the middle eigenvalue of the stretch matrix measuring the relative volume change of the transforming phases,  $\lambda$ , and the two cofactors measuring the mutual compatibility of type I and II twins, CCI and CCII (18)—attains the values (1,0,0). Combinatorial techniques were used to identify compositions fulfilling the first condition in the systems Ni-Ti-Cu and Ni-Ti-Pd (7). In  $\text{Zn}_{45}\text{Au}_{30}\text{Cu}_{25}$  polycrystals, all compatibility conditions are close to their ideal values. Hence, the alloy displayed superior functional stability. This translated to the observation of a small decrease of the latent heat of  $\approx 10\%$  that persisted up to  $1.6 \times 10^4$  transformation cycles (19).

Additional interest in shape memory materials arises from the development of thin-film technology—which has led to miniaturized applications (20) such as microelectromechanical sys-

tem (MEMS) actuators (21)—as medical implants and for elastocaloric cooling (22). Besides miniaturization, these materials and related devices benefit from the high surface-to-volume ratio of thin-film SMAs and high specific work and power output owing to their enhanced frequency capabilities. In addition, free-standing thin-film materials, fabricated by use of a special sacrificial layer technique (23), exhibit improved mechanical and fatigue properties because of the absence of inclusions (24).

This study was undertaken so as to better understand the reversibility of the martensitic transformation in TiNiCu alloys with Cu substitution of  $12.5 \pm 0.5$  atomic % on Ni positions because they are known to have lower functional fatigue as compared with that of binary TiNi (22). We conducted experiments on thin films so as to minimize the influence of inclusions. TiNi-based devices are commonly made of near-equiatomic compositions (between the Ti- and the Ni-site) in order to minimize the fraction of precipitates and thereby maximize the fraction of phase-transforming material. We intentionally examined a Ti-rich composition in comparison with a near-equiatomic alloy in order to investigate the influence of two types of Ti-rich precipitates,  $\text{Ti}_2\text{Ni}$  and  $\text{Ti}_2\text{Cu}$ , on the functional fatigue. Magnetron-sputtered equiatomic  $\text{Ti}_{51}\text{Ni}_{36}\text{Cu}_{13}$  (sample 1) and Ti-rich  $\text{Ti}_{54}\text{Ni}_{34}\text{Cu}_{12}$  (sample 2) free-standing samples (25) show an austenite finish temperature ( $A_f$ ) of  $\sim 62^\circ\text{C}$  (fig. S1). We investigated both samples' mechanical (Fig. 1)

and thermal (fig. S1) fatigue characteristics (25), their structure before and after deformation cycling, as well as the crystallographic structures above and below  $A_f$  by means of synchrotron-based x-ray diffraction (XRD) (25). Additionally, we used high-resolution transmission electron microscopy (HRTEM) to characterize the B2/ $\text{Ti}_2\text{Cu}$  and B19/ $\text{Ti}_2\text{Cu}$  interfaces. We found that the presence of  $\text{Ti}_2\text{Cu}$  precipitates and next-to-ideal values of the compatibility triplet increase the fatigue limit of the Ti-rich sample to more than  $10^7$  full cycles without any degradation in the effect size. This insight allows us to transfer the principle to other phase transformation-controlled materials such as TiNiCuCo thin films (fig. S2).

The fatigue characteristics are different between the two samples within the first 200 cycles: A traditional SMA (sample 1) shows large functional fatigue (Fig. 1A), characterized by accumulation of remanent martensite (Table 1). The transformation is stabilized after 100 cycles, but high-cycle tests revealed an early rupture of this material after several thousand cycles. Increased surface roughness originating from stabilized martensite, which served as crack nucleation sites, is the likely mechanism (26). In contrast, the Ti-rich alloy (sample 2) displayed no measurable fatigue (Fig. 1B). However, as a result of the higher-mass fraction of precipitates (Table 1), the low-fatigue sample 2 showed a reduced superelastic plateau. A similar difference of the fatigue characteristics is found for TiNiCuCo samples. The near-equiatomic sample exhibits distinct fatigue (fig. S2A), whereas the Ti-rich sample displays no fatigue and a reduced superelastic strain (fig. S2B). Most noteworthy, the ultralow fatigue for the Ti-rich samples can be extended to 10 million cycles (Fig. 2 and fig. S3).

A comparison of the results of the diffraction experiments to the fatigue data (Figs. 1 and 2)

**Table 1. Refinement of mass fraction ( $m$ ) and lattice parameters ( $a$ ,  $b$ , and  $c$ ) of the phases identified before and after 200 deformation cycles for the high- and low-fatigue  $\text{Ti}_{51}\text{Ni}_{36}\text{Cu}_{13}$  and  $\text{Ti}_{54}\text{Ni}_{34}\text{Cu}_{12}$ .** The Rietveld mass fraction uncertainties are much smaller than expected (31), which explains the apparent inconsistencies of the  $\text{Ti}_2\text{Cu}$  mass fractions at  $22^\circ\text{C}$  and  $87^\circ\text{C}$ . Numbers in parentheses are rounded.

		At $22^\circ\text{C}$		At $87^\circ\text{C}$	
		Before cycling	After cycling	Before cycling	After cycling
$\text{Ti}_{51}\text{Ni}_{36}\text{Cu}_{13}$ , sample 1: Identified phases					
B2 ( $Pm\bar{3}m$ )	$m$ [%]			81.35(2)	74.77(2)
	$a$ [Å]			3.036050(5)	3.03691(1)
	$m$ [%]	93.484(8)	92.414(8)	12.31(7)	18.52(6)
B19 ( $Pmma$ )	$a$	$a = 4.24731(5)$	$a = 4.24864(6)$	$a = 4.2546(5)$	$a = 4.2668(5)$
	$b$	$b = 2.89549(5)$	$b = 2.89582(5)$	$b = 2.9028(4)$	$b = 2.9127(4)$
	$c$	$c = 4.52777(4)$	$c = 4.52669(4)$	$c = 4.5157(4)$	$c = 4.5089(3)$
$\text{Ti}_2\text{Ni}$ ( $Fd\bar{3}m$ )	$m$ [%]	6.52(5)	7.59(4)	6.34(5)	6.71(4)
	$a$ [Å]	11.3421(4)	11.3467(3)	11.3519(2)	11.3575(2)
$\text{Ti}_{54}\text{Ni}_{34}\text{Cu}_{12}$ , sample 2: Identified phases					
B2 ( $Pm\bar{3}m$ )	$m$ [%]			67.89(3)	70.30(3)
	$a$ [Å]			3.038542(4)	3.038653(4)
	$m$ [%]	71.45(3)	73.65(2)		
B19 ( $Pmma$ )	$a$	$a = 4.25653(7)$	$a = 4.25486(7)$		
	$b$	$b = 2.90113(6)$	$b = 2.90214(6)$		
	$c$	$c = 4.51964(7)$	$c = 4.52099(7)$		
$\text{Ti}_2\text{Ni}$ ( $Fd\bar{3}m$ )	$m$ [%]	22.84(5)	19.15(4)	24.20(5)	20.33(5)
	$a$ [Å]	11.33396(5)	11.33495(6)	11.33981(3)	11.34131(4)
	$m$ [%]	5.71(4)	7.21(4)	7.91(3)	9.37(4)
$\text{Ti}_2\text{Cu}$ ( $I4/mmm$ )	$a = b$	$a = b =$	$a = b =$	$a = b =$	$a = b =$
	$c$	$c = 2.95131(3)$	$c = 2.95100(3)$	$c = 2.95556(2)$	$c = 2.95549(2)$
	$c$	$c = 10.4993(2)$	$c = 10.5015(2)$	$c = 10.49195(9)$	$c = 10.49451(9)$

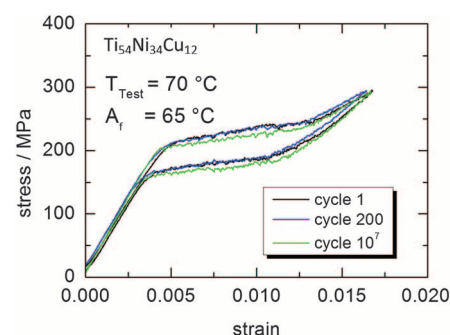


**Fig. 2. Ultralow fatigue in SMA films.** Ultralow fatigue of the Ti-rich sample 2 demonstrated by next-to-identical 1st, 200th, and  $10^7$ th superelastic transformation cycles. The testing temperature ( $T_{\text{Test}}$ ) was  $70^\circ\text{C}$  with an austenite-finish temperature ( $A_f$ ) of  $65^\circ\text{C}$ . The high-cycle fatigue at  $70^\circ\text{C}$  was measured with a special fatigue test device, consisting of a load cell, a temperature chamber, and a solenoid as actuator. The fatigue test is conducted force-controlled at a frequency of 20 Hz (fig. S4). Cycle 1 to 200 and cycle  $10^7$  was measured by using a conventional tensile test device (25).

shows that the Ti-rich sample 2 with ultralow fatigue contains Ti<sub>2</sub>Cu precipitates, which are not present in the near-equiatomic sample 1 film (figs. S5 and S6). Both samples contain B2, B19, and Ti<sub>2</sub>Ni phases with phase contents (Table 1) and strain distributions (table S1) determined by

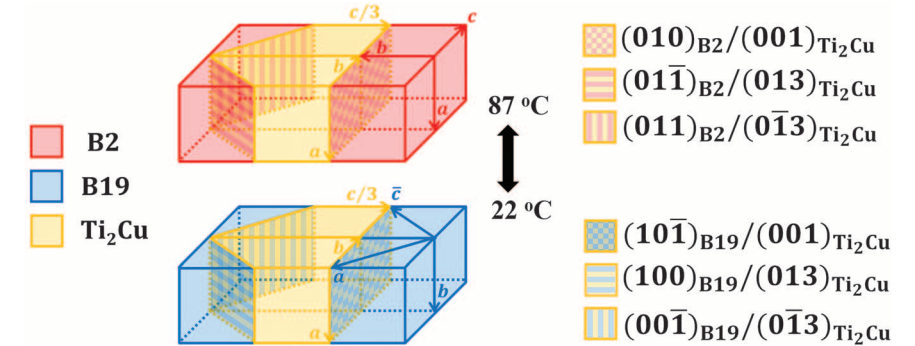
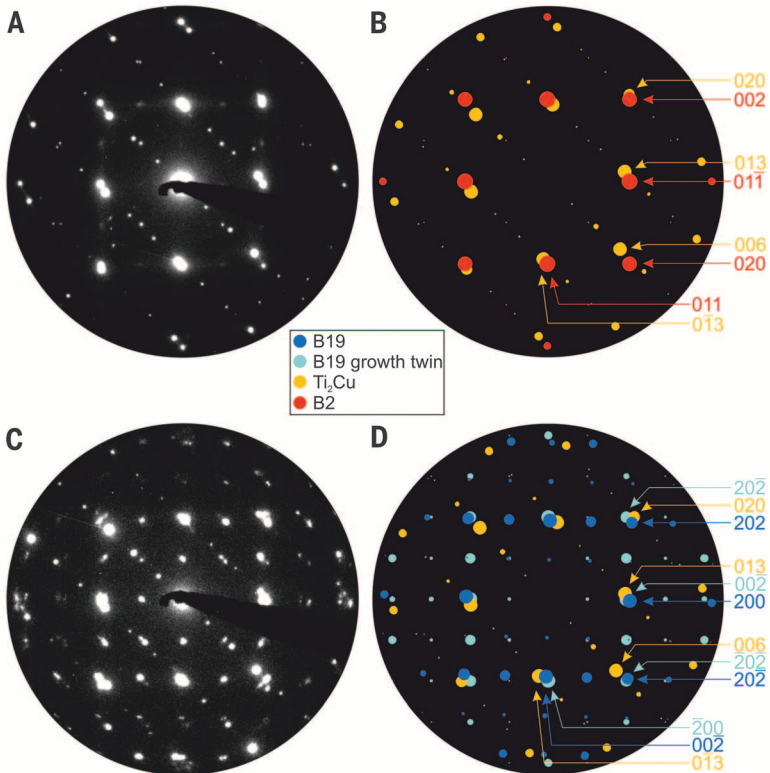


**Fig. 3. Dual epitaxies in Ti<sub>54</sub>Ni<sub>34</sub>Cu<sub>12</sub> films.** B2↔Ti<sub>2</sub>Cu↔B19 epitaxies in Ti<sub>54</sub>Ni<sub>34</sub>Cu<sub>12</sub> film (sample 2). Color coding is shown on the left. The smallest misfit strains, calculated on the basis of the lattice parameters (Table 1), are  $\epsilon_{||}[(010)_{B2}/(001)_{Ti_2Cu}] = \frac{2c(B2)}{2b(Ti_2Cu)} - 1 = 2.80\%$ ,  $\epsilon_{\perp}[(010)_{B2}/(001)_{Ti_2Cu}] = \frac{a(B2)}{a(Ti_2Cu)} - 1 = 2.80\%$ ,  $\epsilon_{||}[(100)_{B19}/(013)_{Ti_2Cu}] = \frac{c(B19)}{\sqrt{b^2 + (c/3)^2(Ti_2Cu)}} - 1 = -1.28\%$ , and  $\epsilon_{\perp}[(100)_{B2}/(013)_{Ti_2Cu}] = \frac{b(B19)}{a(Ti_2Cu)} - 1 = -1.70\%$ . B19 growth twin epitaxies are shown in fig. S7. Additional misfit strains are given in table S3.

**Table 2. Values of the compatibility triplet, middle eigenvalue ( $\lambda$ ), and cofactor conditions for type I and II twins (CCI and CCII).** These are evaluated by using the lattice parameters extracted from Table 1.

Alloy	$a_o$ (Å)	$a$ (Å)	$b$ (Å)	$c$ (Å)	$\lambda$	CCI [10 <sup>-4</sup> ]	CCII [10 <sup>-4</sup> ]
	B2, 87°C	B19, 22°C					
Ti <sub>51</sub> Ni <sub>36</sub> Cu <sub>13</sub>	3.03605	4.24732	2.89549	4.52777	0.9892	2.4542	2.9473
Ti <sub>54</sub> Ni <sub>34</sub> Cu <sub>12</sub>	3.03854	4.25654	2.90114	4.51964	0.9905	1.8661	2.2742

**Fig. 4. Electron microscopical evidence of dual epitaxies.** TEM-generated and simulated diffraction patterns of the B2/Ti<sub>2</sub>Cu and B19/Ti<sub>2</sub>Cu interfaces. The experimental patterns have been recorded on sample 2, patterns (A) and (C), at an elevated and room temperature, respectively. A HRTEM of the interfacial region is shown in fig. S2. (A) Selected-area electron diffraction (SAED) pattern recorded at the B2/Ti<sub>2</sub>Cu interface, zone axes [100]. (B) Simulation of the pattern in (A), showing that 020<sub>Ti<sub>2</sub>Cu</sub> nearly coincides with 002<sub>B2</sub>. (C) SAED pattern recorded at the B19/Ti<sub>2</sub>Cu interface; zone axes are [100]<sub>Ti<sub>2</sub>Cu</sub> and [010]<sub>B19</sub>. (D) Simulation of the pattern in (C) demonstrating near-overlap of the 020<sub>Ti<sub>2</sub>Cu</sub> and 202<sub>B19</sub>/202<sub>B19twin</sub> diffraction spots. The patterns confirm the proposed epitaxies at high and low temperatures: (010)<sub>B2</sub>/(001)<sub>Ti<sub>2</sub>Cu</sub>, red/yellow in Fig. 3; (101)<sub>B19</sub>/(001)<sub>Ti<sub>2</sub>Cu</sub>, dark blue/yellow in Fig. 3; and (101)<sub>B19twin</sub>/(001)<sub>Ti<sub>2</sub>Cu</sub>, light blue/yellow in fig. S7



means of Rietveld refinements that included grain size (table S2, A and B) (27) as well as anisotropic strain parameters (28). The incomplete temperature-induced B2↔B19 transformation in sample 1 indicated stabilized martensite in the austenite phase. The presence or absence of Ti<sub>2</sub>Cu phase appears to control the transformation and fatigue characteristics of the two samples. We reason that the potential epitaxy of the phase pairs B2/Ti<sub>2</sub>Cu and B19/Ti<sub>2</sub>Cu is responsible for the almost complete reversibility of the stress-strain curves and identified the relevant misfit strains (Fig. 3 and table S3) along with the corresponding Rietveld strain parameters ( $S_{hkl}$ ) (table S1) (28) for these interfaces. Taking the strain parameters into consideration improves the refinement considerably (table S4A). The small misfits of the transforming phases' lattice parameters with Ti<sub>2</sub>Cu in the low-fatigue sample 2 (Fig. 3) suggest that B19 and B2 are epitaxially related to Ti<sub>2</sub>Cu and to each other. The Rietveld strain parameters (table S1) support the epitaxy because the symmetry is identical to that of the anisotropic broadening of diffraction peaks associated with epitaxial strains. TEM diffraction patterns also suggest epitaxy, taken at the B2/Ti<sub>2</sub>Cu and B19/Ti<sub>2</sub>Cu interfaces (Fig. 4), as also confirmed with HRTEM observations (fig. S8). In contrast, the Ti<sub>2</sub>Ni precipitates display larger misfits and small values of the Rietveld strain parameters (fig. S9 and tables S1 and S3). This demonstrates incoherent precipitation in the B2 and B19 phase, respectively.

The refined x-ray and TEM diffraction data suggest the following scenario leading to the low-fatigue state in Ti-rich sample 2. Ti<sub>2</sub>Cu coherently



and Ti<sub>2</sub>Ni incoherently precipitate in the B2 matrix upon cooling from 700°C to 87°C. The B2 matrix transforms completely to B19 upon further cooling to 22°C, aided by the simultaneous Ti<sub>2</sub>Cu/B19 epitaxies (Figs. 3 and 4, Table 1, and table S3). The B19/Ti<sub>2</sub>Cu epitaxy provides an internal stress pattern, which stabilizes the B19 phase at low temperatures. During stress cycling, the equivalent epitaxy alternately stabilizes the B2 phase. At each temperature and stress, the transforming phases attain equilibrium by forming a compatible morphology directed by the internal epitaxy-generated stress distribution. Complete transformation is attained at each cycle because the epitaxial stresses are reversible. Hence, we propose that the epitaxially promoted completion of the B2↔B19 phase transformation creates the low-fatigue state of the Ti<sub>54</sub>Ni<sub>34</sub>Cu<sub>12</sub> films. The Ti<sub>2</sub>Cu precipitates act like sentinels, assuring that the B2↔B19 transformation proceeds toward completion at each cycle. The transformation will return the film to a stress state and morphology that are compatible with the pristine state. The decrease of the anisotropic peak broadening of the epitaxy-effected XRD peaks indicates trainability.

This proposal must be revisited in light of the favorable values of the quantitative compatibility criteria calculated from the lattice parameters of both alloys Ti<sub>57</sub>Ni<sub>36</sub>Cu<sub>13</sub> and Ti<sub>54</sub>Ni<sub>34</sub>Cu<sub>12</sub> (Table 2). These values approach the ideal triplet ( $\lambda = 1$ , CCI = CCII = 0) and suggest good reversibility even in polycrystals (29), although they are inferior to those for Zn<sub>45</sub>Au<sub>30</sub>Cu<sub>25</sub> (19). The values for sample 2 are closer to the ideal than those for sample 1, which is in accord with the vastly better fatigue characteristics of sample 2. The question then arises whether this large difference of the fatigue life results from the observed epitaxy or that of the two triplets listed in Table 2. We observe that despite their reversibility, the phase transformations in SMAs are of first order (nucleation- and growth-controlled). We suggest that the epitaxy leads to reversible nucleation, whereas the low cofactors promote reversible near-equilibrium growth so that the combination of both mechanisms yields the observed ultralow fatigue. In the limit of CCI and CCII→0, no energy will be stored in the product phase in the form of twin boundaries. This creates a strongly reproducible, and therefore repeatably transformable, equilibrium state.

Given the fatigue-controlling importance of the dual epitaxy of Ti<sub>2</sub>Cu in TiNiCu-based (SMA) films, it is natural to search for other alloying elements that have the potential to play a similar role. Following this lead, we can assume that structurally related Ti<sub>2</sub>Ag precipitates will act very similar to Ti<sub>2</sub>Cu. Because TiNiAg SMAs display transformation characteristics comparable with that of TiNiCu (30), they could be promising candidates for biocompatible ultralow fatigue SMA films. Elastocaloric cooling requires bulk materials, which is a difficult but, in principle, solvable challenge. More generally, we expect similar behavior in phase-transforming materials that contain dual-epitaxial precipitates.

## REFERENCES AND NOTES

1. K. Otsuka, X. Ren, *Prog. Mater. Sci.* **50**, 511–678 (2005).
2. J. Mohd Jani, M. Leary, A. Subic, M. A. Gibson, *Mater. Des.* **56**, 1078–1113 (2014).
3. T. Duerig, A. Pelton, D. Stöckel, *Mater. Sci. Eng. A* **273–275**, 149–160 (1999).
4. D. W. Raboud, M. G. Faulkner, A. W. Lipsett, *Smart Mater. Struct.* **9**, 684–692 (2000).
5. E. Bonnot, R. Romero, L. Mañosa, E. Vives, A. Planes, *Phys. Rev. Lett.* **100**, 125901 (2008).
6. K. Otsuka, C. M. Wayman, Eds., *Shape Memory Materials* (Cambridge Univ. Press, Cambridge, 1999).
7. J. Cui et al., *Nat. Mater.* **5**, 286–290 (2006).
8. K. Bhattacharya, S. Conti, G. Zanzotto, J. Zimmer, *Nature* **428**, 55–59 (2004).
9. X. Moya, S. Kar-Narayan, N. D. Mathur, *Nat. Mater.* **13**, 439–450 (2014).
10. W. J. Buehler, J. V. Gilfrich, R. C. Wiley, *J. Appl. Phys.* **34**, 1475–1477 (1963).
11. S. A. Shabalovskaya, *Biomed. Mater. Eng.* **12**, 69–109 (2002).
12. N. B. Morgan, *Mater. Sci. Eng. A* **378**, 16–23 (2004).
13. A. R. Pelton, *J. Mater. Eng. Perform.* **20**, 613–617 (2011).
14. G. Eggeler, E. Hornbogen, A. Yawny, A. Heckmann, M. Wagner, *Mater. Sci. Eng. A* **378**, 24–33 (2004).
15. S. Miyazaki, K. Mizukoshi, T. Ueki, T. Sakuma, Y. Liu, *Mater. Sci. Eng. A* **273–275**, 658–663 (1999).
16. E. Hornbogen, *J. Mater. Sci.* **39**, 385–399 (2004).
17. K. Gall, H. J. Maier, *Acta Mater.* **50**, 4643–4657 (2002).
18. R. D. James, Z. Zhang, in *Magnetism and Structure in Functional Materials*, A. Planes, L. Manosa, A. Saxena, Eds. (Springer, New York, 2005), vol. 79.
19. Y. Song, X. Chen, V. Dabade, T. W. Shield, R. D. James, *Nature* **502**, 85–88 (2013).
20. S. Miyazaki, Y. Q. Fu, W. M. Huang, Eds., *Thin Film Shape Memory Alloys* (Cambridge Univ. Press, Cambridge, 2009).
21. K. Bhattacharya, R. D. James, *Science* **307**, 53–54 (2005).
22. C. Bechtold, C. Chluba, R. Lima de Miranda, E. Quandt, *Appl. Phys. Lett.* **101**, 091903 (2012).
23. R. Lima de Miranda, C. Zamponi, E. Quandt, *Adv. Eng. Mater.* **15**, 66–69 (2013).
24. G. Siekmeyer, A. Schüßler, R. de Miranda, E. Quandt, *J. Mater. Eng. Perform.* **23**, 2437–2445 (2014).
25. Materials and methods are available as supplementary materials on Science Online.
26. K. Bhattacharya, *Microstructure of Martensite: Why It Forms and How It Gives Rise to the Shape-Memory Effect* (Oxford Univ. Press, Oxford, 2003).
27. A. C. Larson, R. B. Von Dreele, “General Structure Analysis System (GSAS),” Los Alamos National Laboratory Report LAUR 86-748 (2004).
28. P. Stephens, *J. Appl. Cryst.* **32**, 281–289 (1999).
29. K. Bhattacharya, R. V. Kohn, *Acta Mater.* **44**, 529–542 (1996).
30. C. Zamponi, M. Wuttig, E. Quandt, *Scripta Mater.* **56**, 1075–1077 (2007).
31. H. Scott, *J. Appl. Cryst.* **16**, 159–163 (1983).

## ACKNOWLEDGMENTS

The work at the University of Kiel was supported by the Deutsche Forschungsgemeinschaft (DFG) via the Priority Program 1599. L.K. and J.S. appreciate the assistance of V. Duppel (Max Planck Institute for solid state research) for recording the electron diffraction patterns, B. V. Lotsch for enabling electron microscopy, and C. Szillars for TEM sample preparation. The work at the University of Maryland was supported by grant DOE DESC0005448; use of the Advanced Photon Source - Argonne National Laboratory was supported by the U.S. Department of Energy (DOE) Office of Science, under contract DE-AC02-06CH11357. M.W. and W.G. thank P. Zavali for his guidance with the Rietveld refinement and J. Steiner for the compatibility calculations. The synchrotron diffraction data are available from the corresponding author. Other data are available in the main text and the supplementary materials.

## SUPPLEMENTARY MATERIALS

www.sciencemag.org/content/348/6238/1004/suppl/DC1  
Materials and Methods

Figs. S1 to S9

Tables S1 to S4

Reference (32)

12 September 2014; accepted 14 April 2015  
10.1126/science.1261164

## MEMORY

# Engram cells retain memory under retrograde amnesia

Tomás J. Ryan,<sup>1,2\*</sup> Dheeraj S. Roy,<sup>1\*</sup> Michele Pignatelli,<sup>1\*</sup>  
Autumn Arons,<sup>1,2</sup> Susumu Tonegawa<sup>1,2†</sup>

Memory consolidation is the process by which a newly formed and unstable memory transforms into a stable long-term memory. It is unknown whether the process of memory consolidation occurs exclusively through the stabilization of memory engrams. By using learning-dependent cell labeling, we identified an increase of synaptic strength and dendritic spine density specifically in consolidated memory engram cells. Although these properties are lacking in engram cells under protein synthesis inhibitor-induced amnesia, direct optogenetic activation of these cells results in memory retrieval, and this correlates with retained engram cell-specific connectivity. We propose that a specific pattern of connectivity of engram cells may be crucial for memory information storage and that strengthened synapses in these cells critically contribute to the memory retrieval process.

**M**emory consolidation is the phenomenon by which a newly formed memory transitions from a fragile state to a stable, long-term state (1–3). The defining feature of consolidation is a finite time window that begins immediately after learning,

during which a memory is susceptible to disruptions, such as protein synthesis inhibition (4–6), resulting in retrograde amnesia. The stabilization of synaptic potentiation is the dominant cellular model of memory consolidation (7–10) because protein synthesis inhibitors disrupt late-phase

long-term potentiation of in vitro slice preparations (11–13). Although much is known about the cellular mechanisms of memory consolidation, it remains unknown whether these processes occur in memory engram cells. It may be possible to characterize cellular consolidation and empirically separate mnemonic properties in retrograde amnesia by directly probing and manipulating memory engram cells in the brain. The term memory engram originally referred to

the hypothetical learned information stored in the brain, which must be reactivated for recall (14, 15). Recently, several groups demonstrated that specific hippocampal cells that are activated during memory encoding are both sufficient (16–18) and necessary (19, 20) for driving future recall of a contextual fear memory and thus represent a component of a distributed memory engram (21). Here, we applied this engram technology to the issue of cellular consolidation and retrograde amnesia.

We used the previously established method for tagging the hippocampal dentate gyrus (DG) component of a contextual memory engram with mCherry (supplementary materials, materials and methods, and fig. S1) (16, 22). To disrupt consolidation, we systemically injected the protein synthesis inhibitor anisomycin (ANI) or saline (SAL)

as a control immediately after contextual fear conditioning (CFC) (Fig. 1A). The presynaptic neurons of the entorhinal cortex (EC) were constitutively labeled with ChR2 expressed from an AAV<sub>8</sub>-CaMKII $\alpha$ -ChR2-EYFP virus (Fig. 1B). Voltage clamp recordings of paired engram (mCherry<sup>+</sup>) and nonengram (mCherry<sup>-</sup>) DG cells were conducted simultaneously with optogenetic stimulation of ChR2<sup>+</sup> perforant path (PP) axons (Fig. 1, C and D). mCherry<sup>+</sup> cells of the SAL group showed significantly greater synaptic strength than did paired mCherry<sup>-</sup> cells, whereas in the ANI group, mCherry<sup>+</sup> and mCherry<sup>-</sup> cells were of comparable synaptic strength (Fig. 1E). Calculation of AMPA/N-methyl-D-aspartate (NMDA) receptor current ratios (23) showed that at 24 hours after training, mCherry<sup>+</sup> engram cells displayed potentiated synapses relative to paired mCherry<sup>-</sup> non-engram

<sup>1</sup>RIKEN-MIT Center for Neural Circuit Genetics at the Picower Institute for Learning and Memory, Department of Biology and Department of Brain and Cognitive Sciences, Massachusetts Institute of Technology, Cambridge, MA 02139, USA. <sup>2</sup>Howard Hughes Medical Institute, Massachusetts Institute of Technology, Cambridge, MA 02139, USA.  
\*These authors contributed equally to this work. †Corresponding author. E-mail: tonegawa@mit.edu

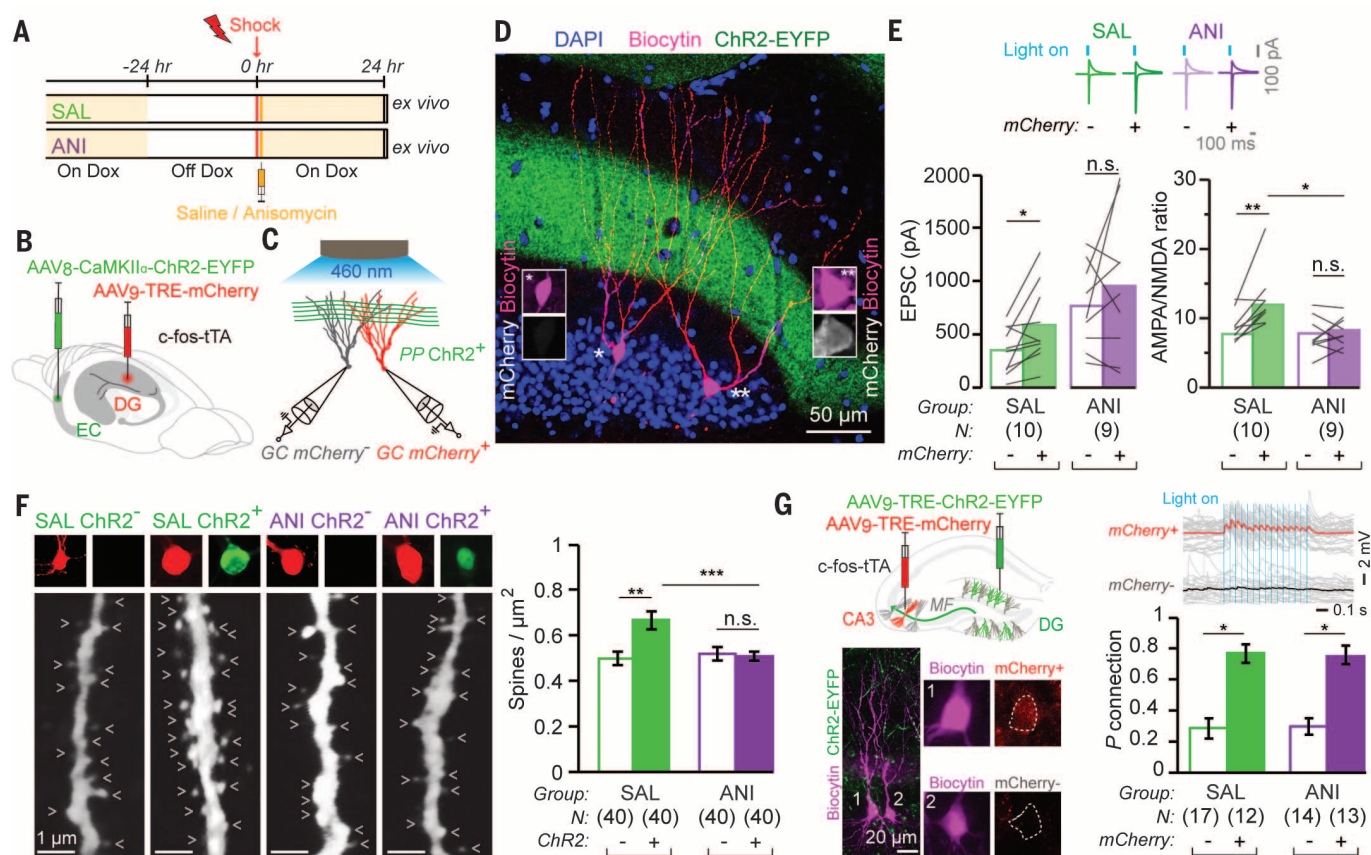


**Fig. 1. Synaptic plasticity and connectivity of engram cells.** (A) Mice taken off doxycycline (DOX) 24 hours before CFC and dispatched 24 hours after training. SAL or ANI was administered immediately after training. (B) AAV<sub>8</sub>-CaMKII $\alpha$ -ChR2-EYFP and AAV<sub>9</sub>-TRE-mCherry viruses injected into the entorhinal cortex and dentate gyrus, respectively, of c-Fos-tTA mice. (C) Paired recordings of engram (red) and nonengram (gray) DG cells during optogenetic stimulation of ChR2<sup>+</sup> PP axons. (D) Representative image of a pair of recorded biocytin-labeled engram (mCherry<sup>+</sup>) and nonengram (mCherry<sup>-</sup>) DG cells. ChR2<sup>+</sup> PP axons are in green. (E) (Top) Example traces of AMPA and NMDA receptor-dependent postsynaptic currents in mCherry<sup>+</sup> and mCherry<sup>-</sup> cells, evoked by means of light activation of ChR2<sup>+</sup> PP axons. (Bottom) EPSC amplitudes and AMPA/NMDA current ratios of mCherry<sup>+</sup> and mCherry<sup>-</sup> cells of the two groups are displayed as means (columns) and individual paired data points (gray lines). Paired *t* test; \**P* < 0.05, \*\**P* < 0.001. SAL group

compared with the ANI group, unpaired *t* test; \**P* < 0.05. (F) (Left) Representative confocal images of biocytin-filled dendritic fragments derived from SAL and ANI groups for ChR2<sup>+</sup> and ChR2<sup>-</sup> cells (arrow heads indicate dendritic spines). (Right) Average dendritic spine density showing an increase occurring exclusively in ChR2<sup>+</sup> fragments. Data are represented as mean  $\pm$  SEM. Unpaired *t* tests \*\**P* < 0.01, \*\*\**P* < 0.001. (G) Engram connectivity. (Top left) AAV<sub>9</sub>-TRE-ChR2-EYFP and AAV<sub>9</sub>-TRE-mCherry viruses, injected into the DG and CA3, respectively, of c-Fos-tTA mice. (Bottom left) Example of mCherry<sup>+</sup> (1) and mCherry<sup>-</sup> (2) biocytin-filled CA3 pyramidal cells. ChR2<sup>+</sup> mossy fibers (MF) are in green. (Top right) mCherry<sup>+</sup> cell but not mCherry<sup>-</sup> cell displayed excitatory postsynaptic potentials in response to optogenetic stimulation of MF. (Bottom right) Probability of connection of DG ChR2<sup>+</sup> engram axons and CA3 mCherry<sup>+</sup> and mCherry<sup>-</sup> cells. Error bars are approximated by using binomial distribution. Fisher's exact test; \**P* < 0.05.



cells in the SAL group (Fig. 1E). However, no such difference between  $mCherry^+$  and  $mCherry^-$  was observed in the ANI group. In addition,  $mCherry^+$  engram cells of the SAL group showed significantly greater AMPA/NMDA current ratios than those of  $mCherry^+$  engram cells of the ANI group. Analysis of spontaneous excitatory postsynaptic

currents (EPSCs) of engram and non-engram cells of both SAL and ANI groups showed the same pattern (fig. S2).

We also quantified dendritic spine density for DG engram cells labeled with an AAV<sub>9</sub>-TRE-ChR2-EYFP virus. Spine density of ChR2<sup>+</sup> cells was significantly higher than corresponding

ChR2<sup>+</sup> cells in the SAL group (Fig. 1F and fig. S3), but spine densities of ChR2<sup>+</sup> and ChR2<sup>+</sup> cells of the ANI group were similar (supplementary materials, materials and methods). Spine density of ChR2<sup>+</sup> cells of the SAL group was significantly higher than that of ANI ChR2<sup>+</sup> cells (Fig. 1F), but ChR2<sup>+</sup> cell spine density was comparable. This result was confirmed with analysis of the membrane capacitance (fig. S4G). ChR2 expression did not affect intrinsic properties of DG cells in vitro (fig. S5, A to E). Direct bath application of ANI did not affect intrinsic cellular properties in vitro (fig. S5F), although it mildly reduced synaptic currents acutely (fig. S5, G to I). When ANI was injected into c-Fos-tTA animals 24 hours after CFC and engram labeling, engram cell-specific increases in dendritic spine density and synaptic strength were undisturbed (fig. S6). We also examined engram cells labeled by means of a context-only experience (17) and found equivalent engram-cell increases in spine density and synaptic strength (fig. S7) as those labeled by means of CFC.

DG cells receive information from EC and relay it to CA3 via the mossy fiber pathway. We labeled DG engram cells using an AAV<sub>9</sub>-TRE-ChR2-EYFP virus and simultaneously labeled CA3 engram cells using an AAV<sub>9</sub>-TRE-mCherry virus (Fig. 1G). Connection probability was assessed 24 hours after CFC by stimulating DG ChR2<sup>+</sup> cell terminals optogenetically and recording excitatory postsynaptic potentials in CA3  $mCherry^+$  and  $mCherry^-$  cells in ex vivo preparations. CA3  $mCherry^+$  engram cells showed a significantly higher probability of connection than did  $mCherry^-$  cells with DG ChR2<sup>+</sup> engram cells, demonstrating preferential engram cell-to-engram cell connectivity. This form of engram pathway-specific connectivity was unaffected by posttraining administration of ANI (Fig. 1G).

We next tested the behavioral effect of optogenetically stimulating engram cells in amnesic mice (Fig. 2A). During CFC training in context B, both SAL and ANI groups responded to the unconditioned stimuli at equivalent levels (fig. S8). One day after training, the SAL group displayed robust freezing behavior to the conditioned stimulus of context B, whereas the ANI group showed substantially less freezing behavior (Fig. 2C). Two days after training, mice were placed into the distinct context A for a 12-min test session consisting of four 3-min epochs of blue light on or off. During this test session, neither group showed freezing behavior during light-off epochs, but both froze significantly during light-on epochs (Fig. 2D). Remarkably, no difference in the levels of light-induced freezing behavior was observed between groups. Three days after training, the mice were again tested in context B in order to assay the conditioned response, and retrograde amnesia for the conditioning context was still clearly evident (Fig. 2E). Subjects treated with SAL or ANI after the labeling of a neutral contextual engram (no shock) did not show freezing behavior in response to light stimulation of engram cells (Fig. 2D). We replicated the DG retrograde amnesia experiment using an alternative widely used protein synthesis inhibitor, cycloheximide (CHM)

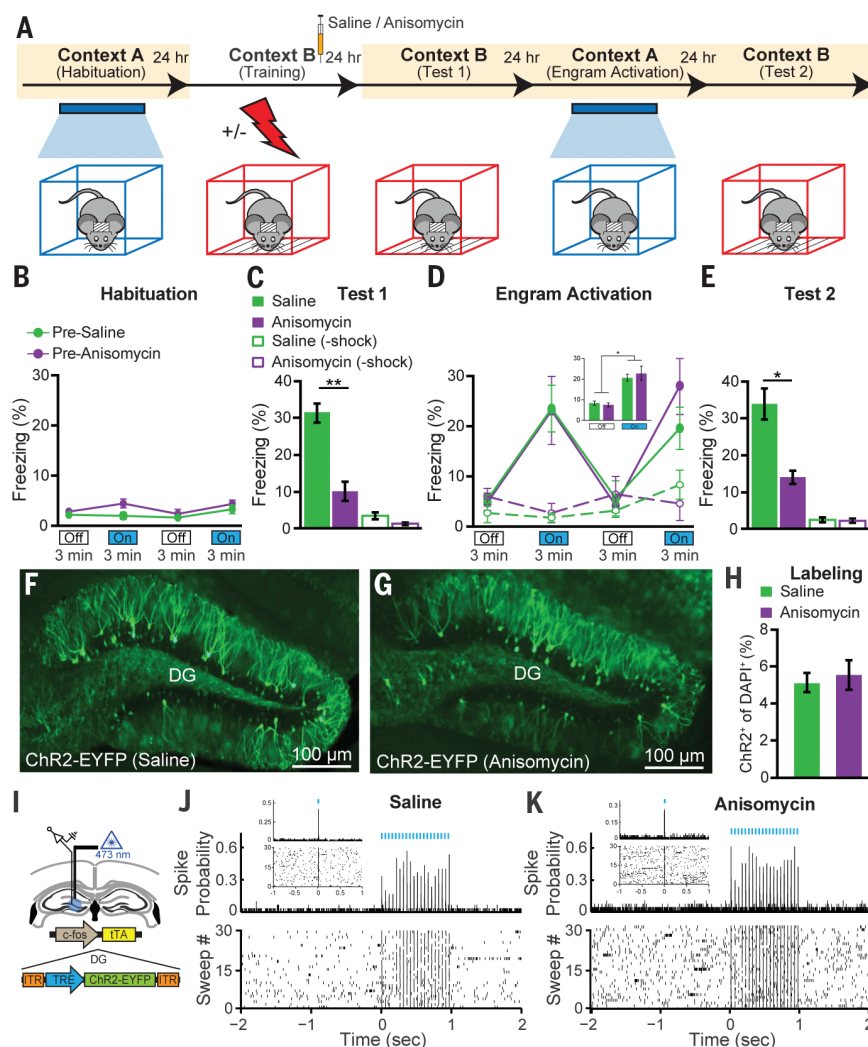


**Fig. 2. Optogenetic stimulation of DG engram cells restores fear memory in retrograde amnesia.**

(A) Behavioral schedule. Beige shading signifies that subjects are on DOX, precluding ChR2 expression. Mice are taken off DOX 24 to 30 hours before CFC in context B. SAL or ANI was injected into the mice after training. (B) Habituation to context A with light-off and light-on epochs. Blue light stimulation of the DG did not cause freezing behavior in naive, unlabeled mice of the pre-SAL ( $n = 10$  mice) or pre-ANI ( $n = 8$  mice) groups. (C) Memory recall in context B 1 day after training (test 1). ANI group displayed significantly less freezing than SAL group ( $P < 0.005$ ). No-shock groups with SAL ( $n = 4$  mice) or ANI ( $n = 4$  mice) did not display freezing upon reexposure to context B. (D) Memory recall in context A 2 days after training (engram activation) with light-off and light-on epochs. Freezing for the two light-off and light-on epochs are further averaged in the inset. Significant freezing due to light stimulation was observed in both the SAL ( $P < 0.01$ ) and ANI groups ( $P < 0.05$ ). Freezing levels did not differ between groups. SAL and ANI-treated no-shock control groups did not freeze in response to light stimulation of context B engram cells. (E) Memory recall in context B 3 days after training (test 2). ANI group displayed significantly less freezing than SAL group ( $P < 0.05$ ). (F and G) Images showing DG sections from c-Fos-tTA mice 24 hours after SAL or ANI treatment. (H) ChR2-EYFP cell counts from DG sections of SAL ( $n = 3$  mice) and ANI ( $n = 4$  mice) groups. (I) In vivo anesthetized recordings (supplementary materials, materials and methods). (J and K) Light pulses induced spikes in DG neurons recorded from head-fixed anesthetized c-Fos-tTA mice 24 hours after treatment with either SAL or ANI. Data are presented as mean  $\pm$  SEM.

(fig. S9). We examined whether ANI administration immediately after CFC altered the activity-dependent synthesis of Chr2-EYFP in DG cells and found that this was not the case (Fig. 2, F to H). Nevertheless, the dosage of ANI used in this study did inhibit protein synthesis in the DG, as shown with Arc<sup>+</sup> cell counting (fig. S10). Thus, the dosage of ANI used was sufficient to induce amnesia but was insufficient to impair c-Fos-TA-driven synthesis of virally delivered Chr2-EYFP in DG cells. Extracellular recordings from SAL- and ANI-treated mice confirmed the cell counting results (Fig. 2, I to K). In line with fig. S6 and previous reports (24), ANI injection 24 hours after CFC did not cause retrograde amnesia (fig. S11). To provide a negative control for light-induced memory retrieval in amnesia, we disrupted memory encoding by activating hM4Di DREADDs receptors (25) downstream of the DG, in hippocampal CA1, during CFC, and found that subsequent DG engram activation did not elicit memory retrieval (fig. S12).

The recovery from amnesia through the direct light activation of ANI-treated DG engram cells was unexpected because these cells showed neither synaptic potentiation nor increased dendritic spine density. We conducted additional behavioral experiments in order to confirm and characterize the phenomenon. First, we investigated whether recovery from amnesia can be demonstrated by means of light-induced optogenetic place avoidance test (OptoPA); this would be a measure of an active fear memory recall (supplementary materials, materials and methods) (18), rather than a passive fear response monitored with freezing. SAL and ANI groups displayed equivalent levels of avoidance of the target zone in response to light activation of the DG engram (Fig. 3A). Second, in our previous study we showed that an application of the standard protocol (20 Hz) for activation of the CA1 engram was not effective for memory recall (17). However, we found that a 4-Hz protocol applied to the CA1 engram of the SAL and ANI groups

elicited similar recovery from amnesia (Fig. 3B). Third, we used tone fear conditioning (TFC) and manipulated the fear engram in lateral amygdala (LA) (26) and found light-induced recovery of memory from amnesia. Fourth, we asked whether amnesia caused by disruption of reconsolidation of a contextual fear memory (27, 28) can also be recovered through the light-activation of DG engram cells, which was found to be the case (Fig. 4A). We applied the memory inception method (supplementary materials, materials and methods) (17, 29) to DG engram cells and found that both SAL and ANI groups showed freezing behavior that was specific to the original context A, demonstrating that light-activated context A engrams formed in the presence of ANI can function as a conditioned stimulus (CS) in a context-specific manner (Fig. 4B). Last, we tested the longevity of CFC amnesic engrams for memory recovery by means of light activation and found that memory recall could be observed 8 days after training (fig. S13).

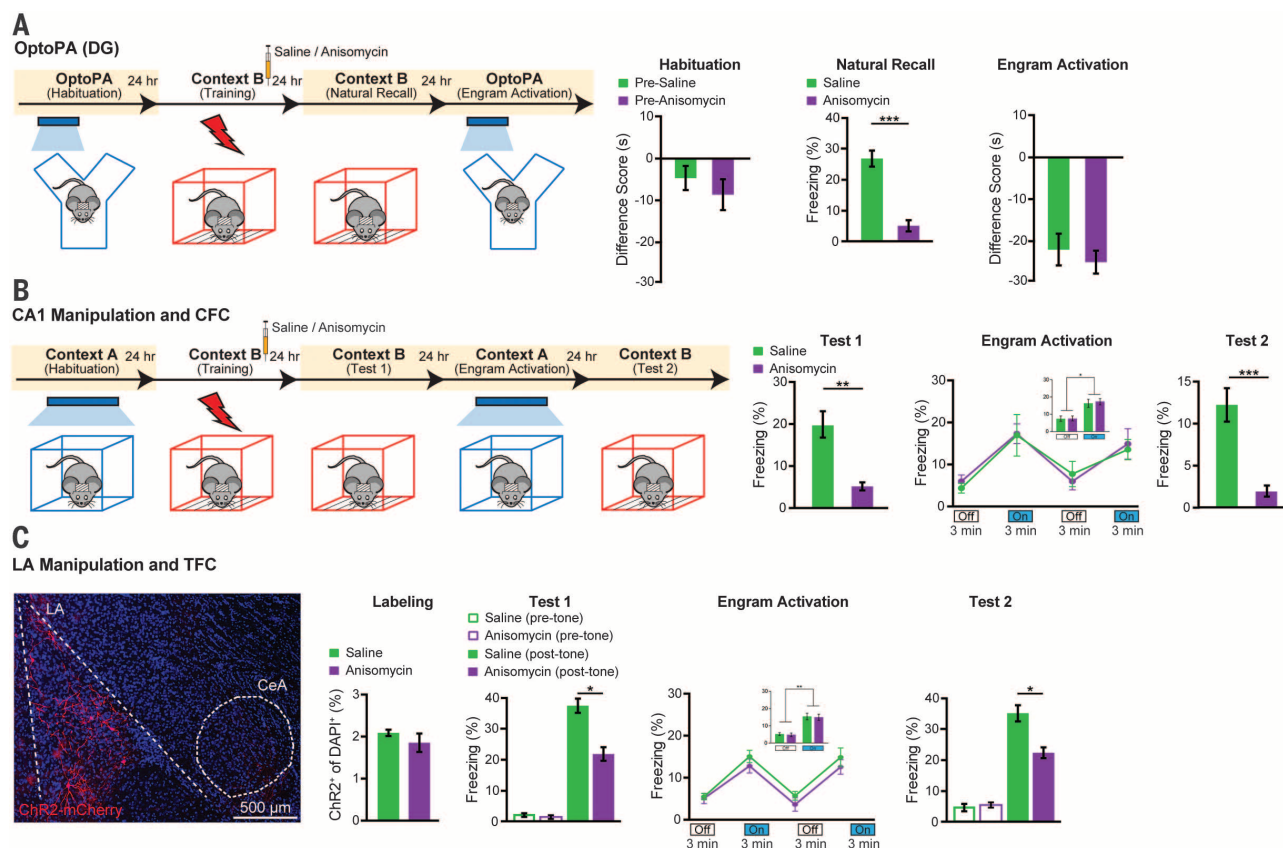


**Fig. 3. Recovery of memory from amnesia under a variety of conditions.**

(A) DG engram activation and optogenetic place avoidance (OptoPA). During habituation, neither group displayed significant avoidance of target zone. For natural recall, the ANI group ( $n = 10$  mice) displayed significantly less freezing than SAL group ( $n = 12$  mice) in context B ( $P < 0.005$ ). SAL and ANI groups displayed similar levels of OptoPA. (B) CA1 engram activation and CFC. 1 day after CFC (test 1), ANI group ( $n = 9$  mice) displayed significantly less freezing than that of SAL group ( $n = 10$  mice) in context B ( $P < 0.01$ ). Two days after training (engram activation), light-activation of CA1 engrams elicited freezing in both SAL ( $P < 0.01$ ) and ANI groups ( $P < 0.001$ ). Three

days after training (test 2), ANI group froze less than did SAL group in context B ( $P < 0.01$ ). (C) LA engram activation and TFC. The behavioral schedule was identical to that in Fig. 3B, except that context tests were replaced with tone tests in context C (supplementary materials, materials and methods). (Left) Example image of Chr2-mCherry labeling of LA neurons. Of DAPI cells, 2% were labeled with Chr2. (Right) One day after training (test 1), ANI group ( $n = 9$  mice) displayed significantly less freezing to tone than did SAL group ( $n = 9$  mice) ( $P < 0.05$ ). Two days after training (engram activation), significant light-induced freezing was observed for both SAL ( $P < 0.005$ ) and ANI groups ( $P < 0.005$ ). Three days after training (test 2), ANI group froze less to tone than did SAL group ( $P < 0.05$ ).



Interactions between the hippocampus and amygdala are crucial for contextual fear memory encoding and retrieval (18). c-Fos expression increases in the hippocampus and amygdala upon exposure of an animal to conditioned stimuli (30, 31). These previous observations open up the possibility of obtaining cellular-level evidence to support the behavioral-level finding that the recovery from amnesia can be accomplished with direct light activation of ANI-treated DG engram cells. Thus, we compared the effects of natural recall and light-induced recall on amygdala c-Fos<sup>+</sup> cell counts in amnesic mice (Fig. 5, A to C). c-Fos<sup>+</sup> cell counts (Fig. 5B) were significantly lower in basolateral amygdala (BLA) and central amygdala (CeA) of ANI-treated mice as compared with SAL mice when natural recall cues were delivered, showing that amygdala activity correlates with fear memory expression (Fig. 5C). In contrast, light-induced activation of the contextual engram cells resulted in equivalent amygdala c-Fos<sup>+</sup> counts in SAL and ANI groups (Fig. 5C), which supports the optogenetic behavioral data.

Next, we modified this protocol in order to include labeling of CA3 and BLA engram cells with mCherry and examined the effects of light-

induced activation of DG engram cells on the overlap of mCherry<sup>+</sup> engram cells and c-Fos<sup>+</sup> recall-activated cells in CA3 and BLA (Fig. 5D). The purpose of this experiment was to investigate whether there is preferential connectivity between the upstream engram cells in DG and the downstream engram cells in CA3 or BLA. Natural recall cues resulted in above-chance c-Fos<sup>+</sup>/mCherry<sup>+</sup> overlap in both CA3 and BLA, which supports the physiological connectivity data (Fig. 5, E to K). c-Fos<sup>+</sup>/mCherry<sup>+</sup> overlap was significantly reduced in the ANI group as compared with the SAL group but was still higher than chance levels, presumably reflecting incomplete amnesic effects of ANI (Fig. 5K). Light-activation of DG engram cells resulted in equivalent c-Fos<sup>+</sup>/mCherry<sup>+</sup> overlap as natural cue-induced recall, and this was unaffected by post-CFC ANI treatment. These data suggest that there is preferential and protein synthesis-independent functional connectivity between DG and CA3 engram cells, which supports the physiological data (Fig. 1G), and that this connectivity also applies between DG and BLA engram cells.

We previously showed that DG cells activated during CFC training and labeled with ChR2 via

the promoter of an immediate early gene (IEG) can evoke a freezing response when they are reactivated optogenetically 1 to 2 days later (16), and this has since been achieved in the cortex (21). We have also shown that these DG cells, if light-activated while receiving an unconditioned stimulus (US), can serve as a surrogate context-specific CS to create a false CS-US association (17, 18), and that activation of DG or amygdala engram cells can induce place preference (18). Furthermore, recent studies showed that optogenetic inhibition of these cells in DG, CA3, or CA1 impairs expression of a CFC memory (19, 20). Together, these findings show that engram cells activated through CFC training are both sufficient and necessary to evoke memory recall, satisfying two crucial attributes in defining a component of a contextual fear memory engram (15). What has been left to be demonstrated, however, is that these DG cells undergo enduring physical changes as an experience is encoded and its memory is consolidated. Although synaptic potentiation has long been suspected as a fundamental mechanism for memory and as a crucial component of the enduring physical changes induced by experience, this has not been directly demonstrated,

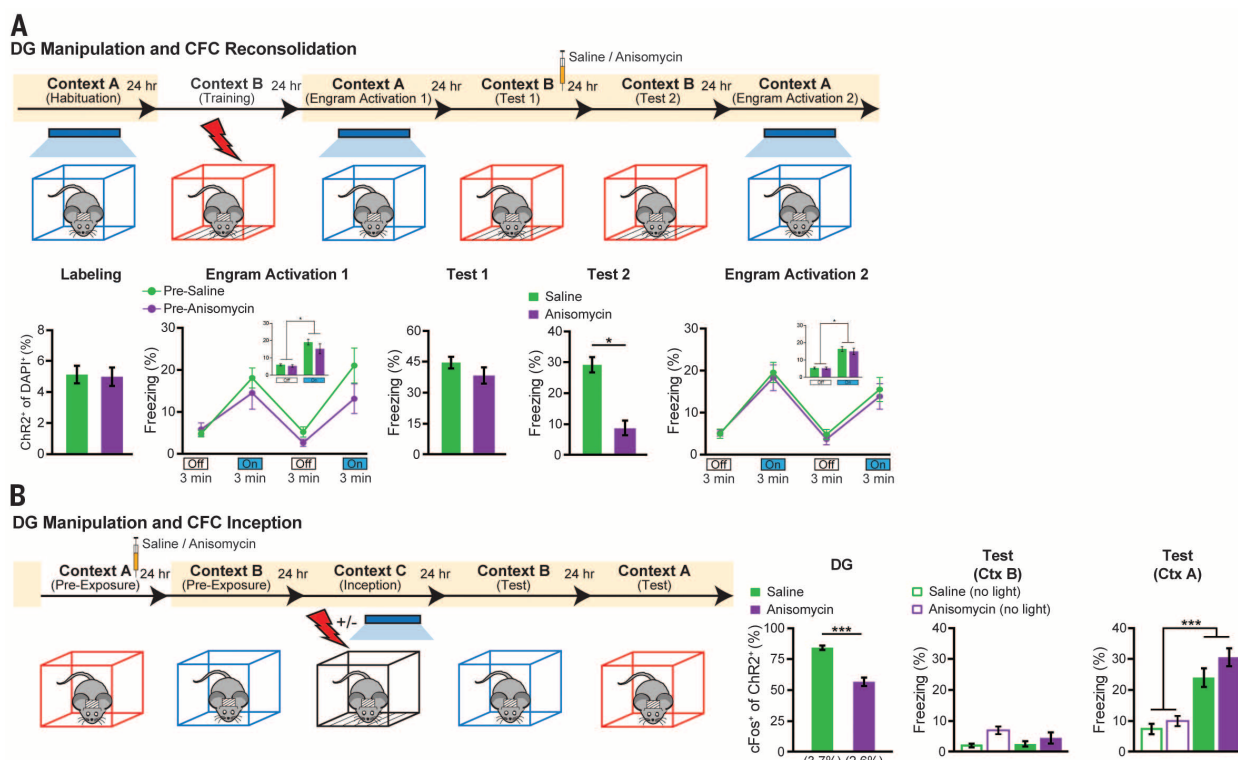


**Fig. 4. Reconsolidation and memory updating.** (A) DG engram activation and CFC reconsolidation. ANI ( $n = 11$  mice) and SAL ( $n = 11$  mice) groups showed similar levels of ChR2 labeling. Both groups showed light-induced freezing behavior 1 day after training (engram activation 1), pre-SAL ( $P < 0.001$ ), pre-ANI ( $P < 0.02$ ). Two days after training (test 1), the fear memory was reactivated by exposure to context B, and SAL or ANI was injected. Three days after training (test 2), the ANI group froze significantly less than did the SAL group to context B ( $P < 0.01$ ). Four days after training (engram activation 2), significant light-induced freezing was observed for the SAL ( $P < 0.001$ ) and ANI ( $P < 0.003$ ) groups. (B) DG inception (supplementary materials,

materials and methods) after contextual memory amnesia. Context-only engram was labeled for target context A, followed by injection of SAL ( $n = 11$  mice) or ANI ( $n = 11$  mice). Amnesia was demonstrated in the ANI group through decreased ChR2<sup>+</sup>/c-Fos<sup>+</sup> colabeling after context A reexposure 1 day after labeling. After fear inception, neither SAL nor ANI groups displayed freezing behavior in context B, whereas both groups displayed significant freezing in context A, with no significant difference between groups. No-light inception SAL ( $n = 7$  mice) and ANI ( $n = 6$  mice) controls displayed no freezing to context A or B. Statistical comparisons are performed by using unpaired  $t$  tests; \*\*\* $P < 0.001$ . Data are presented as mean  $\pm$  SEM.

until the current study, as a property of the engram cells. Our data have directly linked the optogenetically and behaviorally defined memory engram cells to synaptic plasticity.

On the basis of a large volume of previous studies, (1–3, 7, 8, 32–34), a concept has emerged

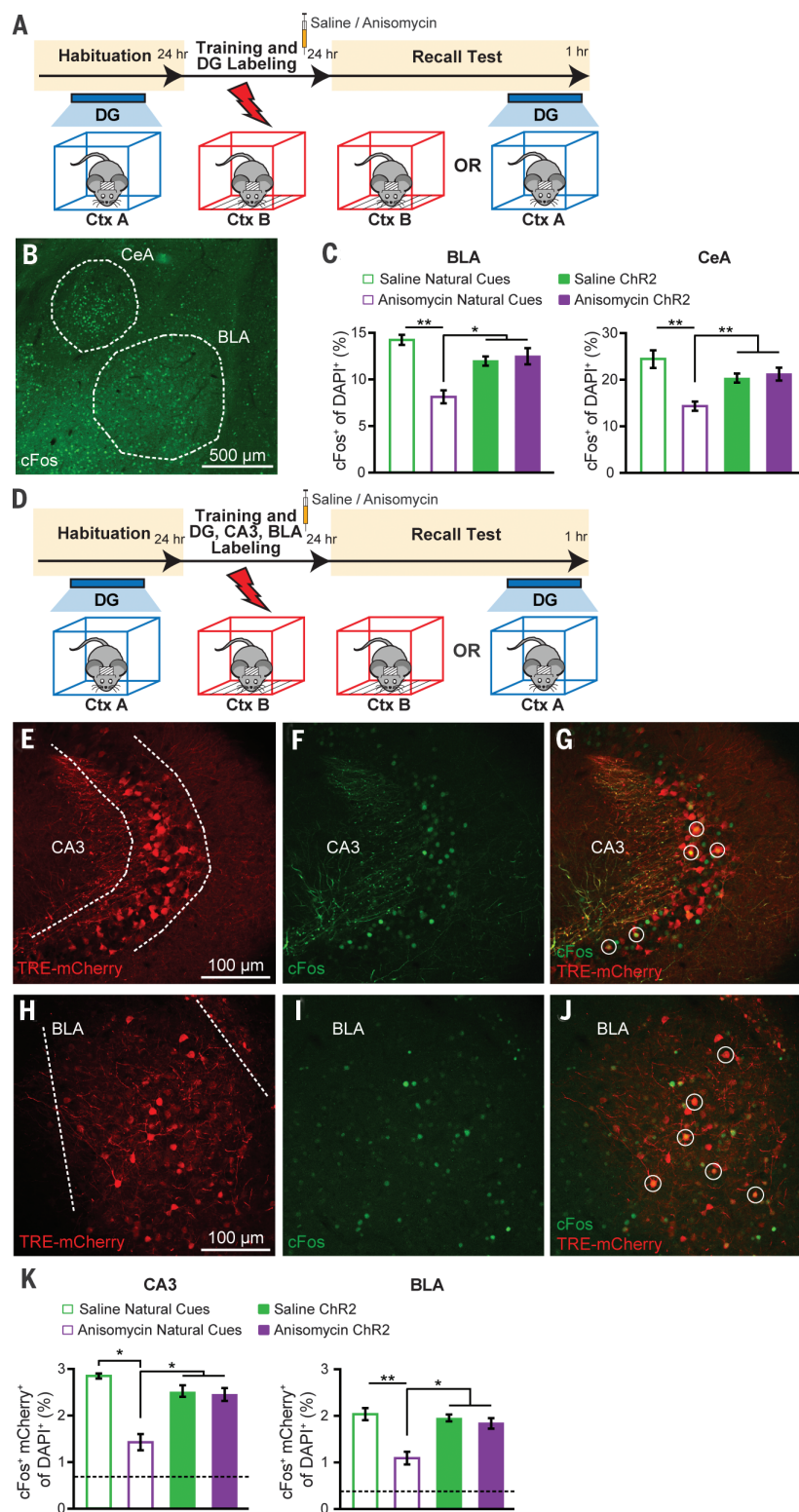
in which retrograde amnesia arises from consolidation failure as a result of disrupting the process that converts a fragile memory engram, formed during the encoding phase, into a stable engram with persistently augmented synaptic strength and spine density. Indeed, our current

study has demonstrated that amnesic engram cells in the DG 1 day after CFC training display low levels of synaptic strength and spine density that are indistinguishable from nonengram cells of the same DG. This correlated with a lack of memory recall elicited by contextual cues.

**Fig. 5. Amygdala activation and functional connectivity in amnesia through light activation of DG engram.** (A) Schedule for cell-counting experiments. Mice were either given a natural recall session in context B or a light-induced recall session in context A. Mice were perfused 1 hour after recall.

(B) Representative image showing c-Fos expression in the BLA and CeA. (C) c-Fos<sup>+</sup> cell counts in the BLA and CeA of mice after natural or light-induced recall ( $n = 3$  or 4 mice per group). (D) Schedule for cell-counting experiments. c-Fos-tTA mice with AAV<sub>9</sub>-TRE-ChR2-EYFP injected into the DG and AAV<sub>9</sub>-TRE-mCherry injected into both CA3 and BLA were fear-conditioned off DOX and 1 day later were given a natural recall session in context B or a light-induced recall session in context A. Mice were perfused 1 hour after recall.

(E to G) Representative images showing mCherry engram cell labeling, c-Fos expression, and mCherry<sup>+</sup>/c-Fos<sup>+</sup> overlap in CA3. (H to J) Representative images showing mCherry engram cell labeling, c-Fos expression, and mCherry/c-Fos overlap in BLA. (K) c-Fos<sup>+</sup>/mCherry<sup>+</sup> overlap cell counts in CA3 and BLA of mice after natural or light-induced recall ( $n = 3$  or 4 mice per group). Chance levels were estimated at 0.76 (CA3) and 0.42 (BLA). Data are presented as mean  $\pm$  SEM. Statistical comparison are performed by using unpaired  $t$  tests; \* $P < 0.05$ , \*\* $P < 0.01$ .





However, direct activation of DG engram cells of the ANI group elicited as much freezing behavior as did the activation of these cells of the SAL group. This unexpected finding is supported by a set of additional cellular and behavioral experiments. Whereas amygdala engram cell reactivation upon exposure to the conditioned context is significantly lower in the ANI group as compared with the SAL group, optogenetic activation of DG engram cells results in normal reactivation of downstream CA3 and BLA engram cells (Fig. 5). At the behavioral level, the amnesia rescue was observed under a variety of different conditions in which one or more parameters were altered (Figs. 2 and 3 and Figs. S9 and S13). Thus, our overall findings indicate that memory engrams survive a posttraining administration of protein synthesis inhibitors during the consolidation window and that the memory remains retrievable by means of ChR2-mediated direct engram activation even after retrograde amnesia is induced. The drive initiated with light-activation of one component of a distributed memory engram (such as that in the DG) is sufficient to reactivate engrams in downstream regions (such as that in CA3 and BLA) that would also be affected by the systemic injection of a protein synthesis inhibitor (ANI).

These findings suggest that although a rapid increase of synaptic strength is likely to be crucial during the encoding phase, the augmented synaptic strength is not a crucial component of the stored memory (35–37). This perspective is consistent with a recent study showing that an artificial memory could be reversibly disrupted by depression of synaptic strength (38). On the other hand, persistent and specific connectivity of engram cells that we find between DG engram cells and downstream CA3 or BLA engram cells in both SAL and ANI groups may represent a fundamental mechanism of memory information storage (39). Our findings also suggest that the primary role of augmented synaptic strength during and after the consolidation phase may be to provide natural recall cues with efficient access to the soma of engram cells for their reactivation and, hence, recall.

The integrative memory engram-based approach used here for parsing memory and amnesia into encoding, consolidation, and retrieval aspects may be of wider use to other experimental and clinical cases of amnesia, such as Alzheimer's disease (40).

## REFERENCES AND NOTES

- G. E. Müller, A. Pilzecker, *Z. Psychol.* **1**, 1–288 (1900).
- C. P. Duncan, *J. Comp. Physiol. Psychol.* **42**, 32–44 (1949).
- J. L. McGaugh, *Science* **287**, 248–251 (2000).
- J. B. Flexner, L. B. Flexner, E. Stellar, *Science* **141**, 57–59 (1963).
- L. B. Flexner, J. B. Flexner, R. B. Roberts, *Science* **155**, 1377–1383 (1967).
- H. P. Davis, L. R. Squire, *Psychol. Bull.* **96**, 518–559 (1984).
- E. R. Kandel, *Science* **294**, 1030–1038 (2001).
- R. J. Kelleher 3rd, A. Govindarajan, S. Tonegawa, *Neuron* **44**, 59–73 (2004).
- T. Takeuchi, A. J. Duszkievicz, R. G. Morris, *Philos. Trans. R. Soc. Lond. B Biol. Sci.* **369**, 20130288 (2014).
- A. Govindarajan, I. Israly, S. Y. Huang, S. Tonegawa, *Neuron* **69**, 132–146 (2011).
- M. Krug, B. Lössner, T. Ott, *Brain Res. Bull.* **13**, 39–42 (1984).
- U. Frey, M. Krug, K. G. Reymann, H. Matthies, *Brain Res.* **452**, 57–65 (1988).
- Y. Y. Huang, P. V. Nguyen, T. Abel, E. R. Kandel, *Learn. Mem.* **3**, 74–85 (1996).
- R. Semon, *Die Mneme als erhaltendes Prinzip im Wechsel des organischen Geschehens* (Wilhelm Engelmann, Leipzig, 1904).
- S. A. Josselyn, *J. Psychiatry Neurosci.* **35**, 221–228 (2010).
- X. Liu et al., *Nature* **484**, 381–385 (2012).
- S. Ramirez et al., *Science* **341**, 387–391 (2013).
- R. L. Redondo et al., *Nature* **513**, 426–430 (2014).
- C. A. Denny et al., *Neuron* **83**, 189–201 (2014).
- K. Z. Tanaka et al., *Neuron* **84**, 347–354 (2014).
- K. K. Cowansage et al., *Neuron* **84**, 432–441 (2014).
- L. G. Reijmers, B. L. Perkins, N. Matsuo, M. Mayford, *Science* **317**, 1230–1233 (2007).
- R. L. Clem, R. L. Huganir, *Science* **330**, 1108–1112 (2010).
- A. Suzuki et al., *J. Neurosci.* **24**, 4787–4795 (2004).
- B. N. Armbruster, X. Li, M. H. Pausch, S. Herlitze, B. L. Roth, *Proc. Natl. Acad. Sci. U.S.A.* **104**, 5163–5168 (2007).
- J. H. Han et al., *Science* **323**, 1492–1496 (2009).
- J. R. Misanin, R. R. Miller, D. J. Lewis, *Science* **160**, 554–555 (1968).
- K. Nader, G. E. Schafe, J. E. LeDoux, *Nature* **406**, 722–726 (2000).
- X. Liu, S. Ramirez, S. Tonegawa, *Philos. Trans. R. Soc. Lond. B Biol. Sci.* **369**, 20130142 (2014).
- A. Besnard, S. Larocque, J. Caboche, *Brain Struct. Funct.* **219**, 415–430 (2014).
- J. Hall, K. L. Thomas, B. J. Everitt, *Eur. J. Neurosci.* **13**, 1453–1458 (2001).
- J. L. McGaugh, *Science* **153**, 1351–1358 (1966).
- Y. Dudai, *Annu. Rev. Psychol.* **55**, 51–86 (2004).
- J. P. Johansen, C. K. Cain, L. E. Ostroff, J. E. LeDoux, *Cell* **147**, 509–524 (2011).
- R. R. Miller, L. D. Matzel, *Learn. Mem.* **13**, 491–497 (2006).
- C. A. Miller, J. D. Sweatt, *Learn. Mem.* **13**, 498–505 (2006).
- S. Chen et al., *eLife* **3**, e02844 (2014).
- S. Nabavi et al., *Nature* **511**, 348–352 (2014).
- D. O. Hebb, *The Organization of Behavior; A Neuropsychological Theory* (Wiley, New York, 1949).
- S. Daumas et al., *Learn. Mem.* **15**, 625–632 (2008).

## ACKNOWLEDGMENTS

We thank X. Liu and B. Roth for sharing reagents; X. Zhou, Y. Wang, W. Yu, S. Huang, and T. O'Connor for technical assistance; J. Z. Young for proofreading; and other members of the Tonegawa Laboratory for their comments and support. This work was supported by the RIKEN Brain Science Institute, Howard Hughes Medical Institute, and the JPB Foundation (to S.T.). pAAV-TRE-ChR2-EYFP, pAAV-TRE-ChR2-mCherry, and pAAV-TRE-mCherry were developed by X.L., in the group of S.T., at the Massachusetts Institute of Technology; therefore, a materials transfer agreement (MTA) is required to obtain these virus plasmids.

## SUPPLEMENTARY MATERIALS

www.sciencemag.org/content/348/6238/1007/suppl/DC1  
Materials and Methods  
Figs. S1 to S13  
Reference (41)

22 December 2014; accepted 30 April 2015  
10.1126/science.aaa5542

## COGNITIVE NEUROSCIENCE

# Unlearning implicit social biases during sleep

Xiaoqing Hu,<sup>1,2</sup> James W. Antony,<sup>1,3</sup> Jessica D. Creery,<sup>1</sup> Iliana M. Vargas,<sup>1</sup> Galen V. Bodenhausen,<sup>1</sup> Ken A. Paller<sup>1\*</sup>

Although people may endorse egalitarianism and tolerance, social biases can remain operative and drive harmful actions in an unconscious manner. Here, we investigated training to reduce implicit racial and gender bias. Forty participants processed counterstereotype information paired with one sound for each type of bias. Biases were reduced immediately after training. During subsequent slow-wave sleep, one sound was unobtrusively presented to each participant, repeatedly, to reactivate one type of training. Corresponding bias reductions were fortified in comparison with the social bias not externally reactivated during sleep. This advantage remained 1 week later, the magnitude of which was associated with time in slow-wave and rapid-eye-movement sleep after training. We conclude that memory reactivation during sleep enhances counterstereotype training and that maintaining a bias reduction is sleep-dependent.

**S**ocial interactions are often fraught with bias. Our preconceptions about other people can influence many types of behavior. For example, documented policing errors have repeatedly shown the potential harm of racial profiling (1). In experiments that used a first-person-shooter videogame, both White and Black participants were more likely to shoot Black

than White individuals, even when they held a harmless object rather than a gun (2). When hiring potential research assistants, both male and female faculty members were more likely to hire male than equally qualified female candidates (3).

Although the tendency for people to endorse racist or sexist attitudes explicitly has decreased in recent years (4), social biases may nevertheless influence people's behavior in an implicit or unconscious manner, regardless of their intentions or efforts to avoid bias (5). Ample evidence indicates that implicit biases can drive discriminatory behaviors and exacerbate intergroup conflict (5–8). For instance, implicit racial biases decrease investments given to racial out-group members

<sup>1</sup>Department of Psychology, Northwestern University, Evanston, IL 60208, USA. <sup>2</sup>Department of Psychology, University of Texas at Austin, Austin, TX 78712, USA. <sup>3</sup>Princeton Neuroscience Institute, Princeton University, Princeton, NJ 08544, USA.

\*Corresponding author. E-mail: kap@northwestern.edu

in a trust game (6). At a broader level, the gender gap in science achievement in a nation is correlated with the level of implicit stereotyping of females as not having an aptitude for science (8).

Whereas discriminatory behaviors can be detrimental to individuals and society, implicit social bias can be difficult to correct because of a range of affective, cognitive, motivational, and social factors, as follows (9, 10). First, out-group members can be perceived as threatening, and the fear response to those individuals can resist extinction (11). Second, biases are acquired over many years of exposure to stereotypes, and they can efficiently operate without occupying cognitive resources (5, 10). Third, motivation to seek higher status or self-enhancement commonly results in out-group derogation (9, 10). Last, perceived social norms can prescribe people's expression of stereotyping and prejudice (12). Despite such challenges, implicit biases can be reduced by learning about counterstereotype cases (13). However, benefits of this counterbias training can be fragile, subject to reversal when the original stereotypes are again reinforced in typical circumstances, such as through the media (14). Longer-term reductions in implicit social biases may necessitate that counterbias training be followed by further memory consolidation, as is the case for many other types of learning (15).

Recent findings suggest that memory consolidation during sleep may be essential for preserving newly acquired information, such as declarative and procedural memories (15–19). During sleep, information recently stored in the brain can be integrated with other information and transformed into stable representations through a process known as systems-level consolidation (15). The mechanisms of this transformation are thought to involve repeated reactivation of information, particularly during sleep, leading to subsequent improvement in postsleep memory performance (19–24).

Taking into consideration the role of sleep in memory consolidation, we adapted procedures for (i) reducing implicit social biases and (ii) reactivating this training during sleep. We were particularly interested in factors that can influence whether such training procedures produce transient or persistent effects. Because pervasive stereotypes in the media and broader culture could function to regenerate a bias that is momentarily reduced (14), maintaining the benefits of training is crucial for the ultimate usefulness of potential bias-reducing interventions.

We reactivated counterbias information during sleep using subtle auditory cues that had been associated with counterbias training. Participants were White males and females from a university community ( $N = 40$ ) and were recruited as two subsamples that allowed for a direct replication (25). First, biases were quantified using two versions of the implicit association test (IAT) (26). The IAT allows for an assessment of the strength of implicit associations between social groups and attributes (26). One test examined the degree to which female faces were preferentially associated with art versus science words—or the re-

verse for male faces (gender-bias IAT). The other test examined the degree to which Black faces were preferentially associated with bad versus good words—or the reverse for White faces (racial-bias IAT). Results were quantified by using a conventional scoring procedure (27), in which zero indicates no bias and larger scores indicate greater bias. Consistent with previous research (7), IAT scores showed that participants held implicit social biases for both gender and race, with both scores significantly greater than zero [mean  $\pm$  SEM,  $0.559 \pm 0.044$ ; gender  $t(39) = 9.076$ ,  $P < 0.001$ ; race  $t(39) = 8.388$ ,  $P < 0.001$ ].

After this confirmation of baseline levels of implicit bias, participants engaged in training designed to reduce gender and racial bias (13). In

both cases, bias reduction was expected because participants intentionally selected counterstereotype information intermixed with other information. Participants viewed several types of face-word pairing but were required to attend and respond only to pairings that countered the typical bias (Fig. 1A) (25). Two unusual frequency-modulated sounds were presented during training, one after correct counter-gender bias responses and the other after correct counter-racial bias responses. To reinforce these associations, we administered another task wherein the same two sounds prompted participants to form a corresponding face-word pairing (25). Training thus established a strong association between each sound and one type of counterbias training.

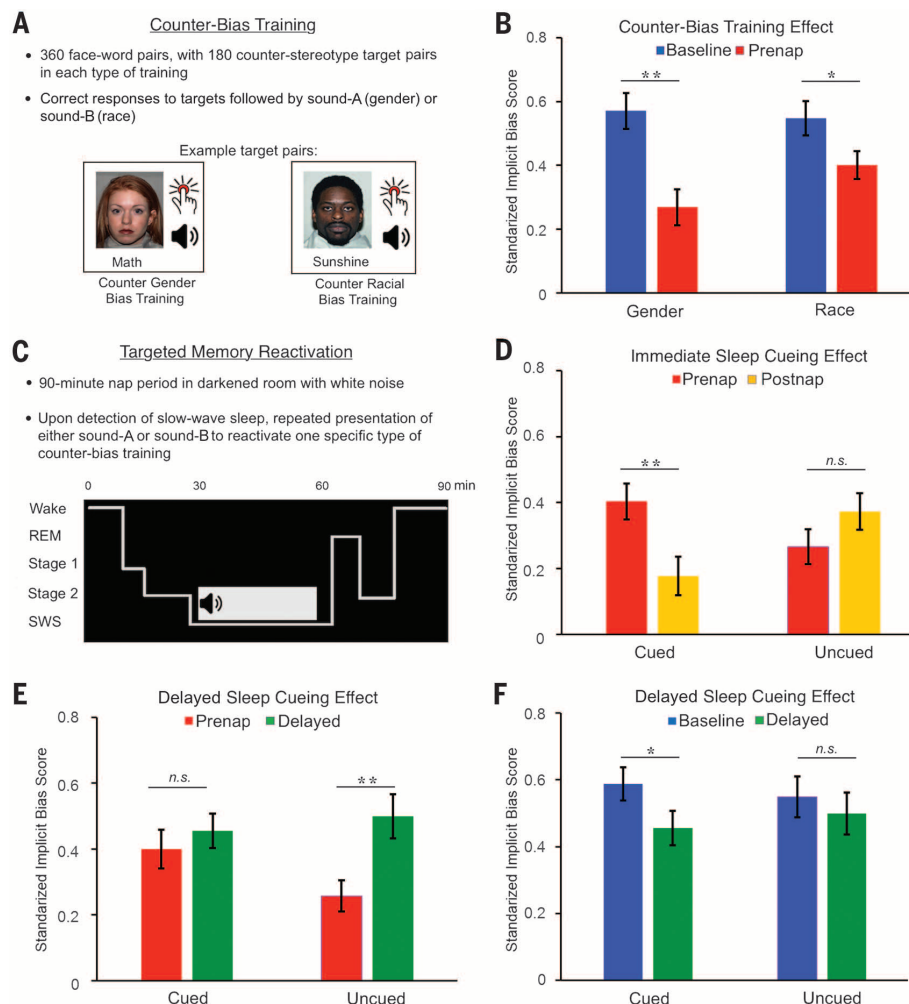


**Fig. 1. Experimental procedures and results.** (A) Procedures for counterbias training with sound cues. (B) Implicit bias reduction was found for both counter-racial bias training and counter-gender stereotype training. Bias was measured using the IAT before training (baseline) and after training (prenap). Error bars indicate  $\pm 1$  SEM adjusted for within-subject comparisons. (C) Procedures for the nap phase of the experiment, when one sound was repeatedly played to participants during SWS, using a low intensity to avoid arousal from sleep. (D) The change in implicit bias from prenap to postnap diverged as a function of cueing condition, with a further reduction only for the cued social bias. (E) The change in implicit bias from prenap to the 1-week delay diverged as a function of cueing condition, with a significant increase only for the uncued social bias. (F) The change in implicit bias from baseline to the 1-week delay diverged as a function of cueing condition, with a significant reduction only for the cued social bias. Significant pairwise differences are indicated: \* $P < 0.05$  or \*\* $P \leq 0.01$ .



Biases were reduced compared with baseline levels (Fig. 1B) [within-subject analysis of variance (ANOVA),  $F_{1,39} = 15.453$ ,  $P < 0.001$ ,  $\eta_p^2 = 0.284$ ]. The mean IAT score was 0.559 at baseline and 0.335 at the prenap test. This bias reduction did not differ as a function of bias type ( $F_{1,39} = 1.840$ ,  $P = 0.183$ ).

Next, participants were invited to take a 90-min afternoon nap (Fig. 1C; see table S1 for sleep-stage information). When electroencephalographic signals showed clear signs of slow-wave sleep (SWS), we repeatedly played one auditory cue, randomly selected as the counter-gender bias sound ( $n = 21$ ) or the counter-racial bias sound ( $n = 19$ ). Stimulation was discontinued at any sign of arousal from sleep. The number of presentations averaged  $258 \pm 24$  (SEM).

Implicit biases were measured again after waking. Bias change from prenap to postnap varied with cueing condition as predicted [substantiated by a two-way interaction (cued or uncued by prenap or postnap),  $F_{1,39} = 14.612$ ,  $P < 0.001$ ,  $\eta_p^2 = 0.273$ ]. As shown in Fig. 1D, implicit bias was significantly reduced from prenap to postnap when cued [ $t(39) = 2.698$ ,  $P = 0.010$ ] and unchanged when not cued [ $t(39) = -1.378$ ,  $P = 0.176$ ] (fig. S1 and S2). This differential bias reduction was not moderated by bias type (fig. S3). Thus, reactivating counterbias learning during sleep can selectively reduce implicit racial or gender bias, depending on which form of counterbias training was cued.

Implicit biases were measured again after 1 week, revealing that the differential bias reduction endured (Fig. 1E) ( $n = 38$ ;  $F_{1,37} = 4.672$ ,  $P = 0.037$ ,  $\eta_p^2 = 0.112$ ). Cueing during sleep resulted in sustained counterbias reduction, such that the cued bias did not differ between prenap and delayed testing

[ $t(37) = -0.774$ ,  $P = 0.444$ ], whereas the uncued bias increased during the delay [ $t(37) = -3.078$ ,  $P = 0.004$ ]. When compared with baseline (Fig. 1F), cued biases were weaker after 1 week [ $t(37) = 2.203$ ,  $P = 0.034$ ], whereas uncued biases were not [ $t(37) = 0.524$ ,  $P = 0.603$ ], although the interaction was not significant ( $F_{1,37} = 0.471$ ,  $P = 0.497$ ).

Neurophysiological activity during sleep—such as sleep spindles, slow waves, and rapid-eye-movement (REM) duration—can predict later memory performance (17). Accordingly, we explored possible relations between cueing-specific bias reduction and measures of sleep physiology. We found that only SWS  $\times$  REM sleep duration consistently predicted cueing-specific bias reduction at 1 week relative to baseline (Fig. 2) [ $r(38) = 0.450$ ,  $P = 0.005$ ] (25).

Past research indicates that by pairing learning episodes with auditory or olfactory stimuli and then presenting these stimuli again during postlearning SWS, learned information can be specifically reactivated and strengthened (19). Benefits of this targeted memory reactivation (TMR) have been documented for declarative, procedural, and emotional memories (19). Such learning typically does not challenge preexisting knowledge nor compete with daily experiences outside the laboratory. In contrast, we examined learning-induced changes in long-standing social biases. We showed that selectively reactivating counterbias learning during sleep weakened preexisting implicit social biases immediately after the nap and facilitated the retention of this learning going forward. Without TMR during sleep, training effects tended to dissipate, and the bias returned to baseline levels. These results thus enlarge our conception of sleep's role in socially relevant learning.

Observed relations between sleep neurophysiology and behavior further reinforced the conclusion that bias reduction is sleep-dependent. Current thinking about consolidation emphasizes sets of cortical networks that can become integrated through interactions with hippocampal networks, possibly by means of cyclic SWS-REM periods (15–17, 28). The correlation with SWS  $\times$  REM duration implicates a benefit from REM-based processing subsequent to SWS-based reactivation, perhaps to integrate learning within associative knowledge networks. These findings support the notion that both SWS and REM are operative in sleep-dependent memory consolidation (16, 17, 28, 29).

Future research is needed to address many outstanding questions in relation to our findings. For example, how much training is needed to make implicit benefits persist for long periods of time and transfer to explicit benefits in interpersonal interactions? To what extent do persistent benefits depend on repeated training, the nature of other waking activities after training, and repeated memory reactivation during sleep? Although IAT measures are imperfect and may sometimes reflect knowledge of cultural stereotypes rather than implicit bias per se (30), prior research has demonstrated consequences for social behavior, such that low implicit bias as measured with the IAT may

indeed be linked with egalitarianism (6, 7). Given that training to reduce implicit bias can be conceptualized as a type of habit learning (31), perhaps novel sleep manipulations could be adapted to aid people in changing various unwanted or maladaptive habits, such as smoking, unhealthy eating, catastrophizing, or selfishness (32).

## REFERENCES AND NOTES

1. J. Glaser, *Suspect Race: Causes and Consequences of Racial Profiling* (Oxford Univ. Press, New York, 2014).
2. J. Correll et al., *J. Pers. Soc. Psychol.* **92**, 1006–1023 (2007).
3. C. A. Moss-Racusin, J. F. Dovidio, V. L. Brescoll, M. J. Graham, J. Handelsman, *Proc. Natl. Acad. Sci. U.S.A.* **109**, 16474–16479 (2012).
4. L. Bobo, C. L. Zubrinsky, *Soc. Forces* **74**, 883–909 (1996).
5. P. G. Devine, *J. Pers. Soc. Psychol.* **56**, 5–18 (1989).
6. D. A. Stanley, P. Sokol-Hessner, M. R. Banaji, E. A. Phelps, *Proc. Natl. Acad. Sci. U.S.A.* **108**, 7710–7715 (2011).
7. A. G. Greenwald, T. A. Poehlman, E. L. Uhlmann, M. R. Banaji, *J. Pers. Soc. Psychol.* **97**, 17–41 (2009).
8. B. A. Nosek et al., *Proc. Natl. Acad. Sci. U.S.A.* **106**, 10593–10597 (2009).
9. G. W. Allport, *The Nature of Prejudice* (Addison-Wesley, Reading, MA, 1979).
10. S. Fiske, in *The Handbook of Social Psychology*, D. T. Gilbert, S. T. Fiske, G. Lindzey, Eds. (Oxford Univ. Press, New York, ed. 4, 1998), vol. 2, pp. 357–411.
11. A. Olsson, J. P. Ebert, M. R. Banaji, E. A. Phelps, *Science* **309**, 785–787 (2005).
12. C. S. Crandall, A. Eshleman, L. O'Brien, *J. Pers. Soc. Psychol.* **82**, 359–378 (2002).
13. B. Gawronski, R. Deutsch, S. Mbirikou, B. Seibt, F. Strack, *J. Exp. Soc. Psychol.* **44**, 370–377 (2008).
14. M. Weisbuch, K. Pauker, N. Ambady, *Science* **326**, 1711–1714 (2009).
15. K. A. Paller, in *Encyclopedia of Neuroscience*, L. R. Squire, Ed. (Academic Press, Oxford, 2009), pp. 741–749.
16. B. Rasch, J. Born, *Physiol. Rev.* **93**, 681–766 (2013).
17. S. Diekelmann, J. Born, *Nat. Rev. Neurosci.* **11**, 114–126 (2010).
18. R. Stickgold, M. P. Walker, *Nat. Neurosci.* **16**, 139–145 (2013).
19. D. Oudiette, K. A. Paller, *Trends Cogn. Sci.* **17**, 142–149 (2013).
20. B. Rasch, C. Büchel, S. Gais, J. Born, *Science* **315**, 1426–1429 (2007).
21. J. W. Antony, E. W. Gobel, J. K. O'Hare, P. J. Reber, K. A. Paller, *Nat. Neurosci.* **15**, 1114–1116 (2012).
22. M. A. Wilson, B. L. McNaughton, *Science* **265**, 676–679 (1994).
23. P. Peigneux et al., *Neuron* **44**, 535–545 (2004).
24. J. D. Rudoy, J. L. Voss, C. E. Westerberg, K. A. Paller, *Science* **326**, 1079 (2009).
25. Materials and methods are available as supplementary materials on Science online.
26. A. G. Greenwald, D. E. McGhee, J. L. K. Schwartz, *J. Pers. Soc. Psychol.* **74**, 1464–1480 (1998).
27. A. G. Greenwald, B. A. Nosek, M. R. Banaji, *J. Pers. Soc. Psychol.* **85**, 197–216 (2003).
28. R. Stickgold, D. Whidbee, B. Schirmer, V. Patel, J. A. Hobson, *J. Cogn. Neurosci.* **12**, 246–254 (2000).
29. M. V. Ambrosini, A. Giuditta, *Sleep Med. Rev.* **5**, 477–490 (2001).
30. H. R. Arkes, P. E. Tetlock, *Psychol. Inq.* **15**, 257–278 (2004).
31. P. G. Devine, P. S. Forscher, A. J. Austin, W. T. L. Cox, *J. Exp. Soc. Psychol.* **48**, 1267–1278 (2012).
32. A. Arzi et al., *J. Neurosci.* **34**, 15382–15393 (2014).

## ACKNOWLEDGMENTS

Support was provided by Northwestern University and by NSF grants BCS-1025697, BCS-1461088, and DGE-0824162, and by NIH grants T32-AG020418 and F31-MH100958. Data are archived and available on the Open Science Framework (<https://osf.io/b3k9a/>). K.A.P. served as an advisor to Sheepdog Sciences (a company developing educational technologies related to sleep) in exchange for equity compensation. The authors declare no conflict of interests.

## SUPPLEMENTARY MATERIALS

[www.sciencemag.org/content/348/6238/1013/suppl/DC1](http://www.sciencemag.org/content/348/6238/1013/suppl/DC1)  
Materials and Methods  
Supplementary Text  
Figs. S1 to S3  
Table S1  
Sound Files  
References (33–36)

2 December 2014; accepted 20 April 2015  
10.1126/science.aaa3841

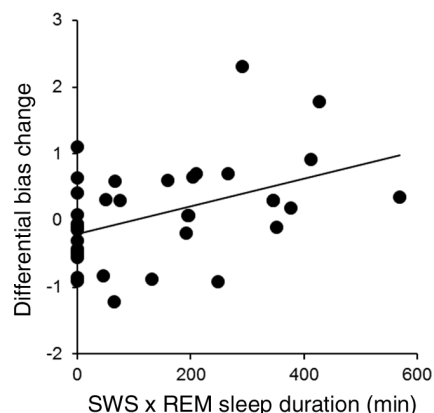


**Fig. 2. Relation between long-term bias reduction and sleep physiology.** The quality of sleep after training as indexed by the product of (minutes in SWS)  $\times$  (minutes in REM sleep), predicted differential bias change, quantified as follows. Given that standardized implicit bias scores were preferentially reduced for the cued relative to uncued condition overall (Fig. 1F), we computed the reduction separately for cued and uncued conditions [(baseline score) – (delayed score) in both cases]. Differential bias change was taken as the cued reduction minus the uncued reduction, such that higher values indicated larger bias reduction over this interval for the cued compared to the uncued bias.

## PALEOCLIMATE

# Enhanced tropical methane production in response to iceberg discharge in the North Atlantic

Rachael H. Rhodes,<sup>1\*</sup> Edward J. Brook,<sup>1</sup> John C. H. Chiang,<sup>2</sup> Thomas Blunier,<sup>3</sup> Olivia J. Maselli,<sup>4</sup> Joseph R. McConnell,<sup>4</sup> Daniele Romanini,<sup>5</sup> Jeffrey P. Severinghaus<sup>6</sup>

The causal mechanisms responsible for the abrupt climate changes of the Last Glacial Period remain unclear. One major difficulty is dating ice-rafted debris deposits associated with Heinrich events: Extensive iceberg influxes into the North Atlantic Ocean linked to global impacts on climate and biogeochemistry. In a new ice core record of atmospheric methane with ultrahigh temporal resolution, we find abrupt methane increases within Heinrich stadials 1, 2, 4, and 5 that, uniquely, have no counterparts in Greenland temperature proxies. Using a heuristic model of tropical rainfall distribution, we propose that Hudson Strait Heinrich events caused rainfall intensification over Southern Hemisphere land areas, thereby producing excess methane in tropical wetlands. Our findings suggest that the climatic impacts of Heinrich events persisted for 740 to 1520 years.

Paleoclimate proxy evidence suggests that the climatic impacts of Heinrich events extended far beyond the North Atlantic basin (1). Enduring questions include whether Heinrich events initiated climate change or occurred in response to it, and how they may be linked to abrupt millennial-scale climate oscillations, typified by Dansgaard-Oeschger (DO) cycles in Greenland ice cores (2). Early correlation between DO cycle variability and sea surface temperature (SST) proxies found that Heinrich events occurred within the coldest, longest stadials of the Greenland  $\delta^{18}\text{O}_{\text{ice}}$  record (3), referred to as Heinrich stadials (HSs) 1 to 6. This correlation could suggest causation: The addition of fresh water causes a shutdown of the Atlantic meridional overturning circulation (AMOC) and prolonged cold conditions (4). However, proxy evidence suggests that AMOC had already slowed and that North Atlantic SSTs were already cold before ice-rafted debris (IRD) deposition, challenging this view (2). Reconstructing event phasing across different proxy records is hampered by the difficulty in dating Heinrich sediment deposits (1). As of yet, the intrastadial timings of individual Heinrich events have not been well determined, and estimates of individual event duration vary by an order of magnitude (1). The sequence and phasing of millennial-scale climate phenomena appear to be intrinsically linked to the ini-

tiation of deglaciation (5), providing additional impetus for investigation.

Here we present a precise, highly resolved record of atmospheric methane ( $\text{CH}_4$ ) concentrations, determined by a recently developed continuous measurement technique (6), for the Last Glacial Period and the deglacial transition from the West Antarctic Ice Sheet (WAIS) Divide (WD) ice core (Fig. 1). Ice core  $\text{CH}_4$  is a globally integrated signal, primarily reflecting the response of the terrestrial biosphere, predominantly wetlands, to hydroclimatic change (7). The WD trace gas record is especially appropriate for paleoreconstruction because rapid occlusion of air bubbles in the firn column results in minimal smoothing of atmospheric signals (estimated gas age distribution width 20 to 50 years, fig. S1). The sampling resolution of our  $\text{CH}_4$  record varies between 0.5 and 13 years, meaning that all climate-driven  $\text{CH}_4$  signals preserved in the ice are captured (8). Continuous  $\text{CH}_4$  analysis produces measurements with excellent internal precision [ $\pm 0.5$  parts per billion (ppb),  $2\sigma$ ] that are reproducible to within  $\pm 3$  ppb ( $2\sigma$ ) over intervals of days to weeks (table S1).

Our continuous  $\text{CH}_4$  record spanning 67.2 to 9.8 thousand years before the present (ky B.P.) (present = 1950 CE) (Fig. 1) resolves growth rates that exceed maximum values previously reported for abrupt climate transitions in this time period (9), the fastest rate occurring at the Younger Dryas termination ( $>6$  ppb  $\text{year}^{-1}$ ). These are minimum estimates of atmospheric growth rate, because firn-related smoothing processes may have attenuated rapid atmospheric  $\text{CH}_4$  changes. We observe no systematic decrease in  $\text{CH}_4$  growth rate across successive DO interstadial onsets (9); however,  $\text{CH}_4$  growth from stadial to interstadial is significantly faster than decay back to stadial levels.

WD  $\text{CH}_4$  covaries with Greenland  $\delta^{18}\text{O}_{\text{ice}}$  and Hulu cave  $\delta^{18}\text{O}_{\text{calcite}}$  at millennial to centennial

time scales (Fig. 1). The close correspondence of these records can be related to latitudinal shifts in the Intertropical Convergence Zone (ITCZ) and its terrestrial component, which we refer to as tropical rain belts; during warm interstadials, the tropical rain belts migrate northward, intensifying Northern Hemisphere monsoonal rainfall and wetland  $\text{CH}_4$  production, whereas the reverse occurs in cool stadials (7, 10). Southern Hemisphere monsoonal strength proxies show an antiphase relationship across DO cycles: relatively wet during stadials and dry during interstadials (Fig. 1E). However, these relationships break down within HSs 1, 2, 4, and 5.

In each case, the early HS is characterized by relatively low  $\text{CH}_4$  concentrations, and the late HS commences with an abrupt 32 to 53 ppb  $\text{CH}_4$  increase (Fig. 2), which occurs at growth rates comparable to those of DO interstadial onsets (Fig. 1A). Within late HSs 4 and 5,  $\text{CH}_4$  concentrations overshoot before returning to a stable level after ~90 and 160 years, respectively (Fig. 2). No overshoot associated with the abrupt  $\text{CH}_4$  increase within HS 2 (24.03 ky B.P.) is resolved, possibly due to inadequate sampling resolution through this section (Fig. 2). The Greenland ice core temperature proxy  $\delta^{15}\text{N}$  of  $\text{N}_2$  indicates clearly that this abrupt  $\text{CH}_4$  increase is not associated with DO 2, which occurred  $>750$  years later (fig. S7).  $\text{CH}_4$  concentrations are steadily rising throughout HS 1 as a result of deglaciation, but an abrupt increase of 32 ppb is resolved at 16.15 ky B.P. (11).  $\text{CH}_4$  levels return to the underlying trend within ~190 years. All late HS phases are characterized by elevated  $\text{CH}_4$  concentrations, relative to early HS phases, that persist until the following DO event (Fig. 2). No similar anomalous  $\text{CH}_4$  signals are observed within other stadials, including HSs 3, 5a, and 6 (fig. S3).

The abrupt  $\text{CH}_4$  signals within HSs 1, 2, 4, and 5 are comparable in magnitude and rate to DO interstadial onsets (Fig. 1A), and yet  $\text{CH}_4$  appears to be completely decoupled from Greenland  $\delta^{18}\text{O}_{\text{ice}}$  (Fig. 2) and  $\delta^{15}\text{N}$  (12). Neither temperature proxy shows the complementary abrupt increases characteristic of interstadials. Furthermore, the  $\text{CH}_4$  signals of HSs 1, 2, 4, and 5 are associated with isotopic enrichment of Hulu  $\delta^{18}\text{O}_{\text{calcite}}$  (Fig. 2) rather than depletion, indicating reduction in the strength of the East Asian monsoon (10). The excess  $\text{CH}_4$  within late HSs 1, 2, 4, and 5 must therefore result from fundamentally different climatic conditions than interstadial  $\text{CH}_4$ .

Other paleoclimate proxies from the Arabian Sea (13), northern Africa (14), and Borneo (15) provide evidence for anomalously dry conditions across the Northern Hemisphere during HSs. Furthermore, South American speleothems (Figs. 1 and 2), Australian sediment archives (16), and ice core  $\delta^{18}\text{O}_{\text{atm}}$  data (17) (fig. S8) suggest concurrent intensification of precipitation across the Southern Hemisphere tropics and subtropics during these intervals. Taken together, the paleoclimatic evidence suggests that the ITCZ occupied an extreme southerly location during HSs. Absolute dates on the Hulu speleothem in HSs

<sup>1</sup>College of Earth, Ocean, and Atmospheric Sciences, 104 CEOAS Administration, Oregon State University, Corvallis, OR 97331, USA. <sup>2</sup>Department of Geography and Berkeley Atmospheric Sciences Center, University of California, Berkeley, CA, USA. <sup>3</sup>Center for Ice and Climate, Niels Bohr Institute, University of Copenhagen, Copenhagen, Denmark. <sup>4</sup>Division of Hydrologic Sciences, Desert Research Institute, 2215 Raggio Parkway, Reno, NV 89512, USA. <sup>5</sup>Joseph Fourier University-Grenoble 1/CNRS, LIPHY UMR 5588, Grenoble, F-38041, France. <sup>6</sup>Scripps Institution of Oceanography, University of California, San Diego, 9500 Gilman Drive, La Jolla, CA 92093-0244, USA.

\*Corresponding author. E-mail: rhodesra@geo.oregonstate.edu



1 and 2, and speleothems from NE Brazil in HS 1 only, indicate that this southerly shift occurred abruptly partway through the stadial, as the anomalous  $\text{CH}_4$  signals do (Fig. 2). Southerly ITCZ displacement can occur in response to Northern Hemisphere cooling and sea-ice expansion (18) and is a consistent outcome of freshwater hosing experiments (19, 20) designed to simulate the effects of iceberg discharge.

This leads us to hypothesize that extended sea-ice cover and associated cold air temperatures in the north, resulting from Heinrich events (1), severely restricted the northerly seasonal migration of the tropical rain belts, forcing them to reside at southerly latitudes for longer periods during their seasonal evolution, thereby extending and intensifying the wet season across the Southern Hemisphere. A similar change in pre-

cipitation seasonality across South America has been observed in response to an extreme freshwater hosing experiment (20). If the resultant gain in Southern Hemisphere tropical wetlands were to exceed the loss in the north, a net gain of  $\text{CH}_4$ -producing wetland would result. The excess stadial  $\text{CH}_4$  we observe could therefore have been sourced from the Southern Hemisphere, as speculated for individual events (11, 27).

A first-order comparison of WD  $\text{CH}_4$  and Greenland  $\text{CH}_4$  data (9) suggests that little change in the  $\text{CH}_4$  inter-pole difference occurred between early and late HSs 4 and 5, supporting our hypothesized tropical source for the additional  $\text{CH}_4$ . Ice core  $\text{CH}_4$  isotopic data may also indicate an increased contribution of Southern Hemisphere wetlands to the  $\text{CH}_4$  budget during late HS 4 (27).

To explore our idea quantitatively, we use a heuristic approach in which the modern-day seasonal distribution of tropical (40°S to 40°N) land rainfall is modified in an idealized manner. We adopt an intense precipitation threshold [monthly average >5 mm day<sup>-1</sup> (8)] as indicative of potential wetland presence. We highlight that potential wetland area peaks twice a year using this metric, once during the summer (monsoon season) of each hemisphere (Fig. 3A), which is similar to the seasonal distribution of tropical  $\text{CH}_4$  emissions (22). The land rainfall distribution is modified by incrementally reducing the intensity of the boreal summer land rainfall peak and redistributing that rainfall, forcing it to occupy more southerly latitudes during the transitional seasons (fig. S5) (8).

As the boreal summer rainfall maximum is progressively reduced, the land area with intense rainfall in boreal summer decreases (Fig. 3A), as does the annual average of land area with intense rainfall (Fig. 3B). This is consistent with colder stadials having lower  $\text{CH}_4$  concentrations, as observed (Fig. 1). A minimum in the annual average land area with intense rainfall is reached at ~60% of the boreal summer rainfall peak amplitude, corresponding to an ~7% total loss of potential wetland area. Crucially, a further reduction of boreal summer rainfall causes a relative increase in potential wetland area of 400,400 km<sup>2</sup> as compared to the minimum (Fig. 3B), primarily during October and November (Fig. 3A).

Assuming that all of this additional land is indeed wetland, the increase can be roughly approximated to an increase in  $\text{CH}_4$  emissions of 29 Tg year<sup>-1</sup> (8). This outcome should be treated with caution because, although rainfall is a powerful control on tropical wetland  $\text{CH}_4$  emissions, several other factors, which we do not account for, influence wetland formation and/or  $\text{CH}_4$  emissions (23). However, our ice core  $\text{CH}_4$  data show a similar magnitude of  $\text{CH}_4$  emissions rate increase (6.5 to 21.2 Tg year<sup>-1</sup>) between early and late HS phases (8), supporting our approach. This scenario provides a simple, heuristic explanation for the observations, but more complex changes in rainfall distribution, not captured by our seasonal modification, probably occurred. For example, warmer Southern Hemisphere temperatures may have caused southward movement of the austral

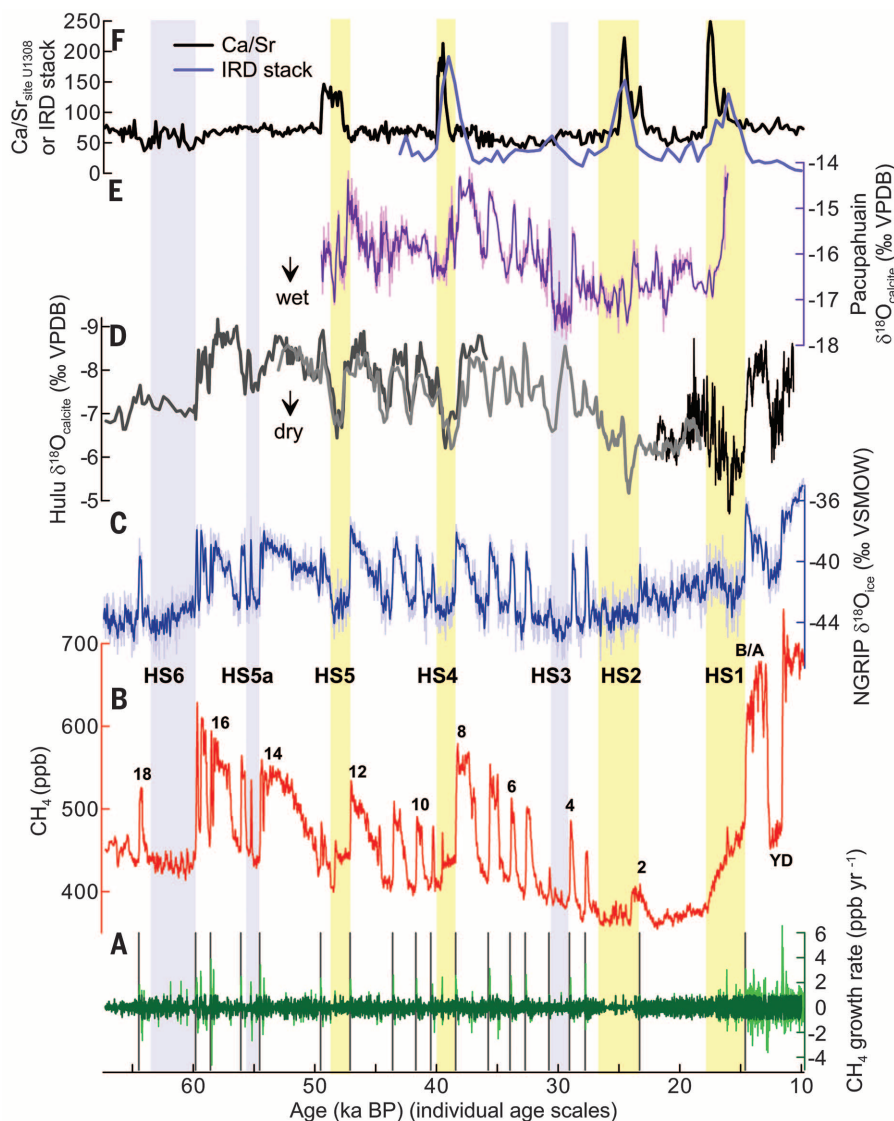


**Fig. 1. WD continuous  $\text{CH}_4$  and other environmental proxies.** (A) WD  $\text{CH}_4$  growth rates between  $\sim 1$  to 1 ppb year<sup>-1</sup> (dark green) and growth rates exceeding these bounds (light green), plotted with vertical gray lines marking interstadial onsets; (B)  $\text{CH}_4$  2-year spline fit (red) (8) on the WD2014 time scale; (C) North Greenland Ice Core Project (NGRIP)  $\delta^{18}\text{O}_{\text{ice}}$  20-year mean record (five-point running mean, dark blue) (27) on a modified Greenland Ice Core Chronology 2005 time scale (8); (D) Hulu cave (China)  $\delta^{18}\text{O}_{\text{calcite}}$  from speleothems: H82 (black) (28), MSD (light gray) and MSL (dark gray) (10) (note inverted y axis); (E) Pacupahuain (Peru) speleothem  $\delta^{18}\text{O}_{\text{calcite}}$  (three-point running mean, dark purple) (29); and (F) Ca/Sr, an indicator of detrital carbonate, from marine sediment core U1208 (reoccupied Deep Sea Drilling Project site 609) (30) and IRD stack of North Atlantic sediment cores (arbitrary units multiplied by 300) (26). HSs 1 to 6 are shaded: pale yellow-shaded HSs contain Heinrich events sourced from the Hudson Strait (high Ca/Sr) and pale blue-shaded HSs contain Heinrich events with a different (or mixed) provenance. Even-numbered DO cycles and the Bølling/Allerød (B/A) and Younger Dryas (YD) intervals are indicated. VSMOW, Vienna standard mean ocean water; VPDB, Vienna Bee Dee belemnite standard.

summer rainfall peak (24), whereas we assume an unaltered austral summer rainfall peak. We have not adopted a coupled climate-biogeochemistry modeling approach because it is not yet clear how to effectively represent a regular Greenlandic stadial versus a Heinrich stadial; the different processes

occurring in the North Atlantic are not adequately understood.

Given the framework outlined above—increased Southern Hemisphere  $\text{CH}_4$  production in response to Northern Hemisphere cooling caused by a Heinrich event—and given that the atmospheric

reorganization can occur within a decade (18), we propose timings for the first impacts of Heinrich events on tropical hydroclimate, which could closely correspond to the initiation of the Heinrich events themselves. The  $\text{CH}_4$  increases we ascribe to Heinrich events 1, 2, 4, and 5 are

**Fig. 2. Detailed view of HSs 1, 2, 4, and 5.** Abrupt  $\text{CH}_4$  increases (A) linked to the onset of Heinrich events are observed within HSs 1, 2, 4, and 5. Discrete  $\text{CH}_4$  measurements (brown symbols) used to construct the  $\text{CH}_4$  2-year spline fit [red, (8)] within HS 2 are displayed. HSs are divided into early HSs (green shading), before the abrupt  $\text{CH}_4$  increase (left-hand vertical line), and late HSs (yellow shading). NGRIP (Greenland)  $\delta^{18}\text{O}_{\text{ice}}$  (27) [(B), five-point running mean, dark blue] shows no abrupt temperature signal in HSs 1, 2, 4, and 5. Hulu (China)  $\delta^{18}\text{O}_{\text{calcite}}$  (10, 28) (C) suggests weakening of the East Asian monsoon, whereas growth phases of speleothems from northeastern Brazil (31) [(D), purple diamonds] suggest strengthening of the South American summer monsoon. U-Th age control points for Hulu speleothems are displayed for HSs 2, 4, and 5 (black/gray diamonds) with  $2\sigma$  uncertainties. Age control points for HS1 are too numerous to display. A stack of IRD records from North Atlantic sediment cores is displayed [(E), purple] with upper (pale blue) and lower (dark blue) 95% confidence intervals in age model (26). Late HSs durations, suggested as maximum durations for the climatic impacts of Heinrich events, are indicated with  $2\sigma$  uncertainty estimates (8). Yellow shading is extended upward to highlight speleothem signals with timings coincident with late HSs 1 and 2.

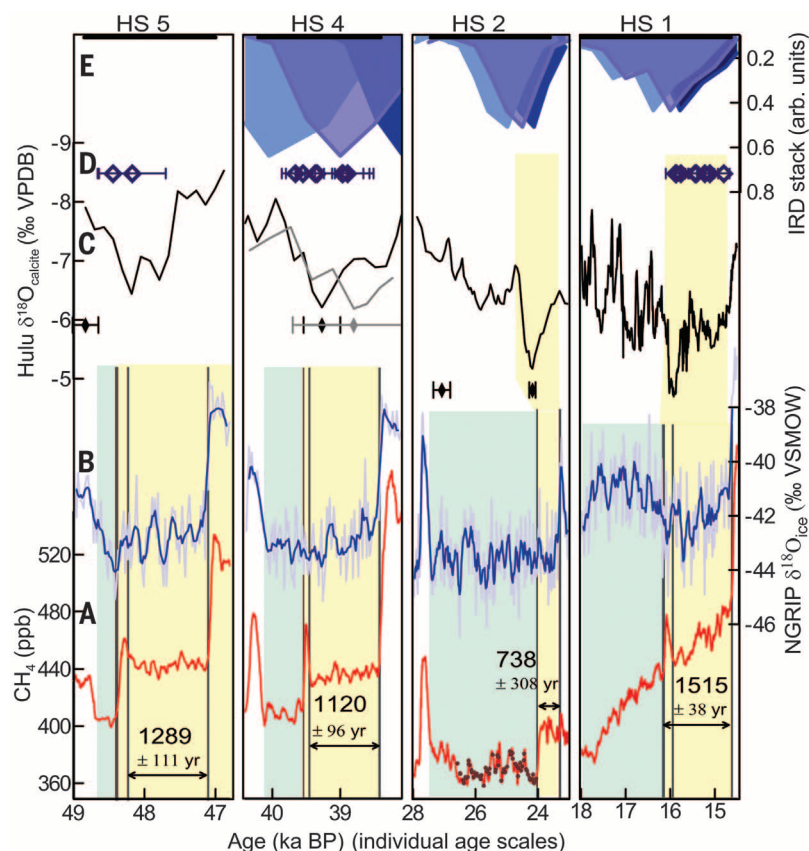
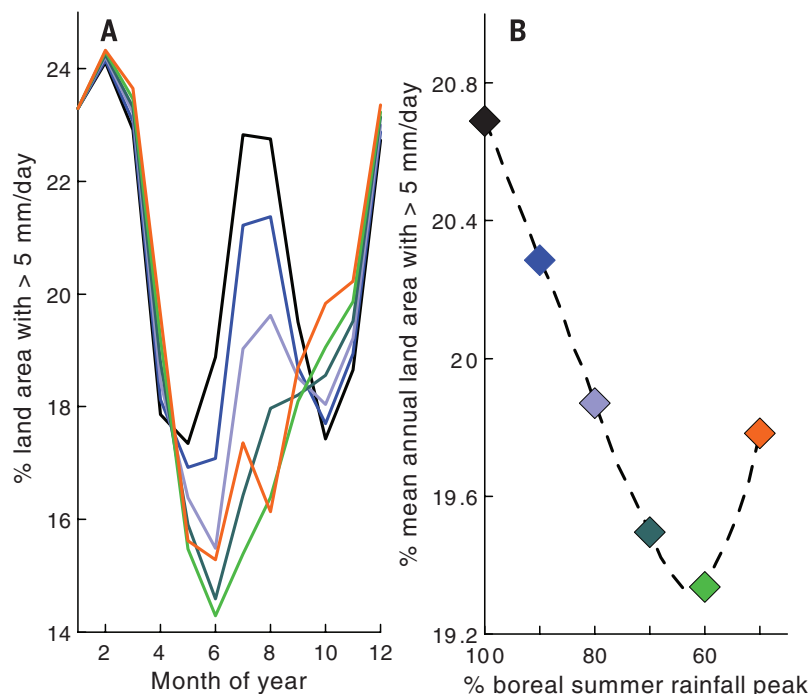


**Fig. 3. Effect of increased Southern Hemisphere weighting of tropical rainfall seasonality on intense land rainfall distribution.** (A) Monthly distribution of the percent of land area with intense (monthly average  $>5 \text{ mm day}^{-1}$ ) rainfall within  $40^\circ\text{S}$  to  $40^\circ\text{N}$ . Modern-day monthly distribution peaks twice a year, once in the summer of each hemisphere (black). The effect of modifying rainfall seasonality on this distribution is shown. Rainfall seasonality becomes increasingly Southern Hemisphere-weighted by incrementally reducing the intensity of the boreal summer land rainfall peak, from 100% (black) to 90% (blue), 80% (light blue), 70% (dark green), 60% (light green), and 50% (orange), with the austral summer rainfall peak held fixed (8). (B) Annual mean percent of land area with intense rainfall for the same increments of the boreal summer land rainfall peak amplitude.





dated as  $16.13 \pm 0.12$  ky B.P.,  $24.03 \pm 0.37$  ky B.P.,  $39.54 \pm 0.38$  ky B.P. and  $48.39 \pm 0.38$  ky B.P., respectively, in the WD2014 chronology (25) [ $2\sigma$  uncertainty (8)]. Our proposed ages for Heinrich events 1 and 2 match the timing of maximum IRD observed in a stack of North Atlantic sediment records (26) (Fig. 2), and closely correspond to calibrated  $^{14}\text{C}$ -based estimates (7). Despite these encouraging signs, we cannot be certain of the phasing of events. For example, the scenario of Northern Hemisphere cooling leading to  $\text{CH}_4$  increase that we describe could potentially occur before the Heinrich event, maybe even triggering the event. This seems an unlikely possibility, given the requirement for another forcing mechanism, the abrupt nature of the  $\text{CH}_4$  signals, and their unique occurrence in Heinrich stadials, but it cannot be ruled out.

The direct impact of a Heinrich event must cease once the ensuing interstadial commences and Northern Hemisphere climate warms (Fig. 1). We calculated maximum durations for the climatic impact of individual Heinrich events, perhaps largely on tropical hydrology, as ranging from 740 to 1520 years (Fig. 2). These estimates are significantly higher than the best guess for the duration of the actual iceberg armada (1 to 500 years) (7). We therefore suggest that this duration is related to a prolonged state of severely slowed or collapsed AMOC, maintained by extensive North Atlantic sea ice. This does not preclude the likelihood that AMOC was already relatively weak before Heinrich events, but rather explains why AMOC strength remained low through an extended stadial period when most coupled models suggest recovery of the overturning circulation within a few hundred years (19). The late HS plateaus in  $\text{CH}_4$  concentration, particularly in HSs 4 and 5, are remarkably stable in comparison to interstadials (Fig. 1), suggesting limited variability in tropical precipitation and a relatively stable AMOC state. It is tempting to speculate on whether we capture information about the actual iceberg armada duration in the ~90- to 190-year  $\text{CH}_4$  overshoots resolved during HSs 1, 4, and 5 (Fig. 2). However, short-duration  $\text{CH}_4$  overshoots are not unique to these events and are in fact a feature of nearly all interstadial onsets, possibly resulting from an intrinsic response of the atmospheric system to rapid reorganization or intensive methanogenesis in newly inundated wetlands.

We suggest that our results provide motivation for climate modeling experiments to further investigate the difference between regular stadials and Heinrich stadials in the North Atlantic region and their respective impacts on tropical climate. Moreover, it is intriguing that only Heinrich events 1, 2, 4, and 5 are associated with Southern Hemisphere  $\text{CH}_4$  signals. These four Heinrich events have relatively thick and spatially extensive sediment deposits, rich in detrital carbonate (Fig. 1) sourced from the Hudson Strait, and are linked to surging of the Laurentide ice sheet (7). Were the remaining Heinrich events too insignificant in scale to greatly perturb tropical climate, or did they not influence the same climate-sensitive location?

## REFERENCES AND NOTES

- S. R. Hemming, *Rev. Geophys.* **42**, RG1005 (2004).
- P. U. Clark, S. W. Hostetler, N. G. Pisias, A. Schmittner, K. J. Meissner, in *Geophysical Monograph Series*, A. Schmittner, J. C. H. Chiang, S. R. Hemming, Eds. (American Geophysical Union, Washington, DC, 2007), vol. 173, pp. 209–246.
- G. Bond et al., *Nature* **365**, 143–147 (1993).
- W. S. Broecker, *Nature* **372**, 421–424 (1994).
- E. W. Wolff, H. Fischer, R. Röthlisberger, *Nat. Geosci.* **2**, 206–209 (2009).
- R. H. Rhodes et al., *Earth Planet. Sci. Lett.* **368**, 9–19 (2013).
- E. J. Brook, S. Harder, J. Severinghaus, E. J. Steig, C. M. Sucher, *Global Biogeochem. Cycles* **14**, 559–572 (2000).
- Materials and methods are available as supplementary materials on Science Online.
- J. Chappellaz et al., *Clim. Past* **9**, 2579–2593 (2013).
- Y. J. Wang et al., *Science* **294**, 2345–2348 (2001).
- S. A. Marcott et al., *Nature* **514**, 616–619 (2014).
- P. Kindler et al., *Clim. Past* **10**, 887–902 (2014).
- G. Deplazes et al., *Nat. Geosci.* **6**, 213–217 (2013).
- J. A. Collins et al., *Clim. Past* **9**, 1181–1191 (2013).
- S. A. Carolin et al., *Science* **340**, 1564–1566 (2013).
- J. Muller et al., *Quat. Sci. Rev.* **27**, 468–475 (2008).
- J. P. Severinghaus, R. Beaudette, M. A. Headly, K. Taylor, E. J. Brook, *Science* **324**, 1431–1434 (2009).
- J. C. H. Chiang, C. M. Bitz, *Clim. Dyn.* **25**, 477–496 (2005).
- M. Kageyama et al., *Clim. Past* **9**, 935–953 (2013).
- L. A. Parsons, J. Yin, J. T. Overpeck, R. J. Stouffer, S. Malyshev, *Geophys. Res. Lett.* **41**, 2013GL058454 (2014).
- M. Guillemin et al., *Clim. Past* **10**, 2115–2133 (2014).
- P. Bergamaschi et al., *J. Geophys. Res. Atmos.* **114**, D22301 (2009).
- B. P. Walter, M. Heimann, E. Matthews, *J. Geophys. Res. Atmos.* **106**, 34207–34219 (2001).
- I. Cvijanovic, P. L. Langen, E. Kaas, P. D. Ditlevsen, *J. Clim.* **26**, 4121–4137 (2013).
- C. Buizert et al., *Clim. Past* **11**, 153–173 (2015).

- J. V. Stern, L. E. Lisiecki, *Geophys. Res. Lett.* **40**, 3693–3697 (2013).
- A. Svensson et al., *Clim. Past* **4**, 47–57 (2008).
- J. Southon, A. L. Noronha, H. Cheng, R. L. Edwards, Y. Wang, *Quat. Sci. Rev.* **33**, 32–41 (2012).
- L. C. Kanner, S. J. Burns, H. Cheng, R. L. Edwards, *Science* **335**, 570–573 (2012).
- D. A. Hodell, J. E. Channell, J. H. Curtis, O. E. Romero, U. Röhl, *Paleoceanography* **23**, PA4218 (2008).
- X. Wang et al., *Nature* **432**, 740–743 (2004).

## ACKNOWLEDGMENTS

This work was supported by NSF grants 1043518, 1142041, 0944552, 0839093, and 1142166. Data will be made available at <http://nsidc.org/data/> and <http://ncdc.noaa.gov/paleo/>. L. Layman, N. Chellman, D. Pasteris, M. Sigl, and C. Stowasser assisted with measurements. Thanks to J. Ahn for collated Siple Dome  $\text{CH}_4$  data, J. Rosen for use of the Oregon State University firn air model, and T. Sowers for fruitful discussion. The authors appreciate the support of the WAIS Divide Science Coordination Office at the Desert Research Institute of Reno Nevada and the University of New Hampshire for the collection and distribution of the WAIS Divide ice core and related tasks (NSF grants 0230396, 0440817, 0944348, and 0944266). We are grateful to all participants in the field effort led by K. Taylor. The NSF Office of Polar Programs also funded the Ice Drilling Program Office and Ice Drilling Design and Operations group, the National Ice Core Laboratory, Raytheon Polar Services, and the 109th New York Air National Guard.

## SUPPLEMENTARY MATERIALS

[www.sciencemag.org/content/348/6238/1016/suppl/DC1](http://www.sciencemag.org/content/348/6238/1016/suppl/DC1)  
Materials and Methods  
Supplementary Text  
Figs. S1 to S8  
Tables S1 and S2  
References (32–53)

2 October 2014; accepted 30 April 2015  
10.1126/science.1262005

## MICROBIAL DIVERSITY

# Fine-scale diversity and extensive recombination in a quasisexual bacterial population occupying a broad niche

Michael J. Rosen,<sup>1</sup> Michelle Davison,<sup>2</sup> Devaki Bhaya,<sup>2\*</sup>† Daniel S. Fisher<sup>1,3\*</sup>†

Extensive fine-scale genetic diversity is found in many microbial species across varied environments, but for most, the evolutionary scenarios that generate the observed variation remain unclear. Deep sequencing of a thermophilic cyanobacterial population and analysis of the statistics of synonymous single-nucleotide polymorphisms revealed a high rate of homologous recombination and departures from neutral drift consistent with the effects of genetic hitchhiking. A sequenced isolate genome resembled an unlinked random mixture of the allelic diversity at the sampled loci. These observations suggested a quasisexual microbial population that occupies a broad ecological niche, with selection driving frequencies of alleles rather than whole genomes.

**T**he traditional view of clonal bacterial populations in laboratory or clinical settings contrasts with the genetic diversity observed in environmental populations (1–4). Clusters of genotypes are often found (5, 6), and neutral drift alone could, in principle, account for them. However, even moderate rates of homologous recombination (HR) can prevent clustering on genomic scales (7), whereas without recombination, occasional periodic selection would eliminate the diversity. An alternative sce-

nario is that microbial species contain numerous subpopulations occupying discrete ecological niches, or ecotypes (8). In marine *Prochlorococcus*,

<sup>1</sup>Applied Physics Department, Stanford University, Stanford, CA 94305, USA. <sup>2</sup>Department of Plant Biology, Carnegie Institution for Science, Stanford, CA 94305, USA.

<sup>3</sup>Bioengineering Department, Stanford University, Stanford, CA 94305, USA.

\*Corresponding author. E-mail: [dbhaya@stanford.edu](mailto:dbhaya@stanford.edu) (D.B.); [dsfisher@stanford.edu](mailto:dsfisher@stanford.edu) (D.S.F.). †These authors contributed equally to this work.

dated as  $16.13 \pm 0.12$  ky B.P.,  $24.03 \pm 0.37$  ky B.P.,  $39.54 \pm 0.38$  ky B.P. and  $48.39 \pm 0.38$  ky B.P., respectively, in the WD2014 chronology (25) [ $2\sigma$  uncertainty (8)]. Our proposed ages for Heinrich events 1 and 2 match the timing of maximum IRD observed in a stack of North Atlantic sediment records (26) (Fig. 2), and closely correspond to calibrated  $^{14}\text{C}$ -based estimates (7). Despite these encouraging signs, we cannot be certain of the phasing of events. For example, the scenario of Northern Hemisphere cooling leading to  $\text{CH}_4$  increase that we describe could potentially occur before the Heinrich event, maybe even triggering the event. This seems an unlikely possibility, given the requirement for another forcing mechanism, the abrupt nature of the  $\text{CH}_4$  signals, and their unique occurrence in Heinrich stadials, but it cannot be ruled out.

The direct impact of a Heinrich event must cease once the ensuing interstadial commences and Northern Hemisphere climate warms (Fig. 1). We calculated maximum durations for the climatic impact of individual Heinrich events, perhaps largely on tropical hydrology, as ranging from 740 to 1520 years (Fig. 2). These estimates are significantly higher than the best guess for the duration of the actual iceberg armada (1 to 500 years) (7). We therefore suggest that this duration is related to a prolonged state of severely slowed or collapsed AMOC, maintained by extensive North Atlantic sea ice. This does not preclude the likelihood that AMOC was already relatively weak before Heinrich events, but rather explains why AMOC strength remained low through an extended stadial period when most coupled models suggest recovery of the overturning circulation within a few hundred years (19). The late HS plateaus in  $\text{CH}_4$  concentration, particularly in HSs 4 and 5, are remarkably stable in comparison to interstadials (Fig. 1), suggesting limited variability in tropical precipitation and a relatively stable AMOC state. It is tempting to speculate on whether we capture information about the actual iceberg armada duration in the ~90- to 190-year  $\text{CH}_4$  overshoots resolved during HSs 1, 4, and 5 (Fig. 2). However, short-duration  $\text{CH}_4$  overshoots are not unique to these events and are in fact a feature of nearly all interstadial onsets, possibly resulting from an intrinsic response of the atmospheric system to rapid reorganization or intensive methanogenesis in newly inundated wetlands.

We suggest that our results provide motivation for climate modeling experiments to further investigate the difference between regular stadials and Heinrich stadials in the North Atlantic region and their respective impacts on tropical climate. Moreover, it is intriguing that only Heinrich events 1, 2, 4, and 5 are associated with Southern Hemisphere  $\text{CH}_4$  signals. These four Heinrich events have relatively thick and spatially extensive sediment deposits, rich in detrital carbonate (Fig. 1) sourced from the Hudson Strait, and are linked to surging of the Laurentide ice sheet (7). Were the remaining Heinrich events too insignificant in scale to greatly perturb tropical climate, or did they not influence the same climate-sensitive location?

## REFERENCES AND NOTES

1. S. R. Hemming, *Rev. Geophys.* **42**, RG1005 (2004).
2. P. U. Clark, S. W. Hostetler, N. G. Pisias, A. Schmittner, K. J. Meissner, in *Geophysical Monograph Series*, A. Schmittner, J. C. H. Chiang, S. R. Hemming, Eds. (American Geophysical Union, Washington, DC, 2007), vol. 173, pp. 209–246.
3. G. Bond et al., *Nature* **365**, 143–147 (1993).
4. W. S. Broecker, *Nature* **372**, 421–424 (1994).
5. E. W. Wolff, H. Fischer, R. Röthlisberger, *Nat. Geosci.* **2**, 206–209 (2009).
6. R. H. Rhodes et al., *Earth Planet. Sci. Lett.* **368**, 9–19 (2013).
7. E. J. Brook, S. Harder, J. Severinghaus, E. J. Steig, C. M. Sucher, *Global Biogeochem. Cycles* **14**, 559–572 (2000).
8. Materials and methods are available as supplementary materials on Science Online.
9. J. Chappellaz et al., *Clim. Past* **9**, 2579–2593 (2013).
10. Y. J. Wang et al., *Science* **294**, 2345–2348 (2001).
11. S. A. Marcott et al., *Nature* **514**, 616–619 (2014).
12. P. Kindler et al., *Clim. Past* **10**, 887–902 (2014).
13. G. Deplazes et al., *Nat. Geosci.* **6**, 213–217 (2013).
14. J. A. Collins et al., *Clim. Past* **9**, 1181–1191 (2013).
15. S. A. Carolin et al., *Science* **340**, 1564–1566 (2013).
16. J. Muller et al., *Quat. Sci. Rev.* **27**, 468–475 (2008).
17. J. P. Severinghaus, R. Beaudette, M. A. Headly, K. Taylor, E. J. Brook, *Science* **324**, 1431–1434 (2009).
18. J. C. H. Chiang, C. M. Bitz, *Clim. Dyn.* **25**, 477–496 (2005).
19. M. Kageyama et al., *Clim. Past* **9**, 935–953 (2013).
20. L. A. Parsons, J. Yin, J. T. Overpeck, R. J. Stouffer, S. Malyshev, *Geophys. Res. Lett.* **41**, 2013GL058454 (2014).
21. M. Guillemin et al., *Clim. Past* **10**, 2115–2133 (2014).
22. P. Bergamaschi et al., *J. Geophys. Res. Atmos.* **114**, D22301 (2009).
23. B. P. Walter, M. Heimann, E. Matthews, *J. Geophys. Res. Atmos.* **106**, 34207–34219 (2001).
24. I. Cvijanovic, P. L. Langen, E. Kaas, P. D. Ditlevsen, *J. Clim.* **26**, 4121–4137 (2013).
25. C. Buizert et al., *Clim. Past* **11**, 153–173 (2015).
26. J. V. Stern, L. E. Lisiecki, *Geophys. Res. Lett.* **40**, 3693–3697 (2013).
27. A. Svensson et al., *Clim. Past* **4**, 47–57 (2008).
28. J. Southon, A. L. Noronha, H. Cheng, R. L. Edwards, Y. Wang, *Quat. Sci. Rev.* **33**, 32–41 (2012).
29. L. C. Kanner, S. J. Burns, H. Cheng, R. L. Edwards, *Science* **335**, 570–573 (2012).
30. D. A. Hodell, J. E. Channell, J. H. Curtis, O. E. Romero, U. Röhl, *Paleoceanography* **23**, PA4218 (2008).
31. X. Wang et al., *Nature* **432**, 740–743 (2004).

## ACKNOWLEDGMENTS

This work was supported by NSF grants 1043518, 1142041, 0944552, 0839093, and 1142166. Data will be made available at <http://nsidc.org/data/> and <http://ncdc.noaa.gov/paleo/>. L. Layman, N. Chellman, D. Pasteris, M. Sigl, and C. Stowasser assisted with measurements. Thanks to J. Ahn for collated Siple Dome  $\text{CH}_4$  data, J. Rosen for use of the Oregon State University firn air model, and T. Sowers for fruitful discussion. The authors appreciate the support of the WAIS Divide Science Coordination Office at the Desert Research Institute of Reno Nevada and the University of New Hampshire for the collection and distribution of the WAIS Divide ice core and related tasks (NSF grants 0230396, 0440817, 0944348, and 0944266). We are grateful to all participants in the field effort led by K. Taylor. The NSF Office of Polar Programs also funded the Ice Drilling Program Office and Ice Drilling Design and Operations group, the National Ice Core Laboratory, Raytheon Polar Services, and the 109th New York Air National Guard.

## SUPPLEMENTARY MATERIALS

[www.sciencemag.org/content/348/6238/1016/suppl/DC1](http://www.sciencemag.org/content/348/6238/1016/suppl/DC1)  
Materials and Methods  
Supplementary Text  
Figs. S1 to S8  
Tables S1 and S2  
References (32–53)

2 October 2014; accepted 30 April 2015  
10.1126/science.1262005

## MICROBIAL DIVERSITY

# Fine-scale diversity and extensive recombination in a quasisexual bacterial population occupying a broad niche

Michael J. Rosen,<sup>1</sup> Michelle Davison,<sup>2</sup> Devaki Bhaya,<sup>2\*</sup>† Daniel S. Fisher<sup>1,3\*</sup>†

Extensive fine-scale genetic diversity is found in many microbial species across varied environments, but for most, the evolutionary scenarios that generate the observed variation remain unclear. Deep sequencing of a thermophilic cyanobacterial population and analysis of the statistics of synonymous single-nucleotide polymorphisms revealed a high rate of homologous recombination and departures from neutral drift consistent with the effects of genetic hitchhiking. A sequenced isolate genome resembled an unlinked random mixture of the allelic diversity at the sampled loci. These observations suggested a quasisexual microbial population that occupies a broad ecological niche, with selection driving frequencies of alleles rather than whole genomes.

**T**he traditional view of clonal bacterial populations in laboratory or clinical settings contrasts with the genetic diversity observed in environmental populations (1–4). Clusters of genotypes are often found (5, 6), and neutral drift alone could, in principle, account for them. However, even moderate rates of homologous recombination (HR) can prevent clustering on genomic scales (7), whereas without recombination, occasional periodic selection would eliminate the diversity. An alternative sce-

nario is that microbial species contain numerous subpopulations occupying discrete ecological niches, or ecotypes (8). In marine *Prochlorococcus*,

<sup>1</sup>Applied Physics Department, Stanford University, Stanford, CA 94305, USA. <sup>2</sup>Department of Plant Biology, Carnegie Institution for Science, Stanford, CA 94305, USA.

<sup>3</sup>Bioengineering Department, Stanford University, Stanford, CA 94305, USA.

\*Corresponding author. E-mail: [dbhaya@stanford.edu](mailto:dbhaya@stanford.edu) (D.B.); [dsfisher@stanford.edu](mailto:dsfisher@stanford.edu) (D.S.F.). †These authors contributed equally to this work.



a recent study revealed the presence of multiple genomic backbones—i.e., clusters of core genomes associated with different ecological conditions and with low between-cluster rates of recombination (7). More extensive recombination is inferred in other populations. For marine *Vibrio* and thermophilic archaea (3, 4), a scenario has been proposed in which recombination is fast enough to enable genes to sweep through environments in which they confer fitness without purging genome-wide diversity. Ecological differentiation takes place when the colonization of a new microenvironment generates recombination barriers between subtypes, ultimately leading to distinguishable genomic clusters resembling incipient speciation (9). Here, we produce evidence that some microbial populations may maintain a cloud of fine-scale genotypic and phenotypic diversity, with varying selection acting on individual loci (and combinations of loci) but without subdivision into genome-wide subtypes. Such a population spread over a range of environmental conditions resembles a sexual population occupying a broad niche.

Studies of cyanobacteria in (*Synechococcus* sp.) the dense phototrophic biofilms (“microbial mats”) that develop along hot spring effluent channels in Yellowstone National Park establish that there are correlations between environmental gradients and genetic variation at several loci (10, 11). This is interpreted as evidence for the presence of ecotypes (12). Comparative genomics of two recently sequenced *Synechococcus* isolates (*Syn* OS-A and *Syn* OS-B') from these biofilms reveals that they are closely related yet show extensive large and small genomic rearrangements (13). Metagenomic data corroborates this and also reveals evidence of recent horizontal gene transfer events (13). Furthermore, *Synechococcus* sp. are capable of natural transformation (14), have several active transposons (13, 15), and are host to cyanophages (16), all of which facilitate DNA exchange within closely related populations living in close proximity. This raises questions of whether the genome-scale linkage that should be associated with ecological subpopulations is detectable and whether genomic backbones can be identified in these populations.

Multilocus sequence typing (MLST) [the sequencing of a small number of loci from collections of (usually pathogenic) isolates] has been used extensively to identify variants (17) and, more recently, to analyze recombination (18). To examine the *Synechococcus* populations, we developed a variant of MLST in which we performed deep amplicon sequencing of multiple loci directly from the population (without isolating individuals) followed by correction of polymerase chain reaction (PCR) and sequencing errors (19). We focused on correlations within loci because they are more informative than the low-level linkage between loci when recombination rates are high. This protocol avoids the need for any potential biases associated with the isolation of multiple distinct clonal populations.

We used the previously sequenced *Syn* OS-A and *Syn* OS-B' genomes and metagenomic data

to design primers optimized to maximally capture allelic diversity within the *Synechococcus* population at 90 genomic regions located along the genomes (20). Template DNA was isolated from

a microbial mat sample collected from a 50°C region of the effluent channel at Mushroom Spring (12). Both ends of the 90 amplicons (i.e., a total of 180 loci) were sequenced to an average depth of

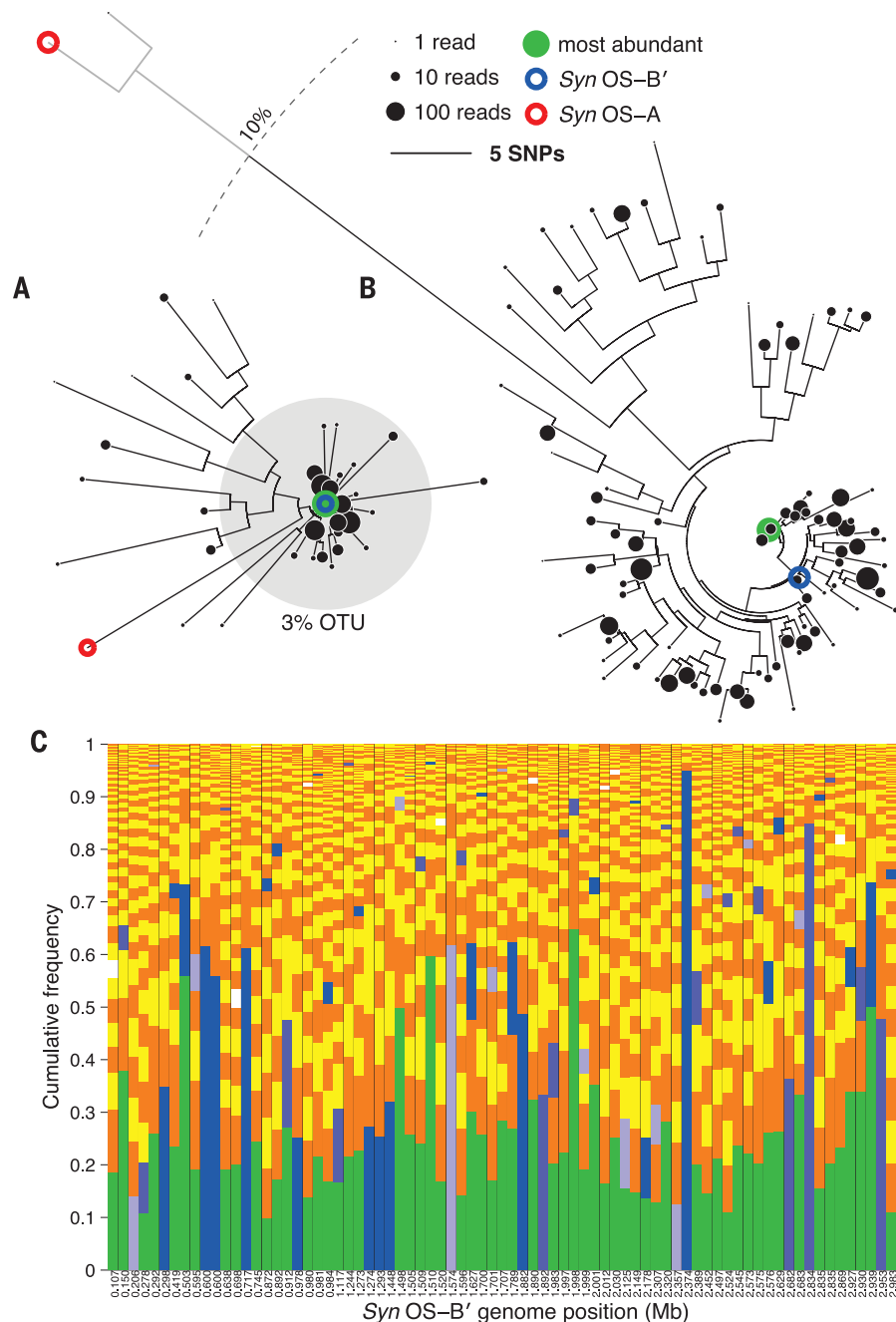


**Fig. 1. Diversity of alleles.** Neighbor-joining trees of alleles, with the leaf area being proportional to log of allele frequency. (A) 16S rRNA alleles. The gray circle highlights the 3% diameter cluster typically used to define an OTU designating a bacterial “species”. The genomes *Syn* OS-B' (blue) and *Syn* OS-A (red) are shown. (B) A locus containing both genic and intergenic sequence (88 alleles derived from 2058 reads). *Syn* OS-B' (blue) is identical to an allele with 11 reads, while *Syn* OS-A (red) is not among the alleles at this locus. The dashed gray line marks 10% sequence divergence from the most abundant allele (green). (C) The spectrum of allele frequencies for 77 loci is ordered along the *Syn* OS-B' genome (left to right) and from most abundant to least abundant at each locus (bottom to top). The allele closest to *Syn* OS-B' is blue when identical, white when >5 SNPs away, and intermediate shades of blue when 1 to 2 or 3 to 5 SNPs away. When not closest to *Syn* OS-B', the most abundant allele is green, and all other alleles are colored as alternating yellow and orange.

1000x and trimmed to a uniform 400-nucleotide (nt) length (a total of ~65.4 Mb, the equivalent of >20x coverage of the 3.1 Mb *Syn* OS-B' genome). To reliably distinguish true allelic variation from PCR-generated errors (21), we applied an algorithm [DADA (19)] that exploits variation in sequence abundances and the distances between them to parametrize a simple error model and correct errors in the raw reads (see fig. S1 for a schematic overview). Consistency checks, particularly using the contrast between the statistics of nonsynonymous and synonymous single-nucleotide polymorphisms (SNPs) in the sample (the ratio  $d_n/d_s$  of the numbers of differences between alleles averages ~0.14) and those of PCR errors, which are agnostic to this difference, validated that the vast majority of inferred alleles, including many with only a single read, are real and cannot be ascribed to errors (20). Furthermore, comparison of the inferred alleles to sequenced bacterial genomes indicates that even these rare alleles almost all have best matches to *Syn* OS-A or *Syn* OS-B' (supplementary materials, text 1).

At the 16S ribosomal RNA (rRNA) locus (V1 to V3 segment, 438 nt), the most abundant allele was identical to the *Syn* OS-B' isolate, consistent with previous findings that *Syn* OS-B' has the dominant V7 to V8 16S allele at 56°C (12). Within the 3% sequence-divergence diameter operational taxonomic unit (OTU) centered on this allele, there were 20 other alleles, which comprised 93% of the *Synechococcus*-like reads. Farther away, we identified another 17 *Synechococcus* alleles, including a few reads identical to *Syn* OS-A, which is rare at 50°C but common at ~65°C (Fig. 1A) (13).

Other loci were more diverse. Focusing on the 136 loci with >300 reads (of the 180 sequenced), we found an average per site heterozygosity (the probability that a random pair of reads differ at a random site) of  $\pi = 3.5\%$  (compare  $\pi_{16S} = 0.5\%$ ) and an average of 44 alleles (range 7 to 121). Figure 1B shows a typical locus with 88 inferred nucleotide alleles. Each locus had a spectrum of allele abundances, from tens of percent to <0.1%. Figure 1C depicts these allele frequencies at 77 of the loci (one end of each amplicon with >300

reads) ordered along the *Syn* OS-B' genome. This graphical view shows how variable the patterns of diversity were across the genome. Furthermore, there is no obvious correlation between nearby loci, which provides a first hint that linkage may be very limited.

Recent recombination events between well-diverged alleles produce alleles with a characteristic “chimeric” structure that is easy to recognize (fig. S2). After finding the most likely pair of parents for each allele, even with conservative criteria, we observed >700 examples of chimeric alleles (table S1). An additional  $d_n/d_s$  consistency check (table S2) showed that most cannot be chimeras caused by PCR; for alleles one or two SNPs away from being a chimeric mixture of two parent alleles, these SNPs had a strong synonymous skew relative to the expectation from errors (22). The large number of chimeric alleles suggested that homologous recombination is common, but we could not estimate the rate at which it occurs because recombination events between highly similar parents, or far

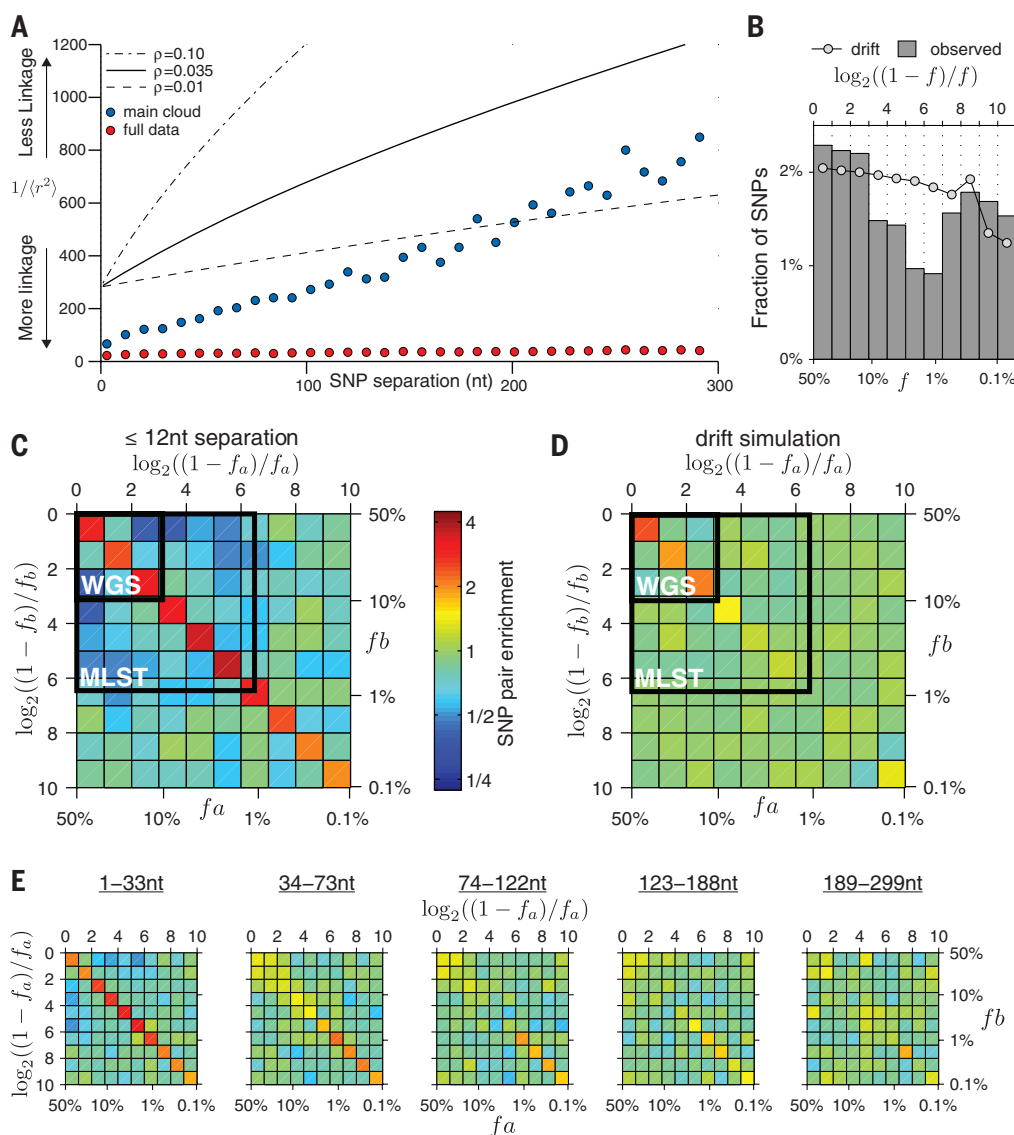


**Fig. 2. Frequency statistics and linkage correlations between pairs of SNPs.** (A) The inverse of the average linkage correlations,  $\langle r^2 \rangle = \langle (f_{ab} - f_a f_b)^2 / [f_a(1 - f_a)f_b(1 - f_b)] \rangle$  (20), are shown as a function of SNP separation. Red, full data; blue, the main cloud, including only alleles within  $\leq 10\%$  of the most abundant allele. The drift expectations, with an observed heterozygosity of  $\pi = 0.03$  and three values of  $\rho = 0.01$  (a rough best fit), 0.035 (giving a similar slope), and 0.1 (giving a similar fractional increase), generated numerically with ER2, are shown for comparison (26). (B) SFS for the synonymous SNPs in the main cloud. The roughly log-spaced frequency bins are chosen so that the neutral-drift expectation (dots) is flat (cutoff by the read depth). (C to E) Two-dimensional histograms of the frequencies of pairs of SNPs from alleles in the main cloud; each bin shows on a logarithmic color scale the ratio of the number of SNP pairs with minority allele frequencies  $f_a$  and  $f_b$ , and the expected number if the frequencies were drawn independently from the SFS. (C) Tightly linked SNP pairs are separated by at most 12 nt, with (D) an asexual drift simulation for comparison; (E) data for several ranges of separations between the SNPs (with ~6400 pairs in each window). The frequency ranges that could be studied with the 10x and 100x depths typical of WGS and MLST, respectively, are indicated in (C) and (D).



in the past (and hence obscured by subsequent mutations and recombinations), are not possible to identify directly. We therefore turned to statistical methods to probe recombination quantitatively.

If recombination rates are comparable to mutation rates, inferring recombination events relative to an asexual phylogeny, as often done for MLST and whole-genome sequencing (WGS) data (23, 24), is not feasible. Likelihood-based methods (25) can be used to infer recombination parameters without an underlying phylogeny. However, these methods are based on the assumptions of a well-mixed population with neutral drift and unrestricted recombination and thus can obscure potentially informative deviations from model assumptions. Extensive deep sequencing data allowed us to avoid the pitfalls of fitting to particular models.

The >7500 synonymous SNPs that we observed serve as convenient neutral markers. Within loci were >50,000 pairs of these SNPs. We studied the dependence of the frequency statistics on the within-pair separation,  $x$ . Each pair has four haplotypes,  $AB$  (the most abundant),  $Ab$ ,  $aB$ , and  $ab$ , with frequencies  $f_{AB}$ ,  $f_{Ab}$ ,  $f_{aB}$ , and  $f_{ab}$ . If  $x$  is large, and thus recombination frequent enough to unlink the two sites, then the frequencies will become independent—i.e.,  $f_{ab} \approx f_a f_b$  (with  $f_a = f_{aB} + f_{ab}$  the frequency of SNP  $a$ ). But if the sites are close together, systematic deviations from this linkage equilibrium are likely.

A measure of the linkage disequilibrium is  $r^2$ , with  $r$  normalized to be unity with full linkage—

i.e., when only  $AB$  and  $ab$  are observed. Figure 2A shows the inverse of  $r^2$  as a function of separation  $x$ . For the complete data set, linkage decayed only slightly with distance (Fig. 2A, red circles). However, this masked the behavior of the large majority of the population because outliers dominated the average linkage. Considering only alleles within some cutoff distance from the most abundant, a more rapid decay of  $r^2$  with separation was observed as the cutoff was decreased. Including only the alleles within 10% of the most abundant (corresponding to 92% of the reads, coincidentally the same fraction as the 3% diameter OTU from the 16S rRNA) characterized well the behavior within an ad hoc “main cloud” (fig. S3A). We also analyzed metagenomic data from a higher temperature sample (13), finding similar behavior (fig. S3B): linkage decayed comparably rapidly, although within a narrower (5% cutoff) cloud. These metagenomic data were much shallower, but because the DNA was not amplified and thus not subject to potential PCR-generated recombination artifacts, they provided an independent confirmation.

Within the main cloud of the amplicon data, linkage dropped by a factor of 10 over 300 nt (Fig. 2A) ( $\sigma_d^2$ , a related measure of linkage, behaves similarly, as defined and shown in fig. S4). As  $1/(r^2)$  is roughly proportional to the probability that a recombination event has unlinked the sites since the SNPs occurred (26), the slope of this curve is related to  $\rho = RT$ , where  $R$  is the rate of creation of a recombination break point between neighboring sites and  $T$  is the average time

since the most recent common ancestor. The data thus suggest that  $\rho$  is in the range  $10^{-2}$  to  $10^{-1}$ , which is at the very high end of values inferred for free-living bacteria (27) and similar to some pathogens (28, 29). Because the synonymous heterozygosity,  $\pi_s$ , is determined by the product of  $T$  and the mutation rate per site,  $\mu$ , and was found to be  $\sim 3\%$  in the main cloud, this implies that the mutation rate and recombination rates are about the same, i.e.,  $R \sim \mu$ . At larger separations than the typical length  $\delta$  of the DNA fragments exchanged, the decay of linkage should saturate. That it did not saturate by  $x = 300$  nt suggests that  $\delta$  is considerably longer than this, consistent with inferences for other bacteria (28, 30).

With abundant data extending to low frequencies, more can be gleaned from the SNP pair statistics than  $\rho$ . Nearby pairs [with  $\delta \gg x$ ] within the main cloud (Fig. 2A) were more linked than expected for a population driven solely by neutral drift and random recombination (26). To explore this excess linkage, we studied the joint distribution of the SNP frequencies  $f_a$  and  $f_b$ . For the main cloud, the single-site SNP frequency spectrum (SFS) (Fig. 2B) had a roughly similar form to the drift expectation, albeit with a dip in the 1 to 10% frequency range, (see fig. S5A for the full data), but the frequency correlations of nearby SNP pairs differed strikingly from drift. Over a broad range of frequency  $f_a$  in the histogram of Fig. 2C, there was a strong excess of SNPs pairs along the diagonal (i.e., with  $f_a \sim f_b$ ), relative to the expectation under the independence of the two SNPs. This contrasted with asexual drift (Fig. 2D), for which only a small excess would occur and only at high frequencies. Much of the excess correlation, as well as the additional linkage in Fig. 2A, was caused by an abundance of  $AB$ - $ab$  pairs in the absence of other combinations, so that  $f_{ab} = f_a = f_b$ .

Over time, correlations between allele frequencies are, like linkage, broken up by recombination, although only indirectly (from  $AB$  and  $ab$  pairs, recombination must first produce  $Ab$  and  $aB$  before fluctuations in allele frequencies can break up the correlation between  $f_a$  and  $f_b$ ). Thus, the frequency correlations should decay with separation. In Fig. 2E, the joint-frequency histograms for increasing separation ranges exhibited this decay, but the correlations persisted over larger separations at lower frequencies, consistent with low-frequency SNPs being, on average, younger (see fig. S5, C and D, for a comparison with full data and drift simulations). Together, the data in Fig. 2, A and E, show that by 300 base pairs (bp) the four pair-haplotype frequencies were close to being independent. This is strong evidence against the presence of subpopulations within the main cloud, as these would manifest as a persistence of frequency correlations.

Despite the weak decay of linkage in the full data, the probability of observing recently formed chimeric alleles with one parent inside the main cloud and the other outside is consistent with recombination occurring at similar rates inside and outside the main cloud (table S3). The observed persistence of linkage to longer distances

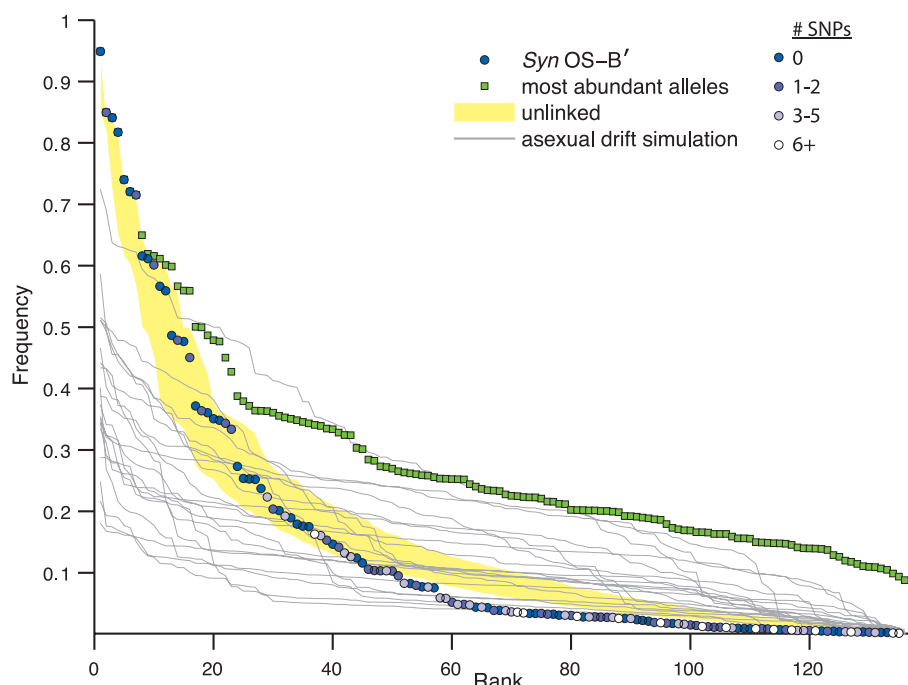


**Fig. 3. Syn OS-B' as a random mixture of the allelic diversity.** The rank-frequency spectrum of the alleles most similar to the Syn OS-B' genome at each locus (blue-white scale from Fig. 1). For comparison, two simple models of genomes are shown: an unlinked, highly recombinant model [the yellow band contains the central 95% of the frequencies at each rank across  $10^5$  simulations (20)] and 20 samples from a neutral asexual model with  $\theta = 0.02$  chosen to match the per-site heterozygosity of the data [gray lines (20)]. The green points show the frequencies of the most abundant alleles.

could instead result from selection against recombinants with the outliers because of epistatic incompatibilities (31) suppressing older recombination events and increasing linkage. However, we cannot rule out some spurious linkage being produced by biased sampling from the choice of PCR primers or other effects.

At least within the main cloud, the precipitous decay of linkage within loci, without evidence of saturation, indicated that there might be very little residual linkage at genomic distance scales. Genomic-scale linkage has been studied by sequencing whole genomes (1, 3, 4), which requires multiple isolates and can be technically challenging. We chose an alternate approach in which allele frequency information from the amplicon data were combined with the extended linkage information of the *Syn* OS-B' genome.

We asked what scenario for the population best describes the relationship of the *Syn* OS-B' genome to the observed allelic diversity. If the population were predominantly clonal, a typical genome of the dominant 16S ribotype, such as *Syn* OS-B', would tend to be similar to high-frequency alleles in other genomic regions; however, at 23 loci, *Syn* OS-B' is not even in the main cloud. More broadly, the alleles closest to *Syn* OS-B' exhibited a wide range of distances, indicated by the shades of blue in Fig. 1C and abundances, which are shown rank-ordered in Fig. 3. Thus, the *Syn* OS-B' genome does not represent a dominant genotype (see the distribution of top allele abundances shown in green), but that does not exclude the possibility of a dominant genomic backbone as seen in *Prochlorococcus* (1). To assess this, we compared two scenarios. At one extreme, we considered the simplest asexual model: a neutrally drifting population with *Syn* OS-B' a random member. Such rank-frequency spectra are widely variable (gray lines in Fig. 3) but generally rather flat because of the correlations between loci arising from a common phylogeny. At the other extreme, we considered a sexual population that is completely unlinked from one locus to the next, with genomes in which each locus consists of a population-frequency-weighted random allele, as shown by the yellow region in Fig. 3. In this latter case, there was little variability in the rank-frequency spectra. This extreme sexual model was a far better fit for *Syn* OS-B', particularly at high frequencies (this is also true for *Syn* OS-A) (fig. S6). We concluded that this cyanobacterial population had undergone sufficiently extensive homologous recombination among close relatives (comprising at least 90% of the population) to make it similar to a sexual population, in which genomes consist of random mixtures of alleles.

The observation of rapidly decaying linkage is a feature that has often been used to infer high rates of recombination via fits to a drift model (32). Our statistical analysis of pairs of neutral SNPs simultaneously evaluated the drift model itself, revealing considerable departures that suggested distinctive dynamics. Selection on other parts of the genome, triggered by environmental or ecological changes, new beneficial alleles, or

other factors, can cause large changes in SNP frequencies before recombination unlinks them from the selected region. Recurrent hitchhiking events with a range of magnitudes can lead to single-SNP frequency spectra that are similar to drift, such as that observed. But the consequences for joint-frequency spectra of nearby pairs of SNPs can be very different. For example, in a population strongly dominated by *AB*, a single hitchhiking event could rapidly raise the *ab* frequency while leaving *AB* and *Ab* rare, in contrast to drift. Such events can give rise to the striking diagonal feature in the joint-frequency histogram evident in Fig. 2C and the large excess linkage at short distances shown in Fig. 2A.

Without the depth of sequencing and error correction used in our study that enabled low-frequency variants to be identified, the striking departures from neutral drift could not have been identified. In Fig. 2, C and D, black squares show the more limited range of frequencies typical of MLST and even more of current WGS. Going forward, for deep microbial population sequencing to achieve its potential for understanding underlying evolutionary dynamics, a range of scenarios, including recombination and recurrent hitchhiking with migration between local populations, needs to be explored. Theoretical predictions of correlations in multiple joint distributions and an understanding of which of these can best distinguish between scenarios are sorely needed.

The existence and persistence of extensive fine-scale microbial diversity is particularly puzzling in a localized population in which multiple variants have persisted for  $T > 10^6$  generations (corresponding to the observed  $\pi$  and assuming a typical bacterial mutation rate of  $<10^{-8}$ ). Based on theoretical modeling (8) and sequencing of a small number of loci (12), this diversity has previously been attributed to the existence of multiple discrete microniches occupied by ecotypes, with typical diameters  $<2\%$  (11). But our results are inconsistent with the presence of multiple ecotypes, at least within the 20% diameter main cloud. This cyanobacterial population is thus a striking contrast to *Prochlorococcus*, for which multiple whole-genome ecotypes have been found each with  $\sim 1\%$  diameter (1). We conjecture that in this dense biofilm with multiple local environmental gradients and ubiquitous recombination, the microbial population behaves as an effectively sexual species in which there are no discrete ecotypes or barriers to gene flow. Rather, it is a single population occupying a broad environmental niche, with spatially varying adaptation maintaining diversity at the scale of genes. For instance, *Syn* OS-A and *Syn* OS-B' contain different suites of genes encoding proteins required for the use of urea (13) and for phosphonate metabolism (33). These differences could have arisen as a result of varying selection pressures along the gradients that exist within the biofilms. Temporally varying selection at some loci could drive the dynamics of the rest of the genome by hitchhiking, with high rates of recombination preventing genomic sweeps that would purge the diversity.

The implications of such a scenario should motivate future studies of fine-scale microbial diversity in biofilms and other localized populations where the effects of nutrient, gas, and light gradients, fluctuations such as phage infections, and migration can be explored.

## REFERENCES AND NOTES

- N. Kashtan et al., *Science* **344**, 416–420 (2014).
- Z. I. Johnson et al., *Science* **311**, 1737–1740 (2006).
- B. J. Shapiro et al., *Science* **336**, 48–51 (2012).
- H. Cadillo-Quiroz et al., *PLOS Biol.* **10**, e1001265 (2012).
- O. X. Cordero, M. F. Polz, *Nat. Rev. Microbiol.* **12**, 263–273 (2014).
- W. P. Hanage, C. Fraser, B. G. Spratt, *Phil. Trans. R. Soc. B* **361**, 1917–1927 (2006).
- C. Fraser, W. P. Hanage, B. G. Spratt, *Science* **315**, 476–480 (2007).
- F. M. Cohan, E. B. Perry, *Curr. Biol.* **17**, R373–R386 (2007).
- M. F. Polz, E. J. Alm, W. P. Hanage, *Trends Genet.* **29**, 170–175 (2013).
- E. D. Becraft, F. M. Cohan, M. Kühl, S. I. Jensen, D. M. Ward, *Appl. Environ. Microbiol.* **77**, 7689–7697 (2011).
- M. C. Melendrez, R. K. Lange, F. M. Cohan, D. M. Ward, *Appl. Environ. Microbiol.* **77**, 1359–1367 (2011).
- D. M. Ward et al., *Phil. Trans. R. Soc. B* **361**, 1997–2008 (2006).
- D. Bhaya et al., *ISME J.* **1**, 703–713 (2007).
- M. R. Gomez-Garcia, F. Fazeli, A. Grote, A. R. Grossman, D. Bhaya, *J. Bacteriol.* **195**, 3309–3319 (2013).
- W. C. Nelson, L. Wollerman, D. Bhaya, J. F. Heidelberg, *Appl. Environ. Microbiol.* **77**, 5458–5466 (2011).
- J. F. Heidelberg, W. C. Nelson, T. Schoenfeld, D. Bhaya, *PLOS One* **4**, e4169 (2009).
- D. Gevers et al., *Nat. Rev. Microbiol.* **3**, 733–739 (2005).
- X. Didelot, M. C. J. Maiden, *Trends Microbiol.* **18**, 315–322 (2010).
- M. J. Rosen, B. J. Callahan, D. S. Fisher, S. P. Holmes, *BMC Bioinformatics* **13**, 283 (2012).
- Materials and methods are available as supplementary materials on Science Online.
- V. Kunin, A. Engelbrektson, H. Ochman, P. Hugenholtz, *Environ. Microbiol.* **12**, 118–123 (2010).
- R. P. Smyth et al., *Gene* **469**, 45–51 (2010).
- X. Didelot, D. Falush, *Genetics* **175**, 1251–1266 (2007).
- M. Vos, X. Didelot, *ISME J.* **3**, 199–208 (2009).
- G. McVean, P. Awadalla, P. Fearnhead, *Genetics* **160**, 1231–1241 (2002).
- Y. S. Song, J. S. Song, *Theor. Popul. Biol.* **71**, 49–60 (2007).
- J. R. Doroghazi, D. H. Buckley, *ISME J.* **4**, 1136–1143 (2010).
- K. A. Jolley, D. J. Wilson, P. Kriz, G. McVean, M. C. J. Maiden, *Mol. Biol. Evol.* **22**, 562–569 (2005).
- X. Didelot, G. Méric, D. Falush, A. E. Darling, *BMC Genomics* **13**, 256 (2012).
- G. Morelli et al., *PLOS Genet.* **6**, e1001036 (2010).
- J. Majewski, *FEMS Microbiol. Lett.* **199**, 161–169 (2001).
- S. Takuno, T. Kado, R. P. Sugino, L. Nakhleh, H. Innan, *Mol. Biol. Evol.* **29**, 797–809 (2012).
- M. R. Gomez-Garcia, M. Davison, M. Blain-Hartnug, A. R. Grossman, D. Bhaya, *ISME J.* **5**, 141–149 (2011).

## ACKNOWLEDGMENTS

We thank J. Blundell and B. Callahan for valuable suggestions and comments. Funding for this work was provided by NSF grants DMS-1120699 (D.S.F.), MCB-1024155 (D.B.), and FIBR EF-0328698 (D.B.), and by the Carnegie Institution for Science (D.B.). M.J.R. was partially supported by a Stanford Graduate Fellowship and an IBM Fellowship. Raw sequences have been deposited in National Center for Biotechnology Information (BioProject PRJNA268121).

## SUPPLEMENTARY MATERIALS

www.sciencemag.org/content/348/6238/1019/suppl/DC1  
Materials and Methods  
Supplementary Text  
Figs. S1 to S7  
Tables S1 to S4  
References (34–46)

8 December 2014; accepted 16 April 2015  
10.1126/science.aaa4456



## CELL ADHESION

# Mechanical strain induces E-cadherin-dependent Yap1 and $\beta$ -catenin activation to drive cell cycle entry

Blair W. Benham-Pyle,<sup>1</sup> Beth L. Pruitt,<sup>2,3,4</sup> W. James Nelson<sup>1,4,5\*</sup>

Mechanical strain regulates the development, organization, and function of multicellular tissues, but mechanisms linking mechanical strain and cell-cell junction proteins to cellular responses are poorly understood. Here, we showed that mechanical strain applied to quiescent epithelial cells induced rapid cell cycle reentry, mediated by independent nuclear accumulation and transcriptional activity of first Yap1 and then  $\beta$ -catenin. Inhibition of Yap1- and  $\beta$ -catenin-mediated transcription blocked cell cycle reentry and progression through G<sub>1</sub> into S phase, respectively. Maintenance of quiescence, Yap1 nuclear exclusion, and  $\beta$ -catenin transcriptional responses to mechanical strain required E-cadherin extracellular engagement. Thus, activation of Yap1 and  $\beta$ -catenin may represent a master regulator of mechanical strain-induced cell proliferation, and cadherins provide signaling centers required for cellular responses to externally applied force.

Cellular responses to mechanical force are important during development and disease and involve reinforcing cell-cell and cell-extracellular matrix (ECM) adhesions, increased cytoskeletal stiffness, and regulation of cell fate (1–4). Increased ECM stiffness leads to cytoskeleton reorganization and cell cycle progression by activating the Hippo pathway transcription factors Yap and Taz (5) downstream of actin remodeling factors (6), indicating that Yap is a mechanotransducer. However, less is known about signaling from cadherin-mediated cell-cell junctions following applied force.

Classical cadherins couple neighboring cells through trans interactions between opposed extracellular domains and force-dependent linkage of the cytoplasmic domain to the actin cytoskeleton through  $\beta$ -catenin and  $\alpha$ -catenin (7–11), resulting in constitutive tension on E-cadherin at the plasma membrane (10). The cadherin-catenin complex is thought to regulate growth signaling by sequestering the transcription factors  $\beta$ -catenin and Yap1 (12–16) in the cytoplasm. However, it is unclear whether cadherin-mediated adhesion is required for the activation of  $\beta$ -catenin and Yap1 in response to mechanical force.

To model mechanical force in multicellular tissues, dense monolayers of quiescent kidney epithelial (Madin-Darby canine kidney, MDCK) cells were formed on compliant silicone substrates in an integrated strain array (ISA) [fig. S1; see also (17)]. The ISA was used to apply and maintain different levels of static biaxial stretch for different times (2 to 24 hours). Cells were then

processed for imaging, data acquisition, and analysis (see supplementary materials). Mechanical strain induced rapid cell cycle reentry (Ki67 positive; Fig. 1, A and C, and fig. S2, A and C) and subsequent DNA replication and progression through S phase [EdU positive; Fig. 1, A and E, and fig. S2, B and D; see also (6)] into G<sub>2</sub> (Geminin positive; fig. S3). Most cells had entered S phase after 24 hours of strain application (Fig. 1E, “24T”), and higher levels of strain resulted in higher levels of cell cycle reentry (fig. S2).

We examined whether the cadherin-associated transcriptional activators Yap1 and  $\beta$ -catenin responded to mechanical strain. In the absence of mechanical strain, Yap1 localized in the cytoplasm and cell cortex [Fig. 1A and fig. S4A; see also (13)].  $\beta$ -Catenin localized at cell-cell contacts (Fig. 1A and fig. S5A), as expected due to cadherin binding (7) and proteasome-mediated degradation of excess cytoplasmic  $\beta$ -catenin (18, 19). Upon mechanical strain, Yap1 and  $\beta$ -catenin relocalized to the nucleus, but on different time scales. Nuclear Yap1 was detected within 1 hour of strain application, peaked at 6 hours, and then declined rapidly to background levels (Fig. 1A and fig. S4, A and B). In contrast, nuclear  $\beta$ -catenin was not observed until 6 hours following strain and remained over 24 hours (Fig. 1A and fig. S5, A and B).

We next determined if nuclear localization of Yap1 and  $\beta$ -catenin corresponded to their transcriptional activities. Analysis of the TBsmCherry reporter for Yap1 transcriptional activity [fig. S4C; (23)] revealed that, like Yap1 nuclear accumulation, activation following strain was rapid and peaked at 6 hours (Fig. 1, A and B, and fig. S4, D and E), then decreased before the majority of cells entering S phase (EdU positive; Fig. 1E and fig. S2, B and D). In contrast,  $\beta$ -catenin transcriptional activity measured with the TOPdGFP reporter (20) increased rapidly 6 hours after strain application, at the same time that nuclear  $\beta$ -catenin was detected (Fig. 1, A and D, and fig. S5).  $\beta$ -Catenin

transcriptional activity then remained high (Fig. 1D and fig. S5, D and E) as cells proceeded through S phase (Fig. 1E and fig. S2, B and D). Thus, mechanical strain induced both Yap1- and  $\beta$ -catenin-mediated transcriptional activities, but at different times after strain application and transiently in the case of Yap1 (Fig. 1F).

Although Yap1 activation preceded  $\beta$ -catenin activation by several hours following strain, we tested whether their activation was coupled. Expression of the YAP1-TEAD inhibitory peptide (YTIP) disrupts interactions between Yap1 and TEAD domain (TEAD) transcription factors and prevents transcription of Yap1/TEAD-targeted genes [fig. S6C; (21)]. When mechanical strain was applied to MDCK cells transiently expressing GFP- or red fluorescent protein (RFP)-tagged YTIP, YTIP-positive cells did not have increased Yap1 activity (Fig. 2A), Ki67 staining (Fig. 2, D and E, and fig. S6, E and F), or EdU incorporation (Fig. 2, F and G), in contrast to their untransfected neighbors. Similar results were obtained with Verteporfin (fig. S8), a small-molecule inhibitor of Yap1 binding to TEAD transcription factors (22). However, inhibition of Yap1 activity with YTIP or Verteporfin did not block increased nuclear  $\beta$ -catenin levels (Fig. 2B and fig. S8) or  $\beta$ -catenin transcriptional activity following mechanical strain (Fig. 2, B and C, and figs. S6, G and H, and S8). In the presence of Verteporfin, Yap1 was still detected in the nucleus after strain application even though it could not bind to TEAD transcription factors (fig. S8). Yap1 has been reported to co-regulate  $\beta$ -catenin transcriptional activity (23), but our results showed that in response to mechanical strain, nuclear Yap1 levels peaked before nuclear  $\beta$ -catenin was detected and then decreased while nuclear  $\beta$ -catenin and TOPdGFP levels remained high (figs. S4A and S5).

Thus, transient Yap1 activation was required for strain-induced cell cycle reentry, but neither Yap1/TEAD-mediated gene transcription nor cell cycle reentry was required for  $\beta$ -catenin nuclear accumulation or transcriptional activity. Additionally,  $\beta$ -catenin transcriptional activity was not sufficient for strain-induced cell cycle reentry or progression in the absence of Yap1 activation.

We next determined if  $\beta$ -catenin transcriptional activity was required for strain-induced cell cycle reentry and progression. The  $\beta$ -catenin-Engrailed chimera ( $\beta$ Eng) selectively inhibits  $\beta$ -catenin-mediated transcription without affecting cadherin-mediated cell-cell adhesion (24) or density-dependent inhibition of proliferation (fig. S7). Application of mechanical strain in  $\beta$ Eng-expressing cells induced nuclear accumulation of  $\beta$ -catenin (Fig. 3A) but did not result in  $\beta$ -catenin transcriptional activity (Fig. 3D) or progression of cells into S phase (Fig. 3, A and C). However, cell cycle reentry (Fig. 3, A and B) and Yap1 nuclear localization and transcriptional activity (Fig. 3, A and E) were still induced by mechanical strain of  $\beta$ Eng cells, similar to normal MDCK cells. Similar results were obtained with iCRT3 (fig. S8), a small-molecule inhibitor of  $\beta$ -catenin binding to TCF (25). Thus,  $\beta$ -catenin

<sup>1</sup>Program in Cancer Biology, Stanford University, Stanford, CA 94305, USA. <sup>2</sup>Stanford Cardiovascular Institute, Stanford University, Stanford, CA 94305, USA. <sup>3</sup>Department of Mechanical Engineering, Stanford University, Stanford, CA 94305, USA. <sup>4</sup>Department of Molecular and Cellular Physiology, Stanford University, Stanford, CA 94305, USA. <sup>5</sup>Department of Biology, Stanford University, Stanford, CA 94305, USA.

\*Corresponding author. E-mail: wjnelson@stanford.edu

transcriptional activity was not required for Yap1 nuclear accumulation and transcriptional activity or cell cycle reentry following strain but was required for cell cycle progression into S phase.

These results are consistent with a model in which mechanical strain in a quiescent epithelial cell monolayer causes the transient nuclear localization and transcriptional activation of Yap1, which is required for cell cycle reentry. Independently, strain also induces the nuclear localization

and transcriptional activation of  $\beta$ -catenin, which is required for progression into S phase. In mammalian tissues, Yap1/TEAD-targeted genes promote proliferation [connective tissue growth factor (CTGF), fibroblast growth factor (FGF), Amphiregulin (AREG), Ki67], anti-apoptosis (Birc5), and adhesion (Dsc3) (26–28), whereas  $\beta$ -catenin/TCF/LEF-targeted genes include additional cell cycle regulators (c-Myc, Cyclin D1, AuroraA, cdc25) (29). Activation of Yap1 and  $\beta$ -catenin gene tar-

gets, therefore, is congruent with our model of cell cycle reentry following mechanical strain. Mechanisms of Yap1 and  $\beta$ -catenin nuclear localization are complex and involve many pathways (12, 15, 16, 30–32), and many cell surface receptors regulate responses to mechanical strain, including integrin-based adhesions to the ECM (33, 34). However, a specific role for E-cadherin extracellular domain binding between cells has not been tested.

Rather than simply removing E-cadherin from MDCK cells, which would result in the loss of binding sites for Yap1 and  $\beta$ -catenin cytoplasmic sequestration, we used MDCK cells stably expressing a mutant E-cadherin (T151) under control of a doxycycline-repressible promoter (35). T151 comprises a truncated, nonfunctional extracellular domain, but a normal plasma membrane-tethered cytoplasmic domain that binds catenins. Expression of T151 caused the down-regulation of endogenous E-cadherin (fig. S9A), resulting in the complete loss of E-cadherin-mediated cell-cell adhesion, but does not prevent the formation of tight junctions and desmosomes (35), growth to confluence, or contact inhibition (fig. S9, B to D). Unlike normal MDCK cells at high cell densities, T151 monolayers without externally applied strain were Ki67-positive (Fig. 4, A and B) and had nuclear Yap1 (Fig. 4A) and increased TBSmCherry signal (Fig. 4D), consistent with cells being in  $G_1$ . Whereas T151 monolayers appeared “primed” for cell cycle progression, levels of nuclear  $\beta$ -catenin (Fig. 4A), TOPdGFP (Fig. 4E), and EdU incorporation were all low (Fig. 4C), indicating inhibition of  $G_1$ -to-S-phase transitions. Application of mechanical strain to T151 monolayers did not increase the level of EdU incorporation (Fig. 4, A and C), nuclear  $\beta$ -catenin (Fig. 4A), or  $\beta$ -catenin transcriptional activity (Fig. 4E), indicating that cells had not progressed into S phase. Thus, in multicellular monolayers, coupling between E-cadherin extracellular domains is required to block cell cycle entry and sequester Yap1 in the cytoplasm and for strain-induced nuclear accumulation and transcriptional activity of  $\beta$ -catenin and subsequent cell cycle progression into S phase.

Mechanical strain in epithelial monolayers results in cell cycle reentry and progression through S phase by the nuclear accumulation and transcriptional activity of first Yap1 and then  $\beta$ -catenin. Activation of Yap1 is required for cell cycle reentry, whereas  $\beta$ -catenin is required for progression from  $G_1$  to S phase. Specific inhibition of Yap1 and  $\beta$ -catenin transcription through use of two independent methods blocked cell cycle reentry and progression, respectively, indicating that other transcription factors were not sufficient for these critical responses to mechanical strain. Thus, activation of Yap1 and  $\beta$ -catenin may be a master regulator for cell cycle reentry and progression through S phase following mechanical strain and an underlying mechanism for regulation of homeostasis in adult tissues. Finally, extracellular E-cadherin engagement and  $\beta$ -catenin represent critical regulators of quiescence and strain-induced proliferation in multicellular assemblies. Thus, cell-cell junctions are not only

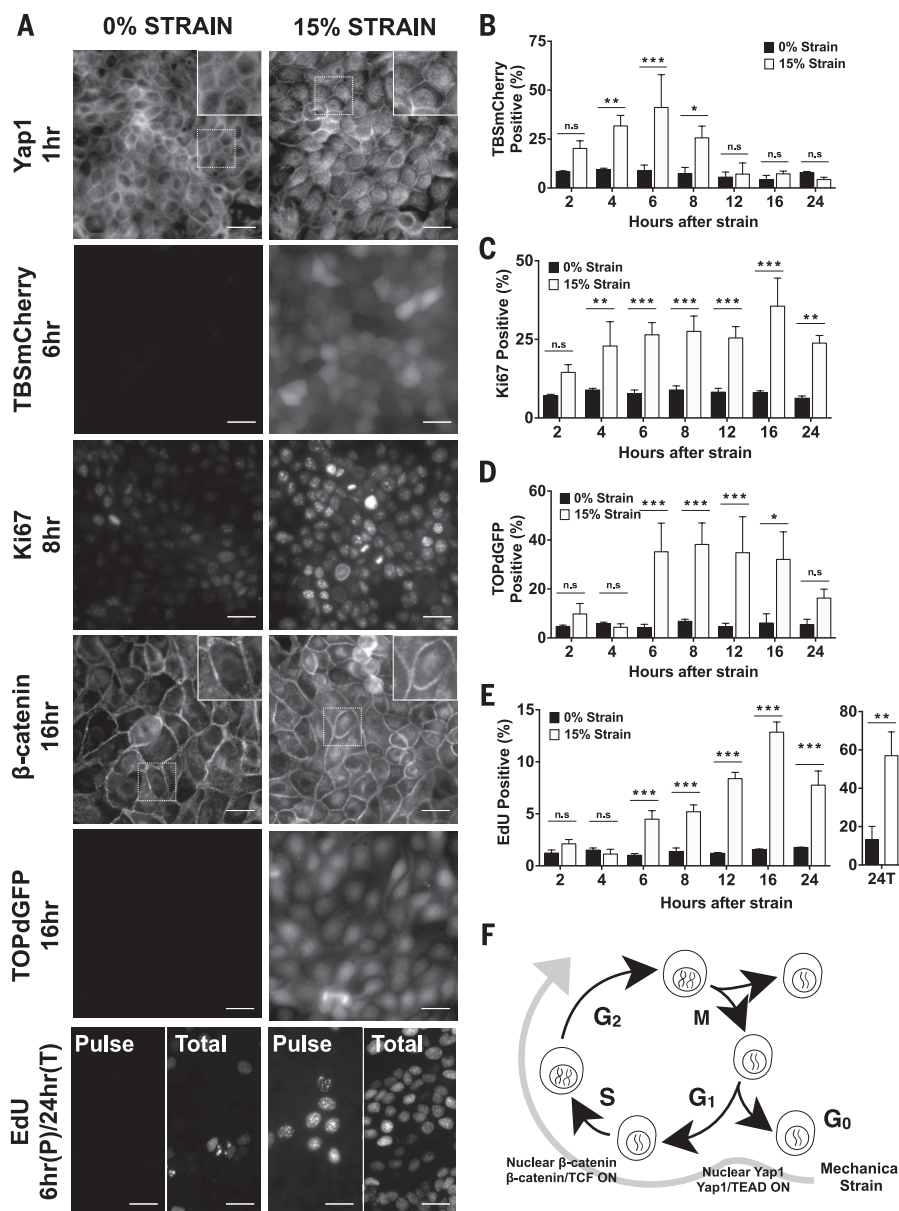


**Fig. 1. Mechanical strain induces cell cycle reentry and sequential activation of Yap1 and  $\beta$ -catenin.** (A) Distribution of Yap1 1 hour after no strain or 15% strain, TBSmCherry after 6 hours, Ki67 after 8 hours,  $\beta$ -catenin after 16 hours, TOPdGFP after 16 hours, and EdU incorporation after a 1-hour pulse (“Pulse”) before fixation at 6 hours, or total EdU incorporation over 24 hours (“Total”). Insets show higher magnification of the region outlined by a dotted line. (B to E) Levels of TBSmCherry (B), Ki67 (C), TOPdGFP (D), and EdU (E) in MDCK monolayers 2 to 24 hours after mechanical strain; for methods used for quantification, see supplementary materials. (F) Summary of cell cycle responses to mechanical strain. Scale bars: 25  $\mu$ m. All quantifications were from at least three independent experiments with two replicate monolayers per experiment (table S1). Quantifications were mean  $\pm$  SEM; unpaired *t* test *P* values <0.05 (\*), <0.01 (\*\*), and <0.001 (\*\*\*). n.s., not significant.



**Fig. 2. Yap1-mediated transcription is required for cell cycle reentry after mechanical strain, but not for  $\beta$ -catenin nuclear accumulation or transcriptional activity.** (A) Percentage of TBSmCherry-positive cells in MDCK monolayers 4 hours after no strain or 15% strain in control (wild type, WT) and YTIP-GFP-expressing cells; (B)  $\beta$ -catenin and TOPdGFP distributions in YTIP-RFP-expressing cells and TOPdGFP quantification (C) after 8 hours; (D) Ki67 distribution and quantification (E) after 8 hours; and EdU incorporation (F) and quantification (G) after 24 hours in WT or YTIP-expressing cells after no strain or 15% strain. YTIP-expressing cells outlined with white dashed lines; insets show higher magnification of the region outlined by a dotted line. Scale bars: 25  $\mu$ m. All quantifications (see supplementary materials) were from at least three independent experiments with two replicate monolayers per experiment (table S1). Quantifications were mean  $\pm$  SEM; unpaired *t* test *P* values <0.05 (\*), <0.01(\*\*), and <0.001(\*\*\*). n.s., not significant.

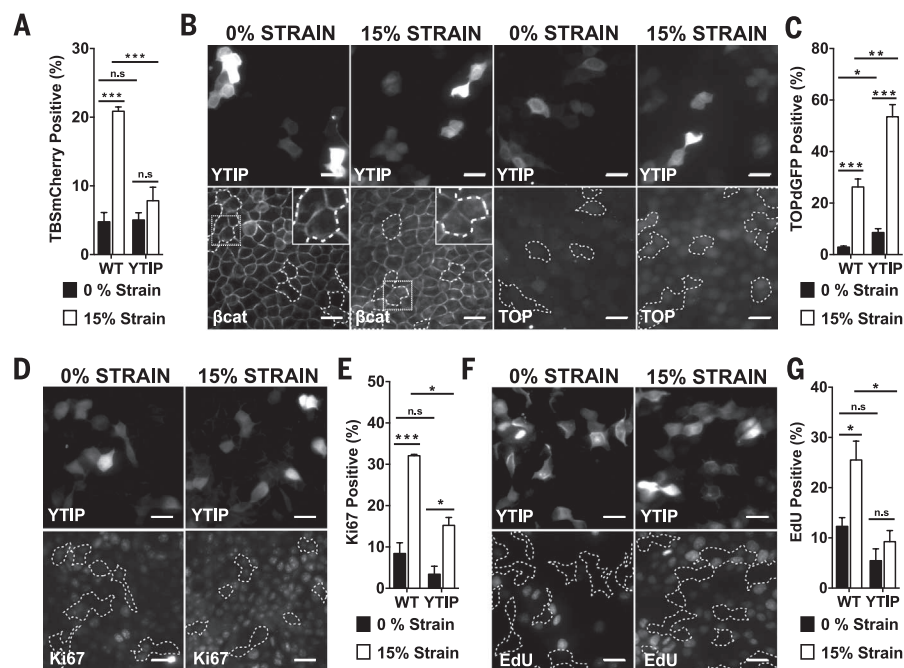
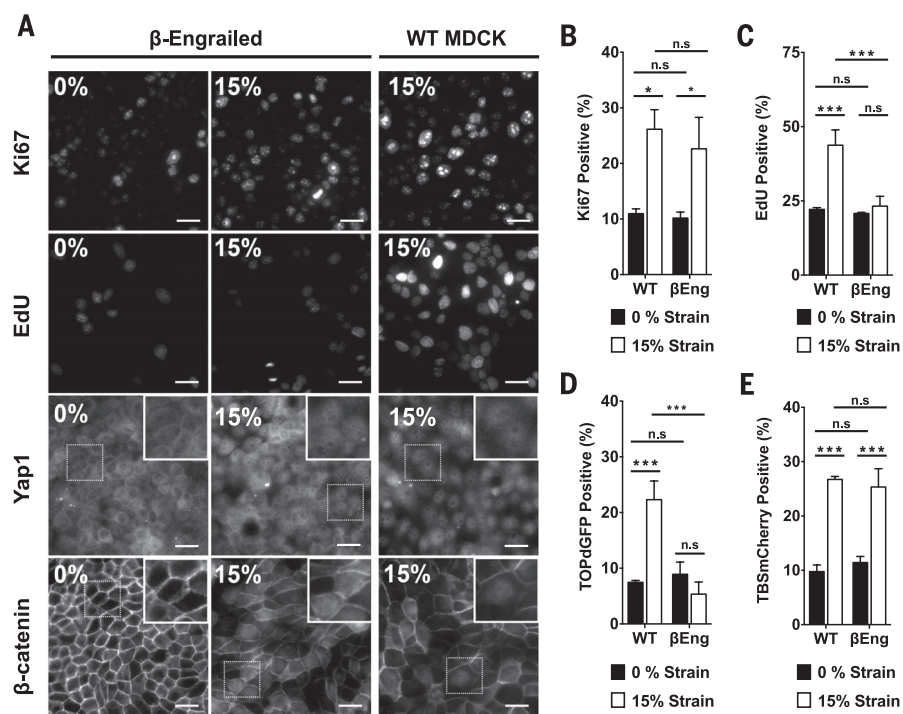


**Fig. 3.  $\beta$ -catenin transcriptional activity was required for cell cycle progression through G<sub>1</sub> into S phase after mechanical strain.** (A) Distributions of Yap1 4 hours after no strain or 15% strain, Ki67 and  $\beta$ -catenin after 8 hours, and EdU incorporation after 24 hours in control (WT) and  $\beta$ Eng-expressing MDCK monolayers. Insets show higher magnification of the region outlined by a dotted line. Quantification of Ki67 (B) and TOPdGFP (D) 8 hours after no strain or 15% strain, EdU (C) after 24 hours, and TBSmCherry (E) after 4 hours in control (WT) and  $\beta$ Eng MDCK cells. Scale bars: 25  $\mu$ m. All quantifications (see supplementary materials) were from at least three independent experiments with two replicate monolayers per experiment (table S1). Quantifications were mean  $\pm$  SEM; unpaired *t* test *P* values <0.05 (\*), <0.01(\*\*), and <0.001(\*\*\*). n.s., not significant.



mechanically responsive structural scaffolds but also signaling centers that coordinate transcriptional responses to externally applied force.

#### REFERENCES AND NOTES

- C. S. Chen, J. Tan, J. Tien, *Annu. Rev. Biomed. Eng.* **6**, 275–302 (2004).
- S. J. Streichan, C. R. Hoerner, T. Schneidert, D. Holzer, L. Hufnagel, *Proc. Natl. Acad. Sci. U.S.A.* **111**, 5586–5591 (2014).
- P. M. Gilbert et al., *Science* **329**, 1078–1081 (2010).
- A. J. Engler, S. Sen, H. L. Sweeney, D. E. Discher, *Cell* **126**, 677–689 (2006).
- S. Dupont et al., *Nature* **474**, 179–183 (2011).
- M. Aragona et al., *Cell* **154**, 1047–1059 (2013).
- S. Pokutta, W. I. Weis, *Annu. Rev. Cell Dev. Biol.* **23**, 237–261 (2007).
- Q. le Duc et al., *J. Cell Biol.* **189**, 1107–1115 (2010).
- Z. Liu et al., *Proc. Natl. Acad. Sci. U.S.A.* **107**, 9944–9949 (2010).
- N. Borghi et al., *Proc. Natl. Acad. Sci. U.S.A.* **109**, 12568–12573 (2012).
- C. D. Buckley et al., *Science* **346**, 1254211–1254211 (2014).
- W. J. Nelson, R. Nusse, *Science* **303**, 1483–1487 (2004).
- K. Schlegelmilch et al., *Cell* **144**, 782–795 (2011).
- M. R. Silvis et al., *Sci. Signal.* **4**, ra33 (2011).
- L. Azzolin et al., *Cell* **158**, 157–170 (2014).
- N.-G. Kim, E. Koh, X. Chen, B. M. Gumbiner, *Proc. Natl. Acad. Sci. U.S.A.* **108**, 11930–11935 (2011).
- C. S. Simmons et al., *J. Micromech. Microeng.* **21**, 54016–54025 (2011).
- H. Aberle, A. Bauer, J. Stappert, A. Kispert, R. Kemler, *EMBO J.* **16**, 3797–3804 (1997).
- S. Ikeda et al., *EMBO J.* **17**, 1371–1384 (1998).
- M. T. Maher, A. S. Flozak, A. M. Stocker, A. Chern, C. J. Gottardi, *J. Cell Biol.* **186**, 219–228 (2009).
- A. von Gise et al., *Proc. Natl. Acad. Sci. U.S.A.* **109**, 2394–2399 (2012).
- Y. Liu-Chittenden et al., *Genes Dev.* **26**, 1300–1305 (2012).
- J. Rosenbluh et al., *Cell* **151**, 1457–1473 (2012).
- W. T. Montross, H. Ji, P. D. McCrea, *J. Cell Sci.* **113**, 1759–1770 (2000).
- F. C. Gonsalves et al., *Proc. Natl. Acad. Sci. U.S.A.* **108**, 5954–5963 (2011).
- Y. Hao, A. Chun, K. Cheung, B. Rashidi, X. Yang, *J. Biol. Chem.* **283**, 5496–5509 (2008).

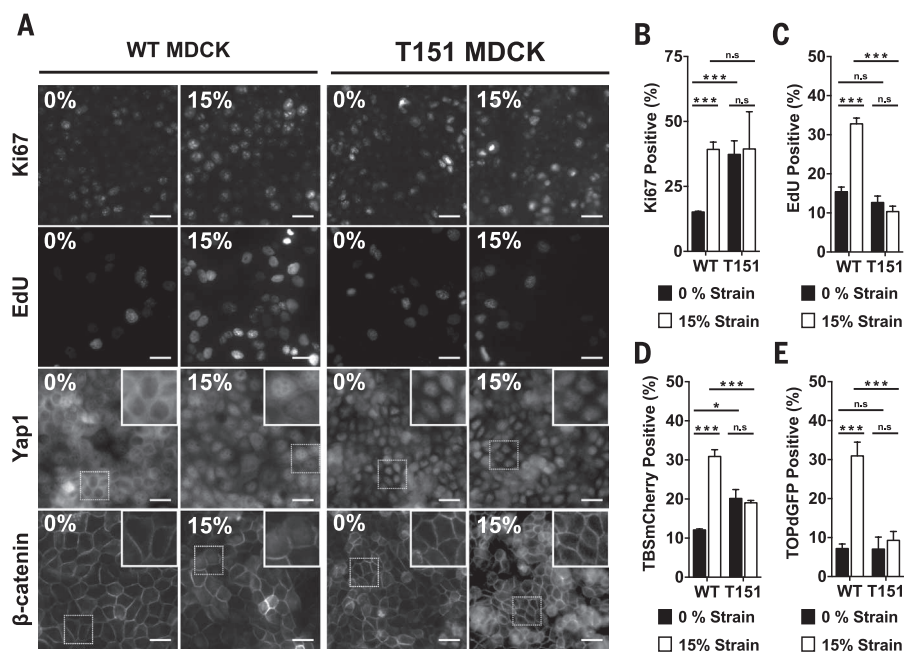


**Fig. 4. E-cadherin extracellular domain interactions were required for quiescence at high density, Yap1 nuclear exclusion, and  $\beta$ -catenin activation following strain.** (A) Distribution of Yap1 after 4 hours, Ki67 and  $\beta$ -catenin after 8 hours, and EdU incorporation after 24 hours in control (WT) and T151 MDCK monolayers after no strain or 15% strain. Insets show higher magnification of the region outlined by a dotted line. Quantification of Ki67 (B) and TOPdGFP (E) after 8 hours, EdU (C) after 24 hours, and TBSmCherry (D) after 4 hours in control (WT) and T151 MDCK cell monolayers after no strain or 15% strain. Scale bars: 25  $\mu$ m. All quantifications (see supplementary materials) were from at least three independent experiments with two replicate monolayers per experiment (table S1). Quantifications were mean  $\pm$  SEM; unpaired *t* test *P* values <0.05 (\*), <0.001 (\*\*\*). n.s., not significant.

27. J. Dong et al., *Cell* **130**, 1120–1133 (2007).
28. L. Lu et al., *Proc. Natl. Acad. Sci. U.S.A.* **107**, 1437–1442 (2010).
29. C. Torre et al., *J. Hepatol.* **55**, 86–95 (2011).
30. B. Zhao, L. Li, K. Tumaneng, C. Y. Wang, K. L. Guan, *Genes Dev.* **24**, 72–85 (2010).
31. J. Whitehead et al., *HFSP J.* **2**, 286–294 (2008).
32. N. Desprat, W. Supatto, P.-A. Pouille, E. Beaupre, E. Farge, *Dev. Cell* **15**, 470–477 (2008).
33. F. J. Alenghat, D. E. Ingber, *Sci. STKE* **2002**, pe6 (2002).

34. V. Vogel, *Annu. Rev. Biophys. Biomol. Struct.* **35**, 459–488 (2006).
35. M. L. Troxell et al., *J. Cell Sci.* **113**, 985–996 (2000).

#### ACKNOWLEDGMENTS

This work was supported by an NSF Predoctoral Fellowship to B.W.B.-P. (DGE-114747) and by grants from the NSF (EFRI-1136790) to B.L.P. and W.J.N. and the NIH to B.L.P. (EB006745) and W.J.N. (GM 35527). C. S. Simmons, B. L. Pruitt, J. Y. Sim, and P. R. Bachtold filed U.S. Patent Application Serial No. 14/376,739 on “Cell Culture Strain Array Systems and Methods for Using the Same.” Data

reported in this paper are further detailed in the supplementary materials.

#### SUPPLEMENTARY MATERIALS

www.sciencemag.org/content/348/6238/1024/suppl/DC1  
Materials and Methods  
Figs. S1 to S9  
Table S1

9 December 2014; accepted 29 April 2015  
10.1126/science.aaa4559

## STRESS RESPONSES

# Mutations in a translation initiation factor identify the target of a memory-enhancing compound

Yusuke Sekine,<sup>1\*</sup> Alisa Zyryanova,<sup>1</sup> Ana Crespiello-Casado,<sup>1</sup> Peter M. Fischer,<sup>2</sup> Heather P. Harding,<sup>1</sup> David Ron<sup>1\*</sup>

The integrated stress response (ISR) modulates messenger RNA translation to regulate the mammalian unfolded protein response (UPR), immunity, and memory formation. A chemical ISR inhibitor, ISRIB, enhances cognitive function and modulates the UPR in vivo. To explore mechanisms involved in ISRIB action, we screened cultured mammalian cells for somatic mutations that reversed its effect on the ISR. Clustered missense mutations were found at the amino-terminal portion of the delta subunit of guanine nucleotide exchange factor (GEF) eIF2B. When reintroduced by CRISPR-Cas9 gene editing of wild-type cells, these mutations reversed both ISRIB-mediated inhibition of the ISR and its stimulatory effect on eIF2B GEF activity toward its substrate, the translation initiation factor eIF2, in vitro. Thus, ISRIB targets an interaction between eIF2 and eIF2B that lies at the core of the ISR.

**T**he integrated stress response (ISR) is a widely conserved mechanism for coupling diverse upstream stresses to the phosphorylation of serine 51 in the  $\alpha$  subunit of eukaryotic translation initiation factor 2 (eIF2 $\alpha$ ) (1, 2).

Underlying the eIF2 $\alpha$  phosphorylation-dependent ISR is a potent attenuation in translation of most mRNAs and selective up-regulation of translation of a few special mRNAs that encode transcriptional regulators. The ISR thus activates a broad

translational and transcriptional program involved in resistance to unfolded protein stress in the endoplasmic reticulum (ER stress) (3), intermediary metabolism (2), memory (4), and immunity (5).

A small-molecule ISR inhibitor (ISRIB) exerts potent effects on the outcome of stress and on memory (6, 7). As expected, ISRIB interfered with the ISR without blocking phosphorylation of eIF2 $\alpha$  (Fig. 1A), suggesting that its molecular target(s) lie between eIF2( $\alpha$ P) and its effects on the translational machinery.

We tested ISRIB's effects on mRNA translation in an in vitro assay—cell-free translation in reticulocyte lysates. Both ISRIB and the eIF2 $\alpha$  kinase inhibitor GSK2606414 (8) increased the luminescent signal of reticulocyte lysates programmed with luciferase-encoding mRNA (fig. S1A). The effect of ISRIB was enhanced further through eIF2 $\alpha$  phosphorylation, which was promoted by preincubating the lysate at 30°C before adding the luciferase mRNA (fig. S1, B and C). ISRIB's

<sup>1</sup>University of Cambridge, Cambridge Institute for Medical Research (CIMR), the Wellcome Trust MRC Institute of Metabolic Science and NIHR Cambridge Biomedical Research Centre, Cambridge CB2 0XY, UK. <sup>2</sup>Division of Medicinal Chemistry and Structural Biology, School of Pharmacy, Centre for Biomolecular Sciences, University of Nottingham, Nottingham NG7 2RD, UK.

\*Corresponding author. E-mail: dr360@medschl.cam.ac.uk (D.R.); ys412@cam.ac.uk (Y.S.)



median effective concentration ( $EC_{50}$ ) for stimulating translation, 35 nM, was similar to that in vivo (6) and was restricted to the trans geometric isomer (Fig. 1B). Thus, the ISR imparted by resident eIF2 $\alpha$  kinase(s) in the reticulocyte lysate could be reversed by ISRIB.

Phosphorylation of eIF2 $\alpha$  inhibits protein synthesis by inhibiting eIF2B, a guanine nucleotide exchange factor (GEF), which accelerates the exchange of guanosine 5'-diphosphate (GDP) for guanosine 5'-triphosphate (GTP) in the eIF2 complex (9, 10). To measure the effects of ISRIB on eIF2B GEF activity, we established an assay in which the GEF activity in cell lysates (11) promoted the release of boron-dipyrromethene (BODIPY-FL)-conjugated GDP (hereafter [b]GDP) from purified eIF2, with an attendant decrease in fluorescent intensity. The eIF2 substrate was purified from Chinese hamster ovary (CHO) cells that also expressed a conditionally active eIF2 $\alpha$  kinase [Fv2E-

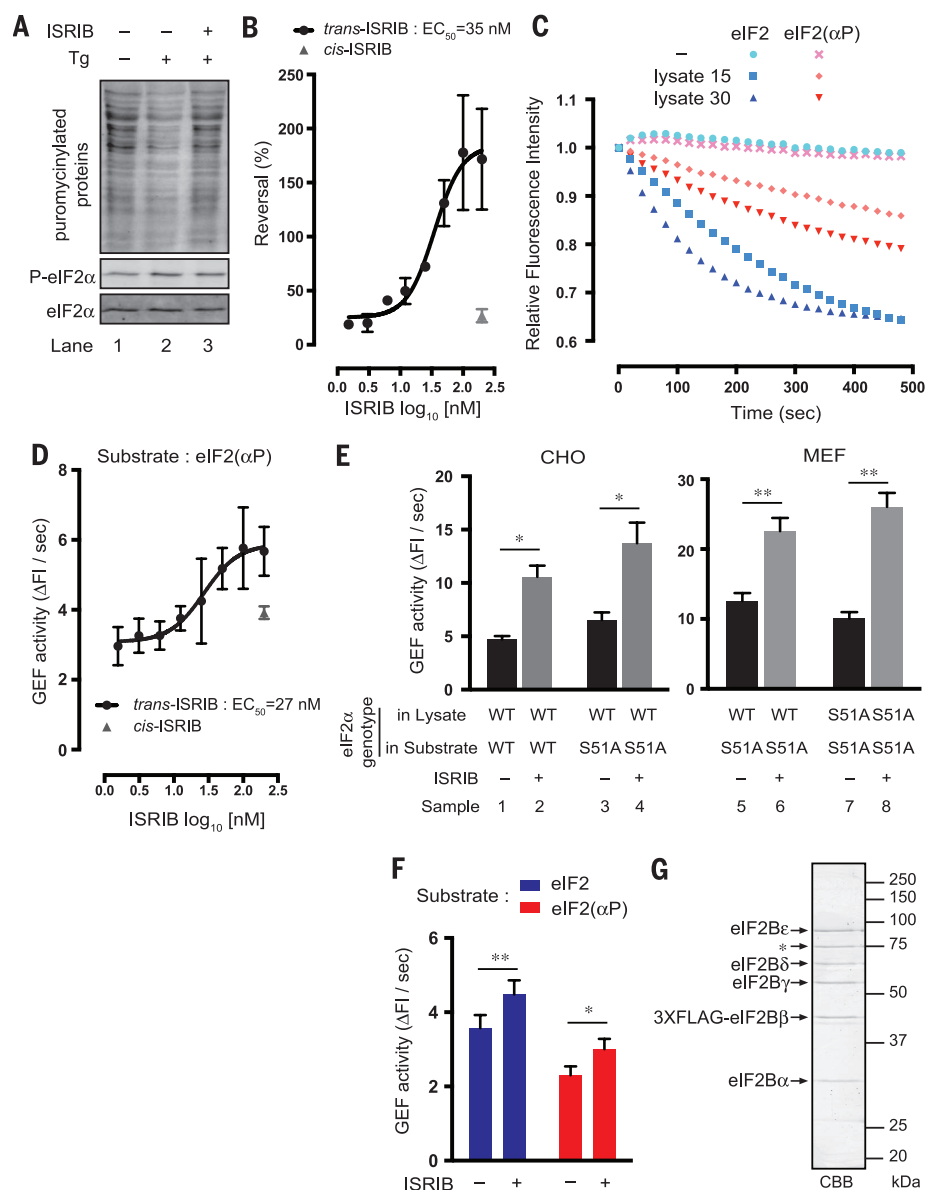
PERK (12)], and eIF2 with low or high levels of phosphorylation was generated by treating the cells briefly with the Fv2E-PERK activator, AP20187 (fig. S2, A to C). A lysate protein concentration- and time-dependent decrease in fluorescence intensity of eIF2-[b]GDP was observed (Fig. 1C), consistent with lysate-induced release of the bound nucleotide. The fluorescent signal declined more slowly in eIF2-[b]GDP with higher levels of phosphorylated eIF2 $\alpha$  (Fig. 1C and fig. S2D), consistent with the inhibitory effect of eIF2( $\alpha$ P) on eIF2B GEF activity (13). ISRIB compensated for the inhibitory effect of eIF2( $\alpha$ P) on the GEF activity in cell lysate, with an  $EC_{50}$  of 27 nM; similar to ISRIB's action in intact cells (Fig. 1D).

ISRIB-mediated acceleration of GEF activity was maintained with an eIF2( $\alpha^{S51A}$ )-[b]GDP substrate that could not be phosphorylated (Fig. 1E, samples 1 to 4) and was observed in lysates from both wild-type (eIF2 $\alpha^{+/+}$ ) and mutant (eIF2 $\alpha^{S51A/S51A}$ )

mouse embryonic fibroblasts (14) (Fig. 1E, samples 5 to 8). Furthermore, ISRIB stimulated the GEF activity of purified eIF2B on both phosphorylated and nonphosphorylated eIF2 (Fig. 1, F and G), suggesting that the molecular target of ISRIB is present in the pure complex and functions independently of eIF2 phosphorylation.

To isolate ISRIB-resistant cells (ISRIB<sup>r</sup>), we used a CHO-K1-based cell line (CHO-C30) with the ISR-activated promoter of the mouse *Ddit3/CHOP* gene fused to green fluorescent protein (*CHOP::GFP*) (15). Activation of *CHOP::GFP* by unfolded protein stress in the ER was only partially inhibited by ISRIB, whereas activation by histidinol, a competitive inhibitor of histidine tRNA synthetase [which activates the eIF2 $\alpha$  kinase GCN2 (16)], was strongly inhibited (fig. S3). Chemically induced mutations that reversed the ISRIB-mediated suppression of the histidinol-induced ISR generated ISRIB<sup>r</sup> CHO-C30 cells (fig. S4, A and B).

### Fig. 1. ISRIB reverses attenuated translation and accelerates eIF2B GEF activity toward eIF2( $\alpha$ P) in vitro. (A) Immunoblot of newly synthesized puromycylated proteins in extracts of CHO cells. Cells were exposed to the ISR-inducing agent thapsigargin (Tg 300 nM, 30 min) in the presence or absence of *trans*-ISRIB (100 nM). Phosphorylated (P-eIF2 $\alpha$ ) and total eIF2 $\alpha$ were detected in the immunoblots below. Quantified signal intensities are shown in fig. S5. (B) Dose-response of ISRIB stimulation of translation in reticulocyte lysate fitted to a nonlinear trace. Mean $\pm$ SEM ( $n = 3$ ) and $EC_{50}$ (for active *trans*-ISRIB). Note the inactivity of *cis*-ISRIB. (C) GEF activity as reflected in time-dependent decrease in fluorescence of weakly and heavily phosphorylated eIF2 loaded with Bodipy-FL-GDP and incubated with unlabeled GDP in the presence or absence of cell lysate ( $\mu$ g). Mean of three independent measurements. (D) Relation between the initial velocities of the release of Bodipy-FL-GDP from heavily phosphorylated eIF2 and ISRIB concentration, fitted to a nonlinear trace. Mean $\pm$ SEM ( $n = 3$ ) and $EC_{50}$ for *trans*-ISRIB. (E) GEF activity reflected in the initial velocities of GDP release reactions with CHO cell lysate (samples 1 to 4), wild-type or mutant eIF2 $\alpha^{S51A/S51A}$ mouse embryonic fibroblast lysate (MEFs, samples 5 to 8), and Bodipy-FL-GDP-loaded eIF2 of the indicated eIF2 $\alpha$ genotype. Mean $\pm$ SEM ( $n = 3$ for samples 1 to 4 and $n = 6$ for samples 5 to 8). \* $P < 0.05$ , \*\* $P < 0.01$ (Student's $t$ test). (F) As in (E), but with purified eIF2B and Bodipy-FL-GDP-loaded non-phosphorylated and phosphorylated eIF2. Mean $\pm$ SEM ( $n = 8$ ). \* $P = 0.012$ , \*\* $P = 0.0054$ (Student's $t$ test). (G) Coomassie-stained SDS-polyacrylamide gel electrophoresis (CBB) of the purified eIF2B used in (F). The five subunits of eIF2B and PRMT5 (\*, a nonspecific contaminant) are noted.



We isolated numerous clones with strong or weak ISRIB<sup>r</sup> phenotypes (Fig. 2A and fig. S4, C to E). The ISRIB<sup>r</sup> mutation(s) reversed both the sensitivity of the ISR reporter gene to ISRIB and the ability of ISRIB to promote protein synthesis in stressed cells (Fig. 2, B and C, and fig. S5). Furthermore, the eIF2-directed GEF activity in lysates from the mutant clones was not stimulated by ISRIB in vitro (Fig. 2D).

ISRIB targets the interaction of eIF2B with eIF2. Therefore, we examined the coding region of the genes encoding the subunits of eIF2B and eIF2. With one exception, the coding regions of eIF2B subunits  $\alpha$ ,  $\beta$ ,  $\gamma$ , and  $\epsilon$  and eIF2 $\alpha$  had no mutations (table S1). This bland mutational landscape contrasted markedly with that of *Eif2b4*, encoding eIF2B $\delta$ . Most of the ISRIB<sup>r</sup> clones isolated had one or more nonsynonymous mutations affecting three closely spaced codons, R171, V178, and L180 (table S1 and fig. S6). These mutations cluster in a unique N-terminal region of eIF2B $\delta$  that is not conserved in the other two regulatory subunits of the GEF, but is well conserved among vertebrate eIF2B $\delta$  (Fig. 3A and fig. S7).

To determine if the mutations in these clustered residues of eIF2B $\delta$  were sufficient to impart an ISRIB<sup>r</sup> phenotype, we promoted homologous recombination at the *Eif2b4* locus of parental CHO-C30 cells by clustered regularly interspaced short palindromic repeats (CRISPR)-Cas9-directed editing, offering a homologous directed repair template with either the eIF2B $\delta$ <sup>R171Q</sup> or eIF2B $\delta$ <sup>L180F</sup> mutation (fig. S8A). With either repair template, a population of ISRIB<sup>r</sup> cells emerged after cotransfection of the CRISPR guide and Cas9 nuclease. A single round of enrichment by sorting delivered clones with weak and strong ISRIB<sup>r</sup> phenotypes (fig. S8, B to D, and table S2). Clones with the weak ISRIB<sup>r</sup> phenotype retained a wild-type copy of the gene encoding eIF2B $\delta$ , whereas clones with the strong ISRIB<sup>r</sup> phenotype had gained the mutation and lost both wild-type alleles (Fig. 3, B to E).

In vitro, the baseline GEF activity in lysates from eIF2B $\delta$ <sup>R171Q</sup> mutant cells was two-fold lower, whereas that of the eIF2B $\delta$ <sup>L180F</sup> was indistinguishable from the wild-type activity (Fig. 3F). Yet both mutations similarly attenuated the effect of ISRIB on lysate GEF activity (Fig. 3G and fig. S9). Thus, mutations in eIF2B $\delta$  can selectively

compromise ISRIB action without affecting other aspects of eIF2B function.

Here we used a chemical genetic approach to identify proteins implicated in ISRIB action. We found that a small segment of eIF2B $\delta$  is involved in the response to ISRIB, providing a molecular clue to how ISRIB might work. Though it is not clear if ISRIB binds eIF2B directly, ISRIB's ability to promote GEF activity in vitro, together with the identification of a clustered set of mutations in the  $\delta$  subunit that selectively eliminate this response (imparting an ISRIB<sup>r</sup> phenotype on cells), suggest that direct modulation of the GEF lies at the heart of ISRIB-mediated reversal of the ISR. The active form of eIF2B is a dimer of pentamers (17–19), whereas the active, trans-isomer of ISRIB has perfect twofold symmetry. Perhaps stabilization of the eIF2B decamer by binding of a symmetric molecule across the interface of its constituent pentamers is important for ISRIB's action and the ISRIB<sup>r</sup> mutations, identified here, interfere with this process.

*Note added in proof:* The delta subunit of eIF2B has been independently fingered as a likely target for ISRIB action (20).

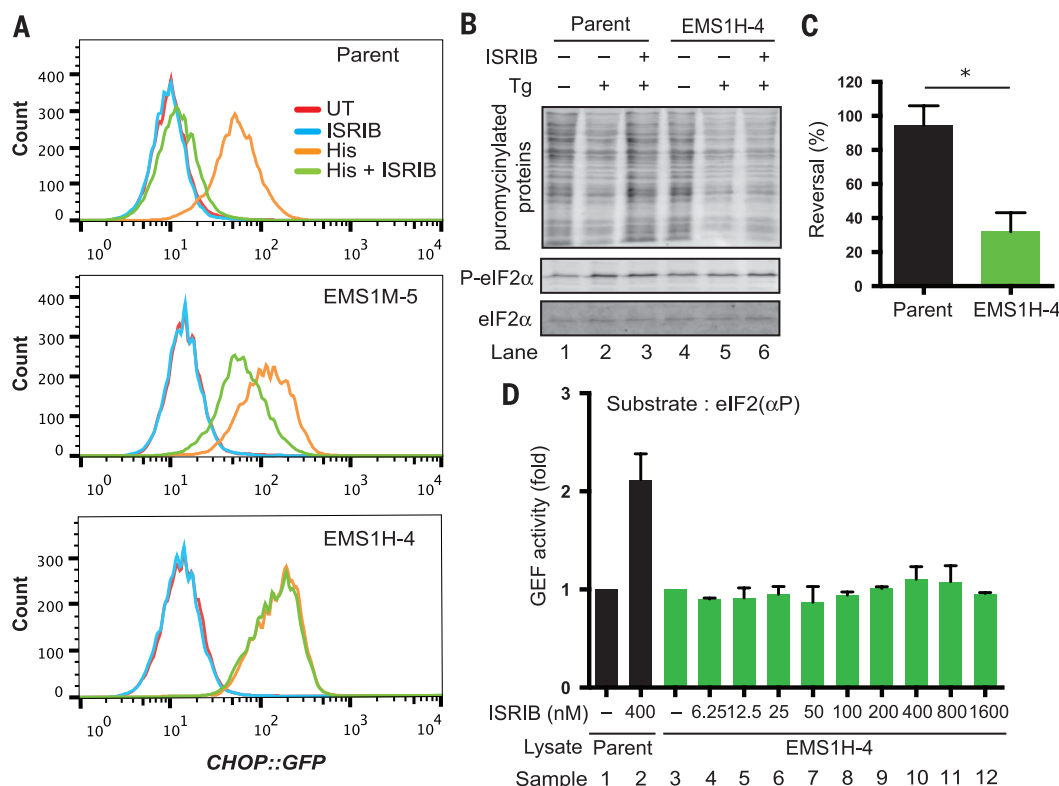
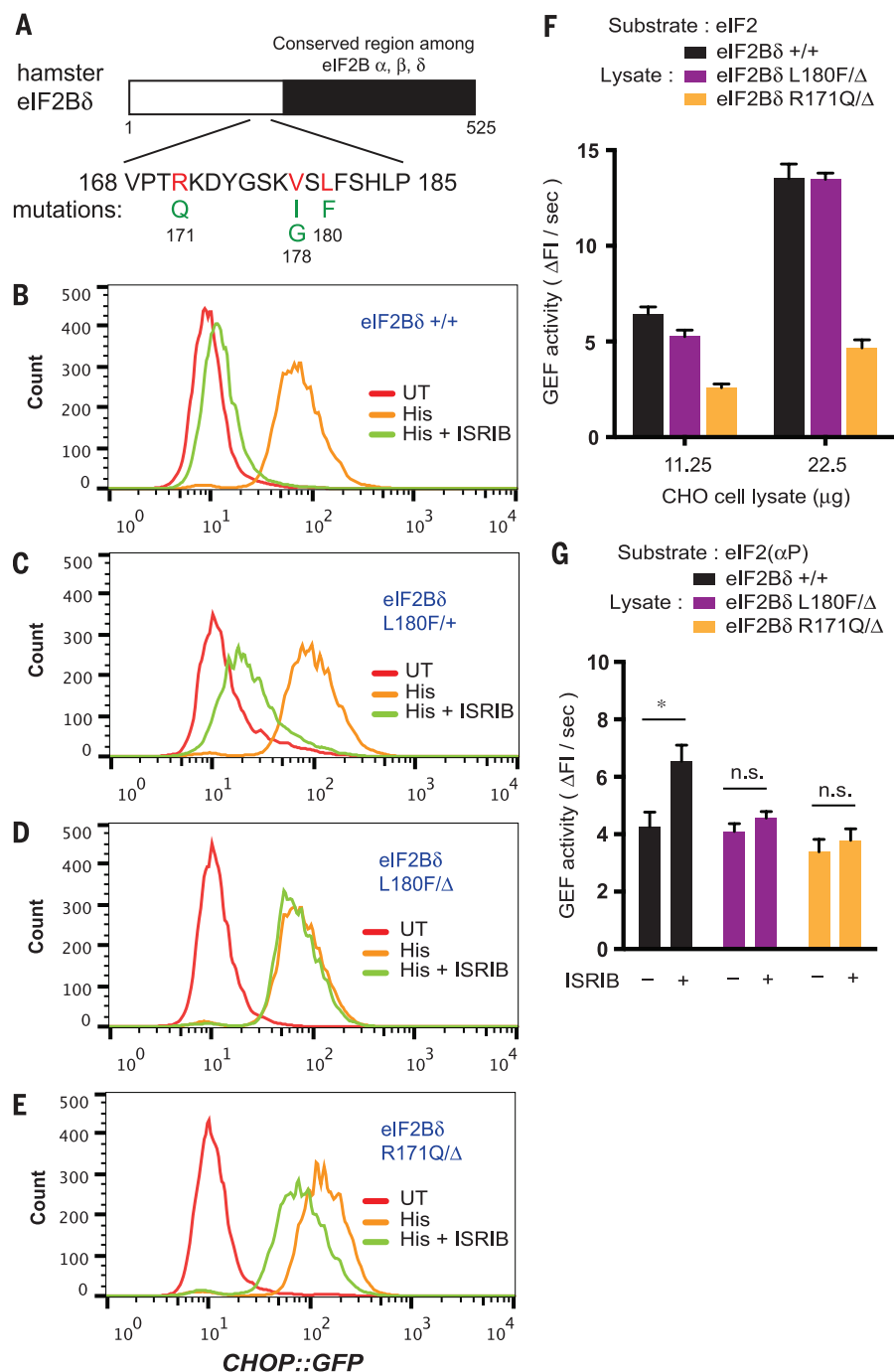


**Fig. 2. Selection of ISRIB-resistant (ISRIB<sup>r</sup>) mutations.** (A) Histograms of the distribution of GFP fluorescence arising from an ISR-inducible *CHOP::GFP* reporter gene in parental CHO-C30 cells and clones bearing the indicated mutations. The cells were left untreated or treated with histidinol (His; 0.5 mM), ISRIB (100 nM), or both. EMS1M-5 exemplifies a class of clones with a weak and EMS1H-4 a class with a strong, ISRIB<sup>r</sup> phenotype. (B) Immunoblot of puromycinylated proteins in extracts of parental CHO-C30 cells or a representative strong ISRIB<sup>r</sup> clone (EMS1H-4) after exposure to thapsigargin (Tg) in the presence or absence of ISRIB (as in Fig. 1A). The images are representative of all three independent experiments that yielded similar results. Quantified signal

intensities are shown in fig. S5. (C) Bar diagram, displaying the reversal of translation attenuation by ISRIB in "B" above: Reversal =  $[(P^{Tg+ISRIB} - P^{Tg}) \div (P^{UT} - P^{Tg})] \times 100$ , ( $P^{Tg+ISRIB}$ ,  $P^{Tg}$ , and  $P^{UT}$  are the puromycinylated signal from the sample treated with Tg and ISRIB (lane 3 or 6), Tg alone (lanes 2 or 5), and the untreated sample (lanes 1 or 3), respectively. Mean  $\pm$  SEM ( $n = 3$ ). \* $P < 0.05$  (Student's  $t$  test). (D) Bar diagram of the GEF activity of lysates from parental and strong ISRIB<sup>r</sup> mutant cells with Bodipy-FL-GDP-loaded eIF2( $\alpha$ P) as a substrate in the absence or presence of ISRIB, as indicated. Mean  $\pm$  SEM of the initial velocity of the decline in Bodipy-FL-GDP fluorescence upon adding lysate, normalized to the rate in the untreated sample ( $n = 4$ ).



**Fig. 3. Clustered mutations in *Eif2b4* impart ISRIB resistance.** (A) Schema of eIF2B $\delta$  with the position of the mutations associated with an ISRIB<sup>r</sup> phenotype indicated. These are clustered at the unique N-terminal region that is not conserved in the other regulatory subunits ( $\alpha$ ,  $\beta$ ) of eIF2B. (B to E) Distribution of *CHOP::GFP* reporter gene activity in parental CHO-C30 cells and derivative subclones bearing the indicated mutations (induced by CRISPR-Cas9 targeted homologous recombination at the *Eif2b4* locus). The cells were left untreated or treated for 24 hours with histidinol (His; 0.5 mM) alone or with ISRIB (100 nM). (F and G) Bar diagram of the GEF activity of lysates from parental or CRISPR-Cas9-induced ISRIB<sup>r</sup> mutant cells with Bodipy-FL-GDP-loaded eIF2 or eIF2( $\alpha$ P) as substrates in the absence or presence of ISRIB, as indicated. Mean  $\pm$  SEM ( $n = 6$ , for (F);  $n = 5$  for (G)). \* $P < 0.05$ , n.s.; not significant (Student's  $t$  test).



## REFERENCES AND NOTES

1. H. P. Harding *et al.*, *Mol. Cell* **11**, 619–633 (2003).
2. T. D. Baird, R. C. Wek, *Adv. Nutr.* **3**, 307–321 (2012).
3. H. P. Harding, Y. Zhang, A. Bertolotti, H. Zeng, D. Ron, *Mol. Cell* **5**, 897–904 (2000).
4. M. Costa-Mattioli *et al.*, *Nature* **436**, 1166–1173 (2005).
5. D. H. Munn *et al.*, *Immunity* **22**, 633–642 (2005).
6. C. Sidrauski *et al.*, *eLife* **2**, e00498 (2013).
7. G. V. Di Prisco *et al.*, *Nat. Neurosci.* **17**, 1073–1082 (2014).
8. J. M. Axten *et al.*, *J. Med. Chem.* **55**, 7193–7207 (2012).
9. R. S. Ranu, I. M. London, *Proc. Natl. Acad. Sci. U.S.A.* **76**, 1079–1083 (1979).
10. C. de Haro, S. Ochoa, *Proc. Natl. Acad. Sci. U.S.A.* **76**, 1741–1745 (1979).
11. S. R. Kimball, W. V. Everson, K. E. Flaim, L. S. Jefferson, *Am. J. Physiol.* **256**, C28–C34 (1989).
12. P. D. Lu *et al.*, *EMBO J.* **23**, 169–179 (2004).

13. S. R. Kimball, J. R. Fabian, G. D. Pavitt, A. G. Hinnebusch, L. S. Jefferson, *J. Biol. Chem.* **273**, 12841–12845 (1998).
14. D. Scheuner *et al.*, *Mol. Cell* **7**, 1165–1176 (2001).
15. I. Novoa, H. Zeng, H. P. Harding, D. Ron, *J. Cell Biol.* **153**, 1011–1022 (2001).
16. P. Zhang *et al.*, *Mol. Cell Biol.* **22**, 6681–6688 (2002).
17. N. C. Wortham, M. Martinez, Y. Gordiyenko, C. V. Robinson, C. G. Proud, *FASEB J.* **28**, 2225–2237 (2014).
18. Y. Gordiyenko *et al.*, *Nat. Commun.* **5**, 3902 (2014).
19. A. M. Bogorad *et al.*, *Biochemistry* **53**, 3432–3445 (2014).
20. C. Sidrauski *et al.*, *eLife* **4**, e07314 (2015).

## ACKNOWLEDGMENTS

We thank P. Walter and C. Sidrauski (University of California, San Francisco) for their gift of ISRIB (used to confirm their observations), R. Schulte from the flow cytometry core, and R. Antrobus from the mass spectrometry core at the CIMR for their

technical assistance. Supported by grants from the Wellcome Trust (Wellcome 084812/Z/08/Z and a strategic award Wellcome 100140), and by fellowships to Y.S. from the Daiichi Sankyo Foundation of Life Science and the Japan Society for the Promotion of Science for research abroad. D.R. is a Wellcome Trust Principal Research Fellow.

## SUPPLEMENTARY MATERIALS

www.sciencemag.org/content/348/6238/1027/suppl/DC1  
Materials and Methods  
Figs. S1 to S9  
Tables S1 to S3  
References (21–30)

15 January 2015; accepted 25 March 2015  
Published online 9 April 2015;  
10.1126/science.aaa6986

## IMMUNE TOLERANCE

# Group 3 innate lymphoid cells mediate intestinal selection of commensal bacteria-specific CD4<sup>+</sup> T cells

Matthew R. Hepworth,<sup>1</sup> Thomas C. Fung,<sup>1,2</sup> Samuel H. Masur,<sup>3</sup> Judith R. Kelsen,<sup>3</sup> Fiona M. McConnell,<sup>4</sup> Juan Dubrot,<sup>5</sup> David R. Withers,<sup>4</sup> Stephanie Hugues,<sup>5</sup> Michael A. Farrar,<sup>6</sup> Walter Reith,<sup>5</sup> Gérard Eberl,<sup>7</sup> Robert N. Baldassano,<sup>3</sup> Terri M. Laufer,<sup>2,8</sup> Charles O. Elson,<sup>9</sup> Gregory F. Sonnenberg<sup>1\*</sup>

Inflammatory CD4<sup>+</sup> T cell responses to self or commensal bacteria underlie the pathogenesis of autoimmunity and inflammatory bowel disease (IBD), respectively. Although selection of self-specific T cells in the thymus limits responses to mammalian tissue antigens, the mechanisms that control selection of commensal bacteria-specific T cells remain poorly understood. Here, we demonstrate that group 3 innate lymphoid cell (ILC3)–intrinsic expression of major histocompatibility complex class II (MHCII) is regulated similarly to thymic epithelial cells and that MHCII<sup>+</sup> ILC3s directly induce cell death of activated commensal bacteria-specific T cells. Further, MHCII on colonic ILC3s was reduced in pediatric IBD patients. Collectively, these results define a selection pathway for commensal bacteria-specific CD4<sup>+</sup> T cells in the intestine and suggest that this process is dysregulated in human IBD.

**P**athologic CD4<sup>+</sup> T cell responses to self are limited by presentation of self-antigens in the thymus on major histocompatibility complex class II–positive (MHCII<sup>+</sup>) thymic epithelial cells (TECs) and dendritic cells (DCs), resulting in clonal deletion (1–6). In contrast, commensal bacteria-specific CD4<sup>+</sup> T cells, which have been implicated in the pathogenesis of inflammatory bowel disease (IBD) (7–11), do not encounter cognate antigen in the thymus and therefore are not subject to negative selection before entering the periphery (12, 13). Although physical and biochemical barriers separate the immune system from intestinal commensal bacteria (7, 13–17), antigens derived from commensal bacteria are continuously sampled from the intestinal lumen and presented by DCs in the draining lymph nodes (7, 10, 15, 18, 19). Regulatory T cells (T<sub>reg</sub>) can in part limit dysregulated CD4<sup>+</sup> T cell responses to commensal bacteria (20, 21). However, whether other mechanisms control commensal bacteria-specific CD4<sup>+</sup>

T cells in lieu of thymic negative selection is poorly defined. In recent studies, group 3 innate lymphoid cells (ILC3s) were found to express MHCII, and genetic deletion of ILC3-intrinsic MHCII resulted in spontaneous CD4<sup>+</sup> T cell-dependent intestinal inflammation (22), suggesting that additional antigen-presentation pathways control commensal bacteria-specific CD4<sup>+</sup> T cell populations.

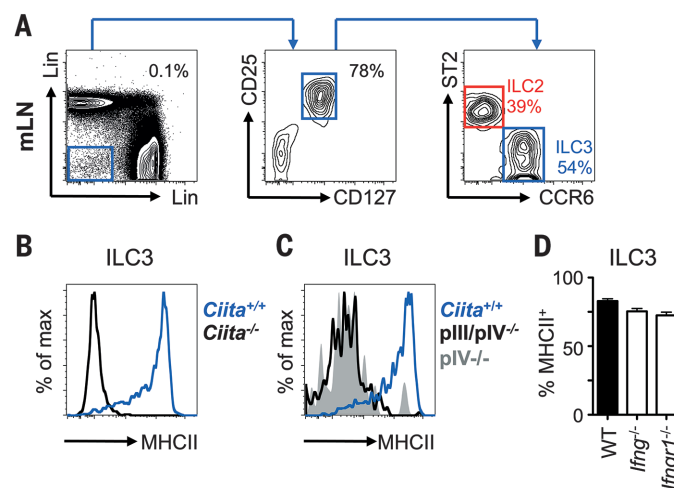
CCR6-expressing lymphoid tissue inducer (LTI)–like ILC3s (CCR6<sup>+</sup> ILC3s) are a major ILC subset present in the mesenteric lymph node (mLN) (Fig. 1A) and colon lamina propria (cLPL) (fig. S1A) of healthy mice and constitutively express retinoic acid–related orphan receptor gamma t (RORγt) and MHCII, relative to ST2<sup>+</sup> group 2 ILCs

(ILC2) (fig. S1, B and C). ILC3s are regulated by various cytokine, environmental, and microbial factors (23, 24). However, interleukin (IL)–23p19, the aryl hydrocarbon receptor (Ahr), or the intestinal microbiota were not required for CCR6<sup>+</sup> ILC3 expression of MHCII (fig. S1, D to F), although ILC3 frequencies were reduced in the intestine of *Ahr*<sup>−/−</sup> mice, as previously described (fig. S1E) (25). Further, in contrast to a recent report (26), expression of MHCII, CD80, and CD86 on CCR6<sup>+</sup> ILC3s was unaffected by ex vivo stimulation with microbial or inflammatory stimuli or by the absence of MyD88 or Caspase 1/11 in vivo (fig. S2).

Next, we examined whether expression of ILC3-intrinsic MHCII was dependent on the class II transactivator (CIITA), a master transcriptional regulator of MHCII expression (27). MHCII expression was absent on both CCR6<sup>+</sup> ILC3s and canonical antigen-presenting cells from *Ciita*<sup>−/−</sup> mice, relative to *Ciita*<sup>+/+</sup> control mice (Fig. 1B and fig. S3A). Transcription of *Ciita* in mice is driven via distinct promoter elements—termed pI, pIII, and pIV—that are indicative of the upstream signaling events that induce MHCII expression (27). In contrast to B cells and DCs, CCR6<sup>+</sup> ILC3-intrinsic MHCII expression was absent in the mLN of both *pIII/pIV*<sup>−/−</sup> and *pIV*<sup>−/−</sup> mice (Fig. 1C and fig. S3, B and C), indicating that the pIV promoter of *Ciita* is required for MHCII expression on CCR6<sup>+</sup> ILC3s. The pIV promoter of *Ciita* is used by multiple cell types, such as epithelial cells, in response to interferon (IFN)–γ signaling (27). However, expression of MHCII on CCR6<sup>+</sup> ILC3s was not impaired in the absence of IFN–γ, IFN–γR1, or STAT-1 (Fig. 1D and fig. S3, D and E). MHCII expression in TECs was also dependent on the pIV promoter of *Ciita* (fig. S3, A and B), and pIV-dependent, IFN–γ–independent CIITA expression has previously only been described in TECs (27–29), suggesting a previously unappreciated link between ILC3s and TECs.

These data provoked the hypothesis that TECs and MHCII<sup>+</sup> ILC3s may share similar

**Fig. 1. ILC3 expression of MHCII is controlled by a transcriptional pathway previously associated with thymic epithelial cells.** (A) mLN cells from naïve mice were gated as CD45<sup>+</sup> lineage (x axis: CD3, CD5, CD8, and NK1.1; y-axis: B220, CD11c, and CD11b) negative, CD25<sup>+</sup>, and CD127<sup>+</sup> and further divided by expression of ST2 (ILC2, red) or CCR6 (ILC3, blue). MHCII expression was determined on ILC3s in mice deficient in



(B) CIITA, (C) CIITA promoter regions (pIII/pIV and pIV) or (D) IFN–γ and IFN–γR1. All data are representative of at least three independent experiments with *n* = 2 to 3 mice per group.

<sup>1</sup>Jill Roberts Institute for Research in Inflammatory Bowel Disease, Joan and Sanford I. Weill Department of Medicine, Gastroenterology Division, and Department of Microbiology and Immunology, Weill Cornell Medical College, Cornell University, New York, NY, USA. <sup>2</sup>Perelman School of Medicine, University of Pennsylvania, Philadelphia, PA, USA. <sup>3</sup>Division of Gastroenterology, Hepatology, and Nutrition, Children's Hospital of Philadelphia, Philadelphia, PA, USA. <sup>4</sup>Medical Research Council, Centre for Immune Regulation, College of Medical and Dental Sciences, University of Birmingham, Birmingham, UK. <sup>5</sup>Department of Pathology and Immunology, University of Geneva Medical School, Geneva, Switzerland. <sup>6</sup>Center for Immunology, Department of Laboratory Medicine and Pathology, University of Minnesota, MN, USA. <sup>7</sup>Institut Pasteur, Microenvironment and Immunity Unit, Paris, France. <sup>8</sup>Philadelphia Veterans Affairs Medical Center, Philadelphia, PA, USA. <sup>9</sup>Departments of Medicine and Microbiology, University of Alabama at Birmingham, Birmingham, AL, USA.

\*Corresponding author. E-mail: gfsonnenberg@med.cornell.edu



functional roles in the selection of CD4<sup>+</sup> T cells. To test this, we examined CD4<sup>+</sup> T cells in the intestines of mice with an ILC3-intrinsic deletion in MHCII (MHCII<sup>ΔILC3</sup> mice). As we previous-

ly reported (22), frequencies and cell numbers of CD44<sup>hi</sup> CD4<sup>+</sup> T cells (T<sub>eff</sub>) in the cLPL of MHCII<sup>ΔILC3</sup> mice were increased relative to *H2-Ab1*<sup>fl/fl</sup> controls (fig. S4, A and B). In contrast,

the total numbers of CD44<sup>lo</sup> naïve T cells and FoxP3<sup>+</sup> T<sub>reg</sub> were unchanged (fig. S4B). T<sub>eff</sub> cell populations used a broad range of T cell receptor (TCR) Vβ chains, and T<sub>eff</sub> expansion was

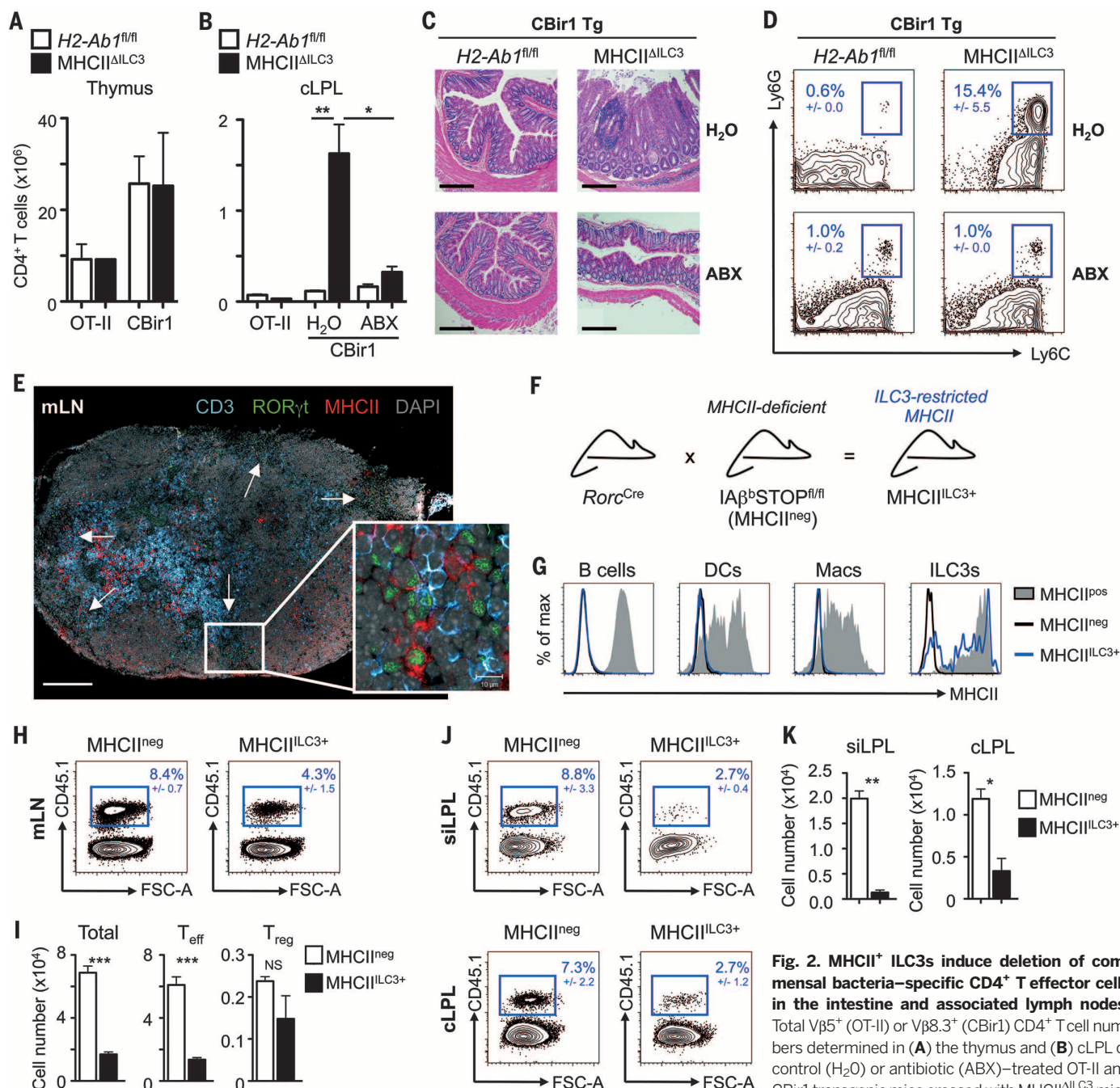


**Fig. 2. MHCII<sup>+</sup> ILC3s induce deletion of commensal bacteria-specific CD4<sup>+</sup> T effector cells in the intestine and associated lymph nodes.**

Total Vβ5<sup>+</sup> (OT-II) or Vβ8.3<sup>+</sup> (CBir1) CD4<sup>+</sup> T cell numbers determined in (A) the thymus and (B) cLPL of control (H<sub>2</sub>O) or antibiotic (ABX)-treated OT-II and CBir1 transgenic mice crossed with MHCII<sup>ΔILC3</sup> mice or *H2-Ab1*<sup>fl/fl</sup> littermate controls. (C) Colon his-

tology (scale bar, 200 μm) and (D) frequencies of (CD45<sup>+</sup> B220<sup>−</sup> CD3<sup>−</sup>) Ly6C<sup>+</sup> Ly6G<sup>+</sup> neutrophils in the cLPL of CBir1<sup>MHCIIΔILC3</sup> and CBir1<sup>H2-Ab1fl/fl</sup> mice. (E) Immunofluorescence imaging of mLN sections stained for CD3 (blue), RORγt (green), MHCII (red), or 4',6-diamidino-2-phenylindole (DAPI) (gray). White arrows indicate RORγt<sup>+</sup> cell clusters. Scale bar, 200 μm. (Inset) Colocalization of RORγt<sup>+</sup> MHCII<sup>+</sup> ILCs and CD3<sup>+</sup> T cells. Scale bar, 10 μm. (F) MHCII expression was restricted to RORγt<sup>+</sup> ILC3s (MHCII<sup>ILC3+</sup> mice) by crossing *Rorc*<sup>Cre</sup> mice with *IAβ*<sup>bSTOP</sup><sup>fl/fl</sup> (MHCII<sup>neg</sup>) mice, and (G) MHCII levels were determined on B220<sup>+</sup> B cells, CD11b<sup>+</sup> CD11c<sup>hi</sup> DCs, CD11b<sup>+</sup> F4/80<sup>+</sup> macrophages (Mac), or Lin<sup>neg</sup> CD25<sup>+</sup> CD127<sup>+</sup> CCR6<sup>+</sup> ILC3s in the mLN of heterozygote littermates (*IAβ*<sup>bSTOP</sup><sup>fl/fl</sup> and MHCII<sup>pos</sup>), MHCII<sup>neg</sup>, or MHCII<sup>ILC3+</sup> mice. (H to K) MHCII<sup>neg</sup> and MHCII<sup>ILC3+</sup> received preactivated CD45.1<sup>+</sup> CBir1 transgenic CD4<sup>+</sup> T cells and were injected with CBir1 peptide intraperitoneally every 2 days. Frequencies and numbers of transferred T cells were analyzed in the mLN [(H) and (I)], siLPL and cLPL 9 days after transfer [(J) and (K)]. All data are representative of at least four independent experiments with *n* = 2 to 3 mice per group. Results are shown as the mean ± SEM. \**P* < 0.05; \*\**P* < 0.01; \*\*\**P* < 0.001 (two-tailed Student's *t* test).

detected in the cLPL but not in the thymus (fig. S4C). Further, sort-purified CD4<sup>+</sup> T cells from MHCII<sup>ΔILC3</sup> mice responded to fecal-derived antigen but not mammalian tissue-derived antigens (fig. S4D).

These data, along with previous studies (20, 30, 31), suggest that the majority of CD4<sup>+</sup> T

cells in the steady-state intestine are specific for commensal bacteria and that ILC3-intrinsic MHCII controls commensal bacteria-specific CD4<sup>+</sup> T cell responses through direct presentation of microbiota-derived antigens. To test this, we crossed MHCII<sup>ΔILC3</sup> mice with either TCR transgenic mice specific for CBir1, an antigen expressed by

*Clostridia* species constitutively present in the murine and human microbiota (13, 32), or TCR transgenic mice specific for ovalbumin (OT-II). Loss of ILC3-intrinsic MHCII had no effect on the frequencies or cell numbers of OT-II or CBir1 T cells in the thymus (Fig. 2A). In contrast, numbers of CBir1, but not OT-II, T cells were increased

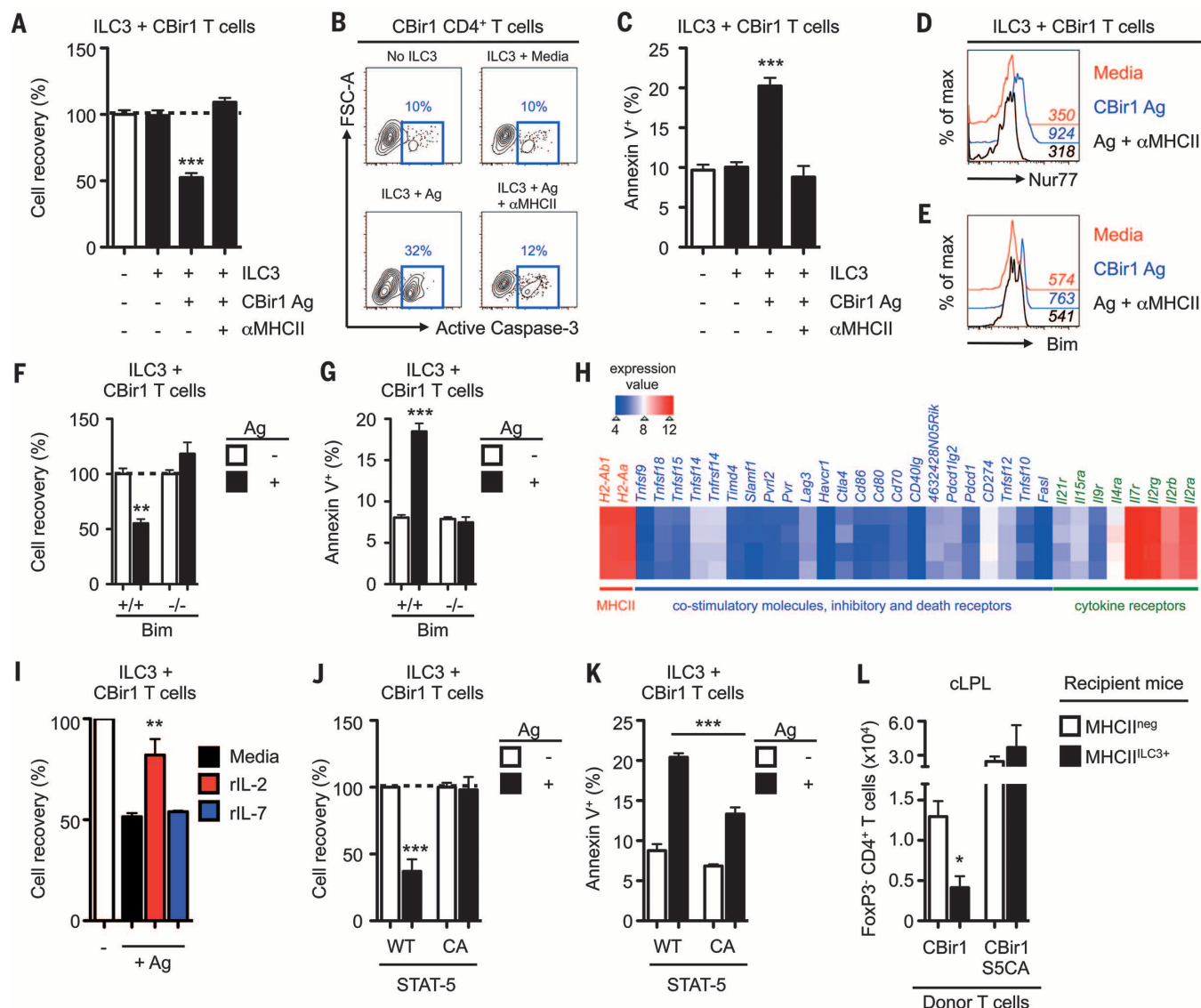


**Fig. 3. MHCII<sup>+</sup> ILC3s directly induce cell death of commensal bacteria-specific CD4<sup>+</sup> T cells.** (A to D) Activated CBir1 CD4<sup>+</sup> T cells were cocultured with sort-purified CCR6<sup>+</sup> ILC3s in the presence or absence of CBir1 antigen or a neutralizing antibody to MHCII, and (A) T cell recovery (%) was quantified relative to T cells cultured alone, (B) frequency of active Caspase-3-expressing T cells was assessed, and (C) frequencies of Annexin V<sup>+</sup> dead-cell exclusion dye-negative (preapoptotic) T cells were quantified. (D) Expression of Nur77 by CBir1 CD4<sup>+</sup> T cells and (E) expression of Bim by preactivated CBir1 CD4<sup>+</sup> T cells after 24 hours (D) or 48 hours (E) coculture with antigen-pulsed MHCII<sup>+</sup> ILC3s in the presence or absence of a neutralizing antibody to MHCII. Mean fluorescent intensity (MFI) values are shown in italics. (F and G) Bim<sup>+/+</sup> or Bim<sup>-/-</sup> CBir1 T cells were cocultured with ILC3s in the presence or absence of CBir1 antigen for 48 hours, and (F) relative T cell recovery (%) and (G) frequencies of Annexin V<sup>+</sup> preapoptotic cells were quantified. (H) Heat map of selected candidate genes from mLN-derived CCR6<sup>+</sup> ILC3s. (I) Relative

T cell recovery (%) of wild-type (WT) CBir1 CD4<sup>+</sup> T cells cocultured with antigen-pulsed ILC3s in the presence or absence of exogenous rIL-2 or rIL-7. (J and K) Activated CBir1 CD4<sup>+</sup> T cells with WT or constitutively active (CA) STAT-5 signaling were cocultured with ILC3s in the presence or absence of CBir1 antigen for 48 hours, and (J) relative T cell recovery (%) and (K) frequencies of Annexin V<sup>+</sup> preapoptotic T cells were quantified. (L) WT CBir1 CD4<sup>+</sup> T cells or CBir1 STAT5-CA CD4<sup>+</sup> T cells were adoptively transferred into MHCII<sup>neg</sup> or MHCII<sup>ILC3+</sup> mice. Mice were administered CBir1 antigen, and numbers of FoxP3<sup>+</sup> CD45.1<sup>+</sup> CBir1 T cells in the cLPL were quantified 9 days after transfer. In vitro assay data are representative of at least two to three independent experiments, with two to three biological replicates per experiment. Array data are representative of a single experiment with four biological replicates. All in vivo data are representative of at least two independent experiments with at least  $n = 3$  mice per group. Results are shown as the mean  $\pm$  SEM. \* $P < 0.05$ ; \*\* $P < 0.01$ ; \*\*\* $P < 0.001$  (two-tailed students  $t$  test).



in the cLPL and mLN (Fig. 2B and fig. S5A), and CBir1<sup>MHCII<sup>ILC3</sup></sup> mice exhibited increased frequencies of antigen-specific IFN- $\gamma$ <sup>+</sup> and tumor necrosis factor (TNF)- $\alpha$ <sup>+</sup> colonic CD4<sup>+</sup> T cells, colonic inflammation, and neutrophil infiltration, which could be prevented by administration of antibiotics (ABX) and was not observed in *Rag1*<sup>-/-</sup> MHCII<sup>ILC3</sup> mice (Fig. 2B-D and fig. S5A-D). Finally, similar to polyclonal MHCII<sup>ILC3</sup> mice, the population expansion and increased cytokine production of CBir1 CD4<sup>+</sup> T cells were associated with a selective increase in CD44<sup>hi</sup>CD62L<sup>lo</sup> T<sub>eff</sub> whereas numbers of FoxP3<sup>+</sup> T<sub>reg</sub> remained unchanged (fig. S5E). These data suggest that CCR6<sup>+</sup> ILC3s selectively limit the expansion of commensal bacteria-specific CD4<sup>+</sup> effector T cells through presentation of antigen derived from the endogenous microbiota. In support of this hypothesis and consistent with recent findings (33), MHCII<sup>+</sup> ILC3s localized in distinct clusters in the mLN at the interface between the B and T cell zones in the marginal and subcapsular sinus (Fig. 2E), a site through which antigen-experienced T cells traffic.

To investigate the in vivo mechanisms through which MHCII<sup>+</sup> ILC3s control commensal bacteria-specific CD4<sup>+</sup> T cells, mice were generated in which MHCII expression was restricted to only ILC3s (Fig. 2F). This was accomplished by using mice with a floxed-STOP sequence cassette inserted between the first and second IAP<sup>b</sup> exons (IAP<sup>b</sup>STOP<sup>fl/fl</sup> mice) (34). IAP<sup>b</sup>STOP<sup>fl/fl</sup> mice lack MHCII on antigen-presenting cells in the absence of Cre recombinase (MHCII<sup>neg</sup>) (Fig. 2G). In contrast, IAP<sup>b</sup>STOP<sup>fl/fl</sup> mice crossed with *Rorc*<sup>Cre</sup> mice demonstrated a partial restoration of MHCII on CCR6<sup>+</sup> ILC3s (MHCII<sup>ILC3+</sup> mice) but not B cells,

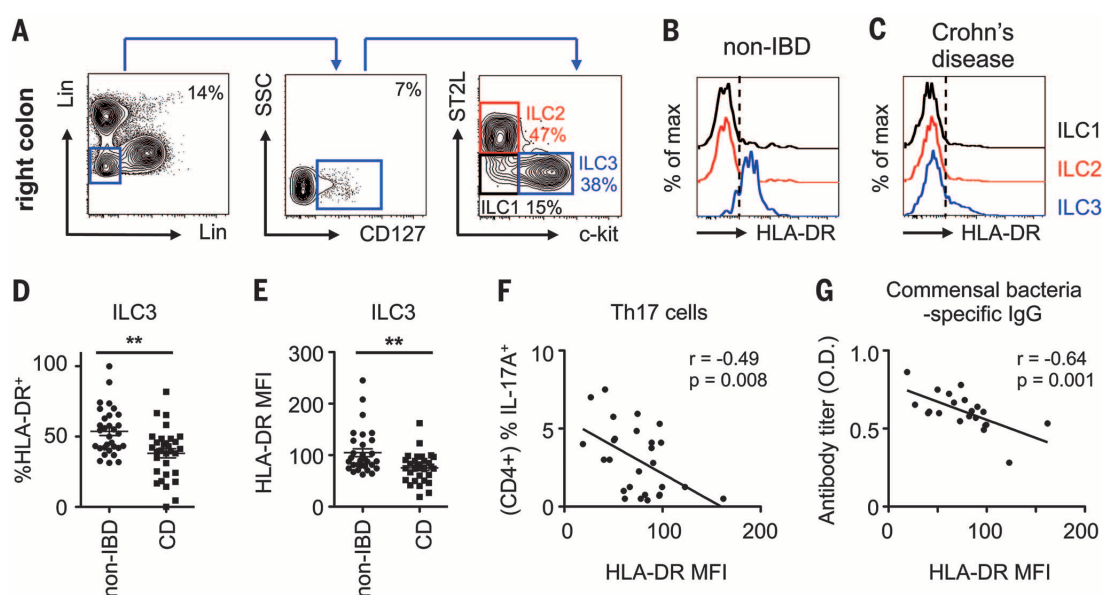
DCs, or macrophages (Fig. 2G). As MHCII<sup>neg</sup> and MHCII<sup>ILC3+</sup> mice lack MHCII on TECs and have disrupted endogenous T cell selection (34), we first employed an adoptive transfer approach with naïve carboxyfluorescein diacetate succinimidyl ester (CFSE)-labeled CD45.1<sup>+</sup> CBir1 T cells. In mice with normal MHCII expression (MHCII<sup>pos</sup>), administration of CBir1 peptide resulted in dilution of CFSE in transferred CBir1 T cells, expansion of CD44<sup>hi</sup>CD62L<sup>lo</sup> CBir1 T<sub>eff</sub> cells, and an increase in FoxP3<sup>+</sup> T<sub>reg</sub> in the mLN (fig. S6A). In contrast, naïve CBir1 CD4<sup>+</sup> T cells transferred into control MHCII<sup>neg</sup> and MHCII<sup>ILC3+</sup> mice failed to proliferate or differentiate into T<sub>eff</sub> or T<sub>reg</sub> after peptide administration (fig. S6A), suggesting that ILC3-intrinsic MHCII does not influence naïve CD4<sup>+</sup> T cells. As MHCII<sup>+</sup> ILC3s localize at lymphoid sites through which antigen-experienced CD4<sup>+</sup> T cells traffic (Fig. 2E) (33), CBir1 CD4<sup>+</sup> T cells were preactivated overnight before transfer into MHCII<sup>neg</sup> or MHCII<sup>ILC3+</sup> mice. After CBir1 peptide administration, MHCII<sup>ILC3+</sup> mice exhibited reduced frequencies and numbers of preactivated CBir1 CD4<sup>+</sup> T cells in the mLN (Fig. 2, H and I), which was due to a selective decrease in effector, but not regulatory CBir1 T cells (Fig. 2I). MHCII<sup>+</sup> ILC3-mediated effects were antigen-specific, could be driven by endogenous microbiota-derived antigen alone, and were specific to ILC3s (fig. S6, B to D, and fig. S7). Further, in complementary loss-of-function studies, adoptively transferred CBir1 CD4<sup>+</sup> T<sub>eff</sub> expanded at higher frequencies and numbers in the mLN and cLPL of mice lacking ILC3-intrinsic MHCII (MHCII<sup>ILC3</sup> mice), despite exhibiting comparable proliferation (fig. S8). Finally, in line with ILC3-mediated control of antigen-experienced T cells, the fre-

quency and number of activated CBir1 CD4<sup>+</sup> T cells reaching the small intestine lamina propria (siLPL) and cLPL of MHCII<sup>ILC3+</sup> mice were significantly decreased relative to MHCII<sup>neg</sup> controls (Fig. 2, J to K).

We hypothesized that the loss of CBir1 CD4<sup>+</sup> T cells from the mLN and intestine of MHCII<sup>ILC3+</sup> mice could be the result of altered migration, proliferation, or induction of cell death. However, preactivated CBir1 T cells did not accumulate in peripheral organs, such as the spleen (fig. S9A), and CBir1 T cells recovered from MHCII<sup>ILC3+</sup> mice exhibited comparable proliferation relative to MHCII<sup>neg</sup> mice (fig. S9B). To further investigate this question, we developed an in vitro ILC3-CD4<sup>+</sup> T cell coculture system. Consistent with our in vivo findings, coculture of activated CBir1 T cells and sort-purified MHCII<sup>+</sup> CCR6<sup>+</sup> ILC3s resulted in a significant reduction in T cell numbers after culture in the presence of cognate antigen, which could be reversed by administration of an MHCII-blocking antibody (Fig. 3A). Reduced cell recovery was associated with an antigen and MHCII-dependent increase in Caspase-3 activation (Fig. 3B) and increased Annexin V staining (Fig. 3C), indicative of programmed cell death. Despite selectively regulating commensal bacteria-specific CD4<sup>+</sup> T cells in the steady state, MHCII<sup>+</sup> ILC3s were also sufficient to influence T cells with other antigen specificities only if antigen was exogenously provided (fig. S10).

Negative selection in the thymus has been shown to be associated with induction of Nur77 and up-regulation of the proapoptotic molecule Bim (35), which together mediate clonal deletion. Presentation of antigen by MHCII<sup>+</sup> ILC3s also resulted in the up-regulation of Nur77 and

**Fig. 4. ILC3-intrinsic MHCII is dysregulated in pediatric Crohn's disease patients and is associated with increased intestinal T<sub>H</sub>17 cells.** (A) Lamina propria cells were isolated from colon biopsies from non-IBD control patients, and ILCs were identified as CD45<sup>+</sup> and lineage (x axis: CD3, CD5, CD14, and Fc $\epsilon$ R1; y axis: CD11b, CD11c, and CD19) negative, CD127<sup>+</sup>, and further divided by expression of ST2L (ILC2s, red) and c-kit (ILC3s, blue) or as lacking expression of both markers (ILC1s, black). Expression of MHC class II (HLA-DR) was determined on ILC subsets in representative biopsies from (B) non-IBD patients or (C) pediatric Crohn's disease



(CD) patients, and the (D) frequencies and (E) MFI of HLA-DR expression on ILC3s was quantified. ILC3 HLA-DR MFI was correlated with (F) frequencies of IL-17A<sup>+</sup> CD4<sup>+</sup> T<sub>H</sub>17 cells in colon biopsies, and (G) commensal bacterial-specific IgG was quantified in the sera of pediatric Crohn's disease patients. [(B) to (E)] Representative of *n* = 31 non-IBD and *n* = 31 CD patients or (F) *n* = 27 and (G) *n* = 21 pediatric Crohn's disease patients. Results are shown as the mean  $\pm$  SEM. Statistical analyses between patient groups were performed using a Mann-Whitney test. \**P* < 0.05; \*\**P* < 0.01; \*\*\**P* < 0.001. Correlative analyses were compared by parametric Pearson's rank correlation coefficient (*r*).

Bim by CB1r1 CD4<sup>+</sup> T cells, the latter of which was required for ILC3-mediated induction of T cell death (Fig. 3D–G). Antigen presentation by ILC3s in vitro selectively led to T<sub>eff</sub> death but did not affect T<sub>reg</sub> numbers (fig. S11A). We next analyzed mLN-derived CCR6<sup>+</sup> ILC3 for expression of surface molecules that directly influence antigen-specific CD4<sup>+</sup> T cell responses (Fig. 3H). ILC3s demonstrated high levels of MHCII-associated transcripts but had negligible expression of transcripts for canonical costimulatory molecules and inhibitory or death receptors (Fig. 3H). Indeed, CCR6<sup>+</sup> ILC3s lacked expression of FasL by flow cytometry, and antibody-mediated neutralization of FasL did not influence ILC3-induced CB1r1 T cell death (fig. S11, B to D). Moreover, in contrast to *Bim*<sup>−/−</sup> mice, *fasl*<sup>gld/gld</sup> mice did not exhibit increased frequencies of endogenous commensal bacteria-specific CD4<sup>+</sup> T cells in gut-associated lymphoid tissues (fig. S11E).

Bim-dependent apoptotic cell death may also be induced via cytokine or growth factor starvation (36, 37). Because CCR6<sup>+</sup> ILC3s constitutively express high levels of the common gamma chain cytokine receptors CD25 (IL-2R) and CD127 (IL-7Rα) (Fig. 1, fig. S1 and Fig. 3H), we hypothesized that MHCII<sup>+</sup> ILC3s may induce cell death of commensal bacteria-specific CD4<sup>+</sup> T cells synergistically through TCR induction of an apoptotic program in concert with cytokine withdrawal. Consistent with this, cell death could be reduced upon addition of exogenous recombinant (r)IL-2, but not rIL-7, to in vitro cocultures (Fig. 3I). MHCII<sup>+</sup> ILC3s exhibited more than twofold higher capacity to bind IL-2 as compared with activated CB1r1 CD4<sup>+</sup> T cells (fig. S11, F and G), suggesting that MHCII<sup>+</sup> ILC3s outcompete activated T cells for pro-survival cytokines. The requirement for IL-2 was T cell-intrinsic as activated CB1r1 CD4<sup>+</sup> T cells expressing a constitutively active STAT-5 molecule (S5CA) were resistant to Bim up-regulation and ILC3-induced cell death in vitro and in vivo (Fig. 3, J to L, and fig. S11, H and I). Taken together, these data indicate that MHCII<sup>+</sup> ILC3s mediate a negative selection process through antigen presentation and withdrawal of IL-2 from the local milieu, resulting in deletion of activated commensal bacteria-specific T cells.

Inflammatory CD4<sup>+</sup> T cell responses against commensal bacteria are causally associated with the pathogenesis of IBD (7–11). Furthermore, inflammatory T cells derived from Crohn's disease patients also exhibit reduced Bim-mediated cell death and cytokine-withdrawal-mediated apoptosis (38, 39). Therefore, we next examined whether ILC3-intrinsic MHCII may be dysregulated in the context of human IBD. Using a previously defined gating strategy (40), all ILC subsets could be identified in intestinal biopsies of pediatric Crohn's disease patients (Fig. 4A), including CD127<sup>+</sup> c-kit<sup>+</sup> ST2L<sup>−</sup> ILC3s, that expressed Nkp44 and RORγt (fig. S12, A and B). Human ILC3s expressed MHCII [human leukocyte antigen-D related (HLA-DR)] in intestinal biopsies from non-IBD controls, whereas MHCII expression was largely absent on other ILC subsets (Fig. 4B).

Although no alterations in the total frequency of ILC3s were observed between patient cohorts (fig. S12C), MHCII expression was significantly reduced on ILC3s (Fig. 4, C to E), but not CD4<sup>+</sup> T cells or professional antigen-presenting cells (fig. S12, D and E), from pediatric Crohn's disease patients in comparison to non-IBD controls. Moreover, we observed an inverse correlation between MHCII levels on ILC3s and frequencies of effector T helper 17 (T<sub>H</sub>17) cells in the colon (Fig. 4F) and circulating commensal bacteria-specific immunoglobulin G (IgG) titers (Fig. 4G) in pediatric Crohn's disease patients. Taken together, these data indicate that alterations in MHCII on human ILC3s are associated with proinflammatory adaptive immune cell responses to commensal bacteria.

The mammalian gastrointestinal tract is colonized with trillions of beneficial commensal bacteria that regulate host nutrient metabolism and immune cell homeostasis and protect from pathogen infection (7, 11, 15). As such, commensal bacteria are an essential component of the mammalian “superorganism” required for the host to thrive (41). It is well characterized that self-specific CD4<sup>+</sup> T cells with the potential to cause pathologic inflammation in mammalian tissues are controlled through antigen-dependent thymic selection (1–5). Here, MHCII-expressing CCR6<sup>+</sup> ILC3s were found to control intestinal homeostasis through induction of apoptotic cell death and deletion of activated commensal bacteria-specific T cells, a process with multiple similarities to negative selection in the thymus, which we propose to term intestinal selection (fig. S13). Thus, intestinal selection controls the peripheral commensal bacteria-specific CD4<sup>+</sup> T cell pool in concert with other previously described tolerogenic pathways, including T<sub>reg</sub> production of IgA, and active maintenance of intestinal barrier function (7, 15, 17, 23). Dysregulated ILC3-intrinsic MHCII in pediatric Crohn's disease patients suggests a possible role for alterations in this pathway in the onset and/or progression of human IBD. Thus, MHCII<sup>+</sup> ILC3 may represent a novel therapeutic target to control pathologic CD4<sup>+</sup> T cell responses in chronic human inflammatory disorders associated with dysregulated host-commensal bacteria relationships (7, 10, 15).

## REFERENCES AND NOTES

- L. Klein, B. Kyewski, P. M. Allen, K. A. Hogquist, *Nat. Rev. Immunol.* **14**, 377–391 (2014).
- H. von Boehmer, F. Melchers, *Nat. Immunol.* **11**, 14–20 (2010).
- T. M. Laufer, L. H. Glimcher, D. Lo, *Semin. Immunol.* **11**, 65–70 (1999).
- D. Mathis, C. Benoist, *Annu. Rev. Immunol.* **27**, 287–312 (2009).
- J. Sprent, H. Kishimoto, *Immunol. Rev.* **185**, 126–135 (2002).
- M. Blackman, J. Kappler, P. Marrack, *Science* **248**, 1335–1341 (1990).
- Y. Belkaid, T. W. Hand, *Cell* **157**, 121–141 (2014).
- A. Kaser, S. Zeissig, R. S. Blumberg, *Annu. Rev. Immunol.* **28**, 573–621 (2010).
- B. Khor, A. Gardet, R. J. Xavier, *Nature* **474**, 307–317 (2011).
- K. J. Maloy, F. Powrie, *Nature* **474**, 298–306 (2011).
- C. L. Maynard, C. O. Elson, R. D. Hatton, C. T. Weaver, *Nature* **489**, 231–241 (2012).

- T. L. Ai, B. D. Solomon, C. S. Hsieh, *Immunol. Rev.* **259**, 60–74 (2014).
- Y. Cong, T. Feng, K. Fujishashi, T. R. Schoeb, C. O. Elson, *Proc. Natl. Acad. Sci. U.S.A.* **106**, 19256–19261 (2009).
- A. J. Macpherson, E. Slack, M. B. Geuking, K. D. McCoy, *Semin. Immunopathol.* **31**, 145–149 (2009).
- L. V. Hooper, D. R. Littman, A. J. Macpherson, *Science* **336**, 1268–1273 (2012).
- J. Bollrath, F. M. Powrie, *Semin. Immunol.* **25**, 352–357 (2013).
- L. W. Peterson, D. Artis, *Nat. Rev. Immunol.* **14**, 141–153 (2014).
- A. J. Macpherson, T. Uhr, *Science* **303**, 1662–1665 (2004).
- M. Rescigno, *Adv. Immunol.* **107**, 109–138 (2010).
- S. K. Lathrop et al., *Nature* **478**, 250–254 (2011).
- A. Cebula et al., *Nature* **497**, 258–262 (2013).
- M. R. Hepworth et al., *Nature* **498**, 113–117 (2013).
- G. F. Sonnenberg, D. Artis, *Immunity* **37**, 601–610 (2012).
- H. Spits et al., *Nat. Rev. Immunol.* **13**, 145–149 (2013).
- E. A. Kiss et al., *Science* **334**, 1561–1565 (2011).
- N. von Burg et al., *Proc. Natl. Acad. Sci. U.S.A.* **111**, 12835–12840 (2014).
- W. Reith, S. LeibundGut-Landmann, J. M. Waldburger, *Nat. Rev. Immunol.* **5**, 793–806 (2005).
- J. M. Waldburger et al., *Blood* **101**, 3550–3559 (2003).
- J. M. Waldburger, T. Suter, A. Fontana, H. Acha-Orbea, W. Reith, *J. Exp. Med.* **194**, 393–406 (2001).
- Y. Goto et al., *Immunity* **40**, 594–607 (2014).
- Y. Yang et al., *Nature* **510**, 152–156 (2014).
- M. J. Lodes et al., *J. Clin. Invest.* **113**, 1296–1306 (2004).
- E. C. Mackley et al., *Nat. Commun.* **6**, 5862 (2015).
- A. S. Archambault et al., *J. Immunol.* **191**, 545–550 (2013).
- G. L. Stritesky et al., *Proc. Natl. Acad. Sci. U.S.A.* **110**, 4679–4684 (2013).
- P. Pandiyan, L. Zheng, S. Ishihara, J. Reed, M. J. Lenardo, *Nat. Immunol.* **8**, 1353–1362 (2007).
- P. Bouillet et al., *Science* **286**, 1735–1738 (1999).
- J. Mudter, M. F. Neurath, *Gut* **56**, 293–303 (2007).
- M. F. Neurath et al., *Trends Immunol.* **22**, 21–26 (2001).
- J. H. Bernink et al., *Nat. Immunol.* **14**, 221–229 (2013).
- G. Eberl, *Mucosal Immunol.* **3**, 450–460 (2010).

## ACKNOWLEDGMENTS

The authors thank members of the Sonnenberg laboratory for discussions and critical reading of the manuscript. We thank C. Hunter and S. Wagage (University of Pennsylvania) for the Ahr-deficient mice; I. Brodsky (University of Pennsylvania) for the Caspase 1/11-deficient mice; and M. Jenkins, J. Walter, and T. Dileepan (University of Minnesota) for tetramer reagents and protocols. Data presented in this manuscript are tabulated in the main paper and in the supplementary materials. Microarray data are accessible at Gene Expression Omnibus ([www.ncbi.nlm.nih.gov/geo](http://www.ncbi.nlm.nih.gov/geo)) via accession number GSE67076. CB1r1 Tg mice are available from University of Alabama, *Rorc*(yt)-*Gfp*<sup>TC</sup> and *Rorc*<sup>Cre</sup> mice are available from Institut Pasteur, STAT5-CA mice are available from University of Minnesota, IAb<sup>STOP</sup><sup>fl/fl</sup> mice and CD11c Tg mice are available from University of Pennsylvania, and *Il23a* deficient mice are available from Janssen Research and Development LLC, all under Material Transfer Agreement. Research in the Sonnenberg laboratory is supported by the National Institutes of Health (DP50D012116), the National Institute of Allergy and Infectious Diseases Mucosal Immunology Studies Team (MIST) Scholar Award in Mucosal Immunity, and the Institute for Translational Medicine and Therapeutics Transdisciplinary Program in Translational Medicine and Therapeutics (UL1-RR024134 from the U.S. National Center for Research Resources). M.R.H. is supported by a research fellowship from the Crohn's and Colitis Foundation of America (CCFA, no. 297365). T.C.F. is supported by a Cancer Research Institute Student Training and Research in Tumor immunology (StART) grant. D.R.W. is supported by a Wellcome Trust Research Career Development Fellowship. C.O.E. is supported by the National Institutes of Health (DK071176).

## SUPPLEMENTARY MATERIALS

[www.sciencemag.org/content/348/6238/1031/suppl/DC1](http://www.sciencemag.org/content/348/6238/1031/suppl/DC1)  
Materials and Methods  
Figs. S1 to S13  
References (42–46)

16 February 2015; accepted 7 April 2015  
Published online 23 April 2015;  
10.1126/science.aaa4812



## CANCER

# The transcription factor GABP selectively binds and activates the mutant TERT promoter in cancer

Robert J. A. Bell,<sup>1,2</sup> H. Tomas Rube,<sup>3,4</sup> Alex Kreig,<sup>4,5</sup> Andrew Mancini,<sup>1</sup> Shaun D. Fouse,<sup>1</sup> Raman P. Nagarajan,<sup>1</sup> Serah Choi,<sup>6</sup> Chibo Hong,<sup>1</sup> Daniel He,<sup>1</sup> Melike Pekmezci,<sup>7</sup> John K. Wiencke,<sup>8,9</sup> Margaret R. Wrensch,<sup>8,9</sup> Susan M. Chang,<sup>1</sup> Kyle M. Walsh,<sup>8</sup> Sua Myong,<sup>4,5</sup> Jun S. Song,<sup>2,3,4,5,\*†</sup> Joseph F. Costello<sup>1,\*†</sup>

Reactivation of telomerase reverse transcriptase (*TERT*) expression enables cells to overcome replicative senescence and escape apoptosis, which are fundamental steps in the initiation of human cancer. Multiple cancer types, including up to 83% of glioblastomas (GBMs), harbor highly recurrent *TERT* promoter mutations of unknown function but specific to two nucleotide positions. We identified the functional consequence of these mutations in GBMs to be recruitment of the multimeric GA-binding protein (GABP) transcription factor specifically to the mutant promoter. Allelic recruitment of GABP is consistently observed across four cancer types, highlighting a shared mechanism underlying *TERT* reactivation. Tandem flanking native E26 transformation-specific motifs critically cooperate with these mutations to activate *TERT*, probably by facilitating GABP heterotetramer binding. GABP thus directly links *TERT* promoter mutations to aberrant expression in multiple cancers.

The human telomerase is an enzyme critical for maintaining telomere length and chromosomal stability in stem cells (1, 2). The transcriptional regulation of the telomerase reverse transcriptase (*TERT*) gene, encoding the catalytic subunit of telomerase, is a rate-limiting step in modulating telomerase activity (3). Although normally silenced in somatic cells, *TERT* is aberrantly expressed in 90% of aggressive cancers, highlighting this event as a hallmark of tumorigenesis (4–6). Reactivating telomerase helps cells with a finite life span to achieve limitless proliferative potential and bypass cellular senescence induced by DNA replication-associated telomere shortening. Understanding the mechanisms of aberrant *TERT* expression is thus a crucial outstanding problem in cancer research.

Recently discovered noncoding mutations in the *TERT* promoter are among the most common genetic alterations observed across multiple cancer types, revealing a potentially causal biological mechanism driving increased telomerase activity in tumors (7–9). Specifically, one of two positions, G228A or G250A, is mutated in 21% of medulloblastomas (10), 47% of hepatocellular carcinomas

(HCC) (11), 66% of urothelial carcinomas of the bladder (12), 71% of melanomas (7, 8), and 83% of primary glioblastomas (GBMs) (9), making them the most recurrent single-nucleotide mutations observed in these cancer types. Both the G228A and G250A mutations are associated with increased *TERT* expression (fig. S1) and telomerase activity (13) and have prognostic power in bladder cancer and GBM (14–16). Both G>A transitions generate an identical 11-base pair (bp) sequence that is hypothesized to generate a de novo binding site for an E26 transformation-specific (ETS) transcription factor (7). Despite these compelling findings and the central importance of *TERT* in human cancer, the precise function of the mutations has remained elusive since their initial discovery in melanoma patients.

To determine whether the de novo ETS motif is necessary for mutant *TERT* activation, we performed site-directed mutagenesis of the core *TERT* promoter (17). The G228C, G250C, and G250T mutations did not increase promoter activity, highlighting the requirement for the G>A transition for *TERT* activation (Fig. 1A). Furthermore, removing the ETS motif while retaining the G228A mutation (A227T, G228A) resulted in a complete reduction of promoter activity to wild-type levels. The G228T mutation also partially increased promoter activity; this induction is consistent with the site being the second adenine position in an ETS motif, a position that is often degenerate for A/T (18). Mutating the second adenine position to thymine in the context of G250A (G250A, A251T) resulted in a similar intermediate level of promoter activity.

A small interfering RNA (siRNA) screen of 13 ETS factors expressed in GBMs revealed 5 ETS factors [ELF1, ETS1, ETV3, ETV4, and GA-binding protein, alpha subunit (GABPA)] whose knockdown reduced *TERT* expression in at least one of

two GBM cell lines harboring *TERT* promoter mutations (Fig. 1B, fig. S2, and fig. S3) (17). Only three factors (ETS1, ETV3, and GABPA) consistently reduced *TERT* expression in both lines. GABPA knockdown reduced *TERT* expression by as much as 50% within the first 24 hours and sustained the largest effect on *TERT* expression among the ETS candidates throughout 72 hours (fig. S3). In contrast, knockdown of ETS1 and ELF1 resulted in a more modest reduction of *TERT* mRNA and only reached statistical significance at 72 hours, suggesting that their regulation of *TERT* is through indirect mechanisms. ETV3 is a transcriptional repressor in the ETS family and was thus not considered a candidate direct regulator of mutant *TERT* (19–21). Thus, the de novo ETS motif is critical for mutant *TERT* promoter activity in GBMs, and one or more candidate ETS factors may regulate *TERT* expression directly through the G228A and G250A mutations.

We next investigated whether regulation of *TERT* by ETS1, ETV3, ETV4, or GABPA depends on the *TERT* promoter mutation status by testing the effect of siRNA knockdowns on the activity of *TERT* promoter-driven luciferase reporters. Only GABPA knockdown significantly reduced mutant promoter activity without affecting wild-type promoter activity (Fig. 2A and fig. S4). Although ETV4 knockdown reduced mutant promoter activity, it also significantly reduced the activity of the wild-type promoter, indicating the potential of ETV4 to bind and regulate the wild-type *TERT* promoter sequence in this assay. Knockdown of ETS1 and ETV3 did not significantly reduce promoter activity (Fig. 2A and fig. S4). GABPA was thus the only ETS factor that reproducibly affected *TERT* expression in a mutation-specific manner. Furthermore, knockdown of GABPA did not significantly affect cell cycle or proliferation rate within this time frame (fig. S5).

To determine the in vivo binding specificity to the mutant *TERT* promoter sequence (CCGGAA) relative to the wild-type sequence (CCGGAG) among the candidate ETS factors, we analyzed publicly available ChIP-seq data for GABPA, ELF1, ETS1, and ETV4 (22, 23). Although all factors display significant enrichment in the sequence found in the mutant *TERT* promoter relative to the wild-type sequence, we found that GABPA peaks contained significantly greater enrichment in the mutant motif as compared to ETS1 or ETV4 peaks ( $P$  value =  $5.1 \times 10^{-8}$  for ETS1 and  $1.8 \times 10^{-8}$  for ETV4, Wilcoxon rank-sum test) (Fig. 2B and fig. S6). This genome-wide analysis supports the binding specificity for the motif created by the *TERT* promoter mutations and suggests that GABPA binding may be more sensitive to these promoter mutations. Furthermore, this enrichment is not observed in DNase I hypersensitivity peaks in the same cells, demonstrating that the motif enrichment does not represent sequence biases in areas of open chromatin (fig. S6). Among the eight ENCODE (Encyclopedia of DNA Elements) Project cell lines with GABPA ChIP-seq, only HepG2 hepatocellular carcinoma cells and SK-N-SH neuroblastoma cells, both of

<sup>1</sup>Department of Neurological Surgery, University of California, San Francisco, CA. <sup>2</sup>Department of Biostatistics and Epidemiology, University of California, San Francisco, CA.

<sup>3</sup>Department of Physics, University of Illinois, Urbana-Champaign, IL.

<sup>4</sup>Institute for Genomic Biology, University of Illinois, Urbana-Champaign, IL.

<sup>5</sup>Department of Bioengineering, University of Illinois, Urbana-Champaign, IL.

<sup>6</sup>Department of Radiation Oncology, University of California San Francisco, San Francisco, CA.

<sup>7</sup>Department of Anatomic Pathology, University of California San Francisco Medical School, San Francisco, CA 94143, USA.

<sup>8</sup>Division of Neuroepidemiology, Department of Neurological Surgery, University of California, San Francisco, San Francisco, CA 94158, USA.

<sup>9</sup>Institute for Human Genetics, University of California, San Francisco, San Francisco, CA 94143, USA.

\*Corresponding author. E-mail: songj@illinois.edu (J.S.S.); joseph.costello@ucsf.edu (J.F.C.) †These authors contributed equally to this work.

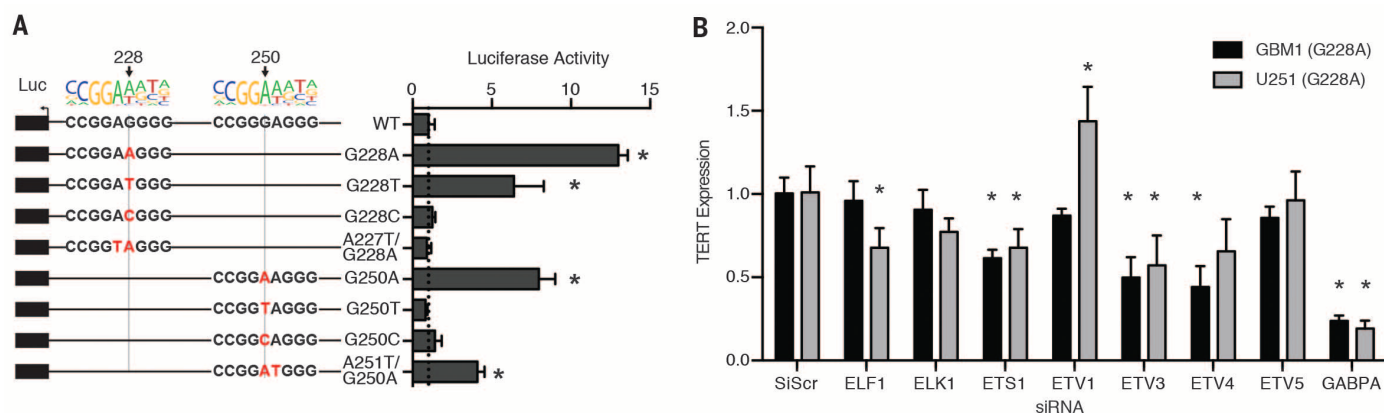


**Fig. 1. The de novo ETS motif is critical for mutant *TERT* promoter activity in GBMs.** (A) *TERT* promoter–luciferase reporter assays for wild-type, G228A, G250A, or targeted mutation sequences. \* $P < 0.05$ , Student's  $t$  test compared to wild-type (WT). (B) *TERT* expression relative to nontargeted siRNA (siScr) 72 hours after ETS factor siRNA knockdown. \* $P < 0.05$ , Student's  $t$  test compared to siScr. The results are an average of at least three independent experiments. Values are mean  $\pm$  SD.

which harbor heterozygous G228A mutations, displayed significant GABPA binding at the *TERT* promoter (Fig. 2C). In contrast, none of the *TERT* mutant cell lines showed ELF1 binding at the *TERT* promoter (fig. S7). Likewise, ChIP of ETS1 and ETV4 did not show binding at the mutant *TERT* promoter in vivo (fig. S7). An in vitro single-molecule protein binding assay further confirmed that ETV4 does not stably bind the mutated sequence (fig. S8) (17). These results are consistent with the fact that only GABPA knockdown shows immediate reduction on *TERT* expression (fig. S3), and they implicate GABPA as the only ETS factor among the candidates to directly bind the mutant *TERT* promoter. All of the cell lines that did not show GABPA binding (K562, GM12878, A549, Hela, MCF-7, and HL-60) were derived from cancers in which *TERT* promoter mutations are absent or uncommon (9). Strikingly, 100% of the GABPA ChIP-seq reads covering the mutated site within the *TERT* promoter contained G228A, suggesting that GABPA selectively binds the mutant allele in vivo and that it cannot recognize and bind the wild-type sequence (Fig. 2C). Recruitment of GABP to the G250A mutant sequence was confirmed in vitro using a single-molecule protein binding assay. In contrast, no binding event of GABP was detected for the wild-type *TERT* sequence (fig. S8). Mutant allele-specific DNase I hypersensitivity and Pol II recruitment were also observed in these lines (fig. S9).

To confirm that GABPA is specifically recruited to the mutant allele, we performed GABPA ChIP in HepG2, SK-N-SH, two GBM lines, and three melanoma lines (table S1) (17). All cell lines harboring either the G228A or G250A mutation showed significant GABPA binding in the *TERT* core promoter ( $P$  value = 0.016, Wilcoxon rank-sum test, Fig. 2D). In contrast, the *TERT* wild-type melanoma line SK-MEL-28 showed no GABPA binding at the *TERT* promoter as compared to the other lines ( $P$  value = 0.007, Weisberg  $t$  test for outliers). Consistent with our findings of specificity for the mutant allele in the ENCODE ChIP-seq data, the GABPA-immunoprecipitated DNA

from the heterozygous mutant cell lines HepG2, SK-N-SH, and GBM1 all showed significant bias toward the mutant allele as compared to input control DNA ( $P$  value =  $1.264 \times 10^{-5}$ , Fisher's exact test, Fig. 2E). Furthermore, we confirmed that both heterozygous mutations in the *TERT* promoter resulted in allelic deposition of H3K4me3 and allele-specific expression (fig. S10). Nucleosome positioning analysis from micrococcal nuclease-digested H3K4me3 ChIP-seq (24) data revealed that both mutation positions lie within a nucleosome-free region, with the upstream nucleosomes containing the H3K4me3 modifications (fig. S10). These data demonstrate that GABPA is selectively recruited to the mutant *TERT* allele across multiple cancer types and results in allele-specific activation of *TERT*.

GABPA is unique among the large ETS transcription factor family as it is the only obligate multimeric factor (25, 26). GABPA dimerizes with GABPB, and the resulting heterodimer (GABP) forms a fully functional transcription factor that can both bind DNA and activate transcription (27). GABPA has a single transcript isoform that is widely expressed across tissue types, whereas GABPB is encoded by either the *GABPB1* or *GABPB2* gene, and GABPB1 contains multiple isoforms (28, 29). A subset of GABPB isoforms contain leucine zipper-like domains, which allow two GABP heterodimers to form a heterotetramer complex capable of binding two GABPA motifs (core consensus CCGGAA) in proximity to each other, and further stimulating transcription (30). Consistent with this fact, genome-wide analysis of ENCODE GABPA ChIP-seq data showed that peaks containing two GABPA motifs have significantly higher binding enrichment scores as compared to peaks with just one or zero motifs ( $P$  value =  $1.6 \times 10^{-157}$ , Wilcoxon rank-sum test, figs. S11 and S12). Analysis of GABPA motif spacing within peaks containing two motifs revealed that strong peaks are more likely to have a separation distance shorter than 50 bp as compared to weak peaks (Fig. 3A and fig. S11). Moreover, this increase in likeli-

hood occurred at discrete spacing that aligned well with the 10.5-bp periodicity of relaxed B-DNA, highlighting the importance of having two GABPA binding sites in phase and separated by full helical turns of double-stranded DNA. This periodicity was unique to GABPA and is not observed in ELF1 or ETS1 ChIP-seq data (fig. S11). The Fourier spectrum of the enrichment also spiked around the helical frequency in strong GABPA peaks, but not in weak peaks or the genomic background (fig. S13). This analysis suggested that two proximal motifs in helical phase act synergistically to recruit a GABP heterotetramer complex.

Investigation of the DNA sequence flanking the mutation sites revealed three native ETS binding motifs (ETS-195, ETS-200, and ETS-294) (Fig. 3B). To determine whether these flanking ETS motifs are required for mutant *TERT* activation, we performed site-directed mutagenesis of the flanking ETS sites with or without the G228A or G250A mutation. Mutating ETS-195 or ETS-200 alone reduced promoter activity from the relatively low level of the wild-type promoter and also significantly reduced activity in the context of G228A or G250A. In contrast, mutating ETS-294 had no effect on promoter activity in the context of G250A, despite being closer than ETS-195 or ETS-200 (Fig. 3C). These data demonstrate that both ETS-195 and ETS-200 are required for aberrant activity of the mutant *TERT* promoter. The GABPB1 isoforms required for GABP heterotetramer formation are the predominant isoforms expressed in GBM melanoma, hepatocellular carcinoma, and bladder urothelial carcinoma, all tumor types prone to *TERT* promoter mutations (fig. S14).

To test whether ETS motif spacing is essential for mutant *TERT* promoter activation, we performed a series of deletions in 2-bp increments between the native ETS site and the G250A mutation, effectively bringing G250A out of phase and back into phase with the native ETS motifs. Although the wild-type reporter construct displayed only noise level fluctuations in activity,



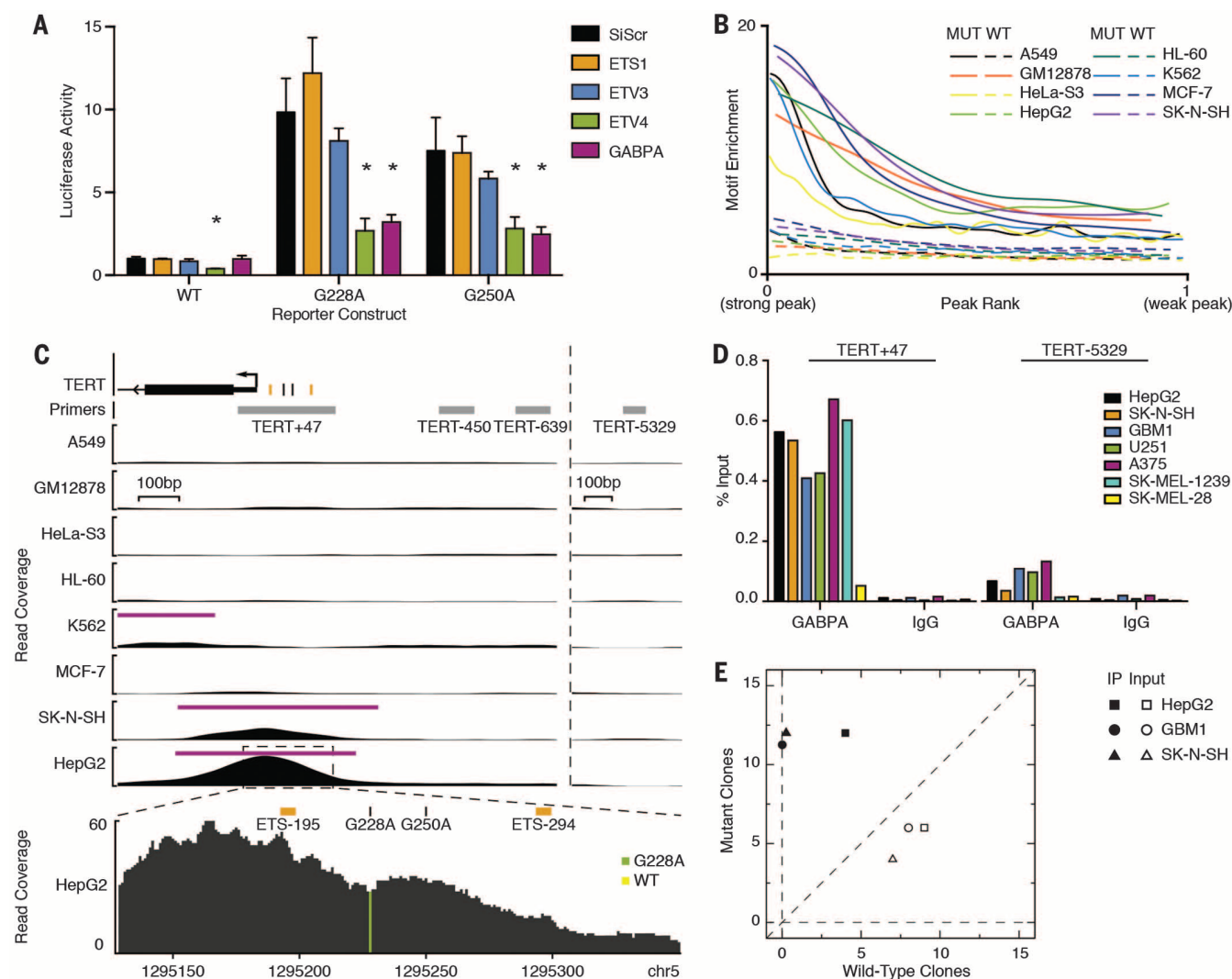


**Fig. 2. GABPA selectively regulates and binds the mutant TERT promoter across multiple cancer types.** (A) Wild-type, G228A, or G250A luciferase activity 72 hours after ETS siRNA knockdown in GBM1 cultured cells, scaled to WT-siScr. The results are an average of at least three independent experiments. Values are mean  $\pm$  SD. \* $P$  < 0.05, Student's  $t$  test compared to siScr. (B) Enrichment of mutant (CCGGAA) or wild-type (CCGGAG) hexamer sequences in ENCODE GABPA ChIP-seq peaks relative to flanking regions. (C) ENCODE GABPA ChIP-seq

data at the proximal TERT promoter and around distal quantitative polymerase chain reaction (qPCR) primers. Native ETS motifs and mutation positions are annotated by orange and black tick marks, respectively. The inset shows allelic read coverage at G228A in HepG2 cells. (D) GABPA ChIP-qPCR for the TERT promoter and a nearby control locus in seven cancer cell lines. Values represent the mean percent of input based on triplicate qPCR measurements.  $n$  = 1 for each cell line. (E) Allelic variant frequency in GABPA (IP) or input control DNA.

we observed clear periodic behavior in the G250A reporter, suggesting the recruitment of a GABP heterotetramer (Fig. 3D and fig. S11). However, G250A promoter activity peaked after deleting 6 bp, which brought the G250A site in phase with the ETS-200 site by a perfect four helical turns. Mutating ETS-195, although reducing the TERT activation level (Fig. 3C), did not change the periodic pattern, implying a preferential interaction of GABP with ETS-200 instead of ETS-195 (fig. S11). Repeating the experiment with a mutated ETS-200, however, led to a translation in 10.5-bp periodicity, which was now consistent with pairing between G250A and ETS-195 (Fig. 3D). These results strongly suggest that GABP may be able to bind and switch between both native ETS motifs in the context of G250A, consistent with the fact that both native ETS

motifs are essential for robust TERT activation (Fig. 3C).

The critical role of two adjacent ETS motifs in aberrant TERT activation was further strengthened by our analysis of an oligodendroglioma tumor containing a unique heterozygous 41-bp tandem duplication within the core TERT promoter. This tumor sample also had the R132H IDH1 mutation and 1p19q co-deletion, genetic aberrations that often co-occur with TERT promoter mutations in oligodendroglioma (31). Although this sample was wild-type at G228A and G250A, we found that the junction of the duplication event generated a de novo ETS motif that is 41 bp away from the native downstream ETS-195 motif (Fig. 3B). The promoter sequence containing this duplication induced elevated promoter activity similar to the G228A and G250A

mutant sequences, despite its wild-type status at these positions (Fig. 3C). Mutagenesis of either the native ETS-195 site or the de novo junction ETS site significantly reduced promoter activity, once again demonstrating that this duplication satisfies the prerequisite for GABP heterotetramer recruitment (Fig. 3C).

We have thus identified GABP as the critical ETS transcription factor activating TERT expression in the context of highly recurrent promoter mutations. Although many ETS transcription factors can bind similar DNA sequence motifs, GABP is unusual in that it can bind neighboring ETS motifs as a heterotetrameric complex. We showed that strong GABPA ChIP-seq peaks contain a periodicity of approximately 10.5 bp between neighboring ETS motifs, consistent with the binding of a GABP complex at two

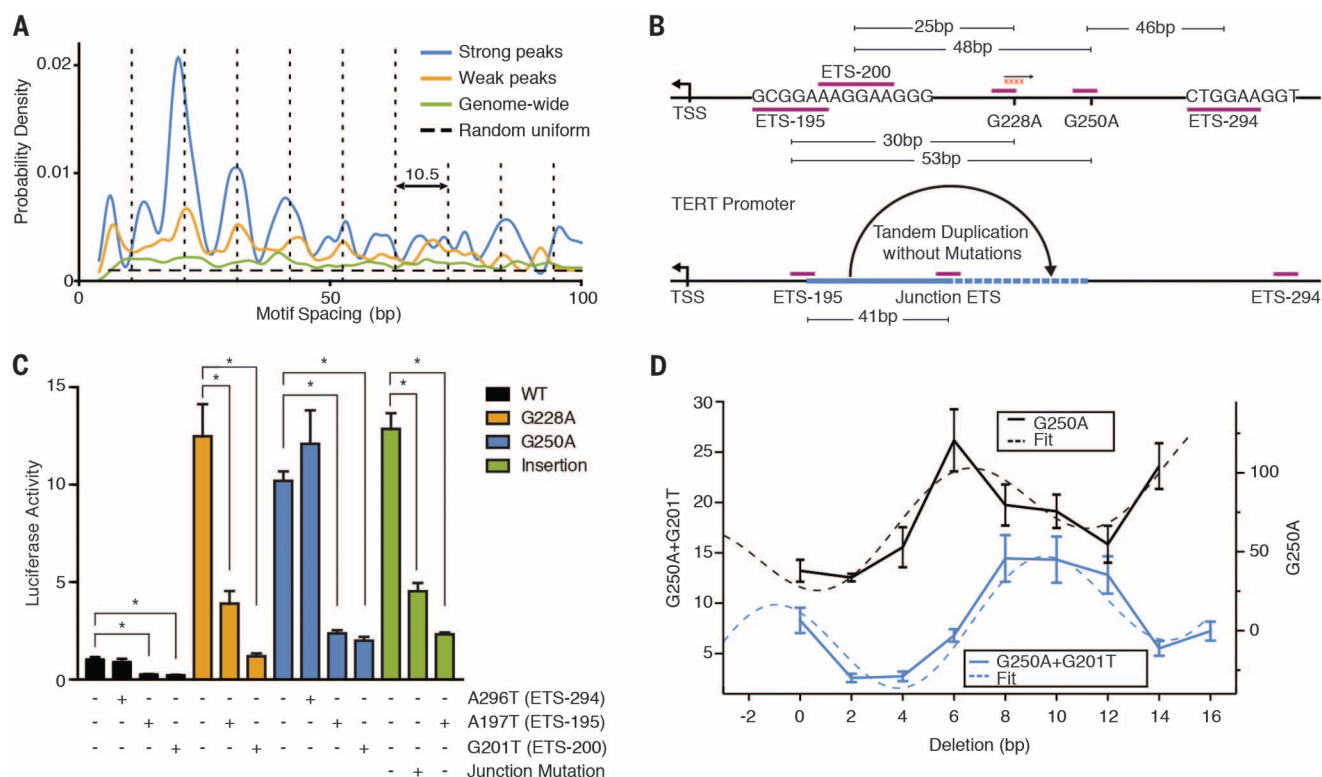


**Fig. 3. G228A and G250A cooperate with the native ETS sites ETS-195 and ETS-200 and fall within spacing for GABP heterotetramer recruitment. (A)** Distribution of motif separation in weak and strong GABP peaks. Vertical dotted lines denote periodicity of 10.5 bp. The horizontal dashed line indicates the theoretical null distribution. **(B)** Native and de novo putative ETS binding sites in the core *TERT* promoter. **(C)** Site-directed mutagenesis of the GABP heterotetramer motifs in the wild-type, G228A, G250A, or insertion *TERT* reporter

constructs. Mutation of the ETS-195, ETS-294, or junction motif are indicated by "+". The results are an average of at least three independent experiments. Values are mean  $\pm$  SD. \* $P < 0.05$ , Student's *t* test. **(D)** Site-directed mutagenesis deleting between 2 to 16 bp at the G228A site. Deletions were tested for promoter activity in a G250A or G250A+G201T background. The sinusoidal fits were obtained by using the model  $a \sin[2\pi(x - b)/10.5] + cx + d$ . The results are an average of at least three independent experiments. Values are mean  $\pm$  SD.

locations separated by full helical turns of DNA. This genome-wide pattern is reproduced in the context of *TERT* promoter mutations, where both G228A and G250A are separated from two tandem proximal native ETS motifs by 2.9/2.4 (ETS-195/ETS-200) and 5.0/4.6 (ETS-195/ETS-200) helical turns, respectively. We propose that *TERT* promoter mutations cooperate with both of these native ETS sites to recruit GABP. Further work is necessary to elucidate which other transcription factors are interacting with GABP at the mutant *TERT* promoter in order to drive aberrant transcription. Additionally, both *TERT* promoter mutations fall within a GC-rich repeat sequence with potential to form a G-quadruplex, a DNA secondary structure that can regulate gene expression (32, 33). A potential impact of *TERT* promoter mutations on this predicted secondary structure and on the complex relationship between secondary structure and GABP recruitment may also play a role in deregulating *TERT* expression. The cancer-specific interaction of GABP with the *TERT* core promoter mutations highlights a common mechanism used by many cancers to overcome replicative senescence.

## REFERENCES AND NOTES

1. T. M. Bryan, T. R. Cech, *Curr. Opin. Cell Biol.* **11**, 318–324 (1999).
2. C. W. Greider, E. H. Blackburn, *Cell* **43**, 405–413 (1985).

3. S. L. S. Weinrich *et al.*, *Nat. Genet.* **17**, 498–502 (1997).
4. P. Castelo-Branco *et al.*, *Lancet Oncol.* **14**, 534–542 (2013).
5. N. W. Kim *et al.*, *Science* **266**, 2011–2015 (1994).
6. J. W. Shay, S. Bacchetti, *Eur. J. Cancer* **33**, 787–791 (1997).
7. S. Horn *et al.*, *Science* **339**, 959–961 (2013).
8. F. W. Huang *et al.*, *Science* **339**, 957–959 (2013).
9. P. J. Killela *et al.*, *Proc. Natl. Acad. Sci. U.S.A.* **110**, 6021–6026 (2013).
10. M. Remke *et al.*, *Acta Neuropathol.* **126**, 917–929 (2013).
11. A. Quas *et al.*, *Virchows Arch.* **465**, 673–677 (2014).
12. I. Kinde *et al.*, *Cancer Res.* **73**, 7162–7167 (2013).
13. J. Vinagre *et al.*, *Nat. Commun.* **4**, 2185 (2013).
14. P. S. Rachakonda *et al.*, *Proc. Natl. Acad. Sci. U.S.A.* **110**, 17426–17431 (2013).
15. M. Simon *et al.*, *Neuro-oncol.* **17**, 45–52 (2015).
16. S. Spiegel-Kreinecker *et al.*, *Neuro-oncol.* (2015).
17. See the supplementary materials on Science Online.
18. G.-H. Wei *et al.*, *EMBO J.* **29**, 2147–2160 (2010).
19. G. W. Klappacher *et al.*, *Cell* **109**, 169–180 (2002).
20. K. C. El Kasmi *et al.*, *J. Immunol.* **179**, 7215–7219 (2007).
21. D. Sawka-Verhelle *et al.*, *J. Biol. Chem.* **279**, 17772–17784 (2004).
22. E. Birney *et al.*, *Nature* **447**, 799–816 (2007).
23. P. C. Hollenhorst *et al.*, *Genes Dev.* **25**, 2147–2157 (2011).
24. R. P. Nagarajan *et al.*, *Genome Res.* **24**, 761–774 (2014).
25. C. C. Thompson, T. A. Brown, S. L. McKnight, *Science* **253**, 762–768 (1991).
26. T. Oikawa, T. Yamada, *Gene* **303**, 11–34 (2003).
27. K. LaMarco, C. C. Thompson, B. P. Byers, E. M. Walton, S. L. McKnight, *Science* **253**, 789–792 (1991).
28. S. Gugneja, J. V. Virbasius, R. C. Scarpulla, *Mol. Cell. Biol.* **15**, 102–111 (1995).
29. F. C. de la Brousse, E. H. Birkenmeier, D. S. King, L. B. Rowe, S. L. McKnight, *Genes Dev.* **8**, 1853–1865 (1994).
30. J. Sawada, M. Goto, C. Sawa, H. Watanabe, H. Handa, *EMBO J.* **13**, 1396–1402 (1994).

31. H. Arita *et al.*, *Acta Neuropathol.* **126**, 267–276 (2013).
32. S. L. Palumbo, S. W. Ebbinghaus, L. H. Hurley, *J. Am. Chem. Soc.* **131**, 10878–10891 (2009).
33. K. W. Lim *et al.*, *J. Am. Chem. Soc.* **132**, 12331–12342 (2010).

## ACKNOWLEDGMENTS

This work was generously supported by National Cancer Institute (NCI) grant R01CA163336 (J.S.S.), the Sontag Foundation Distinguished Scientist Award (J.S.S.), NCI grants P50CA097257 and P01CA18816-06 (M.S.B., S.M.C., J.F.C.); NCI grant R01CA169316-01 (J.F.C.), the Grove Foundation, the Karen Osney Brownstein Endowed Chair (J.F.C.), the Anne and Jason Farber Foundation, and a gift from the Dabbiere family. Additional support was provided by NCI grants R25CA112355 (K.M.W.), R01CA52689 (K.M.W., J.K.W., M.R.W.), and P50CA097257 (K.M.W., M.R.W.); the Stanley D. Lewis and Virginia S. Lewis Endowed Chair in Brain Tumor Research; the Robert Magnin Newman Endowed Chair in Neuro-oncology; the Founder Professorship from the Grainger Engineering Breakthroughs Initiative (J.S.S.); and donations from families and friends of John Berardi, Helen Glaser, Elvera Olsen, Raymond E. Cooper, and William Martinussen. Provisional patent application (application number 62/145,579) has been filed by the University of California, San Francisco, and the University of Illinois. All transcriptome sequencing data have been deposited in the European Genome-phenome Archive under accession number EGAS00001001242.

## SUPPLEMENTARY MATERIALS

www.sciencemag.org/content/348/6238/1036/suppl/DC1  
Materials and Methods  
Figs. S1 to S14  
Tables S1 to S6  
References (34–44)

26 February 2015; accepted 4 May 2015  
Published online 14 May 2015;  
10.1126/science.aab0015



## EMBRYO DEVELOPMENT

# A cysteine-clamp gene drives embryo polarity in the midge *Chironomus*

Jeff Klomp,<sup>1</sup> Derek Athy,<sup>1</sup> Chun Wai Kwan,<sup>1</sup> Natasha I. Bloch,<sup>1\*</sup> Thomas Sandmann,<sup>2,†</sup> Steffen Lemke,<sup>1,‡</sup> Urs Schmidt-Ott<sup>1§</sup>

In the fruit fly *Drosophila*, head formation is driven by a single gene, *bicoid*, which generates head-to-tail polarity of the main embryonic axis. Bicoid deficiency results in embryos with tail-to-tail polarity and no head. However, most insects lack *bicoid*, and the molecular mechanism for establishing head-to-tail polarity is poorly understood. We have identified a gene that establishes head-to-tail polarity of the mosquito-like midge, *Chironomus riparius*. This gene, named *panish*, encodes a cysteine-clamp DNA binding domain and operates through a different mechanism than *bicoid*. This finding, combined with the observation that the phylogenetic distributions of *panish* and *bicoid* are limited to specific families of flies, reveals frequent evolutionary changes of body axis determinants and a remarkable opportunity to study gene regulatory network evolution.

The *bicoid* gene of *Drosophila melanogaster* is involved in a variety of early developmental and biochemical processes. Many studies have examined its activity as a morphogen. *bicoid* mRNA is maternally deposited into the egg and transported to the anterior side, forming a protein gradient that activates transcription of genes in a concentration-dependent manner (1–3). The *bicoid* gene represents an intriguing case of molecular innovation. It is related to Hox-3 genes of other animals but appears to be absent in most insects, including mosquitoes and other “lower” flies (Diptera) (4–6) (Fig. 1). Bicoid-deficient embryos cannot develop a head or thorax and instead develop a second set of posterior structures that become a second abdomen (“double abdomen”) when the activity of another gene, *hunchback*, is disrupted simultaneously (7). Likewise, ectopic expression of *bicoid* in the posterior embryo prevents abdomen development and induces a “double head” (8). Although other genes have been found to play a role in anterior development in beetles (9, 10) and wasps (11, 12), a gene responsible for anterior-posterior (AP) polarity has not been found. Nearly 30 years after the identification of *bicoid* in *Drosophila*, we have identified a gene that is necessary for the symmetry breaking and long-range patterning roles of *bicoid* in the harlequin fly *Chironomus riparius*. Further, we reexamined *bicoid* in several fly families and conclude that *bicoid* has been lost from genomes of some higher flies, including two lineages of agricultural and public health concern, the tephritid and glossinid flies (Fig. 1, figs.

S1 and S2, and table S1). These observations raise the possibility that *bicoid* has been frequently lost or substantially altered during radiations of dipterans.

Ultraviolet light irradiation of anterior chironomid fly embryos induces double-abdomen formation, providing evidence of anterior localized RNA (13, 14). Therefore, we conducted gene expression profiling of AP-bisected early *C. riparius* embryos to search for asymmetrically distributed maternal mRNA transcripts. All of the 6604 identified transcripts were ranked according to the magnitude of their differential expression scores and *P* values (Fig. 2A). Those most enriched in the posterior embryo were primarily homologs of known germ cell or germ plasm components (Fig. 2A, right). This was anticipated because the germ plasm of *Chironomus* is located at the posterior pole. One transcript was highly biased in the anterior end of the early embryo (Fig. 2A, left). We confirmed localized expression in early embryos for the two most biased transcripts (Fig. 2B and fig. S3).

The anteriorly biased transcript contains an open reading frame (ORF) encoding 131 amino acids. This predicted protein possesses a cysteine-

clamp domain (C-clamp, residues 63 to 92) with similarity to the C-clamp of the Wnt signaling effector Pangolin/Tcf (Fig. 2C and fig. S4) (15) and was therefore given the name *panish* (for “pan-ish”). However, neither the high-mobility group (HMG) domain nor the  $\beta$ -catenin interaction domain of Pangolin is conserved in the protein sequence encoded by *panish*. Notably, we also identified a distinct *pangolin* ortholog expressed later in development during blastoderm cellularization at the anterior pole (fig. S5). Duplication of a portion of the ancestral *pangolin* locus is a possibility, given the strong similarity of their C-clamp domains. The *panish* C-clamp region appears to encode a bipartite nuclear localization signal (16); hence, *panish* may be involved in transcriptional regulation. The 5' end of the *panish* transcript (27/131 predicted residues) overlapped with an unrelated *Chironomus* transcript with homology to *Drosophila* ZAP3, a conserved nucleoside kinase gene. We mapped all transcripts onto genomic *Chironomus* sequence containing *panish* and determined that *Chironomus* ZAP3 (*Cri-zap3*) overlaps mostly with the large second *panish* intron (Fig. 2D) but was not differentially expressed between the anterior and posterior halves (*P* = 0.34).

The *panish* transcript was tightly anteriorly localized in freshly laid eggs but was expressed more broadly in an anterior-to-posterior gradient by the beginning of the blastoderm stage (Fig. 2B). The *panish* transcript was not evident after blastoderm cellularization. To test whether the *panish* transcript was necessary for the AP axis, we conducted a series of loss- and gain-of-function experiments using double-stranded RNA (dsRNA) and capped mRNA injections. Early *Chironomus* embryos injected with dsRNA against the *panish* ORF or 3' untranslated region (3'UTR) developed double abdomens (Fig. 3, A to C, and fig. S6A), with similar survival rates between *panish* RNAi (RNA interference) and controls. Notably, *Cri-zap3* RNAi did not cause any obvious cuticle defects (Fig. 3C). Injection of *panish* dsRNA at the later blastoderm cellularization stage also had no effect, indicating that *panish* mRNA is dispensable at later stages (*N* = 112/112 wild type).

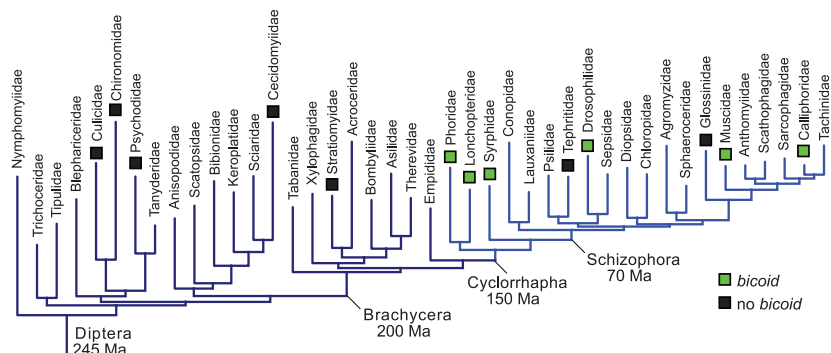


**Fig. 1. *Bicoid* in dipteran families.** Indicated instances of missing *bicoid* orthologs are based on genome sequences; tree is based on molecular phylogeny [see (22) and species list (23)], and cyclorrhapha clade, with *bicoid*, is indicated (light blue). Ma, millions of years ago.

<sup>1</sup>Department of Organismal Biology and Anatomy, University of Chicago, Chicago, IL 60637, USA. <sup>2</sup>Division of Signaling and Functional Genomics, German Cancer Research Center (DKFZ), 69120 Heidelberg, Germany.

\*Present address: Department of Ecology and Evolution, University of Chicago, Chicago, IL 60637, USA. †Present address: Department of Bioinformatics and Computational Biology, Genentech Inc., South San Francisco, CA 94080, USA. ‡Present address: Centre for Organismal Studies, University of Heidelberg, 69120 Heidelberg, Germany. §Corresponding author. E-mail: uschmid@uchicago.edu

To confirm the requirement for *panish* mRNA in establishing the anterior domain, we performed rescue experiments by co-injecting either wild-type or out-of-frame mutated *panish* coding mRNA in combination with *panish* 3'UTR dsRNA. Double-abdomen formation was suppressed in more than 40% of the embryos in which wild-type *panish* mRNA was injected into the anterior third, whereas double-abdomen formation was not suppressed after injection of mutated *panish* mRNA, injection buffer, or *bicoid* mRNA into the anterior third of the embryos (Fig. 3C and fig. S6, B to D) or *panish* mRNA injection into the posterior third of the embryos (130/131 wild type,  $P < 0.0001$ ).

We also did not observe double-head formation (214/214 wild type) when we injected *panish* mRNA into the posterior third of wild-type embryos. This observation suggests that *Panish* activity is constrained to the anterior

embryo, potentially because of missing anterior components or the presence of anterior program inhibitors in the posterior embryo. To distinguish between these possibilities, we examined the expression and function of genes associated with embryonic axis specification in other insects (17). Candidate genes included orthologs of the anterior inhibitor *nanos* (*Cri-nos*), the anterior pattern organizers *hunchback* (*Cri-hb*) and *orthodenticle/ocelliless* (*Cri-oc*), and the posterior pattern organizers *caudal* (*Cri-cad*) and *tailless* (*Cri-tll*).

Maternal *Cri-nos* transcript was enriched at the posterior pole (fig. S3), but neither *Cri-nos* RNAi nor ectopic *Cri-nos* expression affected axial patterning. *Cri-hb* and *Cri-oc* were present in the anterior blastoderm, but RNAi against these genes only caused homeotic and gap phenotypes, respectively (fig. S7, A to D). *Cri-cad* was expressed in the posterior embryo, and

*Cri-cad* RNAi resulted in abdomen truncation (Fig. 4A and fig. S7E). Therefore, these genes do not appear critical for embryonic AP polarity. Unlike *Drosophila tailless*, *Cri-tll* was expressed in a posterior-to-anterior gradient in early blastoderm stages (Fig. 4B). After *panish* RNAi, both *Cri-cad* and *Cri-tll* were no longer expressed on one side, but instead were expressed symmetrically, consistent with their critical roles in abdomen development (Fig. 4, C and D). *Drosophila tailless* encodes a nuclear receptor required for terminal structures of the abdomen and brain development but not the AP axis (18). In contrast, *Cri-tll* RNAi embryos lacked tail segments, and ~70% of them developed malformed, often symmetrical, double heads with duplicated mandible and labrum structures and eye spots ( $N = 45$ ; Fig. 4, E to G, and fig. S8). This result was confirmed in independent RNAi experiments using nonoverlapping dsRNAs (24/87 and 27/88 double heads).

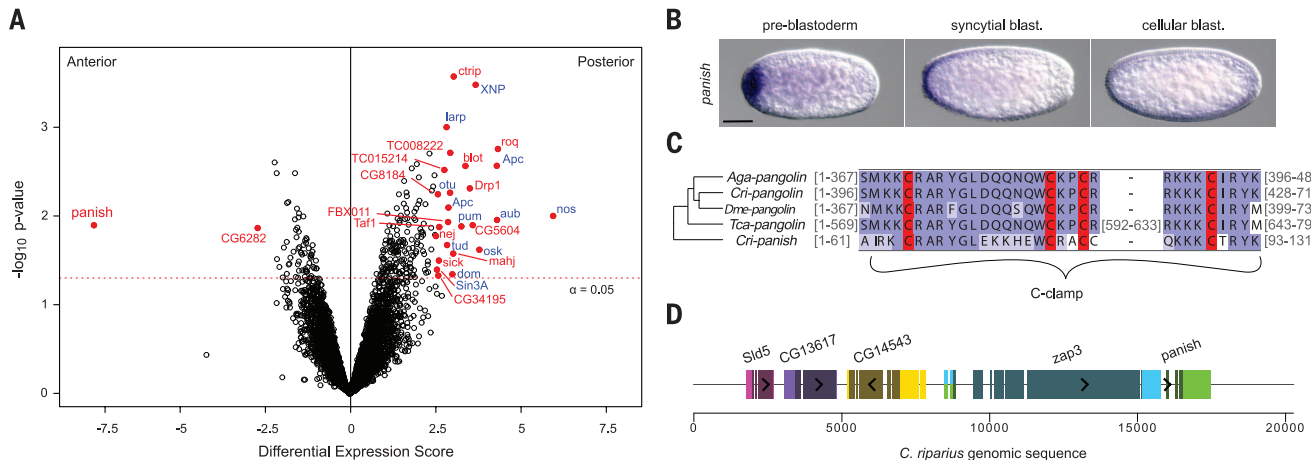


**Fig. 2. *Panish* mRNA is enriched in the anterior embryo and encodes a C-clamp protein.** (A) Differential expression of transcripts based on RNA sequencing data from anterior and posterior embryo halves. Red, score > |2.5| and  $P < 0.05$ ; blue, putative germ cell or germ plasm components. (B) RNA in situ hybridizations of early embryos for *panish*. Anterior is to the left; scale bar, 10  $\mu$ m. (C) C-clamp region of *panish* aligned with Pangolin sequences from *C. riparius* (*Cri*), *D. melanogaster* (*Dme*),

*Anopheles gambiae* (*Aga*), and *Tribolium castaneum* (*Tca*). Gray numbers, residues not shown; red, conserved cysteine residues; blue, residue similarity. Amino acid abbreviations: A, Ala; C, Cys; D, Asp; E, Glu; F, Phe; G, Gly; H, His; I, Ile; K, Lys; L, Leu; M, Met; N, Asn; P, Pro; Q, Gln; R, Arg; S, Ser; T, Thr; W, Trp; Y, Tyr. (D) The *panish* locus. Homology is based on reciprocal-best-BLAST between *C. riparius* transcripts and *D. melanogaster* genes. Longest ORFs (shaded) and orientation (arrowheads) are indicated.

**Fig. 3. *Panish* is required to establish AP polarity in *C. riparius*.** (A) Inverted dark-field image of wild-type first-instar larval cuticle. A, abdominal segment; T, thoracic segment. (B) *Panish* RNAi cuticle of symmetrical double-abdomen larva. Scale bars, 30  $\mu$ m. (C) Comparison of *panish* and *Cri-zap3* RNAi phenotypes and rescue of the *panish* RNAi phenotype by anterior injection of *panish* mRNA. \*Note: In the third column, "wild type" includes 13 partial rescues (deformed head structures; fig. S6, B to D). N.S.,  $P > 0.05$ ; *Eba-bcd* from (6).

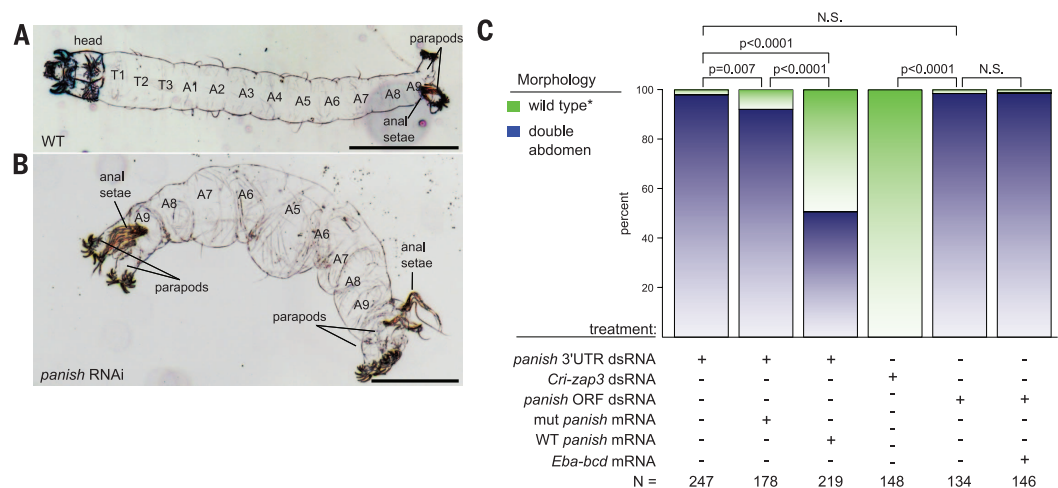
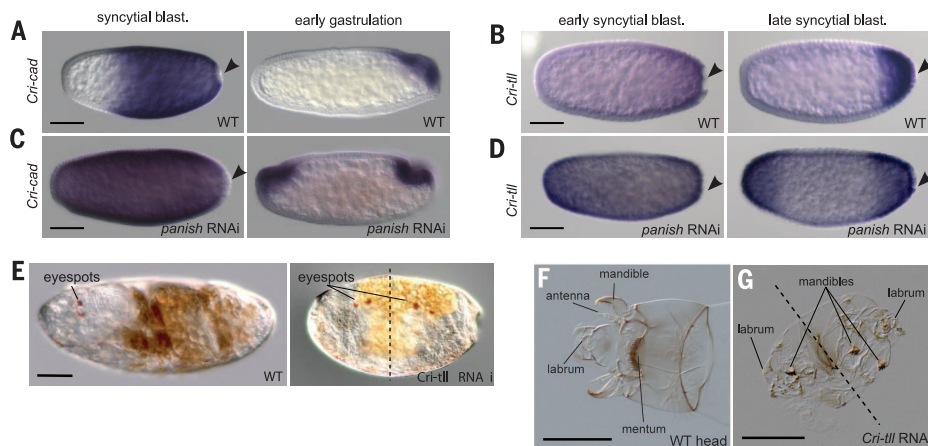




**Fig. 4. *Cri-cad* and *Cri-tll* are regulated by *panish*, and *Cri-tll* is required to establish AP polarity.** (A to D) Staining for *Cri-cad* [(A) and (C)] and *Cri-tll* [(B) and (D)] with RNA in situ hybridization in wild-type and *panish* RNAi embryos. Black arrowheads indicate posterior pole cells. (E) Eye spots indicated on live wild-type and *Cri-tll* RNAi embryos. (F and G) Cuticle preparations of a wild-type larval head (F) and a *Cri-tll* RNAi larva (G). Dashed lines indicate approximate plane of symmetry. Anterior is to the left in all panels; scale bars, 10  $\mu$ m [except (G), 30  $\mu$ m].



Duplication of head structures at both poles of the *Cri-tll* RNAi embryos suggests that unlike the *Drosophila* homolog, *Cri-tll* plays a role in AP polarity. Moreover, because *Cri-tll* is not expressed maternally, maternal *Cri-nos* would not appear to inhibit the formation of the anterior program. The observation that both heads of *Cri-tll* RNAi embryos develop with deformities is not surprising because *Drosophila tll* has a role in head development. *Cri-tll* may also play this part irrespective of its role in AP polarity.

A receptor tyrosine kinase gene, *torso*, controls the activation of *tailless* at the poles of the *Drosophila* blastoderm along with a second target, the zinc finger gene *huckebein* (19). We were unable to detect expression of the *Chironomus* homolog of *huckebein* (*Cri-hkb*) in early embryos (fig. S9A). *Cri-tor* was expressed zygotically at the poles of the blastoderm embryo (fig. S9B). Maternal *Cri-tor* transcript was detected in the RNA sequencing data but not by RNA in situ hybridization. *Cri-tor* RNAi caused tail deletions and head defects similar to those of *Cri-tll* RNAi embryos, but not double heads (fig. S9C). This finding suggests that *Cri-tll* has a role in axis polarity that is outside of its role in the terminal system driven by *torso*.

The double-head phenotype of *Cri-tll* RNAi embryos suggests a permissive role for *panish* in specifying embryonic AP polarity because the *panish* transcript was not detected in the posterior embryo. We suspected that *Cri-tll* might also have a permissive role in AP axis specification, because *Drosophila* Tailless functions as a dedicated repressor (20). This was confirmed by double RNAi experiments against *panish* and *Cri-tll* that resulted in perfect double abdomens (73/95 double abdomen, 20/95 intermediate, 2/95 wild type; fig. S9D). However, it raises the question of why the default developmental program establishes a double abdomen and not a double head.

One possible explanation is that Panish functions as a direct activator of head genes. This would imply that there is Panish activity in the posterior, but it seems unlikely given the lack of detectable mRNA in the posterior of embryos in both the RNA sequencing data and in situ hybridizations and the inability of *panish* mRNA

to rescue the *panish* RNAi phenotype when *panish* mRNA is injected into the posterior third of the embryo. A more cogent possibility is that *panish* protein is more effective in repressing posterior genes than *Cri-tll* is in repressing anterior genes. Knockdown of *panish* would therefore result in proportionally higher levels of posterior transcripts such as *Cri-cad* and consequently inhibit head formation. This interpretation is consistent with high penetrance of the double-abdomen phenotype after *panish* RNAi.

Our results show that *Drosophila bicoid* and *Chironomus panish* encode structurally distinct DNA binding domain proteins that play similar essential roles in establishing AP polarity of the primary axis. In each case, the protein is necessary for breaking the symmetry of the primary axis and, when inactive, results in duplication of the posterior domain. Bicoid is a transcriptional activator of anterior genes. However, Panish appears to be a repressor of posterior patterning genes (fig. S10A). Moreover, maternally expressed *nanos*, which inhibits anterior programming in the posterior *Drosophila* embryo (21), appears to be ineffective in this regard in *Chironomus*. Two pieces of evidence argue against the existence of an additional, maternally localized, instructive factor for anterior development like *bicoid* in *Chironomus*. First, *panish* was the only transcript found strongly enriched at the anterior pole. Second, factors required for head development were also present in the posterior pole of *Cri-tll* embryos. We did not find evidence of *panish* in other dipteran genomes, even though the locus is conserved in two closely related chironomid species, *C. tentans* and *C. piger* (fig. S10B and table S2). This suggests a recent origin of *panish*. Our study shows that mechanisms of AP patterning in insects are more labile than previously acknowledged. The functionally diverse primary axis determinants of fly embryos provide a remarkable opportunity for studying molecular innovations in the context of gene regulatory networks.

#### REFERENCES AND NOTES

1. H. G. Frohnhofer, C. Nüsslein-Volhard, *Nature* **324**, 120–125 (1986).
2. W. Driever, C. Nüsslein-Volhard, *Cell* **54**, 83–93 (1988).

3. W. Driever, C. Nüsslein-Volhard, *Cell* **54**, 95–104 (1988).
4. M. Stauber, H. Jackle, U. Schmidt-Ott, *Proc. Natl. Acad. Sci. U.S.A.* **96**, 3786–3789 (1999).
5. M. Stauber, A. Prell, U. Schmidt-Ott, *Proc. Natl. Acad. Sci. U.S.A.* **99**, 274–279 (2002).
6. S. Lemke et al., *Development* **137**, 1709–1719 (2010).
7. W. Driever, in *The Development of Drosophila melanogaster*, M. Bate, A. M. Arias, Eds. (Cold Spring Harbor Laboratory Press, Cold Spring Harbor, NY, 1993), vol. 1, pp. 301–324.
8. W. Driever, V. Siegel, C. Nüsslein-Volhard, *Development* **109**, 811–820 (1990).
9. J. Fu et al., *Proc. Natl. Acad. Sci. U.S.A.* **109**, 7782–7786 (2012).
10. K. Kotkamp, M. Klingler, M. Schoppmeier, *Development* **137**, 1853–1862 (2010).
11. J. A. Lynch, A. E. Brent, D. S. Leaf, M. A. Pultz, C. Desplan, *Nature* **439**, 728–732 (2006).
12. A. E. Brent, G. Yucel, S. Small, C. Desplan, *Science* **315**, 1841–1843 (2007).
13. K. Kalthoff, *Dev. Biol.* **25**, 119–132 (1971).
14. H. Yajima, *J. Embryol. Exp. Morphol.* **12**, 89–100 (1964).
15. F. A. Atcha et al., *Mol. Cell. Biol.* **27**, 8352–8363 (2007).
16. S. Kosugi, M. Hasebe, M. Tomita, H. Yanagawa, *Proc. Natl. Acad. Sci. U.S.A.* **106**, 10171–10176 (2009).
17. M. I. Rosenberg, J. A. Lynch, C. Desplan, *Biochim. Biophys. Acta* **1789**, 333–342 (2009).
18. T. R. Strecker, J. R. Merriam, J. A. Lengyel, *Development* **102**, 721–734 (1988).
19. G. Brönnner et al., *Nature* **369**, 664–668 (1994).
20. E. Morán, G. Jiménez, *Mol. Cell. Biol.* **26**, 3446–3454 (2006).
21. R. P. Wharton, G. Struhl, *Cell* **67**, 955–967 (1991).
22. B. M. Wiegmann et al., *Proc. Natl. Acad. Sci. U.S.A.* **108**, 5690–5695 (2011).
23. See supplementary materials on Science Online.

#### ACKNOWLEDGMENTS

Transcriptomic data are available at the National Center for Biotechnology Information Sequence Read Archive (PRJNA229141). We thank G. K. Bergtrom for *Chironomus* culture and equipment; T. Hankeln, F. Ripp, L. Wieslander, and N. Visa for chironomid sequence data; J. E. Klomp for technical advice and discussions; M. Ludwig, S. Lott, M. Kim, C. Avila, A. Barnett, E. Davydova, T. Uchanski, C. Martinez, and Y. Yoon for technical help; J. Reinitz, M. Long, P. Rice, P. Faber, A. Ruthenberg, and C. Martinez for discussions; and C. Ferguson and M. Feder for laboratory equipment. Supported by Cell Networks Cluster of Excellence grant EXC81 (T.S.), NIH grant 1R03HD67700-01A1, NSF grants IOS-1121211 and IOS-1355057, and the University of Chicago.

#### SUPPLEMENTARY MATERIALS

www.sciencemag.org/content/348/6238/1040/suppl/DC1  
Materials and Methods  
Figs. S1 to S10  
Tables S1 and S2  
References (24–51)

16 January 2015; accepted 27 April 2015  
Published online 7 May 2015;  
10.1126/science.aaa7105

# Will you be published in *Science* this December?

(If you have a recent PhD you could be.)



To be published in *Science* is a special moment for any scientist. But to do so at the very start of your career is extremely exciting indeed. If you are a recent PhD graduate you could be published in *Science* this December, and receive a very special prize in Stockholm during the week of Nobel.

The journal *Science* & SciLifeLab have established The *Science* & SciLifeLab Prize for Young Scientists, to recognize and reward excellence in PhD research and support young scientists at the start of their careers. It's about bright minds, bright ideas and bright futures.

Four winners will be selected for this international award. They will have their essays published by the journal *Science* and share a new total of 60,000 USD in prize money. The winners will be awarded in Stockholm during the second week of December when the city is alive with excitement and celebrates the new Nobel Laureates at the annual Nobel Prize ceremony. They will take part in a truly unique week of events including meeting leading scientists in their fields.

*"The last couple of days have been exhilarating. It has been an experience of a lifetime. Stockholm is a wonderful city and the Award winning ceremony exceeds my wildest dreams."*  
—Dr. Dan Dominissini, 2014 Prize Winner

Who knows, having your work published in the journal *Science* could be a major stepping stone in your career and the *Science* & SciLifeLab Prize for Young Scientists makes this possible.

**The 2015 Prize is now open. The deadline for submissions is August 1, 2015.**

Enter today: [www.sciencemag.org/scilifelabprize](http://www.sciencemag.org/scilifelabprize)

**The 2015 Prize categories are:**

- Cell and Molecular Biology
- Ecology and Environment
- Genomics and Proteomics
- Translational Medicine

*This prize is made possible with the kind support of the Knut and Alice Wallenberg Foundation. This Foundation grants funding in two main areas; research projects of high scientific potential and individual support of excellent scientists.*

Knut och Alice  
Wallenbergs  
Stiftelse

Science  
AAAS

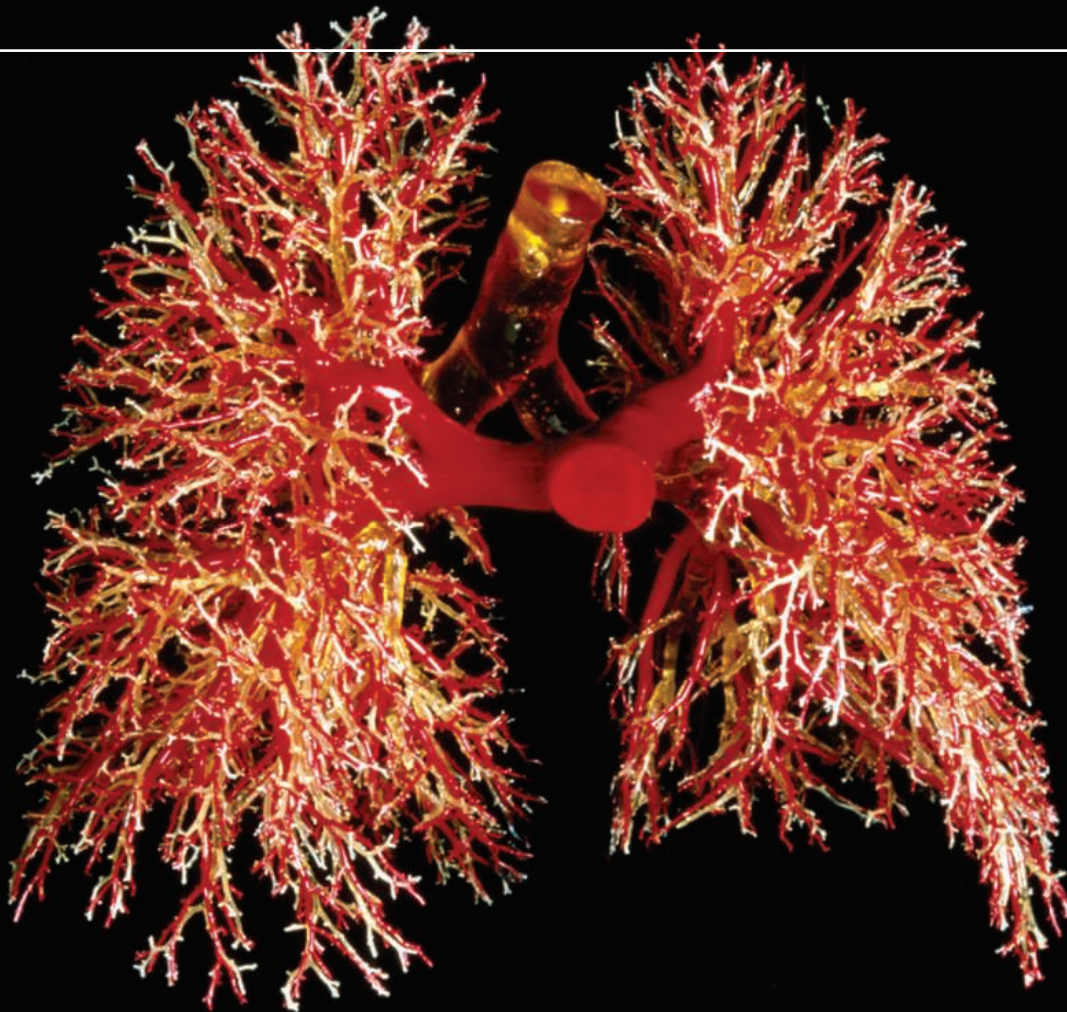
SciLifeLab



---

# WILL YOUR RESEARCH LEAD TO BETTER LIVES FOR PATIENTS?

---



Gopinath Sutendra and Evangelos D. Michelakis. "Pulmonary Arterial Hypertension: Challenges in Translational Research and a Vision for Change", *Sci. Transl. Med.* 5, 208sr5 (2013) Credit: Science Source

**Science** Translational Medicine |  AAAS

INTEGRATING SCIENCE, ENGINEERING, AND MEDICINE

Find out more about the scope of the journal and submit your research today!

**ScienceTranslationalMedicine.org**

advantage

New Promotion March 1–June 30, 2015



# Take Good Care of Your Cells

Smart solutions for your cell biology processes—now with up to 21 % off

As a workflow-oriented provider of lab equipment, Eppendorf offers instruments, consumables, and accessories that perfectly fit your processes in the lab and thus your daily lab work. Our comprehensive solutions are engineered with smart innovations to simplify or even eliminate cumbersome lab work.

**Benefit now from substantial savings on:**

- > Eppendorf Xplorer® electronic multi-channel pipettes
- > Centrifuge 5702 R with rotor
- > Eppendorf ThermoMixer® C
- > Eppendorf BioSpectrometer® fluorescence with  $\mu$ Cuvette G1.0
- > Divisible twin.tec PCR Plates 96

[www.eppendorf.com/advantage](http://www.eppendorf.com/advantage)

Eppendorf®, the Eppendorf logo, Eppendorf BioSpectrometer®, Eppendorf ThermoMixer®, and Eppendorf Xplorer® are registered trademarks of Eppendorf AG, Germany. U.S. Design Patents are listed on [www.eppendorf.com/ip](http://www.eppendorf.com/ip). Offers may vary by country. All rights reserved, including graphics and images. Copyright © 2015 by Eppendorf AG.



**eppendorf**  
**& Science**

**PRIZE FOR  
NEURO  
BIOLOGY**



2014 Winner  
Eiman Azim, Ph.D.  
Columbia University  
For research on skilled  
limb movement

# Call for Entries

**Application Deadline**  
**June 15, 2015**

## **Eppendorf & Science Prize for Neurobiology**

The annual Eppendorf & Science Prize for Neurobiology is an international award which honors young scientists for their outstanding contributions to neurobiological research based on methods of molecular and cell biology. The winner and finalists are selected by a committee of independent scientists, chaired by Science's Senior Editor, Dr. Peter Stern. To be eligible, you must be 35 years of age or younger.

## **You could be next to win this prize and to receive**

- > Prize money of US\$25,000
- > Publication of your work in Science
- > Full support to attend the Prize Ceremony held in conjunction with the Annual Meeting of the Society for Neuroscience in the USA
- > An invitation to visit Eppendorf in Hamburg, Germany

It's easy to apply!

Learn more at: [www.eppendorf.com/prize](http://www.eppendorf.com/prize)

**eppendorf** **Science**  
AAAS

# Join Keystone Symposia in Asia for our October Conferences on Nutrition and Diabetes

## Human Nutrition, Health and Environment

**October 14–18, 2015**

**China World Hotel | Beijing | China**

Scientific Organizers: Martin Kussmann, Hannelore Daniel and Jacqueline Pontes Monteiro

*Understanding interactions of nutrition and lifestyle with an individual's genetic makeup is vital for maintaining health and delaying disease onset. Toward that end, this meeting aims to: 1) Bring together researchers from traditionally separated disciplines: nutrition, (gen)omics, clinics, physiology, epidemiology, analytics, biomathematics; 2) Advance nutrition research as a quantitative, holistic and molecular science; 3) Review/challenge classical pre-clinical models and clinical study designs, incorporating improved translational in vitro and in vivo models, human intervention study designs, and innovative new tools/technologies for molecular phenotyping; and 4) Connect basic science to patient- and consumer-relevant outputs in terms of personalized dietary/nutritional counseling and monitoring/diagnostics.*

**Session Topics:**

- The Interaction between Human Genome, Diet and Environment
- Translational Models for Human Nutrition and Health
- Human Nutritional and Lifestyle Interventions
- Capturing and Monitoring Human Individuality
- From Nutrigenomics to Systems Nutrition
- Nutrition 2.0 – Translation into Solutions for Human Health
- Global Nutrition and Sustainability

*Global Health Travel Award Deadline (for investigators from developing countries): May 12, 2015;*

*Scholarship & Discounted Abstract Deadline: June 16, 2015; Abstract Deadline: July 14, 2015; Discounted Registration Deadline: August 13, 2015*

For additional details, visit [www.keystonesymposia.org/15T1](http://www.keystonesymposia.org/15T1).

## Diabetes: New Insights into Molecular Mechanisms and Therapeutic Strategies

**October 25–29, 2015**

**Westin Miyako Kyoto | Kyoto | Japan**

Scientific Organizers: Takashi Kadowaki, Juleen R. Zierath, Nobuya Inagaki and Barbara B. Kahn

*The prevalence of type 2 diabetes is rising to epidemic proportions worldwide. Type 2 diabetes is a complex disease caused by dysfunction of multiple organ systems, and disease susceptibility is profoundly influenced by both genetic and environmental factors. This meeting brings together leading professionals in the academic and pharmaceutical communities with various specialties in diabetes research to share new approaches and research paradigms. The meeting will present the latest discoveries in diabetes research, highlighting essential aspects of diabetes, as well as emerging themes that are likely to provide novel therapeutic approaches.*

**Session Topics:**

- Islet Dysfunction in Diabetes
- Regenerative Medicine in Diabetes
- Gut Biology and Systemic Metabolism
- CNS Control of Metabolism
- Novel Insights into Adipocyte Biology
- Molecular Mechanisms Underlying Insulin Resistance
- Genetics and Epigenetics of Diabetes
- Diabetes and Healthy Lifespan

*Scholarship & Discounted Abstract Deadline: June 25, 2015; Abstract Deadline: July 23, 2015; Discounted Registration Deadline: August 25, 2015*

For additional details, visit [www.keystonesymposia.org/15T2](http://www.keystonesymposia.org/15T2).





**TIRF Illuminator**

The new one-line illuminator (cellTIRF-1L) complements the high-end four- and two-line (cellTIRF MITICO 4L/2L) illuminators. Ideally suited for use with laser combiners, the cellTIRF-1L with motorized TIRF angle control offers cost-effective flexibility for system builders. The new illuminator can also be used with third-party lasers and enables multi-fluorescence samples to be sequentially imaged at the same penetration depth. Control is effortlessly managed by software integration or via the Olympus Real-Time Controller for accurate live cell imaging. As TIRF imaging is invaluable across a wide spectrum of disciplines to investigate events occurring at cell surfaces, the cellTIRF illuminators provide a series of features supporting both precise imaging and easy operation. Among these features are highly advanced optics, integrated laser safety systems, and high-speed control of penetration depth and laser lines via the RTC. The high-end systems provide ultrasensitive truly simultaneous multicolor TIRF microscopy, with up to four laser channels and independent beam paths.

**Olympus**

For info: +49-(0)-40-23773-5913  
[www.olympus-lifescience.com](http://www.olympus-lifescience.com)

**Scalable RNA-Seq Service**

Stranded, ribodepletion, and globin reduction library construction options have been added to the existing RNA-Seq services. The Illumina TruSeq Stranded Total RNA Sample Prep Kit has been automated on Beckman Coulter instruments to enable scalability and LIMS sample tracking. This expanded offering has been validated for human, mouse, rat, and plant samples and includes the ability to work with samples derived from blood and FFPE tissue. This fully automated sample preparation pipeline delivers consistent results run after run, reducing user variability and bias, and allows processing of a large amount of samples with reduced turnaround time relative to manual library construction. This expanded offering is suited for genome annotation, de novo transcriptome assembly, and accurate digital gene expression analysis thus providing uniform coverage and precise measurement of strand orientation, and discovery across both coding and multiple forms of noncoding RNA.

**Beckman Coulter Genomics**

For info: 800-361-7780  
[www.beckmangenomics.com](http://www.beckmangenomics.com)

**Bioprocess Control Station**

The BioFlo 320 is truly a step into the future for Eppendorf as a bioprocess equipment manufacturer. New features including autoclavable and single-use vessel flexibility, intelligent sensors, and IP network communication for multiunit control set it apart as the new premium choice in the bench-scale bioprocess market. Suitable for microbial and cell culture, scale up to scale down, batch, fed-batch, and continuous processes, the BioFlo 320 can meet the ever-changing needs of all segments of the biotech and pharmaceutical industries. It offers flexibility, better control, and maximum functionality while occupying a fraction of the valuable lab space of similar systems.

**Eppendorf**

For info: 800-645-3050  
[www.eppendorfnna.com](http://www.eppendorfnna.com)

**Bioreactor Systems**

The new version of the ambr systems (ambr 15 and ambr 250) are supplied with integrated BioPAT MODDE Software for Design of Experiments (DoE), powered by Umetrics. This allows bioprocess scientists to easily implement DoE into their work flow for simpler process optimization and scale-up to larger single-use BIOSTAT pilot and manufacturing scale bioreactors, making bioprocess development faster and more cost-effective. The integrated DoE software will enable scientists to quickly establish a Design Space where relevant bioprocessing conditions are varied simultaneously. Users can rapidly configure DoE experiments via work packets that are exported from the software to the ambr system; configuring each microbioreactor with its own DoE defined bioprocessing parameters. The data generated from ambr, including offline analytics, is analyzed within the software to identify critical process parameters, optimize bioprocessing conditions, and define a robust design space for implementation in larger single-use BIOSTAT pilot and manufacturing scale bioreactors.

**Sartorius Stedim Biotech**

For info: 800-368-7178  
[www.sartorius.com](http://www.sartorius.com)

**Liquid Metering Pump**

The enhanced SIMDOS 10 line of diaphragm liquid metering pumps is available with four head material options. The line affords laboratory personnel with simple operation, thanks to a user-friendly display and adjustable transfer parameters from a touch-control knob. The SIMDOS 10 FT version features a PTFE head, a PTFE-covered diaphragm, and chemically resistant FFKM Kalrez valves for the transfer of aggressive chemicals. An optional Chemraz-valve kit allows the pump to be used with highly concentrated acids such as nitric, sulphuric, and hydrochloric acids and solvents such as TFH, DMF, DMSO, and MEK. Also available with heads in PP, PVDF, or stainless steel, each pump in the SIMDOS 10 line transfers liquids with a flow rate of 1–100 mL/min, and dose volumes of 1 mL up to 999 mL. In addition to fast and simple calibration, the pump offers excellent long-term stability and consistent reliability throughout its lifetime.

**KNF Neuberger**

For info: 609-890-8600  
[www.knfusa.com/simdosis10](http://www.knfusa.com/simdosis10)

Electronically submit your new product description or product literature information! Go to [www.sciencemag.org/products/newproducts.dtl](http://www.sciencemag.org/products/newproducts.dtl) for more information.

Newly offered instrumentation, apparatus, and laboratory materials of interest to researchers in all disciplines in academic, industrial, and governmental organizations are featured in this space. Emphasis is given to purpose, chief characteristics, and availability of products and materials. Endorsement by *Science* or AAAS of any products or materials mentioned is not implied. Additional information may be obtained from the manufacturer or supplier.

# want new technologies?

antibodies

apoptosis

biomarkers

cancer

cytometry

data

diseases

DNA

epigenetics

genomics

immunotherapies

medicine

microbiomics

microfluidics

microscopy

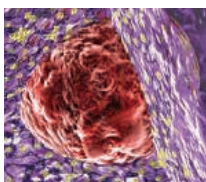
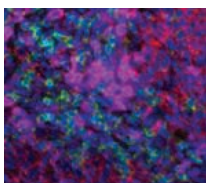
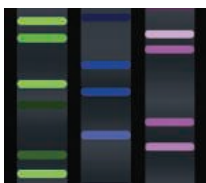
neuroscience

proteomics

sequencing

toxicology

transcriptomics



## watch our **webinars**

Learn about the latest breakthroughs, new technologies, and ground-breaking research in a variety of fields. Our expert speakers explain their quality research to you and answer questions submitted by live viewers.

**VIEW NOW!**

**[webinar.sciencemag.org](http://webinar.sciencemag.org)**

**Science**  
AAAS

Brought to you by the *Science*/AAAS  
Custom Publishing Office



@SciMagWebinars





2015 **MRS**® FALL MEETING & EXHIBIT  
November 29 – December 4, 2015 | Boston, Massachusetts

# CALL FOR PAPERS

Abstract Submission Opens May 18, 2015 | Abstract Submission Deadline June 18, 2015

- A Engaged Learning of Materials Science and Engineering in the 21<sup>st</sup> Century

## BIOMATERIALS AND SOFT MATERIALS

- B Stretchable and Active Polymers and Composites for Electronics and Medicine  
C Tough, Smart and Printable Hydrogel Materials  
D Biological and Bioinspired Materials in Photonics and Electronics—Biology, Chemistry and Physics  
E Engineering and Application of Bioinspired Materials  
F Biomaterials for Regenerative Engineering  
G Plasma Processing and Diagnostics for Life Sciences  
H Multifunctionality in Polymer-Based Materials, Gels and Interfaces  
I Nanocellulose Materials and Beyond—Nanoscience, Structures, Devices and Nanomanufacturing  
J Wetting and Soft Electrokinetics  
K Materials Science, Technology and Devices for Cancer Modeling, Diagnosis and Treatment  
L Nanofunctional Materials, Nanostructures and Nanodevices for Biomedical Applications

## NANOMATERIALS AND SYNTHESIS

- M Micro- and Nanoscale Processing of Materials for Biomedical Devices  
N Magnetic Nanomaterials for Biomedical and Energy Applications  
O Plasmonic Nanomaterials for Energy Conversion  
P Synthesis and Applications of Nanowires and Hybrid 1D-0D/2D/3D Semiconductor Nanostructures  
Q Nano Carbon Materials—1D to 3D  
R Harsh Environment Sensing—Functional Nanomaterials and Nanocomposites, Materials for Associated Packaging and Electrical Components and Applications

## MECHANICAL BEHAVIOR AND FAILURE OF MATERIALS

- S Mechanical Behavior at the Nanoscale  
T Strength and Failure at the Micro- and Nanoscale—From Fundamentals to Applications  
U Microstructure Evolution and Mechanical Properties in Interface-Dominated Metallic Materials  
V Gradient and Laminate Materials  
W Materials under Extreme Environments (MuEE)  
Y Shape Programmable Materials

## ELECTRONICS AND PHOTONICS

- Z Molecularly Ordered Organic and Polymer Semiconductors—Fundamentals and Devices  
AA Organic Semiconductors—Surface, Interface and Bulk Doping  
BB Innovative Fabrication and Processing Methods for Organic and Hybrid Electronics  
CC Organic Bioelectronics—From Biosensing Platforms to Implantable Nanodevices  
DD Diamond Electronics, Sensors and Biotechnology—Fundamentals to Applications  
EE Beyond Graphene—2D Materials and Their Applications  
FF Integration of Functional Oxides with Semiconductors  
GG Emerging Materials and Platforms for Optoelectronics  
HH Optical Metamaterials—From New Plasmonic Materials to Metasurface Devices  
II Phonon Transport, Interactions and Manipulations in Nanoscale Materials and Devices—Fundamentals and Applications  
JJ Multiferroics and Magnetoelectrics  
KK Materials and Technology for Non-Volatile Memories

## ENERGY AND SUSTAINABILITY

- LL Materials and Architectures for Safe and Low-Cost Electrochemical Energy Storage Technologies  
MM Advances in Flexible Devices for Energy Conversion and Storage  
NN Thin-Film and Nanostructure Solar Cell Materials and Devices for Next-Generation Photovoltaics  
OO Nanomaterials-Based Solar Energy Conversion  
PP Materials, Interfaces and Solid Electrolytes for High Energy Density Rechargeable Batteries  
QQ Catalytic Materials for Energy  
RR Wide-Bandgap Materials for Energy Efficiency—Power Electronics and Solid-State Lighting  
SS Progress in Thermal Energy Conversion—Thermoelectric and Thermal Energy Storage Materials and Devices

## THEORY, CHARACTERIZATION AND MODELING

- TT Topology in Materials Science—Biological and Functional Nanomaterials, Metrology and Modeling  
UU Frontiers in Scanning Probe Microscopy  
VV *In Situ* Study of Synthesis and Transformation of Materials  
WW Modeling and Theory-Driven Design of Soft Materials  
XX Architected Materials—Synthesis, Characterization, Modeling and Optimal Design  
YY Advanced Atomistic Algorithms in Materials Science  
ZZ Material Design and Discovery via Multiscale Computational Material Science  
AAA Big Data and Data Analytics for Materials Science  
BBB Liquids and Glassy Soft Matter—Theoretical and Neutron Scattering Studies  
CCC Integrating Experiments, Simulations and Machine Learning to Accelerate Materials Innovation  
DDD Lighting the Path towards Non-Equilibrium Structure-Property Relationships in Complex Materials

- X *Frontiers of Material Research*

[www.mrs.org/fall2015](http://www.mrs.org/fall2015)

*The MRS/E-MRS Bilateral Conference on Energy will be comprised of the energy-related symposia at the 2015 MRS Fall Meeting.*

## Meeting Chairs

**T. John Balk** University of Kentucky  
**Ram Devanathan** Pacific Northwest National Laboratory  
**George G. Malliaras** Ecole des Mines de St. Etienne  
**Larry A. Nagahara** National Cancer Institute  
**Luisa Torsi** University of Bari "A. Moro"

## Don't Miss These Future MRS Meetings!

### 2016 MRS Spring Meeting & Exhibit

March 28 - April 1, 2016  
Phoenix, Arizona

### 2016 MRS Fall Meeting & Exhibit

November 27 - December 2, 2016  
Boston, Massachusetts

**MRS** MATERIALS RESEARCH SOCIETY®  
*Advancing materials. Improving the quality of life.*

506 Keystone Drive • Warrendale, PA 15086-7573  
Tel 724.779.3003 • Fax 724.779.8313  
info@mrs.org • www.mrs.org

# Comprehensive CRISPR/Cas9 Genome Engineering Services

## A SMART CHOICE FOR GENOME ENGINEERING

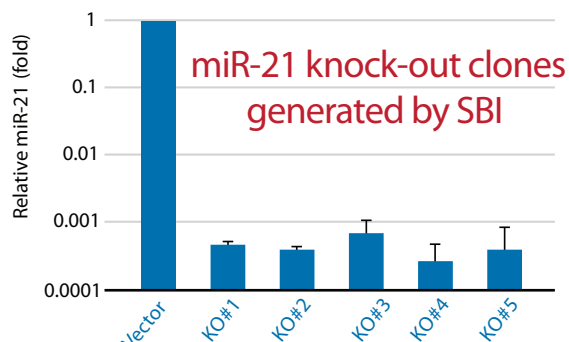
These days, it seems like CRISPR/Cas9 is everywhere. A simple yet powerful technology, CRISPR/Cas9 is already changing the way researchers are doing biology, and the work is only just beginning. But how can you quickly and easily apply this technology to your research? System Biosciences (SBI) has been providing CRISPR/Cas9 systems longer than any other commercial vendor, giving us an edge when it comes to direct experience with this game-changing technology. Because experience matters, your best choice for CRISPR/Cas9 services is SBI.

From the same experts who created our peer-reviewed Cas9 SmartNuclease & OnTarget HR Donor systems, SBI offers a full range of genome engineering services, all performed on-site at our state-of-the-art facility in Mountain View, CA to ensure the highest quality, confidentiality and timeliness of delivery.

### Services include:

- Guide RNA design and cloning
- HR donor design and cloning for knock-out, knock-in, tagging & editing
- Cell line engineering and validation

**FIND OUT MORE:**  
[www.systembio.com/cas9-services](http://www.systembio.com/cas9-services)



Ho, TT, et al. Targeting non-coding RNAs with the CRISPR/Cas9 system in human cell lines. Nucleic Acids Res. 2015 Feb 18; 43(3):e17.





## Science Careers Advertising

For full advertising details, go to [ScienceCareers.org](http://ScienceCareers.org) and click For Employers, or call one of our representatives.

**Tracy Holmes**  
Worldwide Associate Director  
*Science Careers*  
Phone: +44 (0) 1223 326525

### THE AMERICAS

E-mail: [advertise@sciencecareers.org](mailto:advertise@sciencecareers.org)  
Fax: 202 289 6742

**Tina Burks**  
Phone: 202 326 6577

**Nancy Toema**  
Phone: 202 326 6578

**Marci Gallun**  
Sales Administrator  
Phone: 202 326 6582

**Online Job Posting Questions**  
Phone: 202 312 6375

### EUROPE / INDIA / AUSTRALIA / NEW ZEALAND / REST OF WORLD

E-mail: [ads@science-int.co.uk](mailto:ads@science-int.co.uk)  
Fax: +44 (0) 1223 326532

**Axel Gesatzki**  
Phone: +44 (0) 1223 326529

**Sarah Lelarge**  
Phone: +44 (0) 1223 326527

**Kelly Grace**  
Phone: +44 (0) 1223 326528

### JAPAN

**Katsuyoshi Fukamizu** (Tokyo)  
E-mail: [kfukamizu@aaas.org](mailto:kfukamizu@aaas.org)  
Phone: +81 3 3219 5777

**Hiroyuki Mashiki** (Kyoto)  
E-mail: [hmashiki@aaas.org](mailto:hmashiki@aaas.org)  
Phone: +81 75 823 1109

### CHINA / KOREA / SINGAPORE / TAIWAN / THAILAND

**Ruolei Wu**  
Phone: +86 186 0082 9345  
E-mail: [rwu@aaas.org](mailto:rwu@aaas.org)

All ads submitted for publication must comply with applicable U.S. and non-U.S. laws. *Science* reserves the right to refuse any advertisement at its sole discretion for any reason, including without limitation for offensive language or inappropriate content, and all advertising is subject to publisher approval. *Science* encourages our readers to alert us to any ads that they feel may be discriminatory or offensive.

**ScienceCareers**  
FROM THE JOURNAL SCIENCE AAAS

[ScienceCareers.org](http://ScienceCareers.org)



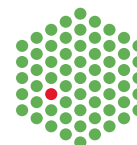
## Learn more and keep your job search out of the cheap seats.

- Search thousands of job postings
- Create job alerts based on your criteria
- Get career advice from our Career Forum experts
- Download career advice articles and webinars
- Complete an individual development plan at "myIDP"

Target your job search using relevant resources  
on **ScienceCareers.org**.

**ScienceCareers**  
FROM THE JOURNAL SCIENCE AAAS

EMBL



*The European Molecular Biology Laboratory offers a highly collaborative, uniquely international culture. It fosters top quality, interdisciplinary research by promoting a vibrant environment consisting of young independent research groups with access to outstanding graduate students and postdoctoral fellows. Significant core funding and limited teaching responsibilities allow EMBL group leaders to undertake ambitious, farsighted research programmes and provide a scientific environment that is particularly attractive for researchers with families.*

## Group Leader / Team Leader Genome Biology and Proteomics at EMBL Heidelberg, Germany

The European Molecular Biology Laboratory (EMBL) is renowned for its innovative, interdisciplinary research conducted in an open, international culture. The Headquarters is located in Heidelberg (Germany), with additional sites in Grenoble (France), Hamburg (Germany), Hinxton (UK) and Monterotondo (Italy).

The Genome Biology Unit studies all aspects of how the genome gives rise to phenotype. It is a highly interdisciplinary department, including groups with expertise in genomics, proteomics, computer science, microfluidics and chemistry, which provides a collaborative and supportive environment to perform cutting edge research. The research focusses on dissecting fundamental principles of how different layers of molecular information (DNA, RNA, Protein, Metabolites) are regulated and interconnected to give rise to diverse phenotypes.

We are looking for outstanding candidates in proteomics and biological mass spectrometry. The position involves running an independent research group within the Genome Biology Unit, developing and applying cutting edge mass spectrometry approaches. We particularly encourage candidates with interests in chromatin biology, regulation of gene expression, posttranslational protein modifications, quantitative or dynamic proteomics or any aspect linking genotype to phenotype. EMBL has an excellent proteomic core facility that provides mass spectrometry service to biological research groups. In addition to running a research group, the position also involves managing this facility and ensuring that the technologies it offers remain at the cutting edge.

EMBL is an inclusive, equal opportunity employer offering attractive conditions and benefits appropriate to an international research organisation with a very collegial and family friendly atmosphere. The remuneration package comprises from a competitive salary, a comprehensive pension scheme, medical, educational and other social benefits, as well as financial support for relocation and installation, including family, and the availability of an excellent child care facility on campus.

Please apply online through [www.embl.org/jobs](http://www.embl.org/jobs) and include a cover letter, CV and a concise description of research interests and future research plans. Please also arrange for 3 letters of recommendation to be emailed to [references@embl.de](mailto:references@embl.de) at the latest by 28 June 2015.

**Interviews** are planned for September 2015.

Further information about the position can be obtained from the Head of Unit Eileen Furlong ([eileen.furlong@embl.de](mailto:eileen.furlong@embl.de)).

An initial contract of 5 years will be offered to the successful candidate. This is foreseen to be extended to a maximum of 9 years, subject to an external review.

Further details on Group Leader appointments can be found under [www.embl.org/gl\\_faq](http://www.embl.org/gl_faq).

[www.embl.org](http://www.embl.org)





Special Job Focus:  
**Biotechnology**  
June 12, 2015

Reserve space by June 8\*

THERE'S A SCIENCE TO REACHING SCIENTISTS.

For recruitment in science, there's only one

**Science**

**What makes *Science* the best choice?**

- Read and respected by 570,400 readers around the globe
- 78% of readers read *Science* more often than any other journal
- Your ad sits on specially labeled pages to draw attention to the ad
- Your ad dollars support AAAS and its programs, which strengthens the global scientific community.

**Why choose this biotechnology section for your advertisement?**

- Relevant ads lead off the career section with special Biotechnology banner
- Bonus distribution to:  
 BIO International Convention  
 June 15–18, 2015, Philadelphia, PA  
 BIO Career Fair  
 June 18, 2015, Philadelphia, PA.

**Expand your exposure. Post your print ad online to benefit from:**

- Link on the job board homepage directly to biotechnology jobs
- Dedicated landing page for jobs in biotechnology
- Additional marketing driving relevant job seekers to the job board.



\* Ads accepted until June 8 on a first-come, first-served basis.

SCIENCECAREERS.ORG

**ScienceCareers**

FROM THE JOURNAL SCIENCE  AAAS

To book your ad: [advertise@sciencecareers.org](mailto:advertise@sciencecareers.org)

The Americas  
202-326-6582

Europe/RoW  
+44(0)1223-326500

Japan  
+81-3-3219-5777

China/Korea/Singapore/Taiwan  
+86-186-0082-9345



**Save the date**

**eci**

4th European Congress of Immunology  
Vienna 2015

September 6-9 / Vienna waits for you!

Register until June 30, 2015  
and benefit from  
reduced registration fees!  
[www.eci-vienna2015.org](http://www.eci-vienna2015.org)

4<sup>th</sup> European Congress of Immunology  
Vienna, Austria  
September 6-9 **2015**



European Federation of  
Immunological Societies

Under the auspices of EFIS, European Federation of Immunological Societies  
[www.efis.org](http://www.efis.org)  
and the Austrian Society for Allergy and Immunology, ÖGAI  
[www.oegai.org](http://www.oegai.org)

## UC San Diego

### Assistant, Associate, or Full Professor, Pulmonary Biology Investigator (10-971)

#### School of Medicine - Pediatrics

**Salary:** Salary is commensurate with qualifications and based on University of California pay scales

**Closing Date:** Review of applications will begin June 26, 2015, and continue until the position is filled.

**Job Description:** The Division of Pediatric Respiratory Medicine at the UCSD School of Medicine (<http://www-pediatrics.ucsd.edu/>) and Rady Children's Hospital of San Diego (<http://www.rchsd.org>) is committed to academic excellence and diversity within the faculty, staff, and student body. The program is seeking a full-time, innovative and productive Pulmonary Biology Investigator to join a highly collaborative research program.

The position will require a PhD, MD or MD/PhD degree or equivalent, and sufficient experience beyond postdoctoral training to have, or to be competitive to achieve, an independent NIH funded program in pulmonary research. The applicant will be provided with a competitive start-up package, including independent laboratory and office space within the UCSD School of Medicine in conjunction with ample protected time for research. He/she will be expected to maintain an independent research program. Preference will be given to applicants who can be involved in bench to bedside translation of discoveries in pulmonary diseases, and those who have a strong track record of successful mentoring. The rank and series of appointment, including the possibility of tenure, will be based on the successful candidate's skills, qualifications and funding.

**To Apply:** Please apply via <http://apptrkr.com/201523228>

The University of California is an Equal Opportunity/Affirmative Action Employer. All qualified applicants will receive consideration for employment without regard to race, color, religion, sex, national origin, disability, age or protected veteran status.



The EGL Charitable Foundation  
invites you to apply to the  
**Gruss Lipper Post-Doctoral  
Fellowship Program**

#### Eligibility

- Israeli citizenship
- Candidates must have completed PhD and/or MD/PhD degrees in the Biomedical Sciences at an accredited Israeli University/Medical School or be in their final year of study
- Candidates must have been awarded a postdoctoral position in the U.S. host research institution.

**Details regarding the fellowship are available  
at [www.eglcf.org](http://www.eglcf.org)**

NW210508R



By Rachel Bernstein

# All in the family

**R**enee JiJi and Jason Cooley work together at the University of Missouri (MU), Columbia, and have a daughter at home. The two met in graduate school and got married when they were postdocs living apart—she in Washington, D.C., and he in Philadelphia. JiJi began a tenure-track faculty position in the MU chemistry department in 2005; Cooley followed suit a year and a half later. JiJi and Cooley sat down for a conversation about working with a spouse and their different experiences traveling similar paths. Their comments have been edited for brevity and clarity.

**JiJi:** Work morphs in and out of the conversations at home. You have an idea while you're drinking coffee in the morning and you have someone to talk to about it, and that's kind of nice. We study protein folding and dynamics, and our work has become very collaborative. We both have very distinct research agendas, but collaboration has worked really well because we have different backgrounds. But sometimes I think our colleagues see us as a unit rather than as two different people, even though we do the work of two people.

**Cooley:** Certainly during each of our tenure processes, there was criticism that we had not worked independently enough.

**JiJi:** I went on the job market, just to test the waters, and happened to get an offer. I took the job here with the understanding that they had mechanisms for spousal accommodation and that, hopefully, would materialize into a position for Jason.

**Cooley:** I still had a year of postdoc funding left. Then I moved to Missouri and they gave me a courtesy appointment, with no money or lab space. Renee graciously shared her office with me. It was only after I got an informal offer from another university that negotiations about a tenure-track job here started in earnest.

I'm the trailing spouse, but my initial salary was based on Renee's salary, plus some small amount because it was inconceivable that I would make less than my wife. It was literally said that way. I said, "Fine, that's more money for us," but maybe I should have said it wasn't appropriate.

My colleagues ask me out for beer every once in a while; that certainly wouldn't happen for Renee.



*"[T]here was criticism that we had not worked independently enough."*

**JiJi:** I don't ever get asked out. My department chair once said to me, "I don't even know you," and I had no idea what that meant. I thought, "You can read my papers. You can talk to me." But it's true. Jason went out and played golf with him once, but nobody's going to invite me out for a beer or to coffee even. Female faculty members go out to coffee with female faculty members. There isn't socialization between male and female faculty members. It just doesn't happen.

**Cooley:** We always said that we'd have a kid when we lived in the same state. Our daughter was born in 2007.

**JiJi:** When I came up for tenure, my tenure extension for the birth of our daughter was held against me. I was expected to have been more productive than my colleagues—not just as productive.

**Cooley:** It was couched as, she was as productive as the other people, but she had an extra year. I didn't take a tenure extension for having a child. I was told not to.

**JiJi:** If I had waited until I had tenure to have kids, it never would have happened. After our daughter was born, I had three miscarriages. Every one of them was horrific. The hormonal shifts were huge and somewhat debilitating, and I decided, for the sake of my career, to not continue to try to have another child. I was in the second half of my 30s, and I think I just waited too long. I tell my grad students that they shouldn't postpone having a family for their career because they never know what their future is going to be. ■

*Rachel Bernstein is a staff writer for Science Careers. For more on life and careers, visit [ScienceCareers.org](http://ScienceCareers.org). Send your story to [SciCareerEditor@aaas.org](mailto:SciCareerEditor@aaas.org).*